UNIVERSIDAD Ð CÓRDOBA

Tesis Doctoral

"Nuevos materiales híbridos para electrodo negativo en baterías de ion litio basados en compuestos de estaño o titanio modificados con carbono o poliacrilonitrilo"

Francisco José Nacimiento Cobos

Directores: Prof. Dr. Ricardo Alcántara Román
Prof. Dr. Pedro Lavela Cabello

Departamento de Química Inorgánica e
Ingeniería Química
Universidad de Córdoba
2013

TITULO: *Nuevos materiales híbridos para electrodo negativo en baterías de ión litio basados en compuestos de estaño o titanio modificados con carbono o poliacrilonitrilo*

AUTOR: *Francisco José Nacimiento Cobos*

INFORME RAZONADO DE LOS DIRECTORES DE LA TESIS

D. Ricardo Alcántara Román y D. Pedro Lavela Cabello, ambos Profesores Titulares del Departamento de Química Inorgánica e Ingeniería Química de la Universidad de Córdoba, informan que la Tesis Doctoral presentada por D. Francisco José Nacimiento Cobos y titulada

"Nuevos materiales híbridos para electrodo negativo en baterías de ion litio basados en compuestos de estaño o titanio modificados con carbono o poliacrilonitrilo"

ha sido desarrollada bajo su dirección en los laboratorios del Departamento de Química Inorgánica e Ingeniería Química de la Universidad de Córdoba durante el disfrute de un contrato de investigación (Proyecto PET2005_0670_01), otro contrato de investigación adscrito al proyecto CTQ2008-03192 y una "Beca de Formación de Personal Docente e Investigador de la Junta de Andalucía en áreas de conocimiento consideradas deficitarias por necesidades docentes" asociada al grupo de investigación FQM-288 del P.A.I., y que a su juicio reúne todos los requisitos exigidos a este tipo de trabajo, como se puede constatar por ejemplo en los artículos publicados en revistas científicas con índice de calidad relativo y en los cuales el doctorando es el primer autor.

Por todo ello, se autoriza la presentación de la tesis doctoral.

Córdoba, a 15 de octubre de 2013

Firma de los directores

Prof. Dr. Ricardo Alcántara Román   Prof. Dr. Pedro Lavela Cabello

Informe de los artículos publicados según el Journal Citation Report

Los artículos que se exponen en la presente memoria han sido publicados en revistas cuyos factores de impacto están recogidos en la siguiente tabla y según el Journal Citation Report de ISI web of Knowledge del año 2012:

Journal	Impact factor	Category	Total Journal in Category	Journal Rank in Category	Quartile in Category
Journal of electroanalytical chemistry	2.672	Chemistry, analytical	75	23	Q2
		Electrochemistry	26	10	Q2
Journal of the electrochemical society	2.588	Electrochemistry	26	11	Q2
		Materials science, coatings & films	17	1	Q1
Journal of power sources	4.675	Electrochemistry	26	3	Q1
		Energy & fuels	81	9	Q1
Materials chemistry and physics	2.072	Materials science, multidisciplinary	239	60	Q2
Journal of alloys and compounds	2.390	Chemistry, physical	134	56	Q2
		Materials science, multidisciplinary	239	48	Q1
		Metallurgy & metallurgical engineering	75	4	Q1
Journal of solid state electrochemistry	2.279	Electrochemistry	26	13	Q3
Ultrasonics sonochemistry	3.516	Acoustics	31	3	Q1
		Chemistry, multidisciplinary	152	38	Q2

"NUEVOS MATERIALES HÍBRIDOS PARA ELECTRODO NEGATIVO EN BATERÍAS DE ION LITIO BASADOS EN COMPUESTOS DE ESTAÑO O TITANIO MODIFICADOS CON CARBONO O POLIACRILONITRILO"

Trabajo presentado para aspirar al grado de Doctor en Química por:

Francisco José Nacimiento Cobos

Dirigido por:

Prof. Dr. Ricardo Alcántara Román   Prof. Dr. Pedro Lavela Cabello

Agradecimientos

Me gustaría mostrar mi agradecimiento a aquellas personas e instituciones que han contribuido a la realización de esta tesis doctoral.

En primer lugar, a los profesores Dr. Ricardo Alcántera Román y Dr. Pedro Lavela Cabello, como directores de tesis, por su dedicación y apoyo durante el período de investigación de la presente Tesis.

Al programa de doctorado "Materiales y energía", al grupo PAI FQM288 y al departamento de Química Inorgánica e Ingeniería Química de la Universidad de Córdoba por aceptarme como estudiante de tercer ciclo y permitir desarrollar mi labor investigadora.

A las diferentes instituciones que han financiado este proyecto, Ministerio de Educación y Ciencia (contratos MAT2008-05880 y MAT2011-22753), Ministerio de Ciencias e Innovación (contratos PET2005_0670_01 y CTQ2008-03192), Junta de Andalucía (proyecto de excelencia FQM-01447 y Beca FPDI).

A la empresa Repsol y al Instituto Nacional del Carbón (INCAR) por el suministro de muestras y posterior discusión de resultados dentro del proyecto PETRI (PET2005_0670_01).

Al Servicio Central de Apoyo a la Investigación (SCAI) de la Universidad de Córdoba, en especial a D. Francisco Gracia Alfonso, del Servicio de Microscopía Electrónica, a D. Juan Isidro Corredor Coca, del Servicio de

A mi hermana

María del Carmen

ÍNDICE

Capítulo 1.-

Introducción

1 Introducción

El consumo de energía es un indicador del desarrollo económico y social de cualquier país. Un análisis del consumo energético mundial pone en evidencia el fuerte crecimiento del mismo en la sociedad actual (Figura 1). Además, actualmente las principales fuentes de energía están basadas en combustibles fósiles, no son renovables, y su uso provoca dos grandes problemas principalmente. Por una parte, estos recursos son limitados y se encuentran desigualmente repartidos en la geografía, lo que genera grandes tensiones socio-económicas entre los países productores y consumidores. Por otro lado, el uso de combustibles fósiles genera emisiones contaminantes que ponen en peligro el equilibrio ecológico y el clima.

Una alternativa a los combustibles fósiles sería la producción de energía nuclear. Pero los graves efectos ambientales que pueden generar las fugas accidentales de radiación en las centrales nucleares y la formación de desechos radiactivos provocan fuertes movimientos sociales de rechazo hacia el uso de esta fuente de energía. Hoy en día se ha reducido el papel previsto para la energía nuclear tras la revisión de las políticas efectuadas por varios países a raíz del accidente en la central nuclear de Fukushima ocurrido en 2011 [1]. Además, el uranio es también un recurso no renovable.

Estas consideraciones conducen a la necesidad de utilizar fuentes de energía alternativas como son las denominadas energías renovables, las cuales son ilimitadas y más respetuosas con el medio ambiente ya que generan escasos o nulos residuos. Entre ellas destacan la solar y la eólica. Aunque las energias renovables suponen actualmente una parte relativamente pequeña del consumo total mundial, según algunos estudios se prevé que las energías renovables se conviertan en la segunda fuente de generación eléctrica en el mundo hacia 2015, con una contribución aproximadamente equivalente a la mitad del carbón y que finalmente se acerque al carbón como la fuente primaria de generación de electricidad el año 2035 [1]. Otros autores estiman que las energías renovables supondrán casi un tercio de la producción total de electricidad para el año 2035. Uno de los problemas que genera el uso de este tipo de fuentes de energía es su discontinuidad a lo largo del tiempo, lo que es un obstáculo para su empleo generalizado. Por todo ello, se hace necesario el uso de dispositivos que almacenen el exceso de energía producida en determinados periodos para emplearlo en aquellos

momentos en los que la fuente está inactiva. El uso de baterías se ha propuesto como sistema de almacenamiento eficaz de energía debido a que presentan numerosas ventajas [2]. Se requieren tiempos relativamente cortos de fabricación, pueden diseñarse en múltiples formas y tamaños según su aplicación, su potencia y capacidad, son adaptables a las necesidades, y se transportan fácilmente. Además del amplio uso en sistemas electrónicos portátiles como ordenadores, teléfonos móviles, y videocámaras, también se está generando un interés importante en el empleo de baterías de ión litio en vehículos eléctricos. Todo ello podría contribuir favorablemente a reducir las emisiones de CO_2 provenientes del uso de combustibles fósiles. Para tener éxito en este objetivo se requiere un avance en la investigación y el desarrollo de nuevos materiales que proporcionen alta densidad de energía, larga vida útil, recarga más rápida y menor coste de la batería.
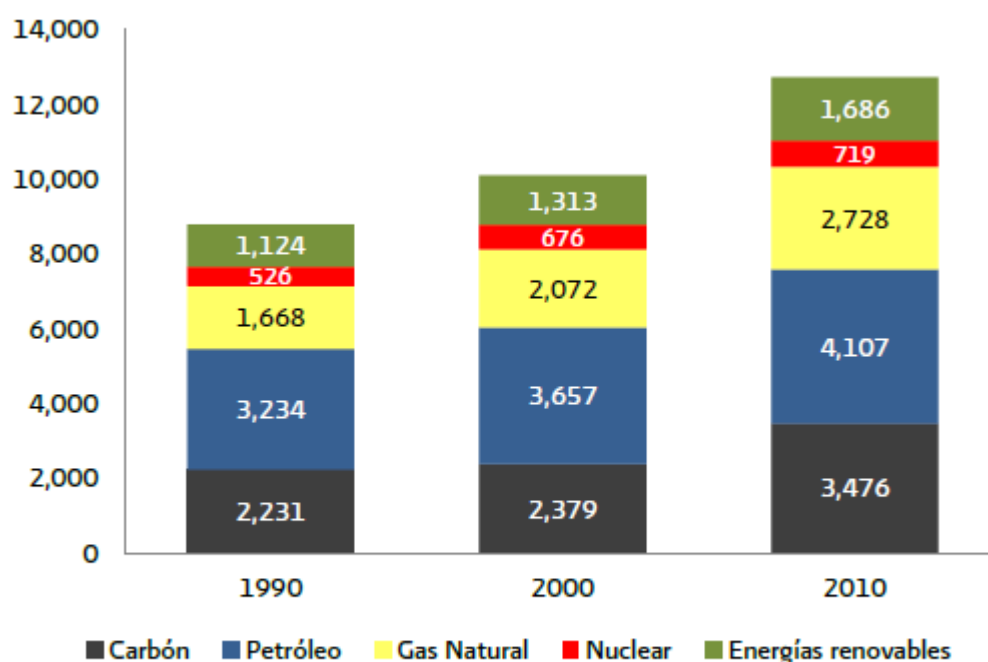
Fuente: *International Energy Agency. 2012. World Energy Balances.*

Figura 1. Distribución de las fuentes mundiales de energía 1990-2010 (millones de toneladas de petróleo equivalente al año).

1.1 Celda galvánica.

El término batería se aplica al conjunto de celdas galvánicas que, conectadas en serie o en paralelo, proporcionan el voltaje o densidad de corriente requerida, transformando reversiblemente la energía química en energía eléctrica. Cada celda está compuesta por un electrodo positivo, o cátodo, y otro negativo, o ánodo, en los que se producen las reacciones electroquímicas [3-9]. Ambos electrodos están separados por una disolución de un electrolito que permite la transferencia de iones entre los electrodos, a la vez que impide la transferencia de electrones a través de ella.

Durante la descarga de la celda galvánica, el ánodo se oxida cediendo electrones al circuito externo para generar una fuerza electromotriz. Por su parte, el cátodo recibe los electrones desde el circuito para reducirse. Esta transferencia de carga eléctrica es compensada por la migración de iones a través del electrolito. Por tanto, el electrolito debe ser un medio que favorezca la conductividad iónica y, simultáneamente, impida la conductividad electrónica. Por ello, en el campo de investigación de las baterías, se persigue elegir la mejor combinación de estos elementos de forma que permitan almacenar gran cantidad de energía en un tamaño y peso reducidos.

Los sistemas electroquímicos de almacenamiento de energía pueden clasificarse en:

- Sistemas no recargables, usualmente conocidos como pilas o baterías primarias, los cuales son capaces de liberar energía directamente después de su ensamblaje y se distinguen por su uso en una sola descarga**.** Como ejemplo podemos citar las llamadas pilas alcalinas.

- Sistemas recargables, acumuladores o baterías secundarias, son los que presentan la posibilidad de ser recargados mediante la aplicación de una fuerza electromotriz, consecuentemente, su vida útil es larga ya que se pueden someter a numerosos procesos de carga y descarga.

Las características principales que debe poseer una batería son: alta densidad de almacenamiento de energía por unidad de volumen y/o de masa, elevado número de ciclos de carga-descarga y bajo coste. El elevado potencial reductor del litio (-3.05 V)

permite obtener baterías con gran densidad de energía. Esta característica hace que las baterías de litio metálico sean dispositivos interesantes para su uso en aparatos electrónicos portátiles, por lo que presentaron un amplio mercado hace unas décadas. Sin embargo, el litio metal presenta serios inconvenientes para ser usado directamente como ánodo. Así pues, podemos citar la falta de seguridad que supone el manejo de metales fuertemente reductores. Otro efecto adverso son las reacciones irreversibles que tienen lugar en la superficie del ánodo de litio en contacto con el electrolito. El resultado en ciclos prolongados es la formación de ramificaciones dendríticas que crecen hacia el electrodo positivo perforando el separador y llegando a cortocircuitar la celda. El esfuerzo para resolver estos problemas condujo hacia un nuevo diseño: las baterías de ión-litio.

1.2 Batería de ión litio.

El concepto de batería ión-litio se basa en la sustitución del ánodo de litio metal por un material capaz de reaccionar reversiblemente con el litio a potenciales cercanos a 0 V frente al par redox Li^+/Li [9]. Se han propuesto diversas familias de materiales anódicos capaces de reaccionar reversiblemente con el litio a través de variados mecanismos. Así podemos citar el empleo de grafito capaz de insertar reversiblemente litio en el espacio interlaminar y los compuestos intermetálicos de estaño y silicio que reaccionan con el litio mediante un mecanismo de aleación [9]. Por otro lado, se ha descrito la reacción reversible con óxidos y oxisales de metales de transición, principalmente Co, Fe, Ni y Cu, mediante el mecanismo de conversión [10-12]. De este modo, se evitan los inconvenientes asociados al uso de un elemento alcalino en estado metálico.

En el esquema clásico de las baterías de ión-litio $LiCoO_2/C_6$, el ión alcalino forma parte inicialmente de la estequiometría del material catódico, mientras que el ánodo está constituido por grafito (Figura. 2). En el proceso de carga, el litio se transfiere desde el cátodo hacia el material anódico, inducido por la aplicación de una fuerza electromotriz externa. Posteriormente, la batería puede iniciar el proceso de descarga por el que espontáneamente los iones alcalinos vuelven al cátodo simultáneamente a la transferencia electrónica a través del circuito externo, produciéndose la liberación de energía.
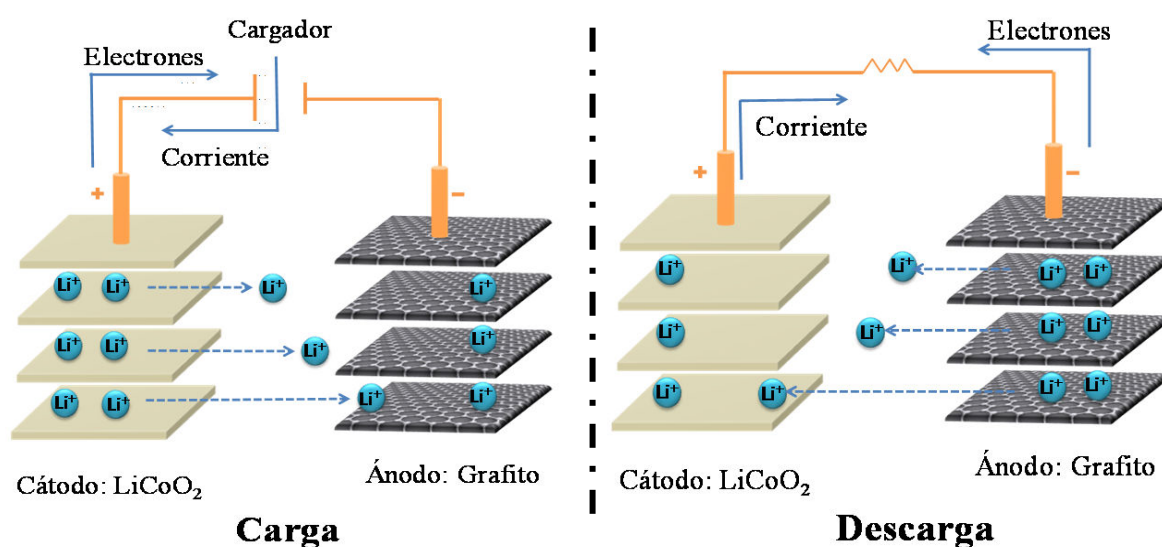
Figura 2. Esquema del funcionamiento de una batería de ión-litio. El cátodo (electrodo positivo) suele ser el LiCoO₂, y el ánodo (electrodo negativo) es el grafito u otro material de carbono.

Las baterías de ión-litio se han comercializado en parte gracias a los esfuerzos de la empresa Sony Energytec, que las introdujo en el mercado en 1992. Así las baterías de ión litio desarrolladas contenían $LiCoO_2$ como electrodo positivo, y un material de carbono (grafito o coque) como electrodo negativo. Autores como Winter y col. [9], han publicado una revisión de los conceptos fundamentales y nuevas perspectivas en este campo. Como materiales catódicos alternativos al $LiCoO_2$ podemos citar $LiNiO_2$, $LiMn_2O_4$ y $LiCoPO_4$, $LiFePO_4$ [9]. Aunque los materiales de carbono son los más usados como electrodo negativo, la limitada capacidad específica liberada por el grafito ha llevado a la investigación de otros materiales que contienen elementos que bien forman aleaciones con el litio o que conducen a reacciones de conversión con el litio los cuales poseen una mayor capacidad específica que los materiales carbonosos [13,14].

En la Figura 3 se representan algunos de los materiales más representativos estudiados en baterías de ión-litio, representando el potencial de operación frente al litio con respecto a las capacidades gravimétricas aportadas por cada uno de los materiales respectivamente.
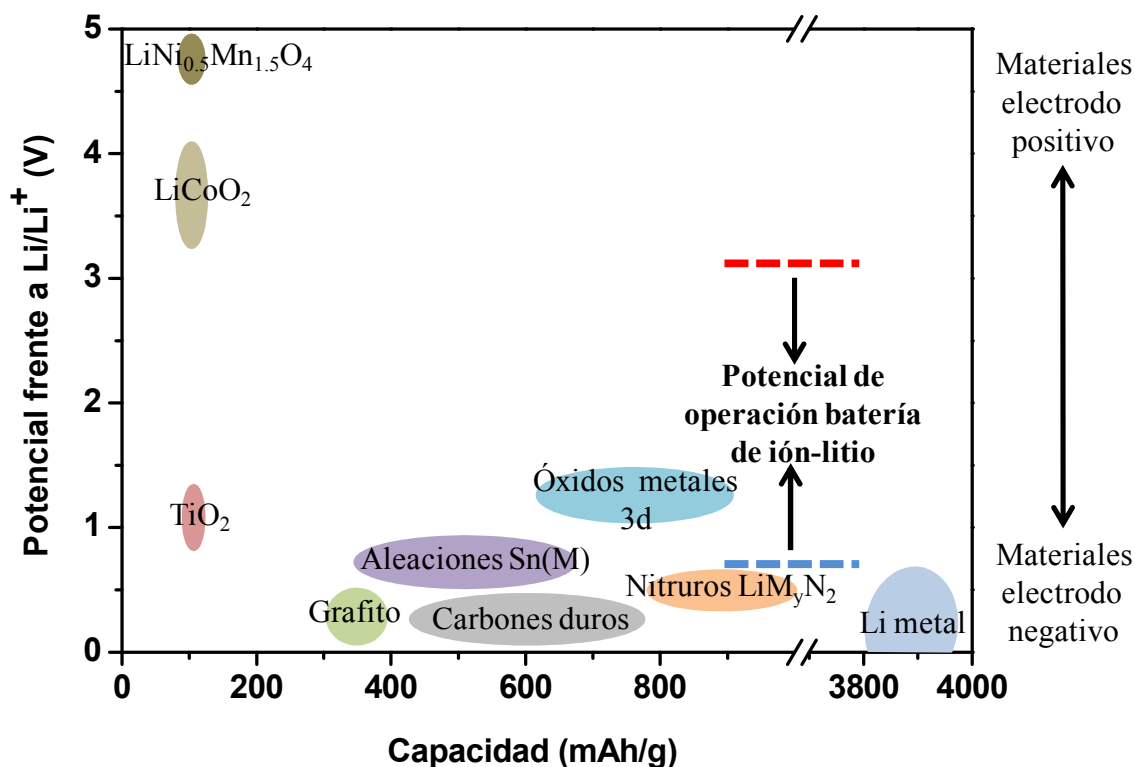
Figura 3. Representación de los principales tipos de materiales usados o potencialmente utilizables como material electrodo en baterías de ión litio [modificada de la referencia número 15].

1.3. Materiales como electrodo negativo en baterías de ión litio

Debido a que esta tesis doctoral está enfocada al estudio de nuevos materiales usados como electrodo negativo en baterías de ión-litio, profundizaremos más en la revisión de la literatura de los electrodos negativos.

1.3.1. Materiales carbonosos.

Los materiales anódicos más ampliamente empleados en las baterías de ión-litio comerciales son los materiales derivados del carbono que incluyen materiales de alta temperatura como el grafito, y de baja temperatura como los coques (turbostráticos, blandos y grafitizables) y los carbonos duros (no grafitizables). El grafito es la opción preferida habitualmente debido al bajo voltaje de trabajo y a la estabilidad de la capacidad durante un largo número de ciclos [16,17]. Pero, la limitada capacidad teórica (372 mAh/g) del grafito es un gran inconveniente para desarrollar nuevas baterías con mayor capacidad en un futuro próximo. Para superar esta limitación se proponen tratamientos que optimizan el rendimiento electroquímico tales como la oxidación superficial [18] y la fluoración [19], entre otros.

Para un material grafítico, es posible escribir la siguiente reacción de intercalación, en la que se alcanza un contenido máximo de un litio por cada seis átomos de carbono:

$$\text{Li}^+ + \text{e}^- + \text{C}_6 \leftrightarrows \text{LiC}_6$$
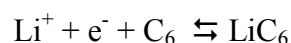
El proceso de intercalación se desarrolla a lo largo de una serie de platós a unos 0.3-0.1 voltios respecto al potencial del par Li^+/Li. Este voltaje implica la posibilidad de que pequeñas cantidades de litio metal se depositen sobre la superficie del carbono mediante electrodeposición, lo que a veces conlleva problemas de seguridad. Materiales de carbono desordenados pirolizados a baja temperatura, como los coques pueden paliar este problema ya que operan a voltajes algo superiores a los del grafito. Por otra parte, la existencia de sitios adicionales para la unión del litio es una característica interesante de los materiales de carbono no grafitizables.

1.3.2. Compuestos intermetálicos de litio-metal.

La limitada capacidad específica liberada por el grafito y ciertos problemas de seguridad anteriormente mencionados han llevado a la búsqueda de materiales alternativos. Algunos metales reaccionan reversiblemente con el litio conduciendo a la formación reversible de aleaciones proporcionando capacidades superiores a la del grafito, según la reacción general:

$$x \, Li^+ + e^- + y \, M \; \leftrightarrows \; Li_x M_y$$

La reacción electroquímica de aleación suele transcurrir por debajo de 1 V pero a potenciales suficientemente mayores que cero para evitar el problema de la formación de dendritas observado en el grafito [20,21]. Sabemos que numerosos metales, como por ejemplo Al, Si y Sn, se pueden combinar con el litio para formar compuestos intermetálicos [9]. Wang y colaboradores, obtuvieron los diferentes potenciales de plató y rangos de composiciones a temperatura ambiente para diferentes sistemas Li-M, Tabla 1 [22]. Estos compuestos intermetálicos, en principio son ánodos ideales para su empleo como ánodos en baterías de ión litio debido a que pueden almacenar y liberar gran cantidad de litio, garantizan altos potenciales de trabajo cuando se combinan con el litio y proporcionan valores de capacidad específica superior al grafito. Panero y colaboradores recogieron las capacidades específicas teóricas para algunos de estos compuestos intermetálicos como electrodos en baterías de ión litio (Tabla 2) [23]. Entre ellos destacamos el estaño por su bajo coste, baja toxicidad y una capacidad máxima teórica de 994 mAh/g, más del doble de la proporcionada por el grafito.

El principal problema que tienen estos materiales es la expansión de volumen que se produce durante el proceso reversible de aleación. El repetido proceso de expansión y contracción, que se sucede durante el ciclado de la celda, origina la ruptura de las partículas del material activo lo que daría lugar a la pérdida de contacto eléctrico con el colector de corriente y por lo tanto, a una pérdida continuada de la capacidad durante el ciclado (Figura 4).

Tabla 1. Potencial frente al litio para diferentes rangos de composición de diferentes sistemas a 25 ºC [22].

E vs Li	Sistema	Rango de y
0.053	Li_yCd	1.50 - 2.0
0.157	Li_yZn	0.67 - 1.0
0.219	Li_yZn	0.5 - 0.67
0.292	Li_yPb	3.4 - 4.4
0.350	Li_yCd	0.5 - 0.8
0.380	Li_ySn	3.5 - 4.4
0.385	Li_yAl	0.0 - 1.0
0.420	Li_ySn	2.6 - 3.5
0.449	Li_yPb	1.0 - 3.0
0.485	Li_ySn	2.33 - 2.63
0.530	Li_ySn	0.7 - 2.33
0.601	Li_yPb	0.0 - 1.0
0.660	Li_ySn	0.4 - 0.7
0.680	Li_yCd	0.0- 0.36
0.810	Li_yBi	1 - 3
0.828	Li_yBi	0 - 1
0.948	Li_ySb	2 - 3
0.956	Li_ySb	0 - 2

Tabla 2. Capacidad específica teórica para algunos compuestos intermetálicos. Por comparación también se incluye LiC_6 [23].

Metal No Litiado	Metal Totalmente Litiado	Capacidad Gravimétrica (mAh/g)	Capacidad Volumétrica (mAh/cm³)
Al	LiAl	993	1.374
Si	$Li_{21}Si_5$	4008	2.323
Sn	$Li_{22}Sn_5$	994	2.025
Sb	Li_3Sb	660	1.881
C,grafito	LiC_6	372	0.760
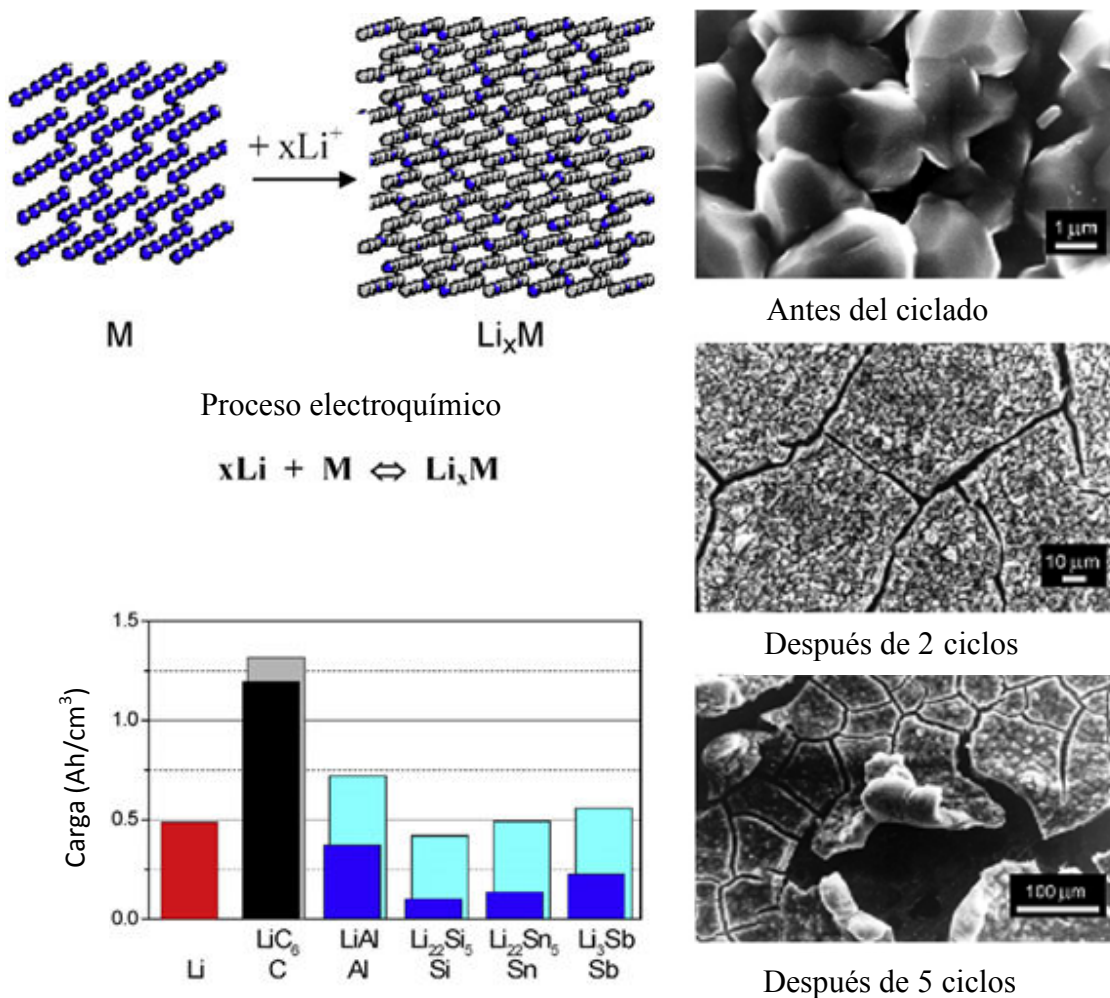
Figura 4. Efectos del cambio de volumen asociado al proceso de carga y descarga en electrodos que forman aleaciones en celdas de litio. Se muestra el esquema de la inserción del ión Li y los respectivos cambios de volumen durante la descarga (después de 2 y 5 ciclos respectivamente) mostrados por las imágenes de SEM para el estaño. Así como la comparación de los cambios de volumen producidos en el material original (columnas de color oscuro) con respecto al material con el Li intercalado (columnas de color claro) para varios metales [24].

Para evitar este efecto, se han propuesto diversas soluciones que abarcan desde la combinación del metal en óxidos o sales [25-27], la combinación con otros metales [28,29], la nanoestructuración del metal [30-32] la formación de materiales compuestos metal-carbono [33-43] y la preparación de películas finas por el método de electrodeposición [44-55]. En muchos de estos casos, la presencia de fases electroquímicamente no activas, que amortiguan la expansión volumétrica del metal y evitan la agregación, mejoran notablemente el rendimiento del material.

El uso de nanoestructuras es un método popular para mejorar la respuesta electroquímica de estos electrodos. Es de esperar que el tamaño nanométrico proporcione: (1) un área superficial grande, lo cual permite una gran superficie de contacto con los iones litio a través del electrolito, lo que conduce a altas velocidades de descarga y carga; (2) distancias cortas para el transporte de litio, resultando un aumento de la potencia; y (3) la disminución de las tensiones producidas en la inserción y desintercalación de litio, lo cual mejora el ciclado electroquímico.

Tirado y colaboradores dedujeron que nanopartículas de $FeSn_2$ forman un electrodo estable que proporciona mejor comportamiento electroquímico, que el electrodo basado en micro-$FeSn_2$ el cual tiene muy poca estabilidad [56]. Por otro lado, es sabido que aleaciones amorfas y de escala nanométrica utilizadas como electrodos negativos para baterías de ion litio muestran mejor comportamiento durante el ciclado que los materiales cristalinos. Uno de los métodos para obtener materiales amorfos de tamaño nanométrico es hacer uso de la sonoquímica. Por ejemplo, Chen y colaboradores describen la preparación de nanopartículas de estaño y bismuto los cuales se funden conjuntamente [57]. Por otro lado, Qiu y colaboradores sintetizaron nanovarillas de estaño usando un método sonoquímico combinado con un método poliol [58].

El uso de nanoestructuras, sin embargo, no es la solución definitiva, ya que estos materiales nanoestructurados también presentan una serie de inconvenientes, incluyendo: (1) una baja densidad aparente, por lo tanto el volumen del electrodo aumenta para la misma masa de material reduciendo la densidad de energía volumétrica; (2) una gran área superficial que conlleva a reacciones colaterales con el electrolito, así como también la posible pérdida de contacto eléctrico entre las partículas; y (3) riesgos e inseguridad asociado a la tendencia a la inflamabilidad y la explosividad de los

metales en forma de nanopolvo. Por otro lado, las nanopartículas tienden a agregarse durante el ciclado, reduciendo al final el ciclo de vida de los electrodos.

A partir de ahí se han dirigido grandes esfuerzos al diseño de nuevos materiales. En particular se ha investigado el concepto de nano-compuestos activo/inactivo. Este concepto implica la íntima mezcla de dos materiales, uno que reacciona con el litio y otro inactivo frente al litio el cual proporciona un desorden estructural o encapsula al material activo evitando la expansión y contracción de volumen en el electrodo. Los sistemas Sn-MT-C (donde MT representa uno o varios metales de transición) son particularmente prometedores. Kawakami y Asao mostraron que de los diferentes sistemas Sn-MT estudiados, el sistema Sn-Co tenía mayor desorden estructural y por lo tanto proporcionaba un mayor rendimiento durante el ciclado [59]. Debido a factores de coste y medioambientales, la introducción de hierro en lugar de cobalto sería ventajoso, pero parece ser difícil lograr un buen comportamiento en el ciclado con aleaciones de estaño que no contengan cobalto [60].

1.3.3. Sistema binario Co-Sn

Existen diferentes fases conocidas para el sistema Co-Sn. Algunos autores han preparado y estudiado diversas fases estequiométricas de cobalto-estaño como CoSn, Co_3Sn_2 y $CoSn_2$ [61-63]. Recientemente ha sido descubierto el compuesto intermetálico $CoSn_3$. Alcántara y colaboradores, estudiaron su comportamiento electroquímico en baterías de ión litio [64].

El complejo diagrama de fases del sistema binario cobalto-estaño se muestra en la Figura 5. La fase β-Co_3Sn_2 funde coherentemente a 1180 ºC, es decir, el sólido y el líquido tienen la misma composición. Por el contrario, CoSn funde incoherentemente a 966 ºC, formando la fase sólida β-Co_3Sn_2 y un líquido (l). Para una composición, que es indicada por la gran flecha que apunta hacia abajo en el diagrama de fases (Figura 5). Si un fundido con una relación Co:Sn de aproximadamente 1:3 es enfriado, la línea del líquido se alcanzará a 966 ºC obteniéndose CoSn. En un enfriamiento adicional, el compuesto CoSn se cristaliza hasta que la muestra llega a 571 ºC. A esta temperatura reacciona con el líquido para formar $CoSn_2$. El problema es que la fase formada envuelve a la sustancia reaccionante CoSn. Por lo tanto, esta reacción ahora proseguirá

solo por difusión a través de la envoltura sólida de $CoSn_2$. Este proceso de difusión toma tiempo y puede que no termine antes que la muestra alcance la próxima temperatura de equilibrio de 345 ºC. A esa temperatura se forman cristales de β-$CoSn_3$. El fundido cambia su composición continuamente, hasta un punto donde se solidifica a la temperatura de 229 ºC formándose una disolución sólida de Co en β-Sn con inclusiones de α-$CoSn_3$.
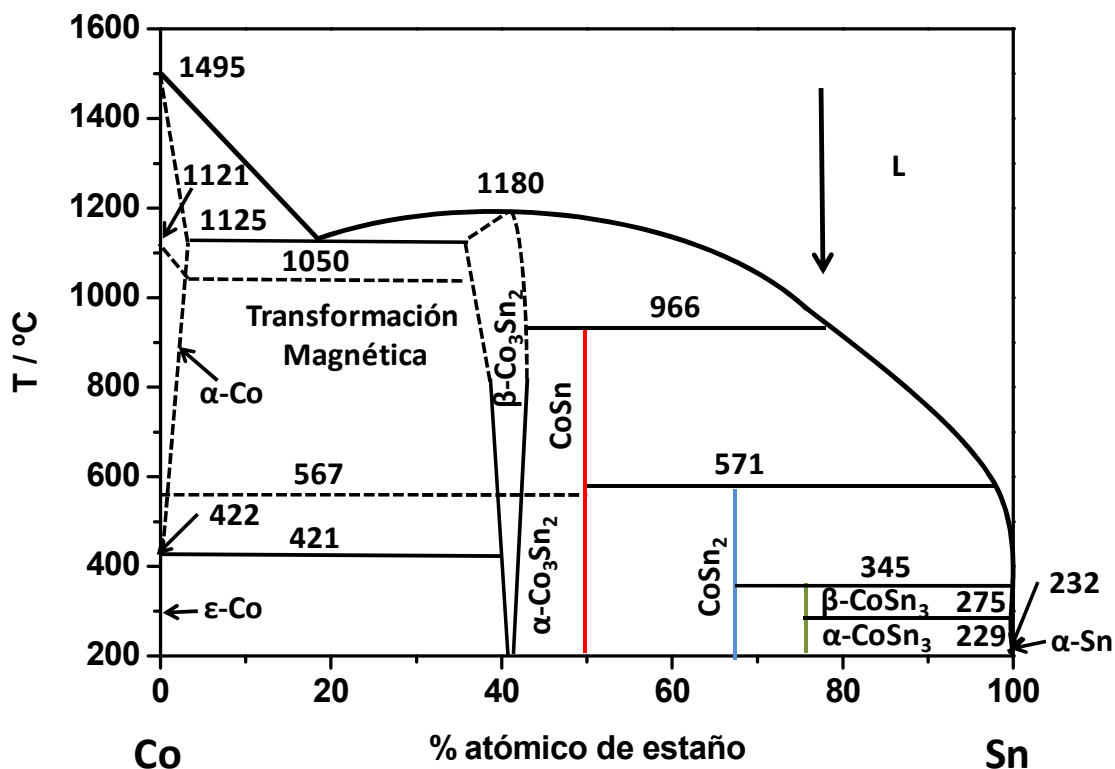
Figura 5. Diagrama de fases binario para el sistema cobalto-estaño (modificada de la referencia número 65).

El comportamiento electroquímico del sistema de Co-Sn difiere mucho de una fase a otra y está también fuertemente influenciado por el tamaño de partícula. Así, las fases ricas en estaño proporcionarán mayor capacidad que las fases pobres en estaño. Ferguson y colaboradores dedujeron que no todas las fases Co-Sn contribuyen positivamente al comportamiento electroquímico de la celda, así pues fases cristalinas ricas en cobalto y con tamaño de grano elevado como Co_3Sn_2 y CoSn tienen poca capacidad para reaccionar electroquímicamente con el litio [66,67].

31

1.3.4. Materiales compuestos de litio-metal-carbono

La encapsulación de partículas basadas en estaño o compuestos de estaño mediante materiales carbonosos es una solución a tener en cuenta para mejorar el comportamiento durante el ciclado en baterías de ión litio [9-14]. Las matrices no metálicas protegen a las partículas intermetálicas contra el consumo irreversible de electrolito, amortiguan los cambios de volumen [36], mejoran la conexión eléctrica entre las partículas [36] y evitan la agregación de partículas durante el ciclado [37]. Dahn y colaboradores, publicaron que la adición de carbono a aleaciones amorfas de Co-Sn para dar lugar a sistemas Co-Sn-C amorfo producen materiales con grandes capacidades reversibles (hasta unos 700 mAh/g) y excelente resistencia a la agregación del estaño durante el ciclado [32].

La empresa Sony lanzó en 2005 una batería de ión-litio que utiliza un ánodo que contiene una aleación amorfa de estaño y cobalto y carbono [68]. Todd y colaboradores demostraron que el cobalto es la mejor opción en el sistema Sn-MT-C. [35], siendo el sistema Co-Sn-C particularmente prometedor [33,34]. El cobalto tiene una gran capacidad para formar nanopartículas amorfas con el estaño [28], pero tenemos que tener en cuenta la falta de reactividad del cobalto metálico con el litio, la cual impedirá la adición de grandes cantidades de este elemento debido a que podría reducir significativamente la capacidad del electrodo. Todd y colaboradores demostraron que la adición de una pequeña cantidad de cobalto contribuye a introducir desorden estructural en la aleación, y lo consideraron como un factor beneficioso para la estabilidad de la capacidad [69]. Ferguson y colaboradores demostraron que es posible la preparación de aleaciones Sn-Co-C nanoestructurados por molienda mecánica, siendo esta una técnica económica e industrialmente escalable [70].

1.4 Polímeros

Se ha determinado que el uso de polímeros conductores de iones litio puede aumentar el rendimiento electroquímico, la estabilidad y la seguridad de los electrodos [71]. Kyeremateng y col. recientemente propusieron el proceso de electropolimerización como una técnica viable para lograr la electrodeposición de un electrolito co-polímero y pudieron controlar con precisión el espesor de la capa electrodepositada [72].

Se ha propuesto el uso de polímeros orgánicos tal como el poliacrilonitrilo (PAN) en electrodos compuestos [73]. El transporte de los iones litio viene dado mediante saltos a través de las cadenas del polímero mediante interacción con los grupos C≡N [74]. Particularmente el poliacrilonitrilo es un polímero muy versátil (-CH_2-CH(CN)]$_n$-) el cual tiene capacidad de interactuar con las superficies metálicas por quimisorción, proporciona conductividad electrónica y una desnitrogenación fácil durante la carbonización [75]. Lecayon y col. interpretaron el mecanismo que regula la adherencia y el crecimiento de una película orgánica homogénea en superficies [76]. Este polímero tiene aplicaciones diversas en el campo de las baterías. Así, moléculas de PAN, junto a un plastificante y una sal de litio, pueden ser usados para preparar un electrolito sólido para baterías de litio [71]. Song y col. realizaron una revisión de las ventajas y características del empleo de electrolitos polímeros en baterías de ión litio de estado sólido [77]. En realidad, la disolución de $LiPF_6$ en disolventes orgánicos tal como carbonato de etileno (EC) actúa como plastificante del PAN resultando en la formación de un gel [78,79].

Por otro lado, las moléculas de PAN también se pueden utilizar como precursor para preparar fibras de carbono [80] y materiales de carbono duros [81] que pueden ser usados como material para electrodos en baterías de ión litio. Después de la pirolisis a temperatura moderada [75] las moléculas de PAN pueden formar una matriz conductora de carbono que envuelve las partículas de estaño [82].

1.5. Otros materiales como electrodo negativo

1.5.1. Reacciones de conversión en compuestos de metales de transición.

Aunque desde hace varias décadas se comercializan pilas (no recargables) de Li que usan electrodo positivo de óxidos metálicos, recientemente se han investigado óxidos de metales de transición como CoO, FeO, CuO [10-12] los cuales pueden reaccionar reversiblemente con el litio de acuerdo con la reacción general [83]:

$$M_xO_y + 2yLi = xM + yLi_2O$$
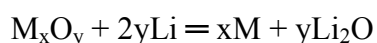
Las denominadas "reacciones de conversión" conducen a la posibilidad de reducir completamente el metal de transición desde el estado iónico inicial hasta su estado metálico (reacción de desplazamiento) de manera reversible durante el proceso de carga-descarga de la batería. La total reducción del metal de transición da lugar a materiales con partículas metálicas nanométricas (2-8 nm) dispersadas en una matriz de Li_2O. Debido a la naturaleza nanométrica, estos materiales proporcionan altas capacidades para almacenar litio (superior a la del grafito) durante un gran número de ciclos.

Estas reacciones de conversión también se presentan en compuestos de metales de transición con otros aniones como sulfuros, nitruros y oxisales del tipo $MnCO_3$ [84-86] y oxalatos como FeC_2O_4 y CoC_2O_4 [26,27]. Por otra parte, el oxalato de estaño ha demostrado ser capaz de reaccionar con 11 Li por fórmula produciendo una capacidad reversible de alrededor de 600 mAh/g en los primeros ciclos [25].

Sin embargo dichos materiales, presentan una reducción gradual de la capacidad debido a la histéresis que presenta el ciclo de carga-descarga. La cinética de las reacciones de conversión se encuentra limitada. Es por ello que para obtener un rendimiento óptimo de los materiales de conversión se están desarrollando estudios para optimizar el tamaño y la morfología de partículas.

1.5.2. Reacciones de inserción en dióxido de titanio

Debido a la abundancia del titanio en la naturaleza, la estabilidad química del óxido de titanio, su baja toxicidad y bajo coste de producción, se ha estudiado con gran interés el empleo de TiO_2 como electrodo negativo en baterías de ión litio. Además de la forma amorfa, las fases más interesantes del dióxido de titanio para baterías son rutilo, anatasa, brookita y TiO_2(B).

En los últimos años, el uso de TiO_2 en el campo de las baterías de ión litio ha resultado ser particularmente prometedor [87,88]. Aunque se obtiene una menor capacidad teórica para la intercalación de litio en el TiO_2 (335 mAh/g para una estequiometria máxima de $LiTiO_2$) en comparación con el grafito (372 mAh/g), el voltaje más alto necesario para la intercalación del litio podría evitar procesos de electrodeposición del litio y por lo tanto aumentar la seguridad de las actuales baterías de litio. Además la capacidad volumétrica del TiO_2 es mayor que la del grafito.

Por desgracia, el óxido de titanio suele tener baja conductividad eléctrica y lenta cinética de inserción-extracción del Li^+. Con el fin de superar este problema se puede obtener TiO_2 nanoestructurado y así lograr distancias más cortas tanto para el transporte de Li-ion como para el transporte de electrones, aumentando la capacidad práctica [89-92]. Por otro lado, se puede obtener nanotubos de óxido de titanio por anodización de una lámina Ti bajo las condiciones experimentales óptimas [93-95].

Estas baterías nanoestructuradas en 3D pueden mejorar la densidad-potencia de las baterías habituales y reducir el tiempo de recarga como se reivindica para seguir desarrollando vehículos eléctricos. No obstante, debido a que la capacidad del TiO_2 no es demasiado satisfactoria se requiere de mucha investigación para modificar y mejorar su eficiencia como ánodo en baterías de ión litio.

1.6. Electrodos preparados en forma de película fina

Durante los últimos años la preparación de materiales en forma de láminas delgadas, denominadas también películas finas, ha experimentado un considerable auge, dada la amplia variedad de aplicaciones tecnológicas que presentan estos dispositivos energéticos cara a suministrar más energía con el menor peso y volumen posibles.

Hasta ahora, los electrodos sintetizados en forma de láminas delgadas se preparaban generalmente mediante *sputtering*, evaporación por haz de electrones, deposición por pulsos de láser y deposición química en fase vapor [96]. Sin embargo, estos métodos además de su elevado coste poseen otras desventajas tales como la dificultad del control de la estequiometría, la necesidad de largos períodos de deposición para la obtención de los recubrimientos y su utilidad muy limitada para recubrimientos de área elevada.

A diferencia de los métodos antes citados, la electrodeposición presenta una importante ventaja ya que se lleva a cabo en disoluciones, generalmente acuosas, las cuales permiten trabajar a presión ambiente y temperaturas bajas (normalmente por debajo de 90ºC) [97]. El depósito tiene lugar por oxidación o reducción de los iones presentes en el baño electrolítico al transferir electrones con el sustrato del electrodo.

Entre las numerosas ventajas que presenta la deposición electroquímica frente otras técnicas de síntesis están las siguientes:

- Control de la estequiometría, del espesor y de la morfología y microestructura de las películas a través de los parámetros electroquímicos.
- Obtención de películas relativamente uniformes sobre sustratos de formas complejas.
- Posibilidad, en muchos casos, de altas velocidades de deposición.
- No se requiere condiciones de síntesis de alto vacío ni altas temperaturas.
- Permite la obtención de materiales de alta pureza.
- Es una técnica económica.

El método de electrodeposición permite la obtención de láminas de espesor y textura controlados, además de una buena adherencia al sustrato, siendo este último aspecto básico y fundamental en la preparación de electrodos para baterías.

La electrodeposición se produce fijando un potencial determinado entre un electrodo de trabajo y otro auxiliar separados por un electrolito, provocando sobre el primer electrodo una reacción de oxidación o reducción que lleva consigo la formación sobre el mismo de un depósito insoluble en el electrolito. Transcurre conforme tiene lugar la transferencia de electrones entre el electrodo-sustrato y la fase disolución adyacente.

Hoy en día la electrodeposición de estaño y de aleaciones de Co-Sn en sustratos en dos y tres dimensiones ha sido concebido como una forma prometedora de mejorar el ciclado electroquímico de electrodos basados en el estaño, principalmente debido al buen contacto eléctrico entre el material activo y el colector de corriente y a la capacidad de amortiguar los cambios de volumen del electrodo [44-55].

1.7 Hipótesis, objetivos y plan de trabajo

Los elementos que forman aleaciones con el litio (e.j.: Al, Sb, Si y Sn) tienen interés en el campo de las baterías debido a que proporcionan capacidades superiores a la del grafito. En particular, los compuestos intermetálicos basados en el estaño muestran interesantes propiedades electroquímicas. Se pueden obtener mejores resultados electroquímicos usando materiales compuestos por un componente electroquímicamente activo (como el estaño) y otro componente electroquímicamente inactivo. Así, el sistema basado en Co-Sn puede ser útil para su uso como material de electrodos para baterías de ión-litio. Se hace necesario el desarrollo de nuevos materiales compuestos así como avances en la comprensión de los materiales ya conocidos.

Por otro lado, la obtención de materiales electrodicos para baterías de ión-litio en forma de película fina electrodepositada ha sido concebida como una forma prometedora de mejorar el ciclado electroquímico de electrodos, principalmente debido al buen contacto eléctrico entre el material activo y el colector de corriente.

Por todo ello, en esta tesis doctoral se diferencian dos claros objetivos generales. En primer lugar, la síntesis y optimización de las propiedades electroquímicas de materiales compuestos basados en Co-Sn y matrices carbonosas u orgánicas. Se espera que la distribución homogénea del compuesto intermetálico o aleación de Co-Sn en una matriz no metálica contribuya a amortiguar los indeseables cambios de volumen que se producen durante la formación de la aleación con el litio (Capítulos 2 y 3). El segundo objetivo general persigue la síntesis y caracterización de materiales electródicos en forma de películas finas electrodepositadas con el fin de obtener comportamientos electroquímicos óptimos para baterías de ion litio (Captulo 4).

Para conseguir estos objetivos se ha llevado a cabo el plan de trabajo que se expone a continuación y cuyos resultados han dado lugar a las diferentes publicaciones que se desarrollan en la presente memoria.

1. Síntesis de materiales compuestos basados en Co-Sn-C por reducción carbotermal de los óxidos metálicos usando diferentes precursores carbonosos. Con este fin se han utilizado un gel resorcinol-formaldehido obtenido mediante

metodología sol-gel, un coque verde y un residuo de pirolisis del Fueloil (FOP).

2. Análisis de las características morfológicas por microscopia electrónica de barrido y estudio de la composición de estos materiales mediante espectrometría de energía dispersiva.

3. Caracterización estructural de las fases de Co-Sn mediante difracción de Rayos-X y Espectroscopia Mössbauer de [119]Sn

4. Estudio del comportamiento electroquímico de materiales electródicos en celdas de litio mediante el empleo de técnicas de ciclado galvanostático. Análisis de la resistencia en la interface electrodo-electrólito calculada a partir de los espectros de impedancia compleja.

5. Análisis post-mortem de los electrodos ciclados mediante Difracción de Rayos-X y Espectroscopia Mössbauer de [119]Sn con el objeto de desvelar el mecanismo de reacción con el litio.

Los puntos 1, 2, 3, 4 y 5 del plan de trabajo se desarrollan a lo largo del capítulo 2 de la presente memoria.

6. Preparación de materiales compuestos que contienen una mezcla de oxalatos de estaño y de cobalto dispersados en una matriz orgánica formada por moléculas de poliacrilonitrilo (PAN).

7. Estudio de la composición de estos materiales mediante microanálisis (detector de Rayos-X tipo EDAX) y análisis elemental de C-N.

8. Caracterización morfológica, estructural y estudio del mecanismo de reacción con el litio mediante Difracción de Rayos-X, Espectroscopia Mössbauer de [119]Sn y Espectroscopia Infrarroja.

9. Estudio del comportamiento electroquímico de estos materiales para su uso como electrodos en baterías de ión-litio mediante ciclado galvanostático en celdas de litio de dos electrodos.

Los puntos 6, 7, 8 y 9 del plan de trabajo se desarrollan a lo largo de la publicación 3.1 de la presente memoria.

10. Síntesis de materiales compuestos $CoSn_2$@PAN mediante reducción de los iones metálicos con borohidruro sódico en presencia de PAN disuelto en dimetilformamida.

11. Caracterización estructural mediante técnica de Difracción de Rayos-X y Espectroscopia de Resonancia Magnética Nuclear del ^{13}C.

12. Estudio del comportamiento térmico de los materiales sintetizados mediante Análisis Térmico Diferencial.

13. Optimización del comportamiento electroquímico de estos materiales para su uso como electrodos en baterías de ión-litio mediante ciclado galvanostático en celdas de litio de dos electrodos.

Los puntos 10, 11, 12 y 13 del plan de trabajo se desarrollan a lo largo de la publicación 3.2 de la presente memoria.

14. Síntesis de diferentes materiales compuestos basados en Co-Sn-PAN mediante reducción química de los iones metálicos con variación en la proporción del polímero empleado. Alternativamente, se ha empleado un método sonoquímico en combinación con la reducción química, así como una carbonización parcial del PAN por calentamiento a diferentes temperaturas.

15. Caracterización química, morfológica y estructural, así como estudio del mecanismo de reacción, mediante análisis químico, Difracción de Rayos-X, Espectroscopia de fotoelectrones de Rayos-X (XPS), Microscopía Electrónica y Espectroscopia Mössbauer de ^{119}Sn.

16. Estudio del comportamiento electroquímico de estos materiales para su uso como electrodos en baterías de ión-litio mediante ciclado galvanostático en celdas de dos electrodos y espectroscopia de impedancia compleja en celdas de tres electrodos.

Los puntos 14, 15 y 16 del plan de trabajo se desarrollan a lo largo de las publicaciones 3.3, 3.4 y 3.5 de la presente memoria.

17. Obtención de películas finas electrodepositadas de Co-Sn-PAN sobre sustrato de titanio.

18. Electrodeposición de PAN, mediante voltametría cíclica del monómero, sobre nanotubos de dióxido de estaño auto-organizados previamente obtenidos por anodización de Ti.

19. Caracterización morfológica y estructural de los compuestos sintetizados mediante técnica de Difracción de Rayos-X, SEM, HRTEM y Espectroscopia Infrarroja (FTIR). Así como caracterización de la superficie por Espectroscopia de fotoelectrones de Rayos-X (XPS).

20. Estudio del comportamiento electroquímico de estos materiales para su uso como electrodos en baterías de ión-litio mediante ciclado galvanostático en celdas de litio de dos electrodos y el registro de espectros de impedancia compleja en celdas de litio de tres electrodos.

Los puntos 17, 18, 19 y 20 del plan de trabajo se desarrollan a lo largo del capítulo 4 de la presente memoria.

Bibliografía

[1] World Energy Outlook 2012. International Energy Agency.

[2] Energy storage. R. Huggins. Springer (2010).

[3] Baterías avanzadas. P. Lavela, J.L. Tirado. Servicio de publicaciones de la Universidad de Córdoba (1999).

[4] Modern batteries. An introduction to electrochemical power sources. C. A. Vincent. Edward Arnold (1984).

[5] Lithium-ion batteries. X. Yuan, H. Liu, J. Zhang (Eds.). CRC Press (2012).

[6] Lithium batteries. Science and Technology. G.A. Nazri, G. Pistoia (Eds.). Springer (2009).

[7] Advances in lithium ion batteries. G.A. Nazri, G. Pistoia (Eds.). Kluwer (2002).

[8] Lithium batteries. W.A. Van Schalkwijk, B. Scrosati (Eds.). Springer (2003).

[9] M. Winter, J. O. Besenhard, M. E. Spahr, P. Novák, Adv. Mater. 10 (1998) 725.

[10] S. Grugeon, S. Laruelle, L. Dupont, J.M. Tarascon, Solid State Sciences 6 (2003) 895.

[11] P. Poizot, S. Laruelle, S. Grugeon, L. Dupont. J.M. Tarascon, Nature 407 (2000) 496.

[12] S. Grugeon, S. Larruelle, R. Herrera-Urbina, L. Dupont, P. Poizot, J.M. Tarascon, J. Electrochem. Soc. 148 (2001) A285.

[13] M. Winter, J. O. Besenhard, Electrochim. Acta 45 (1999) 31.

[14] P. Lavela, J. L.Tirado, J. Power Sources 172 (2007) 379.

[15] R. Alcántara, J.L. Tirado, Dyna 83 (2008) 411.

[16] V. Manev, I. Naidenov, B. Puresheva, P. Zlatilova, G. Pistoia, J. Power Sources. 55 (1995) 211.

[17] T. Ohzuku, Y. Iwakoshi, K. Sawai, J. Electrochem Soc. 140 (1993) 2490.

[18] C. Menachem, Y. Wang, J. Flowers, E. Peled, S.G. Greenbaum, J. Power Sources   76 (1998) 180.

[19] T. Nakajima, M. Koh, R.N. Singh, M. Shimada, Electrochim Acta 44 (1999) 2879.

[20] A. N. Dey, J. Electrochem. Soc. 118 (1971) 1547.

[21] W. Weppner, R. A. Huggins, J. Electrochem. Soc. 124 (1977) 1569.

[22] J. Wang, I. D. Raistrick, R. A. Huggins, J. Electrochem. Soc. 133 (1986) 457.

[23] S. Paneco, B. Scrosati, M. Wachtler, F. Croce, Journal of Power Sources 129 (2004) 90.

[24] B. Scrosati, J. Garche, Journal of Power Sources 195 (2010) 2419.

[25] R. Alcántara, F.J. Fernández-Madrigal, P. Lavela, C. Pérez-Vicente, J.L. Tirado, J. Solid State Electrochem. 6 (2001) 55.

[26] M.J. Aragón, B. León, C. Pérez-Vicente, J.L. Tirado, Inorg. Chem. 47 (2008) 10366.

[27] M.J. Aragón, B. León, C.P. Pérez Vicente, J.L. Tirado, A. Chadwick, A. Berko, S.Y. Beh, Chem. Mater. 21 (2009) 1834.

[28] J.G. Geny, D. Malterre, M. Vergnat, M. Piecuch, G. Marchal, J. Non-Cryst. Solids 62 (1984) 1243.

[29] A.D.W. Todd, R.E. Mar, J.R. Dahn, Journal of the Electrochem. Society 153 (2006) A1998.

[30] J. Hassoun, S. Paneco, B. Scrosati, Fuel cells 9 (2009) 277.

[31] G.Derrien, J. Hassoun, S. Panaco, B. Scrosati, Advanced Materials 19 (2007) 2336.

[32] J.R. Dahn, R.E. Mar, A. Abouzeid, J. Electrochem. Soc. 153 (2006) A361.

[33] P.P. Ferguson, J.R. Dahn, Electrochem. Solid State Lett. 11 (2008) A187.

[34] G.F. Ortiz, R. Alcántara, I. Rodríguez, J.L. Tirado, J. Electroanal. Chem. 605 (2007) 98.

[35] A.D.W. Todd, R.E. Mar, J.R. Dahn, J. Electrochem. Soc. 154 (2007) A597.

[36] Y. Yu, L. Gu, C. Wang, A. Dhanabalan, P. A. van Aken, J. Maier, Angew. Chem. 48 (2009) 6485.

[37] L. Huang, J.S. Cai, Y. He, F.S. Ke, S.G. Sun, Electrochem. Commun. 11 (2009) 950.

[38] J. Hassoun, S. Paneco, G. Mulas, B. Scrosati, J. Power Sources 171 (2007) 928.

[39] H. Kim, J. Cho, J. Electrochem. Soc. 154 (2007) A462.

[40] X. He, W. Pu, L. Wang, J. Ren, C. Jiang, C. Wan, Solid State Ionics 178 (2007) 833.

[41] K.T. Lee, Y.S. Jung, S.M. Oh, J. Am. Chem. Soc. 125 (2003) 5652.

[42] M. Noh, Y. Kwon, H. Lee, J. Cho, Y. Kim, M.G. Kim, Chem. Mater. 17 (2005) 1926.

[43] H. Kim, J. Cho, Electrochim. Acta 52 (2007) 4197.

[44] N. Tamura, M. Fujimoto, M. Kamino, S. Fujitani, Electrochim. Acta 49 (2004) 1949.

[45] T. Tabuchi, N. Hochgatterer, Z. Ogumi, M. Winter, J. Power Sources 188 (2009) 552.

[46] K. Ui, S. Kikuchi, Y. Jimba, N. Kumagai, J. Power Sources 196 (2011) 3916.

[47] A.D.W. Todd, P.P. Ferguson, J.G. Barker, M.D. Fleischauer, J.R. Dahn, J. Electrochem. Soc. 156 (2009) A1034.

[48] J. Wang, N. Du, H. Zhang, J. Yu, D. Yang, J. Phys. Chem. C 115 (2011) 23620.

[49] D. Jian, H. Tian, C. Qiu, X. Ma, Y. Fu, J. Solid State Electrochem. 15 (2011) 2639.

[50] L. Bazin, S. Mitra, P.L. Taberna, P. Poizot, M. Gressier, M.J. Menu, A. Barnabé, P. Simon, J.M. Tarascon, J. Power Sources 188 (2009) 578.

[51] Z. Du, S. Zhang, Y. Xing, X. Wu, J. Power Sources 196 (2011) 9780.

[52] C. Yang, D. Zhang, Y. Zhao, Y. Lu, L. Wang, J.B. Goodenough, J. Power Sources 196 (2011) 10673.

[53] L. Xue, Z. Fu, Y. Yao, T. Huang, A. Yu, Electrochim. Acta 55 (2010) 7310.

[54] C. Arbizzani, M. Lazzari, M. Mastragostino, J. Electrochem. Soc. 152 (2005) A289.

[55] L.J. Xue, Y.F. Xu, L. Huang, F.S. Ke, Y. He, Y.X. Wang, G.Z. Wei, J.T. Li, S.G. Sun, Electrochim. Acta 56 (2011) 5979.

[56] U.G. Nwokeke, R. Alcántara, J.L. Tirado , R. Stoyanova, E. Zhecheva, Journal of Power Sources 196 (2011) 6768.

[57] H. Chen, Z. Li, Z. Wu, Z. Zhang, J. All. Comp. 394 (2005) 282.

[58] L. Qiu, V.G. Pol, J. Calderon-Moreno, A. Gedanken, Ultrason. Sonochem. 12 (2005) 243.

[59] S. Kawakami, M. Asao, Eur.Pat.Appl. EP1039568A1 (2000).

[60] P.P. Ferguson, P. Liao, R.A. Dunlap, J.R. Dahn, J. Electrochem. Soc. 156 (2009) A13.

[61] J.J. Zhang, Y.Y. Xia, J. Electrochem. Soc. 153 (2006) A1466.

[62] M.Z. Xue, Z.W. Fu, Solid State Ionics 177 (2006) 1501.

[63] C.M. Ionica-Bousquet, P.E. Lippens, L. Aldon, J. Oliver-Fourcade, J.C. Jumas, Chem. Mater. 18 (2006) 6442.

[64] R. Alcántara, U. Nwokeke, I. Rodriguez, J.L. Tirado, Electrochem. Solid-State Lett. 11 (2008) A209.

[65] M.G. Kanatzidis, R. Pöttgen, W. Jeitschko, Angew. Chem. Int. Ed. 44 (2005) 6996.

[66] P.P. Ferguson, R.A. Dunlap, J.R. Dahn, J. Electrochem. Soc. 157 (2010) A326.

[67] R. Alcántara, I. Rodríguez, J.L. Tirado, ChemPhysChem. 9 (2008) 1171.

[68] http://www.sony.net/SonyInfo/News/Press/200502/05-006E/.

[69] A.D.W. Todd, R.E. Mar, J.R. Dahn, J. Electrochem. Soc. 153 (2006) A1998.

[70] P.P. Ferguson, A.D.W. Todd, J.R. Dahn, Electrochem. Commun. 10 (2008) 25.

[71] U. G. Nwokeke, F. Nacimiento, R. Alcántara, J. L. Tirado, Electrochem. Solid-State Lett. 14 (2011) A148.

[72] N.A. Kyeremateng, F. Dumur, P. Knauth, B. Pecquenard, T. Djenizian, Electrochem. Commun. 13 (2011) 894.

[73] X. He, W. Pu, L. Wang, J. Ren, C. Jiang, C. Wan, Solid State Ionics 78 (2007) 833.

[74] Y.T. Chen, Y.C. Chuang, J.H. Su, H.C. Yu, Y.W. Cheng-Yang, J. Power Sources 196 (2011) 2802.

[75] C. Reynaud, C. Boiziau, C. Juret, S. Leroy, J. Perreau, Synthetic Metals. 11 (1985) 159.

[76] G. Lecayon, Y. Bouizem, C. Le Greuss, C. Reynaud, C. Boiziau, C. Juret, Chem. Phys. Lett. 91 (1982) 506.

[77] J.Y. Song, Y.Y. Wang, C.C. Wan, J. Power Sources 77 (1999) 183.

[78] B. Huang, Z. Wang, L. Chen, R. Xue, F. Wang, Solid State Ionics 91 (1996) 279.

[79] K.M. Abraham, H.S. Choe, D.M. Pasquariello, Electrochim. Acta 43 (1998) 16.

[80] J.F. Snyder, E.L. Wong, C.W. Hubbard, J. Electrochem. Soc. 156 (2009) A215.

[81] Y.J. Kim, H.J. Lee, S.W. Lee, B.W. Cho, C.R. Park, Carbon 43 (2005) 163.

[82] Y. Yu, L. Gu, C.B. Zhu, P.A. Van Aken, J. Maier, J. Am. Chem. Soc. 131 (2009) 15894.

[83] A. Nytén, A. Abouimrane, M. Armand, T. Gustafsson, J.O. Thomas, Electrochem. Commun. 7 (2005) 156.

[84] Y. Shao-Horn, S. Osmialowski, Q.C. Horn, J. Electrochem. Soc. 149 (2002) A1547.

[85] T. Shodai, S. Okada, S. Tobishma, J. Yamaki, J. Power Sources 68 (1997) 515.

[86] M.J. Aragón, B. León, C.P. Vicente, J.L. Tirado, J. Power Sources 196 (2001) 2863.

[87] G. F. Ortiz, I. Hanzu, T. Djenizian, P. Lavela, J. L. Tirado, P. Knauth, Chem.Mater. 21 (2009) 63.

[88] J. R. González, R. Alcántara, F. Nacimiento, G. F. Ortiz, J. L. Tirado, E. Zhecheva, R. Stoyanova, J. Phys. Chem. C 116 (2012) 20182.

[89] M. Saito, Y. Murota, M. Takagi, M. Tajima, T. Asao, H. Inoue, A. Tasaka, M.J. Inaba, Electrochem. Soc. 159 (2012) A49.

[90] M.C. Yang, Y.Y. Lee, B. Xu, K. Powers, Y.S. Meng, J. Power Sources. 207 (2012) 166.

[91] H. Liu, Z. Bi, X.G. Sun, R.R. Unocic, M.P. Paranthaman, S. Dai, G. Brown, Adv. Mater. 23 (2011) 3450.

[92] J.J. Kelly, Electrochim. Acta. 24 (1979) 1273.

[93] Y. Ren, Z. Liu, F. Pourpoint, A.R. Armstrong, C.P. Grey, P.G. Bruce, Angew. Chem. Int. Ed. 51 (2012) 2164.

[94] G.F. Ortiz, I. Hanzu, P. Knauth, P. Lavela, J.L. Tirado, T. Djenizian, Electrochim. Acta. 54 (2009) 4262.

[95] G.F. Ortiz, I. Hanzu, T. Djenizian, P. Lavela, J.L. Tirado, P. Knauth, Chem. Mater. 21 (2009) 63.

[96] J. Bates, N.J. Dudney, B. Neudecker, A. Ueda, C.D. Evans, Solid State Ion. 135 (2000) 33.

[97] O. Savadogo, Sol. Energy Mater. Sol. Cells. 52 (1998) 361.

Capítulo 2.-

Materiales híbridos de cobalto-estaño y fase carbonosa

2.1 Sn-Co-C composites obtained from resorcinol-formaldehyde gel as anodes in lithium-ion batteries

P. Lavela, F. Nacimiento, G.F.Ortiz, and J. L. Tirado

Abstract

Sn–Co–C composites have been prepared by using the resorcinol/formaldehyde polymerization method combined with the carbothermal reduction of metal oxides during carbonization. Homogeneously dispersed metal/carbon composites were identified by electron microscopy. Scanning electron microscopy images revealed the presence of carbonaceous particles with inclusions of metal agglomerates, and the X-ray diffraction patterns revealed the presence of tin and cobalt–tin phases. The introduction of small amounts of cobalt led to higher capacities as compared to coke and cobalt-free samples. The sample with a Sn/Co molar ratio of 85:15 and a higher, initial metal oxide-to-resorcinol ratio was able to maintain capacity values near 380 mAh/g after 30 cycles. The instability of cobalt–tin phases on cycling was not a hindrance for the electrochemical behavior. Charge transfer resistance values were kept low during cycling for cobalt-containing composites.

Springer

2.1.1 Introduction

At present, the research for new anodes in lithium ion batteries is mature in the field of both carbonaceous materials and metals, such as tin, which are able to form alloys with lithium [1]. Graphite is a preferred option due to the low working voltage and stable capacity for a large number of cycles [2, 3]. On the other hand, the theoretical capacity limit (372 mAh/g) is regarded as a major drawback to develop new batteries with higher capacities in the near future. New approaches are continuously proposed to overcome this limitation including mild oxidation [4] and fluorination [5].

Disordered carbons prepared at low temperatures, as cokes, must not be discarded yet. Their low cost is an advantage for commercial purposes. Also the existence of additional sites for lithium linking, provided by the incomplete structural ordering, is a factor deserving the evaluation of new approaches for their use in lithium ion batteries.

On the other hand, tin metal is able to reversibly react with important amounts of lithium to deliver high capacity. The volume expansion occurring during the reversible alloying process has been attenuated by several means, including preparation of glasses and combination with different counter ions and/or metals [6, 7]. However, a new approach considers the introduction of transition metals, as cobalt, in the anode composition [8]. The lack of reactivity of cobalt metal with lithium prevents the addition of large amounts of this element, which could significantly reduce the electrode capacity. However, it has been reported that small amounts of cobalt contribute to introduce structural disorder in the tin phase. This phenomenon can be envisaged as a beneficial factor for capacity stability [8].

Several methods have been reported to achieve a homogeneous mixture of metal and carbon phases, ensuring a suitable buffering effect of the carbonaceous materials. Milling [9], sputtering [10], or chemical deposition [11] procedures have been employed. Nongraphitic microspherical carbon particles obtained from polymerization of a mixture of resorcinol/formaldehyde have demonstrated to be suitable electrode materials for sodium ion cells [12]. Moreover, these carbon gels are promising materials for encasing metal powder because of the gelly-like texture of the departure precursor. Thus, containing silicon [13] and tin [14] based composite materials have been reported.

This paper reports the evaluation of Sn–Co–C composites prepared by carbothermal reduction of the metal oxides parallel to carbonization of a resorcinol–formaldehyde polymer. The aim was to evaluate the electrochemical behavior in lithium cells of tin–cobalt intermetallics when they are dispersed into a carbon matrix. The gel-like nature of the resorcinol–formaldehyde polymer may ensure a suitable embedding of the resulting alloy.

2.1.2   Materials and methods

The preparation of the Sn–Co–C composites was carried out by the impregnation of a homogeneous mixture of the metal oxides finely powdered in an organic gel formed by the resorcinol/formaldehyde method. For this purpose, commercial SnO_2 (Panreac) and CoO (Aldrich) in 95:5 and 85:15 molar ratios were ball-milled for 5 h at 300 rpm. For the preparation of the organic gel, 4.5 g of resorcinol were added to 6.5 mL of formaldehyde stabilized in methanol [Panreac, 37% (wt)] and 15 mL of distilled water under continuous stirring at room temperature. A volume of 60 mL of 0.035 M sodium carbonate solution was added to promote polymerization. After 1 h of stirring at room temperature, the aquagel was mixed with the metal oxides in the appropriated proportion to prepare several carbons to metal ratios. The content was transferred to a round-bottom flask and was refluxed at 85 °C for approximately 3 h. This was the time needed for a solid gel formation ensuring the homogenous mixture of carbonaceous and metal phases. Then, the gel was transferred in a closed glass flask and cured with acetone for 3 days at room temperature. The role of acetone was the gel dehydration; therefore, the solvent was replaced daily for an optimal operation. The solid gel was eventually filtered, washed, and then heated at 300 °C for 2 h. The composite precursor was ground and re-heated at 800 °C for 4 h under an argon stream in a tube furnace. The heating rate was 2.5 °C/min.

Two different Sn/Co molar ratios, henceforth referred to as 85:15, 95:5, and one tin-only composition, were selected for this study. For the 85:15 ratio, three different ratios between the metal oxides ($MO_x=SnO_2+CoO$) and resorcinol (R) masses were used in the synthesis. The resulting samples are referred to as MO_x/R and ratio took the following values: 0.3, 0.67, and 1.5. Additionally, a coke material prepared in the same conditions, but free of metal elements, was also prepared for comparison purposes.

X-ray diffraction (XRD) patterns were recorded in a Siemens D-5000 apparatus provided with CuKα radiation and graphite monochromator. The 2θ scan rate was 0.04° per 1.2 s. Scanning electron microscopy (SEM) images were obtained in a JEOL-SM6300 microscope provided by the Service of Support to Research at the University of Córdoba. The [119]Sn Mössbauer spectra (MS) were recorded at room temperature with an Ametek–Wissel constant acceleration spectrometer in transmission mode. The source of radiation was [119m]Sn in a $BaSnO_3$ matrix. The isomer shift scale is set by using a $BaSnO_3$ pattern. The center of the peak of the Sn(IV) signal is established as the zero value of the scale. The spectra profile was decomposed in Lorentzian lines using a least-square-based method (F. Landry and P. Schaaf, WinISO—Windows Mössbauer Fitting 625 Programme, 1998, private communication). The goodness of the fit was controlled by the χ^2 value.

The electrochemical performance of the Sn–Co–C composites was evaluated by using two-electrode Swagelok-type cells. The assembly used 9 mm discs of lithium metal as counter electrodes. The working electrode was fabricated by mixing 92% of active material and 8% polyvinylidene difluoride binder. A paste was formed with that mixture and n-methyl pyrrolidinone and eventually deposited as a film on a cooper foil of the same diameter. Both electrodes were separated by a 1 M $LiPF_6$ (EC/DEC= 1:1) electrolyte solution that was supported in Whatman glass fiber discs. The assembly of test cells and handling of the discharged electrode was carried out in an MBraun glove box under an argon atmosphere. An Arbin potentiostat/galvanostat multichannel system was used to cycle galvanostatically the lithium cells at 20 mA/g rate for both charge and discharge branches. Electrochemical impedance spectroscopy was carried out in an Autolab PGSTAT12 system. Three-electrode lithium cells were used, providing a lithium metal disc as a reference electrode. The test cells were previously discharged using a MacPile system by step potential electrochemical spectroscopy. The scan rate was set at 10 mV/0.1 h. Before measuring the impedance values, the cells were kept in open circuit for at least 5 h to achieve a quasi-equilibrium system. An AC voltage signal of 5 mV was applied from 100 kHz to 2 mHz.

2.1.3   Results and discussion

XRD analysis.

XRD patterns of the annealed samples are shown in Figure 1. A set of narrow reflections could be ascribed to the presence of several tin-containing solids, including metallic phases such as tin (JCPDS 04-0673), $CoSn_2$ (JCPDS 25- 0256), and CoSn (JCPDS 02-0559). Some oxide impurities can be ascribed to either an incomplete reduction during the annealing process or to further surface oxidation. The selected annealing temperature prevented an appreciable structural ordering of the carbonaceous phase, and hence, reflections were not detected.
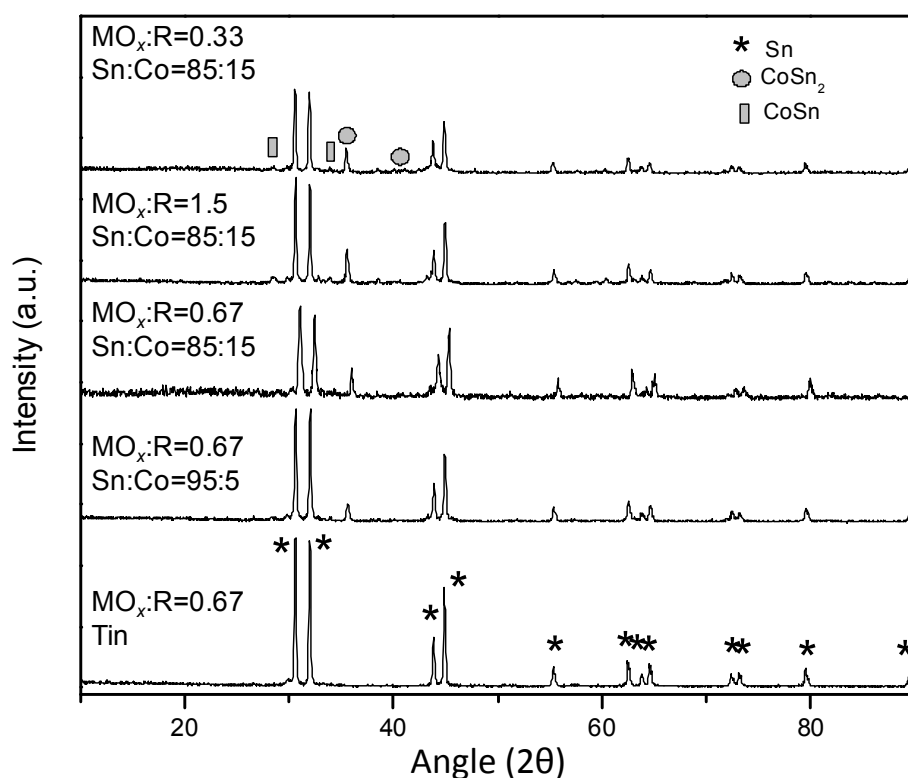
Figure 1. X ray diffraction patterns of Sn-Co-C composites

^{119}Sn Mössbauer spectroscopy.

^{119}Sn Mössbauer spectroscopy is a useful tool to quantify the contribution of tin phases to the studied samples. Figure 2 shows the experimental spectra of the tin containing phases and the Lorentzian signal profiles calculated from the fitting. The hyperfine parameters are written in Table 1.

Figure 2. ^{119}Sn Mössbauer spectra of Sn-Co-C composites.

Table 1. Hyperfine parameters of the deconvoluted Mössbauer spectra.

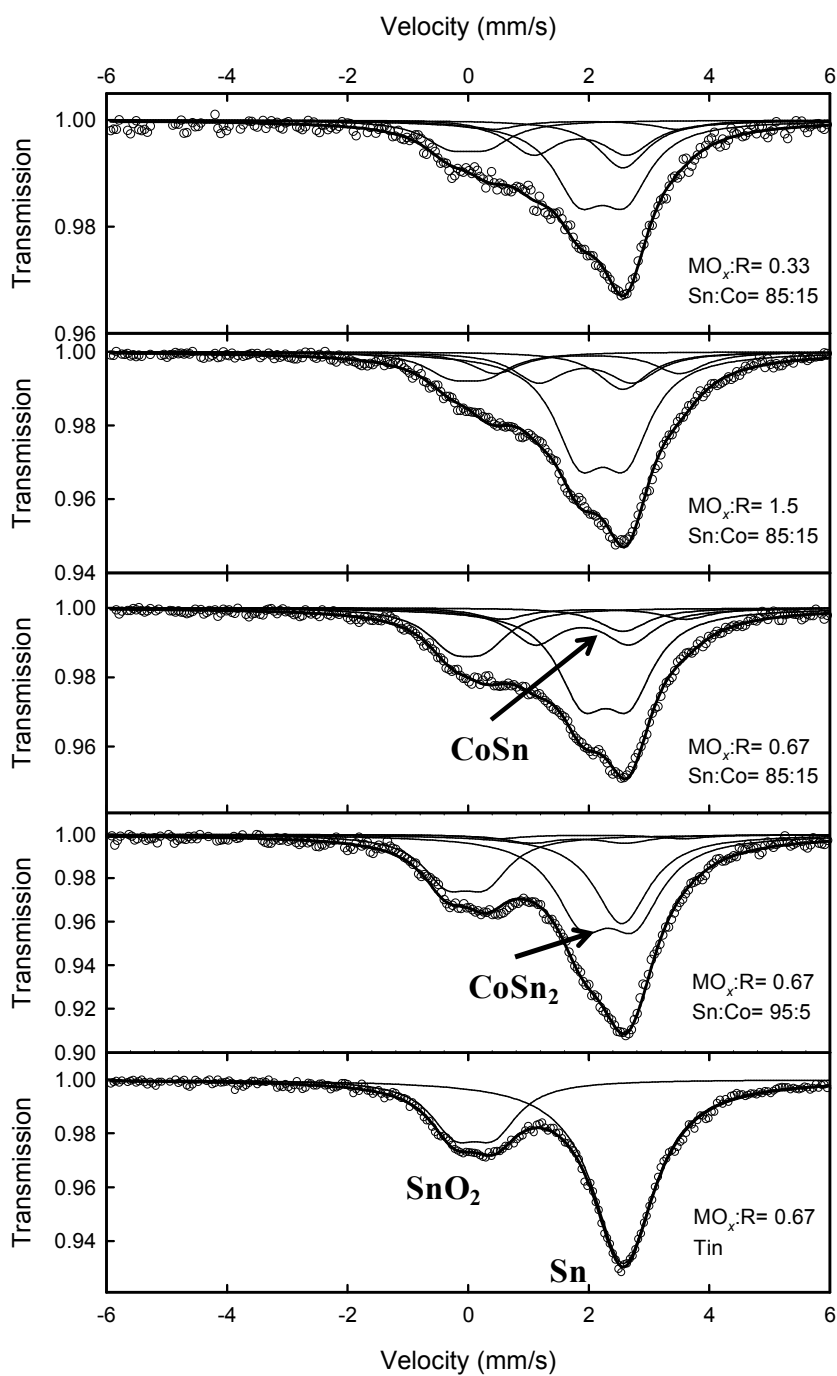| Sample	s/d[1]	Tin phase	δ[2] (mm/s)	Δ[3] (mm/s)	Γ[4] (mm/s)	C[5] (%)	χ^{2} [6]
MO_x:R=0.67 Tin only	d	SnO_2	0.10(3)	0.66(2)	0.98(4)	28.1	0.738
	s	β-Sn	2.58(1)	--	1.2(1)	71.9	
MO_x:R=0.67 Sn:Co=95:5	d	SnO_2	-0.04(4)	0.65(3)	0.96(5)	21.5	0.670
	s	β-Sn	2.55(1)	--	1.1(2)	26.7	
	d	CoSn	1.82(1)	1.57(1)	1.1(1)	4.4	
	d	CoSn	2.038(1)	3.08(2)	1.1(1)	2.2	
	d	$CoSn_2$	2.32(1)	0.86(2)	1.1(2)	45.2	
MO_x:R=0.67 Sn:Co=85:15	d	SnO_2	0.00(2)	0.54(3)	1.0(2)	18.7	0.551
	s	β-Sn	2.57(1)	--	1.1(2)	7.0	
	d	CoSn	1.89(2)	1.56(1)	1.1(1)	20.3	
	d	CoSn	2.08(5)	3.06(1)	1.1(1)	6.7	
	d	$CoSn_2$	2.28(1)	0.77(1)	1.1(2)	47.4	
MO_x:R=1.5 Sn:Co=85:15	d	SnO_2	0.00(3)	0.60(5)	1.0(2)	10.9	0.696
	s	β-Sn	2.57(1)	--	1.0(2)	10.4	
	d	CoSn	1.95(2)	1.56(1)	1.0(1)	16.0	
	d	CoSn	1.98(4)	3.06(1)	1.0(1)	11.8	
	d	$CoSn_2$	2.23(1)	0.77(1)	1.0(2)	50.9	
MO_x:R=0.33 Sn:Co=85:15	d	SnO_2	0.00(4)	0.63(7)	1.0(2)	14.1	0.502
	s	β-Sn	2.57(1)	--	1.0(2)	15.4	
	d	CoSn	1.86(3)	1.56(3)	1.0(1)	20.9	
	d	CoSn	2.0(1)	3.06(1)	1.0(1)	5.8	
	d	$CoSn_2$	2.22(2)	0.77(1)	1.0(1)	43.8	
MO_x:R=0.67 Sn:Co=85:15 Disch. to 0 V	s	β-Sn	2.65(2)	--	1.0(1)	22.6	0.338
	d	$Li_{22}Sn_5$	1.79(2)	0.24(1)	0.94(1)	38.7	
	d	$Li_{22}Sn_5$	1.82(2)	0.94(1)	0.94(1)	38.7	

[1]s/d: singlet (s) or doublet (d); [2]δ: isomeric shift; [3]Δ: quadrupolar splitting; [4]Γ: line-width at half maximum; [5]C: contribution/concentration; [6]χ^2: goodness of the fitting.

The cobalt-free sample showed two resolved signals located at the regions belonging to metallic tin and Sn(IV). According to the XRD pattern, they can be assigned to β-Sn and SnO_2. The presence of SnO_2 can be justified by a partial oxidation of the surface of tin particles. For samples containing cobalt, the spectrum profile progressively changes until it eventually becomes an asymmetric and highly broadened profile. This behavior is due to the occurrence of new bands at intermediate shifts. The overlapped signals are difficult to fit. To overcome this problem, the hyperfine parameters of CoSn and $CoSn_2$ phases were taken from the literature [15] and used as initial values in the fitting procedure. The most remarkable feature is the significant contribution of SnO_2, though it slightly decreased when cobalt and carbonaceous proportion was augmented. This fact evidences the important role of carbon material in the reduction of the initial oxides. In addition, the reactivity of cobalt to form alloys with tin is revealed by the abrupt decrease of β-tin contribution when cobalt content is increased. This effect is parallel to the increasing contribution of cobalt–tin phases.
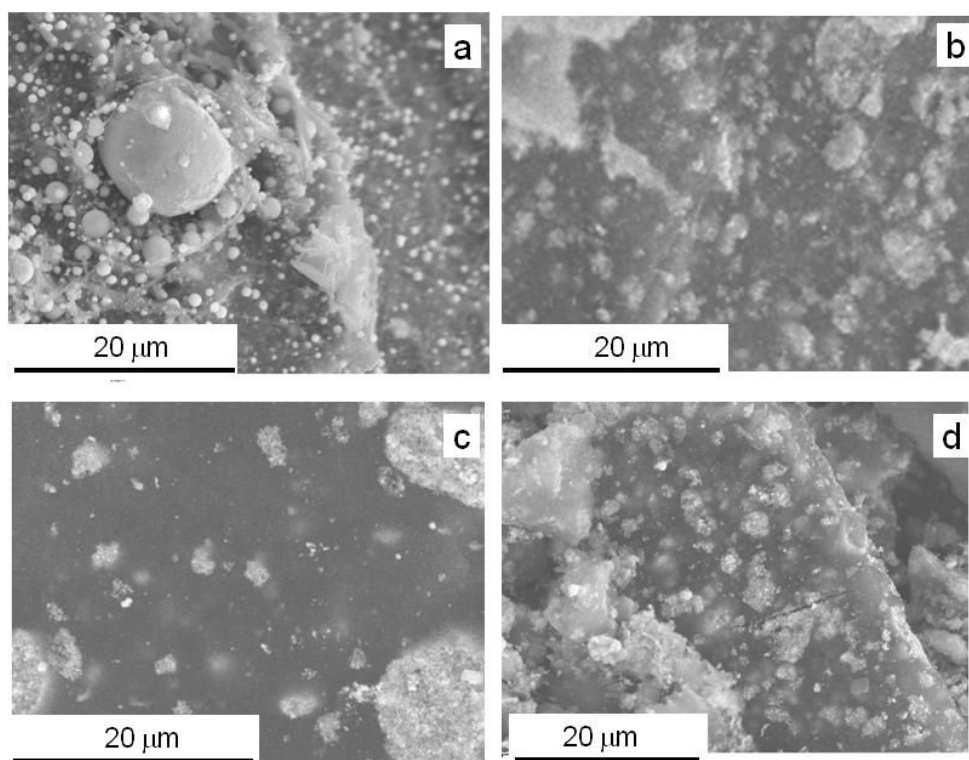

Figure 3. SEM micrographs of metal-carbon composites. a) tin only sample (MO_x:R=0.67); b) Sn:Co=95:5 (MO_x:R=0.67); c) Sn:Co=85:15 (MO_x:R=0.67); d) Sn:Co=85:15 (MO_x:R=1.5).

Electron microscopy.

The morphological properties of these samples were evaluated from the SEM micrographs. Figure 3a shows a close view of sample-only containing tin. Spherical particles of tin, with diameter values ranging from some tenth to several micrometers, are mainly decorating the surface of the carbon substrate. When cobalt atoms are present in the composition, the population of surface particles is drastically reduced. Agglomerates of nanometric particles are mostly embedded in the carbonaceous matrix. The influence of cobalt atoms to provide strong links between tin and carbon that improves the stability of the composite material has been reported [16].

Electrochemical performance.

Figure 4 shows the intensity versus voltage plots for the first few cycles of lithium test cells using composites prepared with different Sn/Co and/or MO_x/R ratios. The first discharge profile differs from subsequent discharges. It is assigned to the drastic structural and morphological changes occurring upon alloy formation that cannot be recovered after the first discharge. Therefore, the new sites for the reaction with lithium possess quite different energy what is reflected in the profile of the second discharge. The contribution of the irreversible reduction of SnO_2 phase, at 0.9 V, was negligible in all cases. The observed bands in the discharge and charge curves correspond to the reversible formation of Li–Sn alloys. The enhanced broadening of the bands would be indicative of low crystalline domains achieved by the dispersion effect of the carbon matrix during the carbothermal reaction. For the samples with Sn/Co=85:15, a decrease in the MO_x/R ratio (Figure 4a–c) led to the decrease of the intensity of the alloy main signal. This behavior is in contrast with the higher contribution of lithium insertion in the carbon material occurring in the 0– 0.2 V range.

On decreasing the cobalt content (Figure 4c–e), the main reduction peak at approximately 0.25 V is shifted to approximately 0.3 V, while a new highly broadened band is observed at approximately 0.1 V (marked with an asterisk). It has been reported that the occurrence of cobalt–tin alloys induces a diminution of the working potential in the main alloying plateau [17]. Hence, the latter signal could be assigned to the increased contribution of these phases when cobalt content is increased. This signal

disappeared on subsequent cycling, and hence, an electrochemical reaction between Li and Sn can be inferred for a long-term cycling.
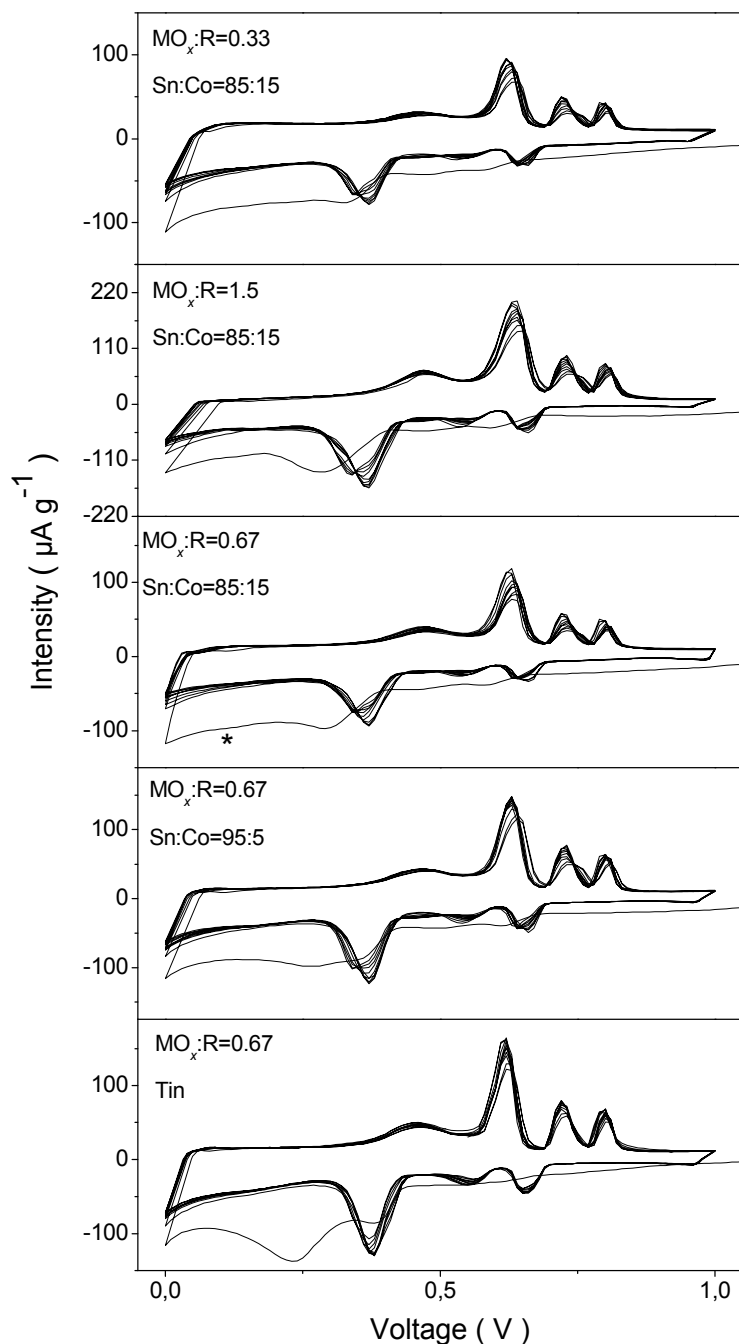

Figure 4. Intensity versus voltage plots recorded by step potential electrochemical spectroscopy. a) Sn:Co=85:15 (MO$_x$:R=0.33); b) Sn:Co=85:15 (MO$_x$:R=1.5); c) Sn:Co=85:15 (MO$_x$:R=0.67). d) Sn:Co=95:5 (MO$_x$:R=0.67); e) tin only. Scan rate: 10 mV/0.1 h.

To unfold the nature of the tin phases yielded by the discharging process, the [119]Sn Mössbauer spectrum of a fully discharged electrode was recorded at room temperature (Figure 5). The asymmetric signal could be decomposed in several components ascribable to $Li_{22}Sn_5$ and β-Sn (Table 1). Different reports have evaluated the ex situ [119]Sn MS of Sn-based intermetallic materials such as $CoSn_2$ [18], Ni_3Sn_4 [18], and Cu_6Sn_5 [19] when used as working electrodes in lithium cells. In these cases, the occurrence of the Li-rich Li_7Sn_2 alloy at the end of the first discharge was reported. In contrast, a recent study on CoSn revealed that no Li_xSn phases were detectable by XRD or Mössbauer spectroscopy [20]. Thus, the absence of signals corresponding to non-reacted Co–Sn alloys could be indicative of a higher reactivity of these intermetallic compounds as compared to tin metal. Nevertheless, its contribution to the $Li_{22}Sn_5$ cannot be established unequivocally.
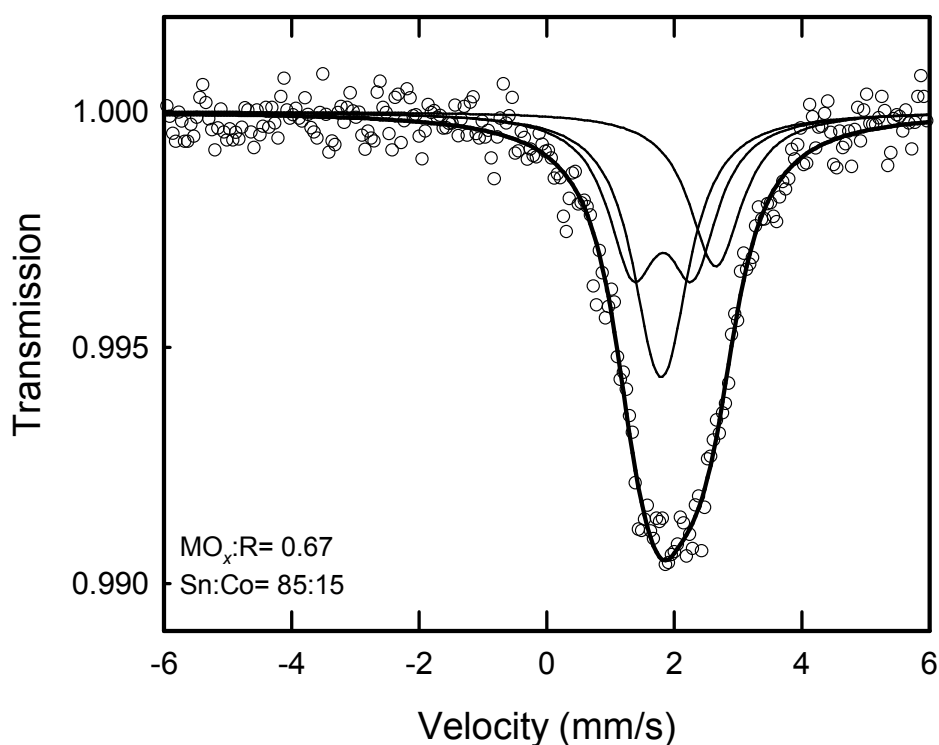

Figure 5. [119]Sn Mössbauer spectrum of a fully discharged electrode with Sn:Co=85:15 and a MO$_x$:R=0.67 ratio.

The presence of non-reacted tin at the end of the discharge can be attributed to kinetic factors contributing to the polarization of the discharge branch. This fact would justify their enhanced performance as electrode materials in lithium cells.

Figure 6 shows the discharge capacity values of lithium test cells assembled using samples with different metal contents. The cells were galvanostatically cycled between 0.02 and 1.0 V. The introduction of tin led to an important increase of the reversible capacity as expected from the significant contribution of Li_xSn alloys formation. Furthermore, an increase of the irreversible capacity in the first discharge is observed (inset in Figure 6). Likely, tin phases also contribute to the initial irreversibility. Thus, a non-negligible contribution of SnO_2 was observed in the MS (Figure 2). Moreover, the significant changes between the profile of the first and second discharges, mainly in the region of lithium–tin alloy formation, may involve additional irreversible reactions to that expected from solid electrolyte interphase (SEI) formation on the carbon surface. On the other hand, some authors have attributed the enhanced initial coulombic efficiency to the nano-tin induced decomposition of the $ROCO_2Li$ species in the SEI layer [21].
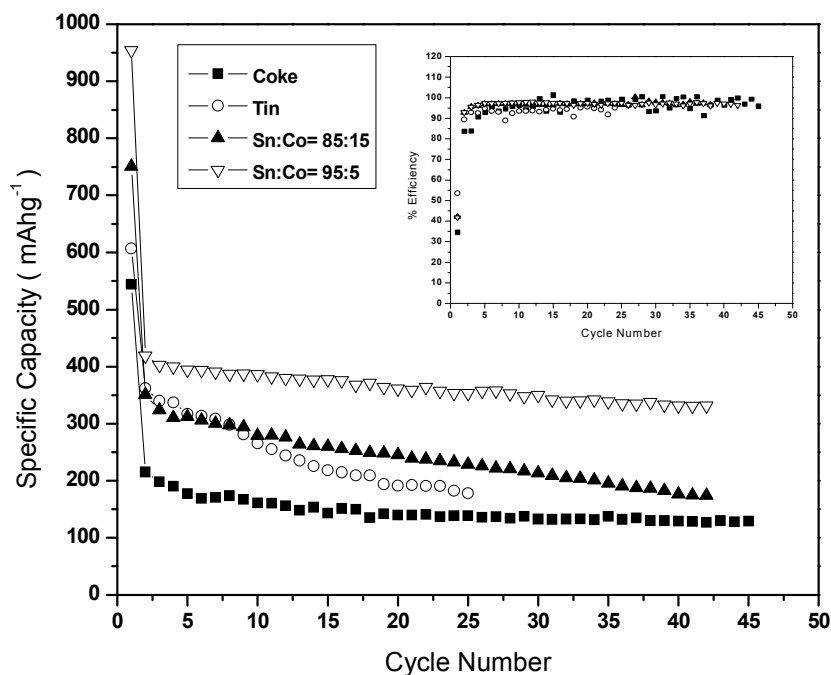

Figure 6. Galvanostatic cycling of Sn-Co-C composites prepared with a metal/carbon ratio equivalent to MO_x:R= 0.67 and different contents of cobalt in their composition. Inset: Plot of coulombic efficiency for the same range of cycles. Kinetic rate: 20 mA/g.

However, it is has been reported that the introduction of tin particles plays an important role on the cyclability upon alloying and de-alloying with lithium. Thus, tin particles confined within the carbon micropores exhibit better performance, since the detrimental effect of the volume expansion is avoided [22]. Unfortunately, the capacity retention was very poor, even if the upper cut off voltage was selected at 1 V to avoid deleterious structural and morphological changes [23]. The introduction of cobalt contributed to improve both capacity and cyclability. Only minor cobalt contents (Sn/Co=95:5) were able to improve the capacity retention as compared to the cobalt-free sample. Capacity values higher than 330 mAh/g were maintained after more than 30 cycles. This result evidences the efficiency of this transition metal to enhance the electrochemical reactivity of the composite. A further increase of the cobalt content (Sn/Co=85:15) did not cause an improvement of the overall capacity. The lack of reactivity versus lithium is responsible for the increase of non-active electrode material. Nevertheless, the response could be improved if the MO_x/R ratio is allowed to increase.
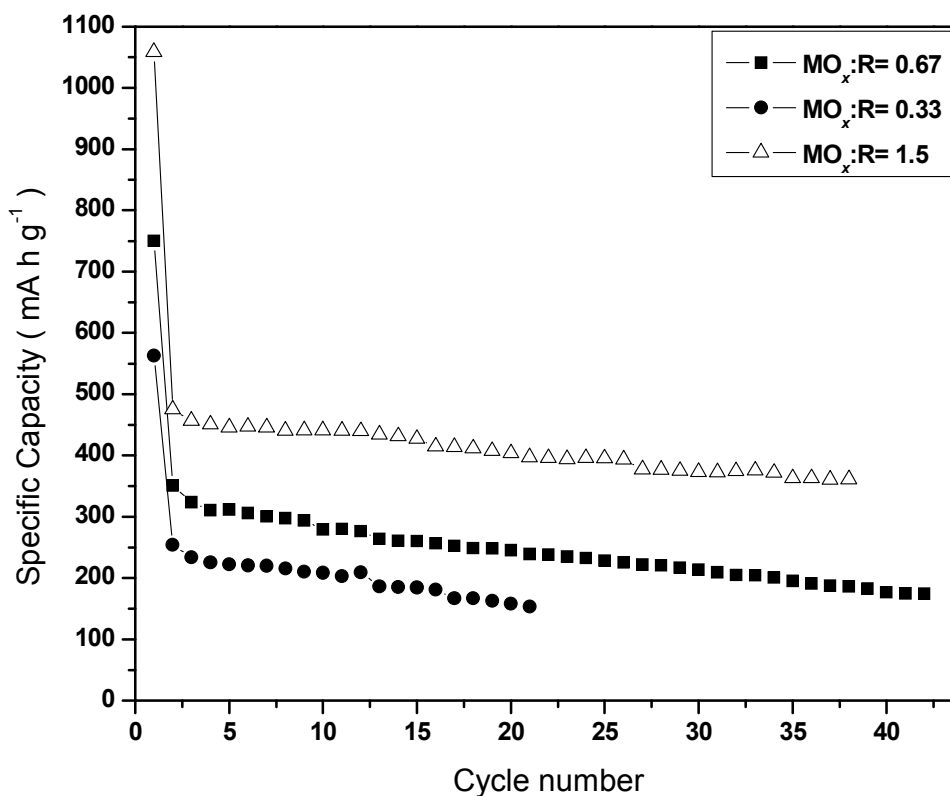

Figure 7. Galvanostatic cycling of Sn-Co-C composites prepared with a Sn:Co=85:15 metal ratio and different MO_x:R ratios (MO_x:R= 0.33, 0.67 and 1.5). Kinetic rate: 20 mA/g.

In order to determine the influence of the carbon matrix on the electrochemical performance, the samples with the Sn/Co=85:15 ratio and different MO_x/R ratios were also cycled. Figure 7 shows a decrease in capacity of the first discharge attributable to the lesser molar capacity of carbon as compared to tin. This fact affected to subsequent cycles, and hence, the sample with higher carbon content (lower ratio, MO_x/R=0.33) delivered the lowest capacities in the whole range. In turn, an increase of the tin content positively contributed to improve both capacity values and retention. A high reversible capacity value (475 mAh/g) was reached in the second cycle. Capacity values higher than 380 mAh/g were maintained after more than 30 cycles.

Electrochemical Impedance Spectroscopy.

Electrochemical impedance spectroscopy provides interesting information concerning the kinetic properties of those electrode/electrolyte interphases playing a significant role in lithium migration. Nyquist plots of selected samples are included in Figure 8a.

The common profile is characterized by two depressed semicircles at high and intermediate frequencies and a straight line at low frequencies. The semicircles are respectively attributed to the kinetic barriers imposed to lithium migration through the SEI film and charge transfer occurring on the electrode surface. Moreover, the line observed at low frequencies corresponds to lithium diffusion into the electrode material [24, 25]. The overall impedance was kept almost constant for the coke material on cycling. This result differs from previous reported data on sulfur-containing vacuum residua in which an important increase of impedance was monitored. In the latter case, the presence of significant sulfur content was considered detrimental for the electrochemical behavior [26]. The inclusion of tin in the composite provoked a huge increment of the impedance for a large number of cycles. Likely, the volume expansion induced by the reversible alloy formation may contribute to a loss of electrical connectivity among particles during a repeated cell operation. The introduction of cobalt in the composite stoichiometry, even at low concentrations, led to a significant decrease of the impedance during cycling. This fact evidences that the beneficial effect of low cobalt contents can be attributed to kinetic effects.
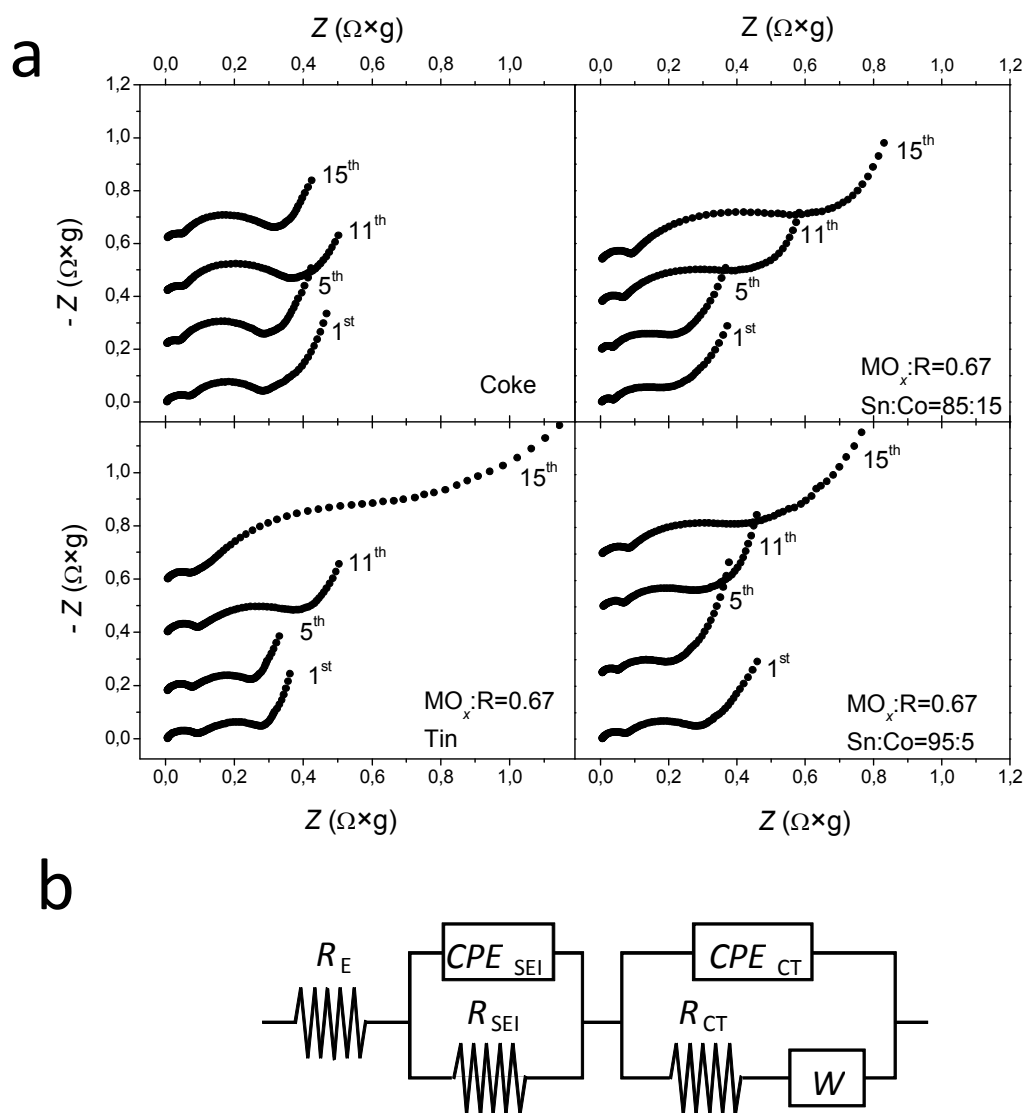
Figure 8. a) Nyquist plots fully discharged electrodes on the first, fifth, eleventh and seventeenth cycles. b) Equivalent circuit used for the fitting of the spectra.

In order to determine the specific influence of the interphases, several examples of equivalent circuits have been proposed in the literature [27, 28]. In this work, the resistance values were calculated from the fitting of the spectra to the selected equivalent circuit displayed in Fig. 8b. In the used circuit, the migration phenomena described above are taken into the necessary account. Figure 9 plots the resistance values (R_{SEI} and R_{CT}) versus cycle number. Although, R_{SEI} values did not reach values higher than 0.11 $\Omega \times$g in the measured range, a clear tendency could not be inferred. The instability of SEI films on both graphitized materials [29] and cokes [30] as a result of

impedance measurements has been reported. Most likely, the erratic behavior of the SEI values in Figure 9 could be ascribed to the presence of dislodges passivation debris migrating cataphoretically. Otherwise, charge transfer resistance steadily increased in cycling for coke and Sn–Co–C composites. Contrarily, an enhanced increase of resistance was recorded for the cobalt-free sample. This result would indicate an important charge accumulation on the electric interphase. In turn, this is likely due to a significant decrease in the electrical conductivity during cycling.
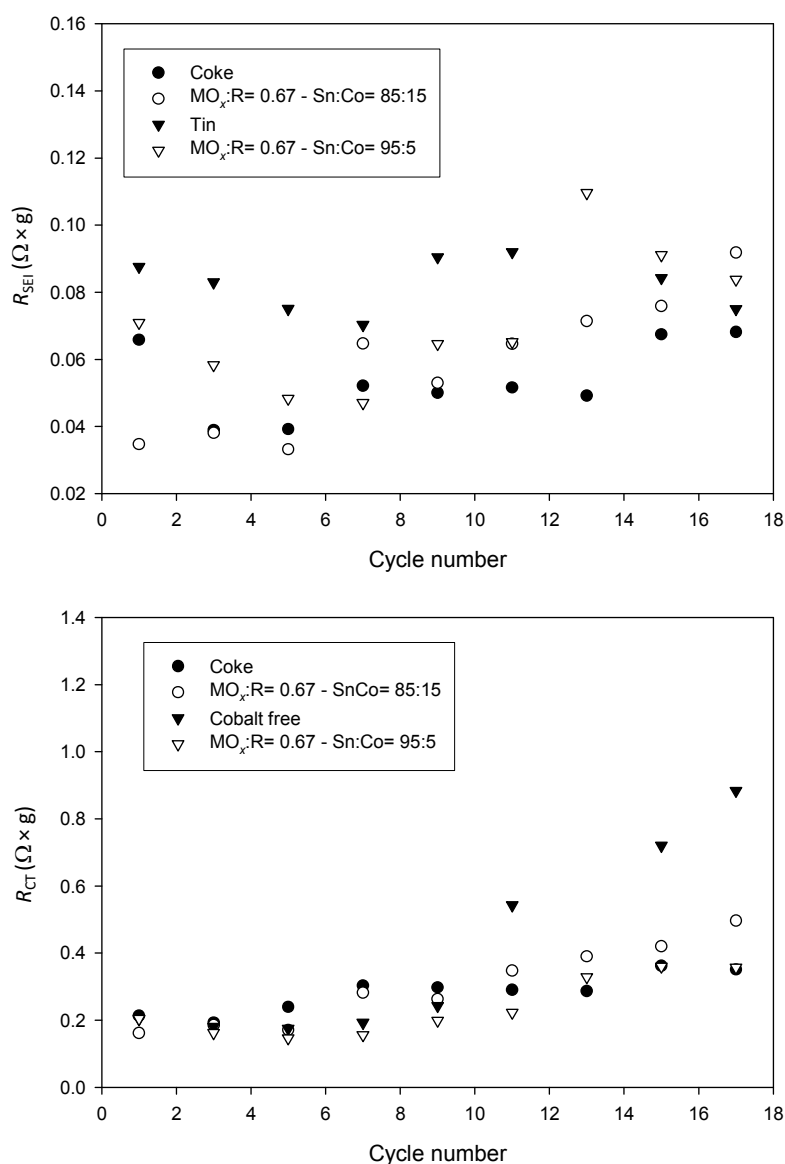

Figure 9. Resistance versus cycle number plots of coke, tin only, Sn:Co=95:5 (MO$_x$:R=0.67) and Sn:Co=85:15 (MO$_x$:R=0.67).

2.1.4   Conclusions

The resorcinol/formaldehyde polymerization–carbonization plus carbothermal reduction process has been used to prepare Sn–Co–C composites. For this purpose, finely powdered tin and cobalt oxides were embedded in the organic gel like precursor. Highly dispersed tin and cobalt– tin phases were eventually obtained by carbothermal reaction after carbonization of the composite precursors. SEM images revealed the presence of carbonaceous particles with metal agglomerates homogeneously dispersed, either decorating the surface or embedded in the carbonaceous matrix. The effective reduction of metal oxides was verified by the XRD technique, in which tin and cobalt– tin phases were predominant.

^{119}Sn Mössbauer spectroscopy evidences the high contribution of cobalt–tin alloys in the initial composites. However, the discharge process involved the disappearance of these phases in further cycling as monitored by step potential electrochemical measurements and ex situ ^{119}Sn Mössbauer spectroscopy of a fully discharged electrode. Nevertheless, the beneficial effect of the presence of cobalt was detected on a galvanostatic cycling and impedance measurements even with small amounts of cobalt added. The sample with Sn/Co=95:5 was able to improve the retention, as compare with tin-only composites. Capacity values around 330 mAh/g after 30 cycles were recorded. In contrast, only 140 and 191 mAh/g were, respectively, measured for coke and cobalt-free samples. This fact would indicate that the presence of crystalline or well-formed cobalt–tin phases is not essential for an improvement of the electrochemical performance of the metal carbon composite. Cobalt plays a determining effect even in amorphous domains and relatively small quantities. However, the moderated capacity values recorded in this study demanded a new strategy in order to achieve more performing results. An increase of the MO_x/R ratio on the Sn/Co=85:15 ratio led to higher reversible capacity values of 380 mAh/g after 30 cycles.

The kinetic response of the electrode materials was determined by impedance measurements. The cobalt containing composites showed a lower increase in charge transfer resistance as compared to the cobalt-free samples. Therefore, the kinetic component seems to play an important role in the improvement of capacity retention observed in Sn–Co–C composites.

Acknowledgements

The authors are grateful to MEC for financial support (Contract PET2005_0670_01). We also thank to M.C. Mohedano for her technical support and the Central Services of the University of Córdoba, especially to F. Gracia for the use of the SEM microscope. F. Nacimiento is indebted to MEC for his predoctoral grant. G.F. Ortiz is indebted to FQM-1447.

References

1. Tirado JL (2003) Mat Sci Eng R 40:103.

2. Manev V, Naidenov I, Puresheva B, Zlatilova P, Pistoia G (1995) J Power Sources 55: 211.

3. Ohzuku T, Iwakoshi Y, Sawai K (1993) J Electrochem Soc 140: 2490.

4. Menachem C, Wang Y, Flowers J E, Peled, Greenbaum SG (1998) J Power Sources 76:180.

5. Nakajima T, Koh, M, Singh, RN, Shimada M (1999) Electrochim Acta 44:2879.

6. Idota Y, Kubota T, Matsufuji A, Maekawa Y, Miyasaka T (1997) Science 276:1395.

7. Alcántara R, Fernández-Madrigal FJ, Lavela P, Tirado JL, Jumas JC, Olivier-Fourcade J (1999) J Mater Chem 9:2517.

8. Todd ADW, Mar RE, Dahn JR (2006) J Electrochem Soc 153:A1998.

9. Hassoun J, Ochal P, Panero S, Mulas G, Bonatto Minella C, Scrosati B (2008) J Power Sources 180:568.

10. Ferguson PP, Todd ADW, Dahn JR (2008) Electrochem Comm;10: 25–31.

11. Trifonova A, Winter M, Besenhard J O (2007) J Power Sources 174 :800.

12. Alcántara R, Lavela P, Ortiz GF, Tirado JL (2005) Electrochem. Solid-State Lett. 8:A222.

13. Hasegawa T, Mukai SR, Shirato Y, Tamon H (2004) Carbon 42:2573.

14. Wang K, He X, Ren J, Wang L, Jiang C, Chunrong W (2006) Electrochim Acta 52: 1221.

15. Jaén J, Varsányi ML, Kovács E, Czakó-Nagy I, Buzás A, Vértes, Kiss L (1984) Electrochim Acta 29: 1119.

16. Inoue H (2006) High capacity negative electrode materials next to carbon; Nexelion. Proceedings of the International Meeting on Lithium Batteries. Biarritz, France. The Electrochemical Society.

17. Dahn JR, Mar RE, Abouzeid A (2006) J Electrochem Soc 153:A361.

18. Naille S, Jumas JC, Lippens PE, Olivier-Fourcade J (2009) J Power Sources 189:814.

19. Choi W, Lee JY, Lim HS (2004) Electrochem Commun 6:816.

20. Alcántara R, Rodríguez, I, Tirado, JL (2008) ChemPhysChem 9:1171.

21. Guo B, Shu J, Tang K, Bai Y, Wang Z, Chen L (2008) J Power Sources 177:205.

22. Grigoriants A, Soffer G, Salitra D, Aurbach D (2005) J Power Sources 146:185.

23. Courtney IA, Dahn J R (1997) J Electrochem Soc 144:2943.

24. Aurbach D, Gnanaraj J S, Levi MD, Levi EA, Fischer JE, Claye A (2001) J Power Sources 97-98: 92.

25. Wang C, Appleby AJ, Little FE (2002) J Electrochem Soc 149:A754.

26. Tirado JL, Santamaría R, Ortiz GF, Menéndez R, Lavela P, Jiménez-Mateos JM, Gómez García FJ, Concheso A, Alcántara R (2007) Carbon 45:1396.

27. Funabiki A, Inaba M, Ogumi Z, Yuasa S, Otsuji J, Tasaka A (1998) J Electrochem Soc 145:172.

28. Wang C, Appleby AJ, Little FE (2002) J Electrochem Soc 149:A754.

29. Aurbach D, Markovsky B, Levi MD, Levi E, Schechter A, Moshkovich M, Cohen Y (1999) J Power Sources 81-82:95.

30. Avery NR, Black KJ J (1997) J Power Sources 68:191.

2.2 A facile carbothermal preparation of Sn-Co-C composite electrodes for Li-ion batteries using low cost carbons

Francisco Nacimiento[a], Pedro Lavela[a], José Luis Tirado[a] and J.M. Jiménez-Mateos[b]

[a]*Laboratorio de Química Inorgánica, Universidad de Córdoba, Marie Curie, Campus de Rabanales, 14071 Córdoba, Spain .* [b] *REPSOL, Ctra. N-V km 18, 28930 Móstoles, Madrid, Spain*

Abstract

Sn-Co-C composites were prepared by carbothermal reaction of ball-milled precursors. X-ray diffraction and [119]Sn Mossbauer spectroscopy of the original composites revealed the predominance of Sn and $CoSn_2$ phases for those samples prepared with a high Sn/Co ratio. Electron microscopy images showed a homogeneous dispersion of submicronic metallic particles in the carbon matrix. Galvanostatic cycling at several kinetic rates revealed that $Sn_7Co_1C_{92}$ and $Sn_8Co_4C_{88}$ are able to maintain 400 mA h g^{-1} after 40 cycles at 35 mA g^{-1}. The large $CoSn_2$ contributions revealed by Mössbauer spectroscopy in the original and cycled electrodes can be responsible for the good electrochemical performance. These results are also supported by impedance spectroscopy measurements.

2.2.1   Introduction

Tin has been regarded as a suitable option to replace graphite in anodes for lithium-ion batteries because of the high Li/Sn ratio know for different intermetallic compounds (up to $Li_{4.4}Sn$), The element is able to deliver specific capacities as high as as 994 mA h g^{-1} [1, 2]. Nevertheless, the real application of metallic tin electrodes is restricted by a limited reversibility, which arises from the dramatic volume changes occurring upon cycling [3, 4]. The detrimental contraction–expansion effects can be attenuated by multiple procedures including the use of glasses and the combination with different elements [5, 6]. More recently, different studies evidenced the advantages of using tin-TM (TM: Ti, V, Cr, Mn, Fe, Ni, Co and Cu) intermetallic compounds [7, 8]. TM is electrochemically inactive [9, 10], although ternary lithiated phases has been identified in some cases, e.g., for Cu_6Sn_5 [11]. In consequence, a reduction in theoretical capacity is inherent to this approach.

On the other hand, the use of Sn-TM-C composites was found to be an effective way of improving electrode performance [12, 13]. The carbon component forms a stable dispersion matrix, which hinders the agglomeration of intermetallic particles upon cycling. Moreover, carbon provides an electron and ion conducting matrix that facilitates the electrochemical reaction with lithium. Also, the ability of the carbon material to reversibly insert lithium contributes positively to the overall reversible capacity. In fact, Sn-TM-C composites are more efficient than their individual components taken separately [14]. In this context, disordered carbons prepared at low temperatures, such as cokes, may play an important role. The reduced cost, of cokes obtained as a by-product of the petroleum industry is an added value for commercial purposes. Also, low structural ordering leads to large number of different sites for lithium insertion [3].

The intimate mixing of composite components can be carried out by several routes [15-17]. Among others, ball milling has recently attracted more attention in the synthesis of anode materials for lithium-ion batteries based on intermetallic compounds [18-21]. Homogeneous mixtures of ultrafine metal particles embedded in the carbon phase are commonly obtained by mechanical treatments.

The aim of this work is to evaluate the validity of a low-cost coke material to act as the carbon source in composites with different Sn/Co and metal/carbon ratios. For

this purpose, several Sn-Co-C composites were prepared by ball milling metal oxides and carbon precursors followed by carbothermal reduction. This is a cost-effective procedure for the large-scale production of electrode materials.

2.2.2 Experimental

Sn-Co-C composites were prepared by a two step process. Suitable amounts of commercial SnO_2 (Panreac) and CoO (Aldrich) and green coke (REPSOL) were used as precursors of the composite materials. Coke was the only source of the electroactive carbon matrix that embeds the particles of intermetallic compounds in the final composite. The precursors were weighed to prepare a set of samples with different elemental contents. A 15% excess of coke was added for balancing the weight loss occurring during carbonization, according to previous reports [14]. The precursors were ground in a planetary ball mill RETSCH S100. The agate jar contained 4 g of precursor material and two 11g agate balls. The material was ball milled for 5 hours at 500 rpm under an air atmosphere. Then, the composite precursors were separated and annealed at 800 °C under a flowing stream of argon (90 mL min^{-1}) for 6 h. The heating rate was 2 °C min^{-1}. Carbon content was analyzed in an Elemental CHNS Analyser *Eurovector EA 3000*, while tin and cobalt contents were determined by EDS. According to their nominal composition samples will be henceforth referred to as $Sn_{27}Co_{14}C_{59}$, $Sn_7Co_1C_{92}$, $Sn_8Co_4C_{88}$, $Sn_6Co_6C_{88}$, $Sn_4Co_2C_{94}$.

X-ray diffraction (XRD) patterns were recorded in a Siemens D-5000 apparatus provided with CuKα radiation and graphite monochromator. The 2θ scan rate was 0.04°/1.2 s. Scanning electron microscopy (SEM) images were obtained in a JEOL-SM6300 microscope located at the Research Support Service, University of Córdoba.. The [119]Sn Mössbauer spectra (MS) were recorded at room temperature with an Ametek-Wissel constant-acceleration spectrometer in transmission mode. The source of radiation was [119m]Sn in a $BaSnO_3$ matrix. The isomer shift scale was set by using a $BaSnO_3$ pattern. The peak centre of the Sn(IV) signal was set as the scale zero. The spectra profile was decomposed in lorentzian lines by using a least-square-based method [22]. The goodness of the fit was controlled by the χ^2 value.

The electrochemical behavior of the Sn-Co-C composites was evaluated by cycling lithium test cells in galvanostatic conditions. The working electrode was prepared by blending active material (60%), carbon black (30%) and PVDF binder (10%). In order to ensure the homogeneous distribution of the polymer binder, n-methyl pyrrolidinone was added to form a paste that was spread on a 9 mm cooper disc. The cell assembly was completed with a lithium metal disk of the same diameter as a counter electrode. The electrodes were separated by Whatman glass fibber discs soaked in 1 M $LiPF_6$ (EC:DEC = 1:1) electrolyte solution. The cell was finally enclosed in a two-electrode Swagelok^{TM} type cell. The assembly of test cells and handling of the discharged electrode were carried out in an MBraun glove box under a controlled Ar atmosphere.

An Arbin multichannel galvanostat system was used to cycle lithium cells, with kinetic rates ranging from 35 to 700 mA g^{-1} for both charge and discharge branches. Electrochemical impedance spectroscopy was carried out in an Autolab PGSTAT12 system. Three-electrode lithium cells were used with a lithium metal disc as reference electrode. Before measuring the impedance values, the cells were kept in open circuit for at least 5 h to achieve a quasi-equilibrium conditions. An AC voltage signal of 5 mV was applied from 100 kHz to 2 mHz.

2.2.3   Results and discussion

The chemical analysis of samples revealed high carbon contents, around 90 at.%, except for $Sn_{27}Co_{14}C_{59}$. In the latter composite, lower carbon content was used during the preparation in order to evaluate the influence of the metallic elements in the electrochemical behavior. Concerning the Sn:Co ratio, the chemical analysis showed substantially differing values. Such diversity was also planned during the synthesis in order to determine the effect of Sn/Co ratios on the performance. Figure 1 shows the XRD patterns of the annealed composites. The short range ordering of the carbon phase precludes its detection by this technique. Contrarily, a set of narrow reflections can be ascribed to the presence of different crystalline tin-cobalt phases, including tetragonal metallic tin (JCPDS 04-0673), tetragonal $CoSn_2$ (JCPDS 25-0256), Co_3Sn_2 (JCPDS 27-1124) and hexagonal CoSn phase (JCPDS 02-0559). No peaks ascribable to Co_3O_4 were identified. Only minor peaks were assigned to SnO_2 cassiterite (JCPDS 14-1445).

The evaluation of the XRD patterns suggests that an efficient carbothermal reduction occurred during the carbonization at 800 ºC. Those samples with close Sn/Co ratios ($Sn_{27}Co_{14}C_{59}$, $Sn_8Co_4C_{88}$, $Sn_4Co_2C_{94}$) were characterized by similar patterns. The diffraction pattern corresponding to $Sn_6Co_6C_{88}$ reveals the major CoSn phase and minor contributions from $CoSn_2$ and Co_3Sn_2. Finally, a significant contribution of metallic tin and $CoSn_2$ is observed for $Sn_7Co_1C_{92}$.
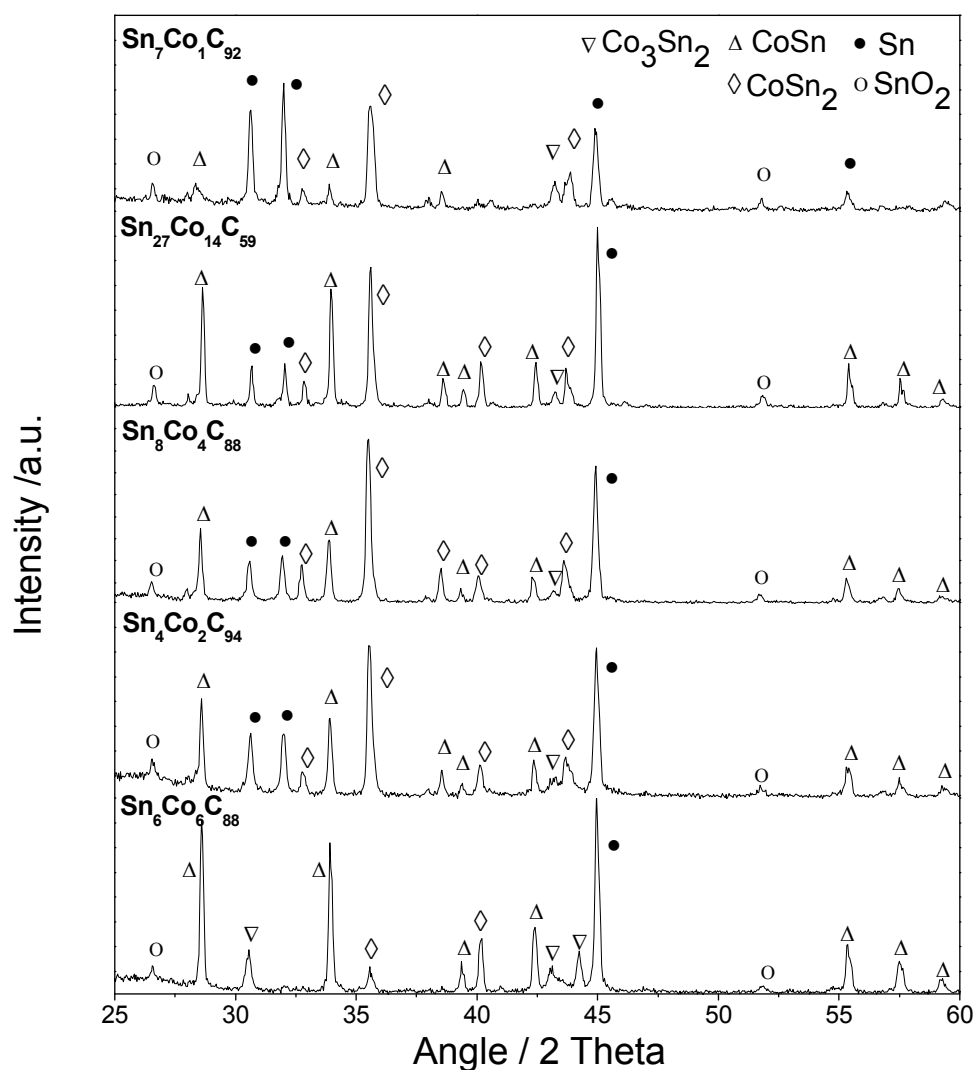

Figure 1. XRD patterns of Sn-Co-C composites. Indexed phases were marked with symbols.

A significant effect of the carbon matrix on the size and morphology of the metallic particles is clearly observed in the SEM micrographs of selected samples (Figure 2). Thus, samples containing high carbon content showed submicrometric metallic particles, embedded in the carbon matrix (Figure 2b, c). The spherical metallic particles attached to the carbon surface can be assigned to tin. The low melting point of this metal leads to its partial exudation during the carbonization process. These particles appear well dispersed and, most probably firmly attached, on the carbon surface. The exudation effect could be considered as detrimental for the reversibility of the electrochemical reaction.
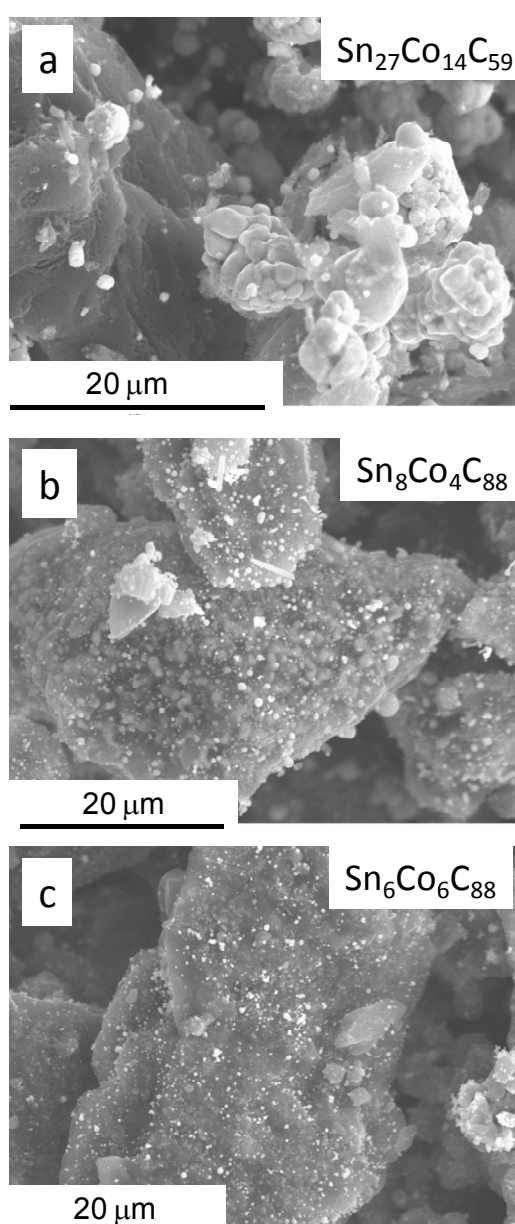
Figure 2. SEM micrographs of $Sn_{27}Co_{14}C_{59}$, $Sn_8Co_4C_{88}$ and $Sn_6Co_6C_{88}$ composites.

However, previous reports have demonstrated that the use of tin nanoparticles as separated nanowires or nanopillars on the electrode surface provides a suitable morphology that prevents tin agglomeration upon the electrochemical reaction [23, 24].

The sample with a low carbon content ($Sn_{27}Co_{14}C_{59}$) revealed large metallic particles of several microns isolated from the carbon phase (Figure 2a). This particular morphology and phase distribution may have a negative effect on the electrochemical reversibility, as compared with nanodispersed materials.

Figure 3. ^{119}Sn Mössbauer spectra of Sn-Co-C composites. Experimental and fitted spectra are plotted with symbols, and lines, respectively.

Table 1. Hyperfine parameters of fitted Mössbauer spectra of Sn-Co-C composites.

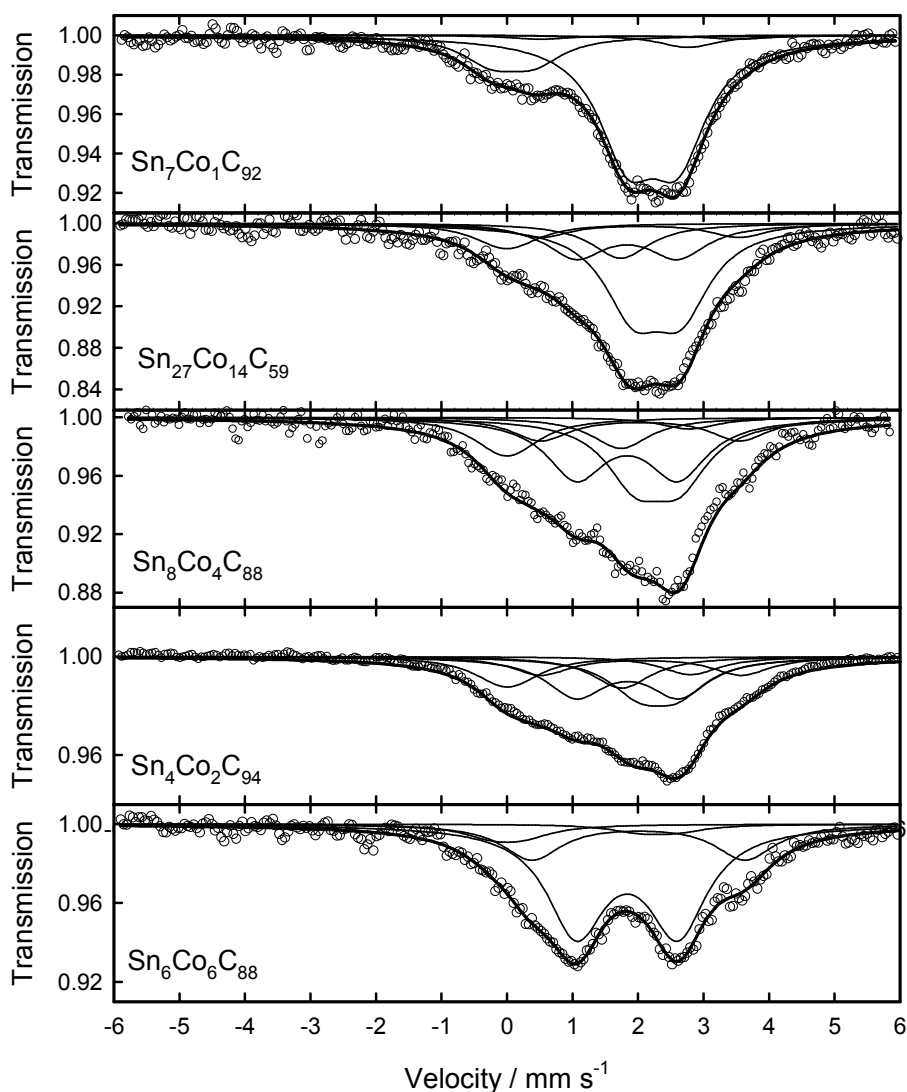| Sample	[1] s/d	Tin phase	[2] δ (mm/s)	[3] Δ (mm/s)	[4] Γ (mm/s)	[5] C (%)	[6] χ^2
Sn₇Co₁C₉₂	s	β-Sn	2.76(2)		1.084(8)	4.23	0.601
	d	CoSn	1.82(3)	1.542(3)	1.084(8)	0.92	
	d		2.02(3)	3.025(7)	1.084(8)	2.7	
	d	CoSn₂	2.22(2)	0.77(1)	1.084(8)	75.09	
	d	SnO₂	0.08(6)	0.64(7)	1.084(8)	17.06	
Sn₂₇Co₁₄C₅₉	d	CoSn	1.83(4)	1.549(3)	1.089(7)	21.03	0.556
	d		2.03(2)	3.038(7)	1.089(7)	8.86	
	d	CoSn₂	2.29(1)	0.73(2)	1.089(7)	50.38	
	s	Co₃Sn₂	1.739(3)		1.089(7)	11.18	
	d	SnO₂	0.001(3)	0.242(1)	1.089(7)	8.55	
Sn₈Co₄C₈₈	s	β-Sn	2.78(1)		1.089(7)	3.21	0.649
	d	CoSn	1.81(4)	1.549(3)	1.089(7)	32.18	
	d		2.05(5)	3.038(7)	1.089(1)	12.7	
	d	CoSn₂	2.29(7)	0.6(1)	1.089(7)	32.09	
	s	Co₃Sn₂	1.74(2)		1.089(7)	8.59	
	d	SnO₂	0.001(8)	0.242(1)	1.089(7)	11.23	
Sn₄Co₂C₉₄	s	β-Sn	2.80(3)		1.095(6)	7.04	0.762
	d	CoSn	1.847(8)	1.558(3)	1.095(6)	29.65	
	d		2.05(2)	3.055(7)	1.095(6)	14.12	
	d	CoSn₂	2.31(4)	0.58(7)	1.095(6)	24.62	
	s	Co₃Sn₂	1.753(7)		1.095(6)	12.19	
	d	SnO₂	0.00(1)	0.243(1)	1.095(6)	12.37	
Sn₆Co₆C₈₈	d	CoSn	1.83(1)	1.55(2)	1.088(9)	66.78	0.556
	d		2.00(5)	3.25(9)	1.088(9)	22.27	
	d	CoSn₂	2.292(3)	0.572(1)	1.088(9)	4.13	
	d	SnO₂	0.001(4)	0.50(9)	1.088(9)	6.82	
Hyperfine parameters from the literature[25, 26]	s	β-Sn	2.559(3)		1.022(9)	100	
	d	CoSn	1.854(6)	1.60(1)	0.99(1)	67	0.97
	d		2.03(1)	3.14(2)	0.99(2)	33	
	s	CoSn₂	2.14	0.78			
	d	Co₃Sn₂	1.74	1.3		100	
	d	SnO₂	-0.011	0.65	1.27	100	0.48

[1]*s/d*: singlet (*s*) or doublet (*d*); [2]δ: isomeric shift; [3]Δ: quadrupole splitting; [4]Γ: line-width at half maximum; [5]*C*: relative contribution; [6]χ^2: goodness of the fitting.

[119]Sn Mössbauer spectroscopy is a valuable technique to evaluate the local environment of the probe atom. The spectra of the original composites are shown in figure 3. They are characterized by large asymmetric profiles in which the contribution of the distinct Sn-Co phases cannot be visually resolved (Figure 3). To overcome this problem, the hyperfine parameters of the Co–Sn phases, previously identified by XRD, were taken from the literature and introduced in the fitting procedure to determine their relative contributions. However, slight changes in the hyperfine parameters were allowed in order to achieve a good fitting (Table 1). Recently, it has been demonstrated that the presence of carbon atoms cause an increase in the isomer shift value of the spectrum barycentre as compared with pure tin-cobalt compound [25]. The quantification of the tin atomic fractions is proportional to the relative contribution to the MS spectrum and the recoil-free fraction. Unfortunately, a complete study of the recoil-free fraction of cobalt-tin compounds is not available in the literature, hence limiting the quantification of tin phases. A Lamb–Mössbauer factor of 0.55 was recently reported for CoSn [27]. On the other hand, a factor as low as 0.039 was reported for β-Sn [28]. The marked difference between these values explains the low contribution of β-Sn to the Mössbauer spectra, as compared with XRD patterns.

Figure 4 shows the voltage vs. capacity plots for the first cycle and second discharge of lithium test cells using the metal-carbon composites as working electrodes. The first discharge evidences a large capacity which is not recovered after subsequent charge. This phenomenon is commonly ascribed to the irreversibility of the quasi-plateau observed at 0.8-1 V, which is attributed to the formation of the solid electrolyte interface that impedes further electrolyte decomposition [29]. Below 0.5 V, a sloping voltage extends for several hundreds of mA h g^{-1}. A good reversibility of this effect is observed in further charge and is attributed to both the reversible formation of Li-Sn intermetallic compounds and the insertion of lithium in the carbon matrix [1, 2, 22].

According to the theoretical capacity of carbon and tin, electrochemical reactions of the composite with lithium can be summarized as:

$$Li + 6\,C \rightleftarrows LiC_6 \qquad\qquad (1)$$

$$4.4\,Li + Sn \rightleftarrows Li_{4.4}Sn \qquad\qquad (2)$$
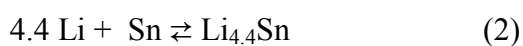
According to these reactions, a maximum $Li_{46}Sn_7Co_1C_{92}$ nominal stoichiometry could be reached, that can be converted to 618 mA h g^{-1}.
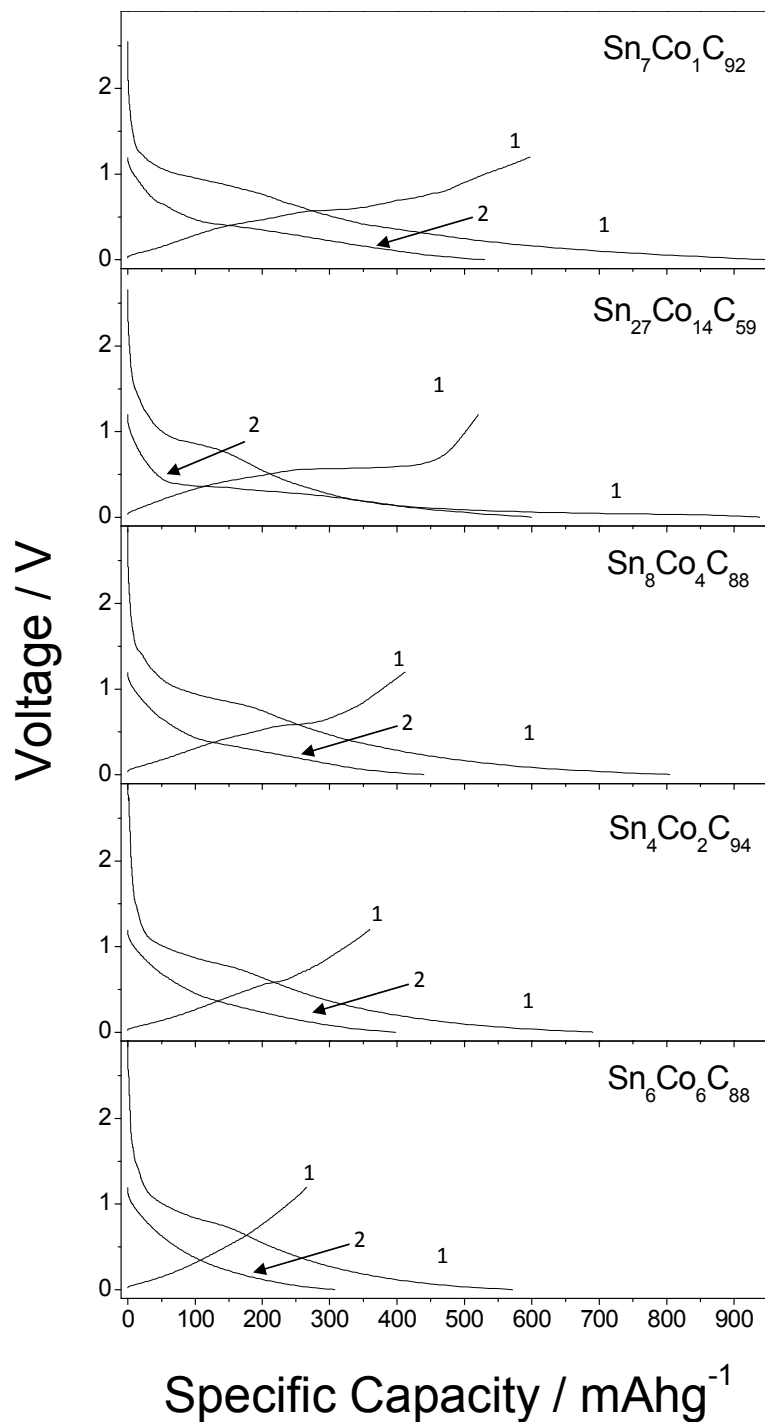

Figure 4. Voltage versus capacity plots of Sn-Co-C composites for the first discharge and charge, and second discharge. Lithium cells were cycled at 35 mAg^{-1}

The experimental capacity value recorded for this sample after the first discharge is higher than the theoretical one. However, it is well known that the disordered structure of coke provides additional sites for lithium reaction. The resulting capacity values are significantly higher than those found when lithium is exclusively hosted in the interlayer space of the grapheme layers. Moreover, the Sn-Co or Sn-Co-C interactions may involve an additional contribution to the electrochemical process which justifies a deeper analysis. Large capacities were observed for $Sn_{27}Co_{14}C_{59}$ and $Sn_7Co_1C_{92}$. In the former sample, the high metal content may explain this behavior, while for $Sn_7Co_1C_{92}$ the high contribution of $CoSn_2$ is responsible for the good performance. The high Sn/Co ratio in the $CoSn_2$ stoichiometry would justify a high theoretical capacity and hence a positive contribution to the overall capacity of the composite. Concerning CoSn and Co_3Sn_2 different cell performances can be found in the literature. Thus, Zhang et al. reported that CoSn and Co_3Sn_2 intermetallics did not completely convert to the Li_xSn during the first discharge, while $CoSn_2$ is able to reach full lithiation [30]. Xie et al. have reported capacity fading in microcrystalline Co_3Sn_2. It was ascribed to a crystallization process during cycling [31]. On the contrary, nanocrystalline Co_3Sn_2 shows capacities around 450 mA h g^{-1} and good capacity retention at different rates [32]. For nanocrystalline CoSn, the reaction with lithium produces a reversible amorphization of the intermetallic compound. The presence of Co atoms avoids the formation of crystalline phases of Li_xSn [33]. These differences imply that, together with composition, both crystallinity and particle morphology play an important role. Concerning the possible effect of Sn-Co-C interactions on the electrochemical response vs. lithium, the addition of both Co and C was envisaged as a way to stabilize the structure during the repeated reaction with lithium [34]. Lithium cells were galvanostatically cycled in order to evaluate capacity retention in the composite electrodes (Figure 5). For the carbonized coke, the capacity was initially high. However, an enhanced capacity fading was observed during the first few cycles. Thus, the separate contribution of the carbon matrix to the electrochemical performance must be considered as having a secondary role. On the contrary, the effect of the carbon matrix on the capacity retention of the composites is clearly evidenced for $Sn_{27}Co_{14}C_{59}$ sample. Thus, the high metal/carbon ratio for this sample can be considered the origin of the enhanced capacity fading, as found in pure tin electrodes [3,4].
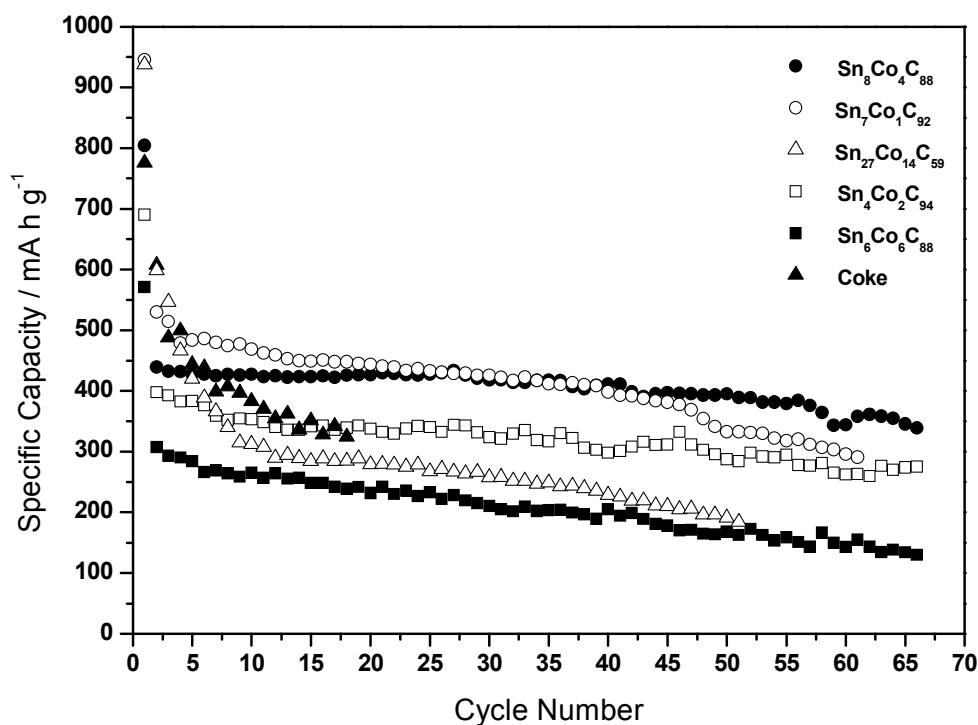
Figure 5. Galvanostatic cycling of Sn-Co-C composites at 35 mAg^{-1}

The differential capacity curves for $Sn_{27}Co_{14}C_{59}$ and $Sn_8Co_4C_{88}$ showed important differences between samples with different carbon content. Thus, the charging curves for $Sn_{27}Co_{14}C_{59}$ are characterized by an intense peak at 0.58 V which is shifted to 0.60 V while its intensity is diminished (Figure 6). This behaviour has been ascribed to the occurrence of microcrystalline $CoSn_2$ with detrimental effect on the lithium cell cycling. On the contrary, $Sn_8Co_4C_{88}$ revealed a cathodic peak at 0.6 V which remained basically unmodified after five cycles. A similar behaviour was observed in nanocrystalline $CoSn_2$ and correlated to the good capacity retention on prolonged cycling [35]. It is well known that the metallic particles detached from the carbonaceous phase (Figure 2a) are more prone to suffer particle aggregation, which leads to electrode degradation [4]. However, a large capacity fading was also observed for $Sn_6Co_6C_{88}$, despite of its high carbon content. It means that additional factors must be considered. Irrespective of their similar Sn/Co ratios, $Sn_8Co_4C_{88}$, $Sn_{27}Co_{14}C_{59}$ and $Sn_4Co_2C_{94}$ show distinct cycling performances.
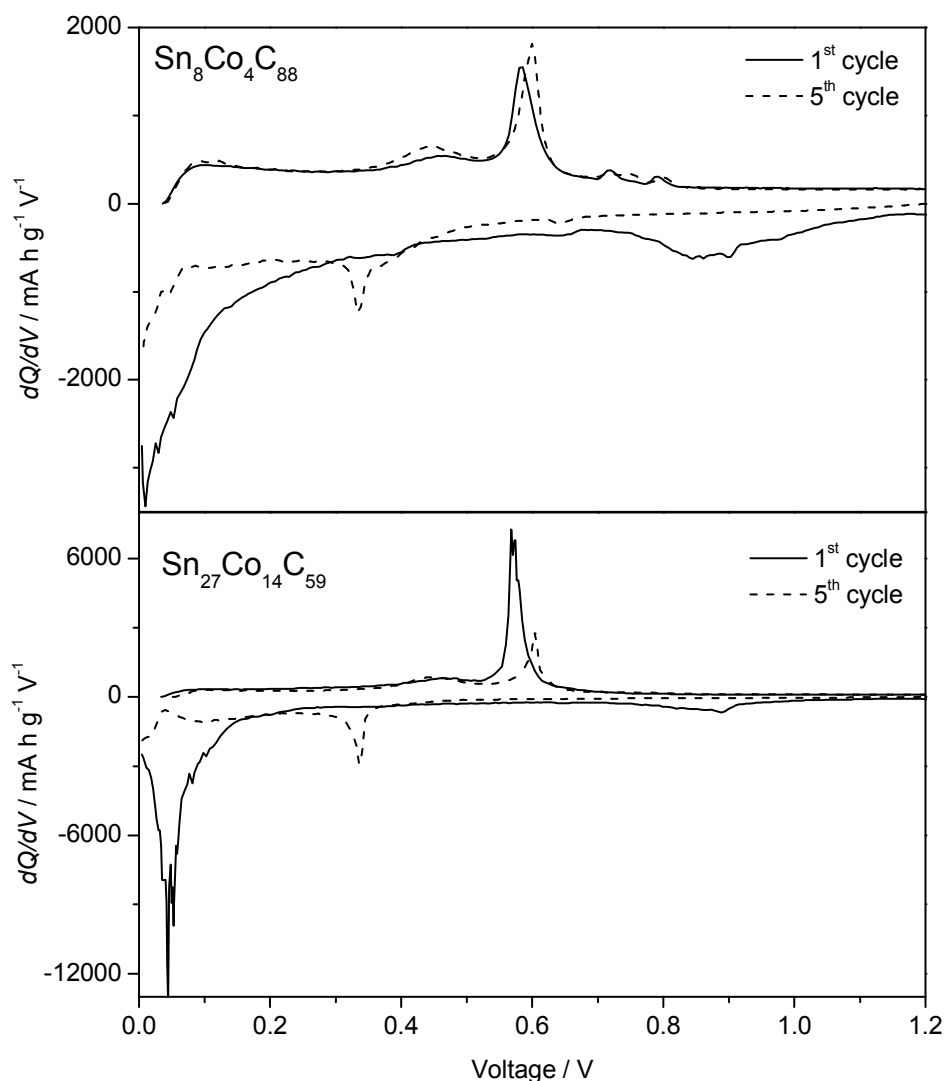
Figure 6. Differential capacity plots for $Sn_{27}Co_{14}C_{59}$ and $Sn_8Co_4C_{88}$ after–1 and 5 cycles.

This behavior evidences that the metal/carbon ratio has more influence on the electrochemical response. Dahn et al. have evaluated a wide variety of $Sn_{1-x}Co_x$ compounds. A plot of specific capacity vs. Co atomic percent showed a non-linear behavior and an enhanced decrease of capacity for low Sn/Co ratios [34]. Thus, the low Sn/Co ratios favoring the presence of less reactive CoSn and Co_3Sn_2 is detrimental as compared with large $CoSn_2$ contributions [30]. Capacity values of 400 mA h g^{-1} at 35 mA g^{-1} were recorded after 40 cycles. This electrochemical behavior is also reflected in the different capability of the electrodes to retain suitable capacity values at high C rates

(Figure 7). These results show that $Sn_7Co_1C_{92}$ and $Sn_8Co_4C_{88}$ are able to maintain 300 mA h g^{-1} at 2 °C after 28 cycles. In contrast, capacity values as low as 203 mA h g^{-1} were recorded at 2°C for $Sn_6Co_6C_{88}$.
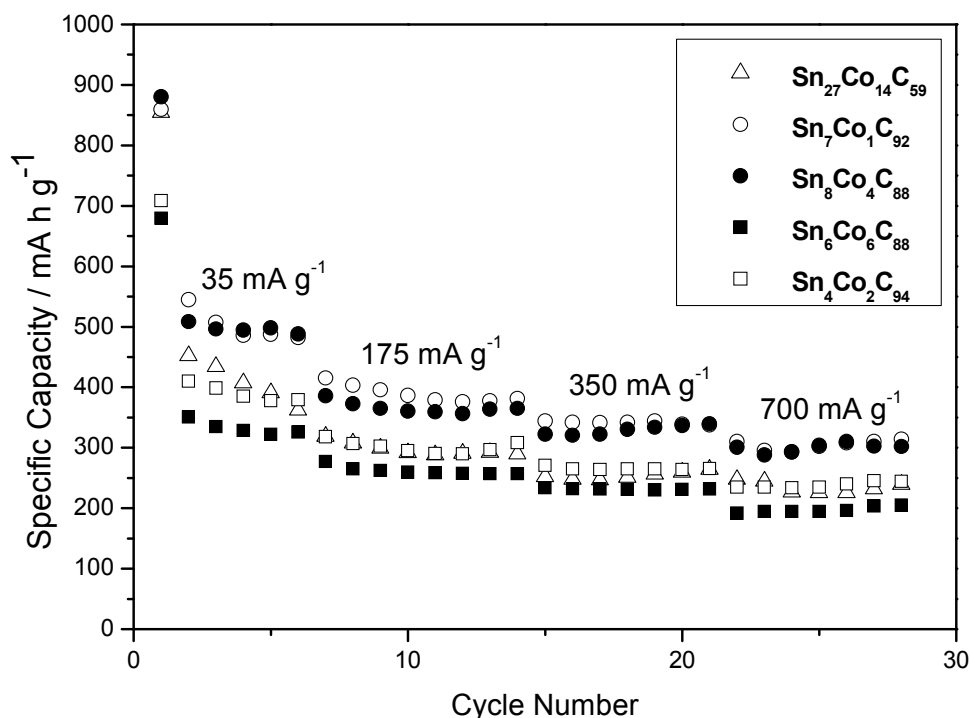

Figure 7. Galvanostatic cycling of Sn-Co-C composites at different kinetic rates.

Electrochemical impedance spectroscopy allows an evaluation of the internal resistance at the working electrode/electrolyte interphase, which plays a significant role in lithium migration. Figure 8a displays the Nyquist plots of selected samples, chosen in the basis of their different composition and electrochemical behavior. The spectra were fitted according to an equivalent circuit commonly reported in the literature for carbonaceous materials (Figure 8b) [36, 37]. RE refers to the resistance of the electrolyte. Two depressed semicircles at high and intermediate frequencies are commonly attributed to the kinetic limitations to lithium migration through the solid-electrolyte interface (SEI) and the charge transfer at the electrode surface.

These phenomena are interpreted in terms of a resistance and a constant phase element (CPE) placed in parallel in the equivalent circuit (R_{SEI}, CPE_{SEI}), (R_{CT}, CPE_{CT}). In

addition, the line observed at low frequencies is ascribed to lithium diffusion into the electrode material and is fitted to a Warburg element (W) [37, 38]. The resulting resistance values are listed in Table 2.
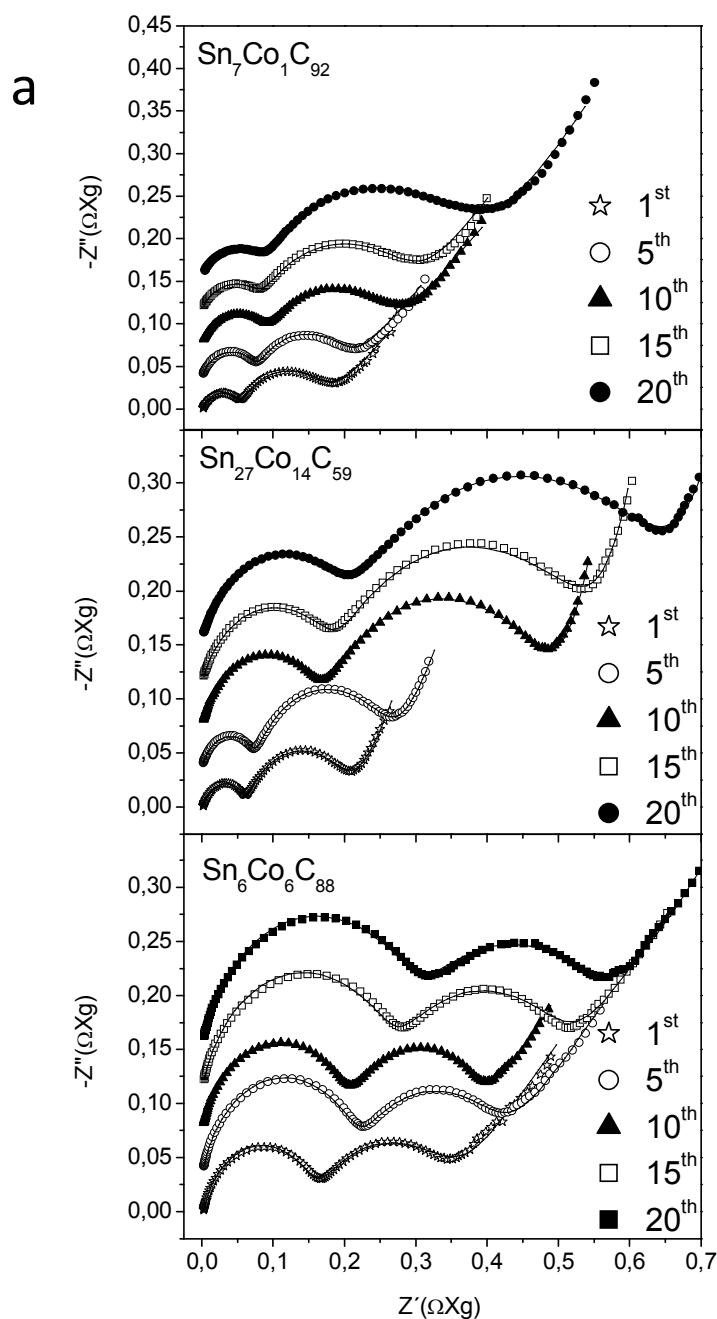

Figure 8. a) Nyquist plots of fully discharged electrodes after several cycles. Experimental data are plotted as symbols and the fitted spectra as lines. b) Equivalent circuit used for the fitting of the spectra.
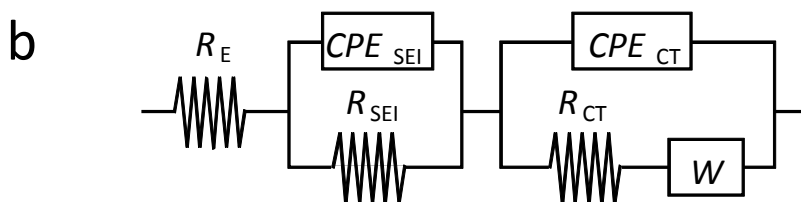
b

R_E CPE_{SEI} R_{SEI} CPE_{CT} R_{CT} W

Table 2. Electrical resistance of selected Sn–C and Sn–Co–C composites as calculated by fitting their impedance spectra.

Sample	Resistance /$\Omega \times$g	1 discharge	5 discharge	10 discharge	15 discharge	20 discharge
$Sn_7Co_1C_{92}$	R_{SEI}	0.0535	0.0766	0.0932	0.0826	0.0865
	R_{CT}	0.1233	0.1292	0.1618	0.2056	0.2880
$Sn_{27}Co_{14}C_{59}$	R_{SEI}	0.062	0.0742	0.1708	0.1843	0.2092
	R_{CT}	0.1329	0.1863	0.3147	0.3589	0.4486
$Sn_6Co_6C_{88}$	R_{SEI}	0.1562	0.2180	0.2034	0.2675	0.2974
	R_{CT}	0.1919	0.1978	0.1868	0.2412	0.2649

The values of solid electrolyte interphase resistance (R_{SEI}) were generally of lower magnitude than charge transfer resistances (R_{CT}). For sample $Sn_7Co_1C_{92}$, the R_{SEI} values were low and tended to stabilize at ca. 0.08 $\Omega \times$g after 20 cycles. In contrast, resistance values higher than 0.2 $\Omega \times$g were recorded for $Sn_6Co_6C_{88}$ and $Sn_{27}Co_{14}C_{59}$. Concerning R_{CT} values, a marked increase on cycling was observed for $Sn_{27}Co_{14}C_{59}$, while the other samples reflect the beneficial effect of the carbon matrix to provide a stable and conductive electrode–electrolyte interphase. Considering both contributions, sample $Sn_7Co_1C_{92}$ has the lower overall resistance values upon 20 cycles. It can be correlated with the higher capacity values retained by this sample after 20 cycles, as shown in Figure 5.

Ex situ XRD and [119]Sn Mössbauer measurements were recorded on cycled electrodes to unveil changes in the intermetallic phases upon cycling. Figure 9 shows the ex situ XRD patterns of $Sn_7Co_1C_{92}$ electrodes after one discharge and after one and five cycles. The discharged electrode revealed the effective Li–Sn alloy formation by the presence of Li_5Sn_2 (JCPDS 29-0839) and $Li_{13}Sn_5$ (JCPDS 29-0838). This fact was also confirmed by [119]Sn Mössbauer spectroscopy (Figure 10). A split signal was observed for the discharged electrode, with the centroid isomer shift value located close to those reported for crystalline $Li_{13}Sn_5$ and Li_5Sn_2 [39].
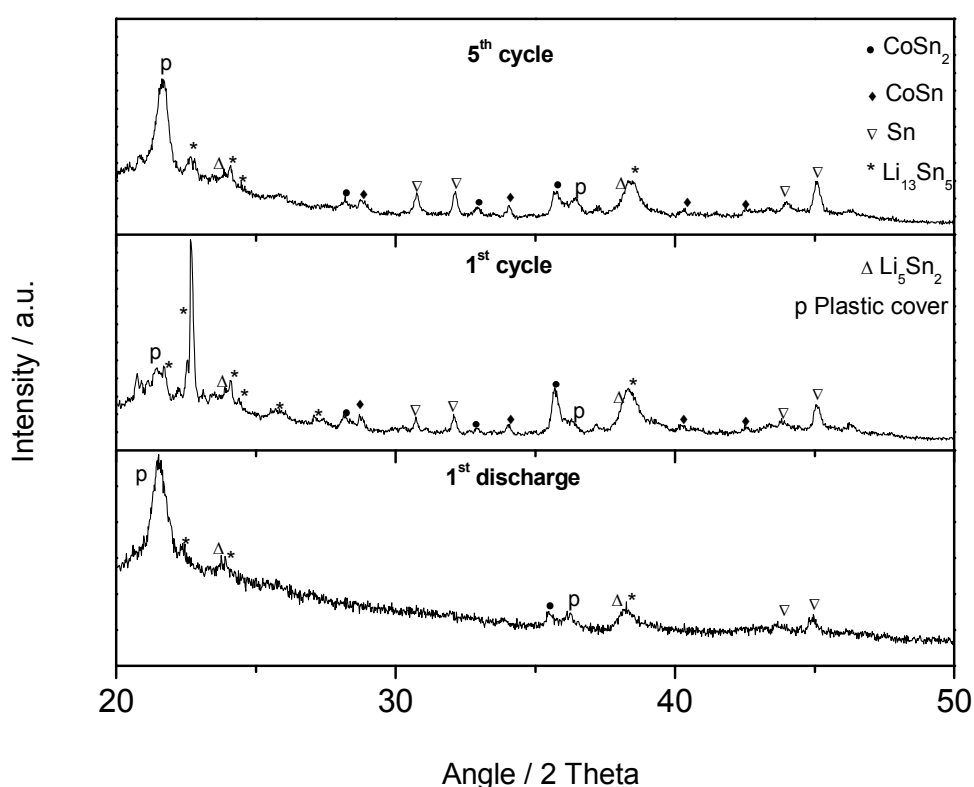
Figure 9. XRD patterns of $Sn_7Co_1C_{92}$ electrodes after 1 discharge, 1 and 5 cycles in lithium cells. Indexed phases were marked with symbols.

Most probably, Li_xSn phases are the products of the electrochemical reaction of tin metal component in the composite material. Recently, it was demonstrated that pure nanodispersed $CoSn_2$ does not show the typical anodic peak commonly ascribed to the formation of Li_xSn phases [40]. On further charge, a large number of reflections could be indexed to Sn, CoSn, $CoSn_2$, and $Li_{13}Sn_5$ (Figure 9). The presence of tin-cobalt

compounds support the reversibility of the electrochemical reaction of lithium with $CoSn_2$. Nevertheless, the presence of minor Li–Sn phases is also visible. It can be assigned to the limited lithium diffusion at the selected charging rate and/or to particle isolation into the composite material.

[119]Sn Mössbauer spectra of cycled electrodes are characterized by asymmetric profiles in which most of the components are overlapped. For this reason, the existing phases were determined from the XRD patterns depicted in Figure 8. Then, their hyperfine parameters were fixed in the fitting process and only their relative contributions were allowed to change (Table 3). The highest contribution corresponded to $CoSn_2$, although a significant increase of CoSn was detected as compared with the original composite, which evidenced a partial recovery of the cobalt-tin intermetallic compound after charging, as found in nanocrystalline CoSn alone [33].
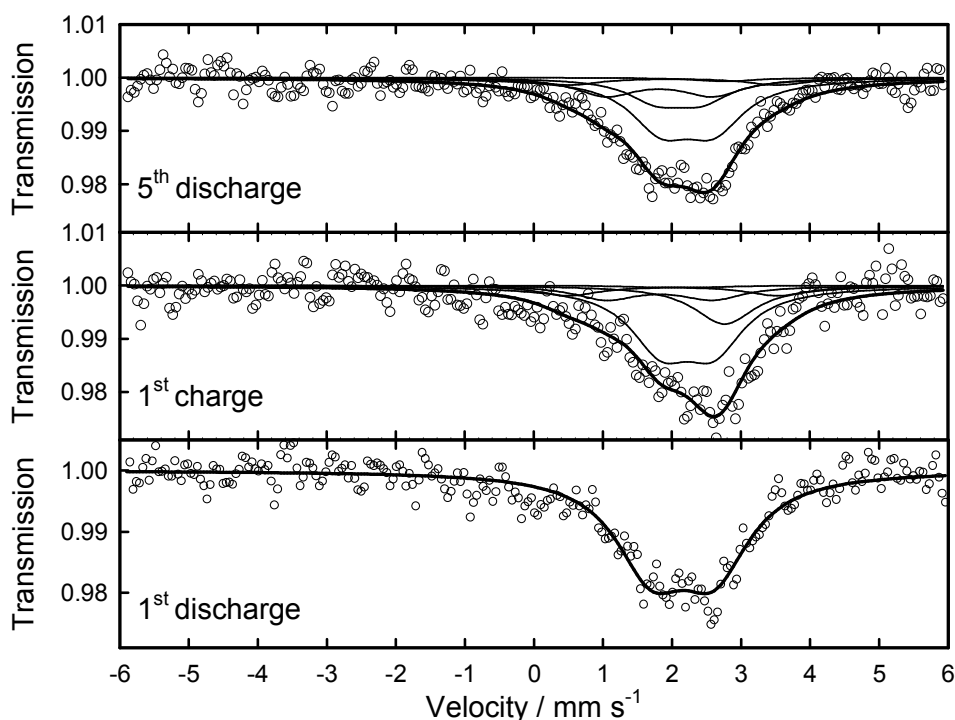

Figure 10. [119]Sn Mössbauer spectra of of $Sn_7Co_1C_{92}$ electrodes after 1 discharge, 1 and 5 cycles in lithium cells. Experimental and fitted spectra are plotted with symbols, and lines, respectively.

The presence of residual $Li_{13}Sn_5$ was less pronounced for the fifth charge and may involve an enhanced cycling efficiency after the first cycle, in agreement with the capacity fading observed during the first cycles. Finally, the increase in β-tin contribution on cycling can be explained in terms of a degradation of the cobalt-tin linkage during cycling.

Table 3. Hyperfine parameters of fitted Mössbauer spectra of $Sn_7Co_1C_{92}$ cycled electrodes.

$Sn_7Co_1C_{92}$	[1] s/d	Tin phase	[2] δ (mm/s)	[3] Δ (mm/s)	[4] Γ (mm/s)	[5] C (%)	[6] χ^2
1st discharge	d	$Li_{13}Sn_5$	2.16(3)	0.91(5)	1.272	100.0	0.531
	d	CoSn	1.82(3)	1.542(3)	1.084(8)	18.9	
	d		2.02(3)	3.025(7)	1.084(8)	7.79	
1st cycle	d	$CoSn_2$	2.22(2)	0.77(1)	1.084(8)	49.98	0.400
	s	β-Sn	2.76(2)	--	1.084(8)	2.0	
	d	$Li_{13}Sn_5$	2.16(3)	0.91(5)	1.084(8)	21.33	
	s	β-Sn	2.76(2)	--	1.084(8)	19.12	
	d	CoSn	1.82(3)	1.542(3)	1.084(8)	13.33	
5th cycle	d		2.02(3)	3.025(7)	1.084(8)	9.78	0.619
	d	$CoSn_2$	2.22(2)	0.77(1)	1.084(8)	56.51	
	d	$Li_{13}Sn_5$	2.16(3)	0.91(5)	1.084(8)	1.26	

[1]s/d: singlet (*s*) or doublet (*d*); [2]δ: isomeric shift; [3]Δ: quadrupole splitting; [4]Γ: line-width at half maximum; [5]C: relative contribution; [6]χ^2: goodness of the fitting.

2.2.4   Conclusions

Sn–Co–C composites were prepared by the carbothermal reaction of precursors containing a green coke and tin and cobalt oxides. The homogeneity of the resulting product was assured by ball milling the precursor mixture before the carbonization under Ar atmosphere. Samples with different carbon and metal content were produced. The XRD and ^{119}Sn Mössbauer spectroscopy of the original composites revealed the prevalence of Sn and $CoSn_2$ phases for those samples prepared with a high Sn/Co ratio. SEM images showed a homogeneous dispersion of sub-micrometric metallic particles in the carbon matrix. In contrast, large isolated metallic grains were present in the sample with the lowest carbon content.

Galvanostatic cycling at several kinetic rates revealed that $Sn_7Co_1C_{92}$ and $Sn_8Co_4C_{88}$ are able to maintain 400 mA h g^{-1} at 35 mA g^{-1} after 40 cycles. A major $CoSn_2$ contribution, revealed by Mössbauer spectroscopy, could be correlated with a good electrochemical performance in these composites. These results are supported by the low internal impedance measured in $Sn_7Co_1C_{92}$ electrodes after several discharges. A more detailed analysis of discharged and cycled electrodes of $Sn_7Co_1C_{92}$ by XRD and Mössbauer spectroscopy allowed to conclude that the presence of non-oxidized $Li_{13}Sn_5$ arising from metallic tin may contribute to the undesirable irreversibility of the first cycle. However, after five cycles, the contribution of $CoSn_2$ remained significant while $Li_{13}Sn_5$ almost disappeared, thus explaining the better capacity retention observed in subsequent cycles.

References

1. Winter M, Besenhard JO (1999) Electrochim Acta 45:31–50

2. Tirado JL (2003) Mater Sci Eng R 40:103–136

3. Winter M, Besenhard JO, Michael E (1998) Adv Mater 10: 725–763

4. Beaulieu LY, Eberman KW, Turner RL, Krause JL, Dahn JR (2001) Electrochem Solid-State Lett 4:A137–A140

5. Idota Y, Kubota T, Matsufuji A, Maekawa Y, Miyasaka T (1997) Science 276:1395–1397

6. Alcántara R, Fernández-Madrigal FJ, Lavela P, Tirado JL, Jumas JC, Olivier Fourcade J (1999) J Mater Chem 9:2517–2521

7. Aboulaich A, Mouyane M, Robert F, Lippens PE, Olivier- Fourcade J, Willmann P, Jumas JC (2007) J Power Sources 174:1224–1228

8. Todd ADW, Mar RE, Dahn JR (2006) J Electrochem Soc 153: A1998–A2005

9. Mao O, Dunlap RA, Courtney IA, Dahn JR (1998) J Electrochem Soc 145:4195–4202

10. Ionica-Bousquet CM, Lippens PE, Aldon L, Olivier-Fourcade J, Jumas JC (2006) Chem Mater 18:6442–6447

11. Choi W, Lee JY, Lim HS (2004) Electrochem Commun 6:816–820

12. Inoue H Proceedings of the International Meeting on Lithium Batteries. The Electrochemical Society, Biarritz, France

13. Lee SI, Yoon S, Park CM, Lee JM, Kim H, Im D, Doo SG, Sohn HJ (2008) Electrochim Acta 54:364–369

14. Tirado JL, Santamaría R, Ortiz GF, Menéndez R, Lavela P, Jiménez-Mateos JM, Gómez García FJ, Concheso A, Alcántara R (2007) Carbon 45:1396–1409

15. Hassoun J, Ochal P, Panero S, Mulas G, Bonatto Minella C, Scrosati B (2008) J Power Sources 180:568–575

16. Ferguson PP, Todd ADW, Dahn JR (2008) Electrochem Commun 10:25–31

17. Fan XY, Ke FS, Wei GZ, Huang L, Sun SG (2009) J Solid State Electrochem 13:1849–1858

18. Zhongxue C, Jiangfeng Q, Xinping A, Yuliang C, Hanxi Y (2009) J Power Sources 189:730–732

19. Mulas G, Enzo S, Bonatto-Minella C, Arca E, Gerbaldi C, Penazzi N, Bodoardo S, Hassoun J, Panero S (2009) J Solid State Electrochem 13:239–243

20. Liang Y, Liu Y, Jia ZJ (2009) J Alloys Compd 474:590–594

21. Lee KM, Lee YS, Kim YW, Sun YK, Lee SM (2009) J Alloys Compd 472:461–465

22. Kündig W (1969) Nucl Instr Methods 75:336–340

23. Li N, Martin CR, Scrosati B (2001) J Power Sources 97–98: 240–243

24. Ortiz GF, Hanzu I, Lavela P, Knauth P, Tirado JL, Djenizian T (2010) Chem Mater 22:1926–1932

25. Ortiz G, Alcántara R, Rodríguez I, Tirado JL (2007) J Electroanal Chem 605:98–108

26. Jaen J, Varsanyi ML, Kovacs E, Czako-Nagy I, Buzas A, Vertes A, Kiss L (1984) Electrochim Acta 29:1119–1122

27. Alcántara R, Lavela P, Ortiz G, Rodríguez I, Tirado JL (2008) Hyperfine Interact 187:13–17

28. Greenwood NN, Gibb TC (1971) Mössbauer spectroscopy. Chapman & Hall, London

29. Fong R, Sacken UV, Dahn JR (1990) J Electrochem Soc 137:2009–2013

30. Zhang JJ, Xia YY (2006) J Electrochem Soc 153:A1466–A1471

31. Xie J, Zhao XB, Cao GS, Tu JP (2007) J Power Sources 164:386– 389

32. Alcántara R, Ortiz G, Rodríguez I, Tirado JL (2009) J Power Sources 189:309–314

33. Alcántara R, Rodríguez I, Tirado JL (2008) ChemPhysChem 9:1171–1177

34. Dahn JR, Mar RE, Abouzeid A (2006) J Electrochem Soc 153: A361–A365

35. Alcántara R, Nwokeke UG, Nacimiento F, Lavela P, Tirado JL Proceedings of the SPIE Defense, Security, and Sensing Conferences. Abstract n° 8035-05 2011 Orlando, USA

36. Funabiki A, Inaba M, Ogumi Z, Yuasa S, Otsuji J, Tasaka A (1998) J Electrochem Soc 145:172–178

37. Wang C, Appleby AJ, Little FE (2002) J Electrochem Soc 149: A754–A760

38. Aurbach D, Gnanaraj JS, Levi MD, Levi EA, Fischer JE, Claye A (2001) J Power Sources 97:92–96

39. Dunlap RA, Small DA, MacNeil DD, Obrovac NN, Dahn JR (1999) J Alloys Compd 289:135–142

40. Nacimiento F, Alcántara R, Tirado JL (2009) J Alloys Compd 485:385–390

2.3 ^{119}Sn Mössbauer spectroscopy analysis of Sn-Co-C composites prepared from a fuel oil pyrolysis precursor as anodes for Li-ion batteries

F.J. Nacimiento,[a] P. Lavela,[a] J. L. Tirado,[a] J. M. Jiménez,[b] D. Barreda,[c] R.Santamaría[c]

[a] *Laboratorio de Química Inorgánica, Universidad de Córdoba, Campus de Rabanales,14071 Córdoba, Spain,* [b] *REPSOL YPF, Ctra. N-V km 18, 28930 Móstoles, Madrid, Spain,* [c] *Instituto Nacional del Carbón, CSIC, Apartado 73, 33080 Oviedo, Spain*

Abstract

The complementary use of X-ray diffraction and ^{119}Sn Mössbauer spectroscopy untangled the cobalt-tin phase's distribution in various Sn-Co-C composites. The composite materials were prepared by a single step procedure based on low-cost reagents and featuring good scalability was employed. The fluidized state of the Fuel Oil Pyrolysis (FOP) carbon precursor during the copyrolysis reaction produced finely dispersed intermetallic phases embedded in the carbon matrix. The electrochemical performance was correlated to the metal composition and cell impedance after a number of cycles. Cycled electrodes analyzed by X-ray diffraction and ^{119}Sn Mössbauer spectroscopy revealed that the increased contribution of electrochemically inactive $Co_3SnC_{0.7}$ may explain the observed capacity fading in those samples with high cobalt content.

ELSEVIER
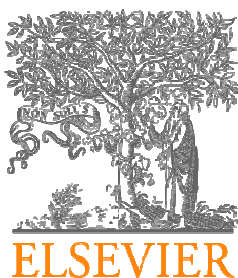
2.3.1 Introduction

Carbon materials are widely used as anodes in commercial lithium-ion batteries. However, the limited specific capacity delivered by graphite has prompted research into new, alternative compositions such as lithium-silicon and lithium-tin based alloys, and transition metal oxides subjected to lithium-driven conversion reactions [1,2]. Although both types of compounds provide extremely high specific capacities, their potential usefulness is limited by their poor long-term cycling performance and increased charge/discharge polarization. Composites consisting of tin containing intermetallic compounds and carbon materials have been envisaged as effective alternatives with a view to overcoming these restrictions. In fact, these composites have proved to be more efficient than the combination of their individual components [3].

The carbon matrix in these metal-carbon composites serves primarily as a cushion to the volume expansion occurring during the formation of the lithium-tin alloy [4]. This can be accomplished by assembling the two components chemically in various ways including insertion of metal particles into carbon nanotubes [5], encapsulation in a carbon matrix [6,7] and coating of graphite particles [8].We recently reported on the use of a cheap petroleum by-product which fluidizes during pyrolysis [9]. This allowed the carbon precursor to be homogeneously mixed with a finely powdered tin dioxide as metal precursor and provided low-cost, easily up-scalable process for producing metal-carbon composites. Recently, transition metals have been also introduced to prepare Sn-TM-C composites, being TM: Ti, V, Cr, Mn, Fe, Ni, Co. Especially improved electrochemical performances were achieved for cobalt containing composites. This transition metal ensured an extended compositional range for amorphous intermetallic phases [10].

The mechanism of the electrochemical reaction with lithium involves the breaking of the Co-Sn links and further Li-Sn alloys formation upon discharging [11]. Not all the Co-Sn phases contribute positively to the electrochemical behavior and cobalt-rich phases as Co_3Sn_2 are electrochemically inactive.

[119]Sn Mössbauer spectroscopy is a powerful technique to unfold the changes in the local environment and oxidation state of tin-containing intermetallic compound [12-14]. It has been successfully applied to unveil the alloying mechanism undergoing the lithium electrochemical reaction. Thus, Jumas et al. have proposed a predictive model to

determine the Li-Sn alloys formed during cycling, including composition and structure based on the use of correlation diagrams calculated from the hyperfine parameters [15]. In a recent report, we have evidenced that the presence of the tin-rich $CoSn_2$ phase in both original and cycled electrodes favorably contributes to the good electrochemical performance [16].

The aim of this work is to provide a single and easily scalable method for preparing Sn-Co-C composites that could be used as anode materials for lithium-ion batteries. In addition, it will be shown that ^{119}Sn Mössbauer spectroscopy will allow to evaluate in detail the tin phases existing in the raw samples and their changes after cycling, thus providing a unique tool for the study and further improvement of the electrochemical performance of Sn-C and Sn-Co-C composites in lithium test cells.

2.3.2   Material and methods

The Sn-Co-C composites were obtained by copyrolysis (440 ºC, 5 bar) of a Fuel Oil Pyrolysis residue (FOP) (supplied by REPSOL) in the presence of estimated amounts of SnO_2 (Panreac) and Co_3O_4 (Panreac) in a stirring reactor under a nitrogen atmosphere for 4 h. Such a high pressure was needed to ensure highly efficient carbonization. The pyrolysis products obtained were ground and sieved below 200 mm for further carbonization under an N_2 atmosphere at 800 ºC for 2 h, using a heating rate of 2 ºC min^{-1}. Samples will be named as FOPSnXCoY, being X and Y the estimated percentage of tin and cobalt, respectively. The amounts of the oxides were estimated considering that both are properly reduced and losses by metal evaporation are negligible at the carbonization temperature. According to this assumption, the estimated values of Sn and Co were calculated. The carbon content can be inferred from the ashes content which in turn is determined from the weight loss of the carbonized samples heated in air atmosphere. These thermogravimetic measurements were carried out in a TA Instruments SDT 2960. The precise carbon content in these metal-carbon composites was determined by using an Elemental CHNS Eurovector EA3000 analyser.

X-ray diffraction (XRD) patterns were recorded on a Siemens D-5000 instrument using CuKα radiation and a graphite monochromator. The 2q scan rate used was 0.04º per 1.2 s. Scanning electron microscopy (SEM) images was obtained with a

JEOL SM6300 microscope. Quantitative electron dispersive spectroscopy (EDS) may obtain a map of the element dispersion in an analyzed particle. The surface area was characterized by N_2 adsorption-desorption isotherms at 196 ºC (Nova 1200e, Quanta chrome). The pristine samples were previously out gassed under primary vacuum at 120 ºC overnight. ^{119}Sn Mössbauer spectra were recorded at room temperature on an Ametek-Wissel constant-acceleration spectrometer operated in the transmission mode. The radiation source was ^{119m}Sn in a $BaSnO_3$ matrix. The isomer shift scale was set by using a $BaSnO_3$ pattern and zeroing in on the Sn(IV) peak. Spectral profiles were deconvoluted into Lorentzian lines by using a least-squares based method and goodness of the fit was assessed via χ^2.

Electrochemical performance in the Sn-Co-C composites was evaluated galvanostatically. For this purpose, two-electrode Swagelok type cells were assembled by using 9 mm discs of lithium metal as counter electrodes. The working electrode was prepared by mixing 92% of active material and 8% of PVDF binder in n-methyl pyrrolidone. The paste was deposited as a film onto a copper foil of the same diameter. Whatman glass fiber discs soaked in the electrolyte solution, 1 M $LiPF_6$ (EC/DEC = 1:1), were used as electrode separators. Test cells were assembled, and the discharged electrode was handled, in an M-Braun glove box under an argon atmosphere. An Arbin galvanostat multichannel system was used to cycle the lithium cells between 0 and 1.5 V at 35 mA g$^-$1 both the charge and the discharge branches. Electrochemical impedance spectra were recorded with an Autolab PGSTAT12 system. Three electrode Swagelok-type cells were used, containing lithium metal discs as reference and auxiliary electrodes. Test cells were previously discharged by step potential electrochemical spectroscopy, using a MacPile system at a scan rate of 10 mV/0.1 h. The cells were kept at open circuit for at least 5 h to reach quasi-equilibrium before impedance measurements. An AC voltage signal of 5 mV was applied at frequencies from 100 kHz to 2 mHz.

2.3.3 Results and discussion

Sample analysis and X Ray diffraction

Table 1. Atomic composition of FOP based Sn-C and Sn–Co–C composite materials as estimated from the proportions of carbon precursor and added metal oxides.

Composite	Atomic content			
	C (%)	Sn (%)	Co (%)	Ashes (%)
FOPSn30	74.4	27.2	–	27.4
FOPSn20Co5	64.3	17.7	4.4	30.6
FOPSn30Co15	58.6	26.7	13.2	48.1
FOPSn50Co25	40.6	40.9	23.3	73.5

Table 1 shows the estimated metal content of the samples assuming that the solid residue obtained after the copyrolysis reaction contains the whole amount of metal oxides initially added and metal reduction only occurs upon the carbonization process as predicted by Ellingham diagrams. The ash content was determined from the thermogravimetric curves recorded in an oxidative atmosphere. An accurate measurement of the carbon content was carried out by CHNS analysis. The results in Table 1 revealed a progressive decrease of the carbon mass percentage when the metal component was increased. Nitrogen adsorption isotherms provided surface areas lower than 4 m^2 g^{-1}, preventing to infer any clear conclusion about the texture properties of these samples. The XRD patterns of the tin and cobalt-tin phases are displayed in Figure 1. The pattern of FOPSn30 sample is characterized by a crystalline phase of metallic tin. Otherwise, a number of Co-Sn phases including mainly CoSn and $CoSn_2$ were detected for those samples containing cobalt. The absence of reflections ascribable to metal oxides evidences the efficiency of the carbothermal process. Those samples with high cobalt content exhibited a set of reflections which was assigned to $Co_3SnC_{0.7}$ (JCPDS pattern 29-0513) [17]. The crystallite size values, calculated from the Scherrer equation, yielded larger values for β-tin (35-42 nm) than for the intermetallic species (22-31 nm), what may ultimately benefit the electrode electrolyte interface reaction and hence the electrochemical behavior of cobalt-containing composites. The disordered structure of

the coke matrix contributes to the XRD patterns as a highly broadened band at ca. 25º (2θ).
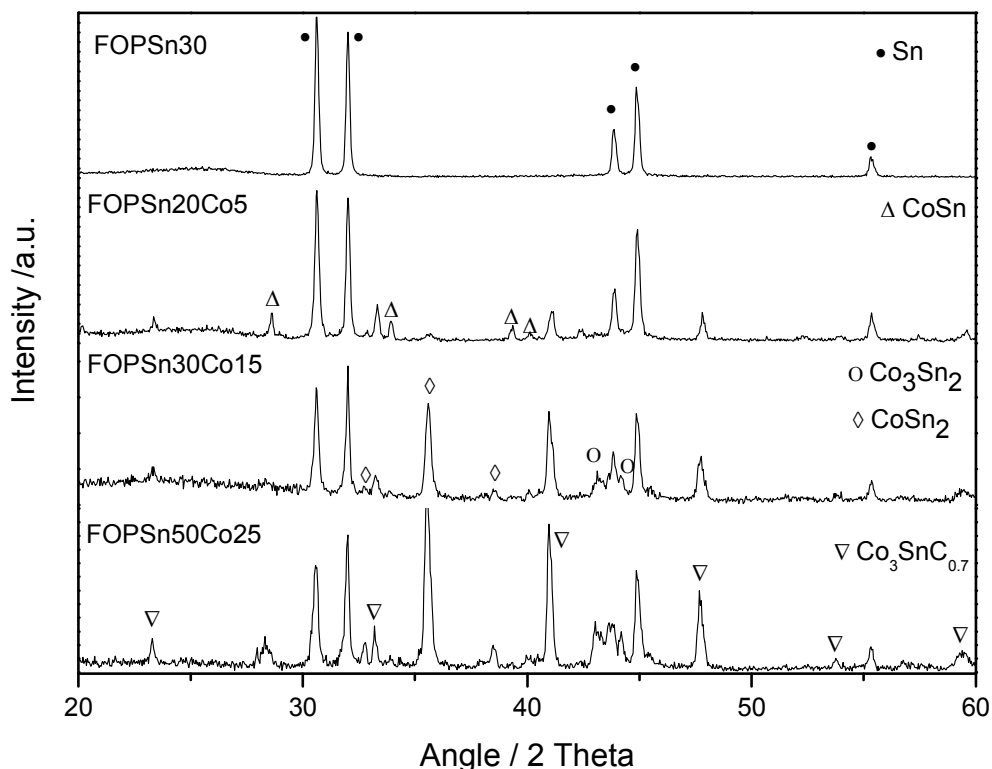

Figure 1. X ray diffraction patterns for Sn–C and Sn–Co–C composites.

Mössbauer spectroscopy

[119]Sn Mössbauer spectroscopy provides a deeper knowledge about the oxidation state and local environment of the probe atom irrespective of the degree of crystallinity [11,18]. Figure 2 shows the experimental spectra and the corresponding subspectra obtained by deconvoluting to Lorentzian curves. The Sn-C composite exhibited a singlet at $\delta = 2.57$ mm s^{-1} that can be unambiguously assigned to metallic tin. In turn, the Mössbauer spectra for the cobalt-containing samples are characterized by an asymmetric profile. In fact, the shifting of the isomer shift centroid to lower values, from 2.57 to 1.5 mm s^{-1}, is a direct proof of the cobalt-tin interaction. This is the result of the decrease of the electron density at the 5s-orbital of the tin atom as a consequence of the electron transfer of the tin valence electrons to the conduction band of the cobalt-tin alloy [19]. In order to quantify the relative contribution of the Mössbauer subspectra, these ones were correlated to the phases previously identified by X-ray diffraction

101

(Figure 1) Their hyperfine parameters were taken from previous reports on the analysis of pure and crystalline CoSn and $CoSn_2$ phases [19,20], and used in the calculations to fit their contributions. The isomer shift of Co_3Sn_2 has been reported as 1.74 mm s^{-1} [19]. Unfortunately, its minor presence in the XRD patterns of FOPSn30Co15 and FOPSn50Co25 may explain the impossibility to discern this phase in the Mössbauer spectra. Eventually, an additional singlet located at ca. 1.7mms^{-1} had to be included to achieve a better fit (Table 2). To our knowledge the ^{119}Sn Mössbauer spectrum of pure $Co_3SnC_{0.7}$ has not be still reported. Because of its highest content of stoichiometrical cobalt, its Mössbauer signal must be located at the lowest isomer shift value. Thus, we are tempted to ascribe this singlet to the presence of $Co_3SnC_{0.7}$.
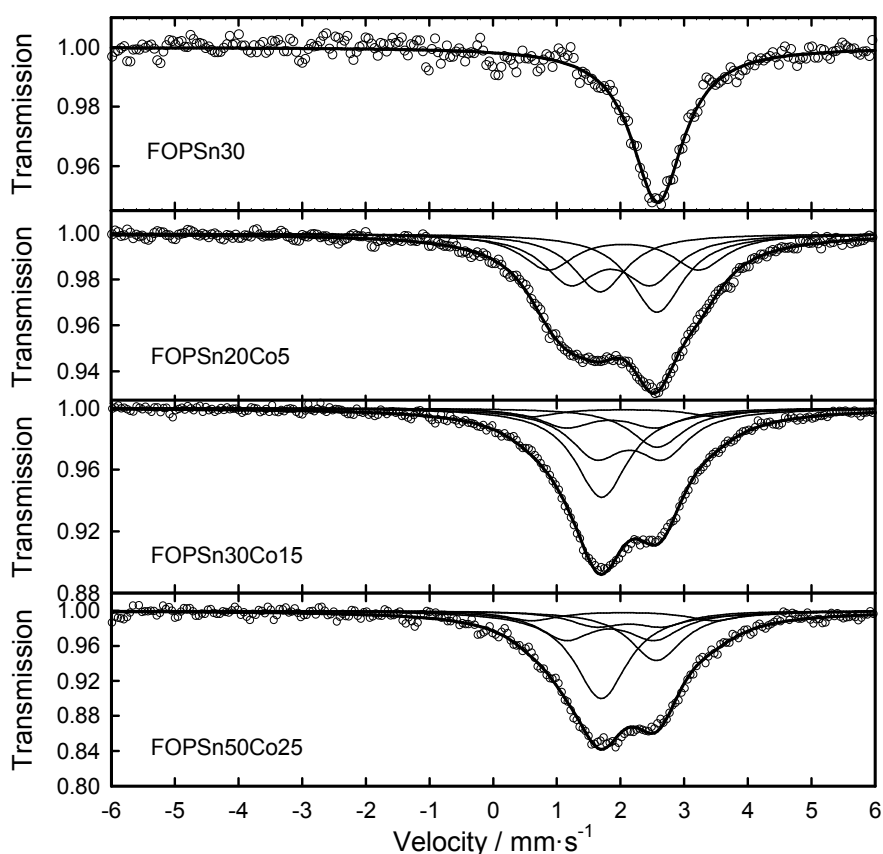

Figure 2. ^{119}Sn Mössbauer spectra for Sn–C and Sn–Co–C composites.

Other authors have identified a modified $CoSn_2$ nano-compound with a variable composition upon electrochemical charge of a Li/$CoSn_2$ cell [21]. Moreover, a

transition from Co_3Sn_2 transformed into $CoSn_2$ during the second cycle has been identified in related composites [22].

Table 2. Hyperfine parameters of the deconvoluted Mössbauer spectra.

Sample	[a] s/d	Tin phase	[b] δ (mm s^{-1})	[c] Δ (mm s^{-1})	[d] Γ (mm s^{-1})	[e] C (%)	[f] χ^2
FOPSn30	s	β-Sn	2.587(8)	--	0.98(3)	100	0.514
FOPSn20Co5	s	β-Sn	2.577(6)	--	1.01(1)	26.35	0.563
	d	CoSn	2.05(2)	2.37(3)	1.01(1)	23.44	
	d	CoSn	1.85(2)	1.27(4)	1.01(1)	30.71	
	s	$Co_3SnC_{0.7}$	1.68 (2)	--	1.01(1)	19.50	
FOPSn30Co15	s	β-Sn	2.577(6)	--	1.01(1)	14.61	0.691
	d	CoSn	2.051(7)	2.891(6)	1.01(1)	6.26	
	d	CoSn	1.847(8)	1.403(3)	1.01(1)	13.42	
	d	$CoSn_2$	2.141(9)	1.052(2)	1.01(1)	32.55	
	s	$Co_3SnC_{0.7}$	1.705	--	1.01(1)	33.17	
FOPSn50Co25	s	β-Sn	2.564(8)	--	1.00(1)	20.88	0.529
	d	CoSn	2.041(9)	2.872(6)	1.00(1)	8.15	
	d	CoSn	1.838(8)	1.394(3)	1.00(1)	22.48	
	d	$CoSn_2$	2.13(1)	1.045(2)	1.00(1)	11.67	
	s	$Co_3SnC_{0.7}$	1.697(6)	--	1.00(1)	36.81	
Crystalline Sn-Co from the literature	d	$CoSn_2$ [18]	2.14	0.78	--	--	--
	d	CoSn [19]	1.854(6)	1.60(1)	0.99(1)	67	0.97
	d	CoSn [19]	2.03(1)	3.14(2)	0.99(2)	33	

[a] *s/d*: singlet (*s*) or doublet (*d*); [b] δ: isomer shift; [c] Δ: quadrupole splitting; [d] 2Γ: full line width at half maximum; [e] C: contribution to total absorption; [f] χ^2: goodness of the fitting.

The low relative contribution of b-tin in the Mössbauer spectra can be ascribed to its low Lambe Mössbauer factor. A value of 0.039 was reported [23]. Otherwise, a value of 0.55 was recently reported for CoSn [24]. This fact has been recently evidenced in related composites [16].

Electron microscopy

Scanning electron micrographs revealed the presence of large composite grains with rough texture due to the presence of embedded submicron particles (Figure 3). Additional bright metallic particles unevenly distributed around the carbonaceous particles were also observed. A close inspection of a composite particle from Figure 3d reveals that most of the metallic particles are embedded into the carbon matrix. Most probably some tin and tin-cobalt particles may exude upon carbonization at 800ºC.
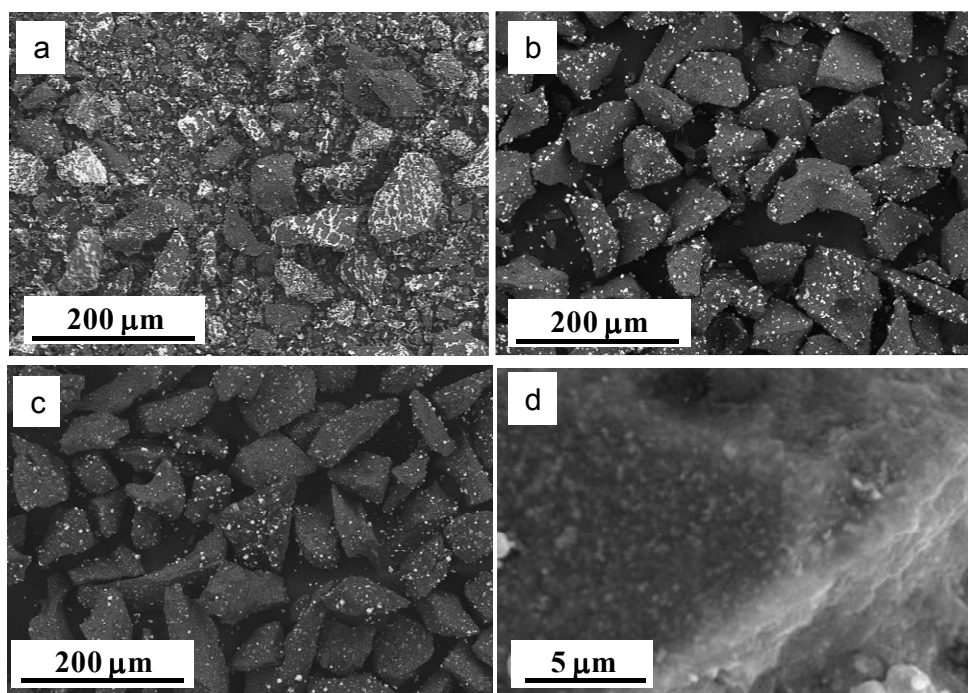

Figure 3. SEM images of selected composites. (a) FOPSn30, (b) FOPSn30Co15, and FOPSn50Co25 (c) low magnification and (d) high magnification image.

In fact, this effect was more enhanced for FOPSn30 sample as expected of the lower melting point of tin than those of the tin-cobalt phases. Figure 4a shows the backscattered electrons image for the FOPSn30 polished sample. The brightest spots correspond to metallic particles embedded in the composite particles.
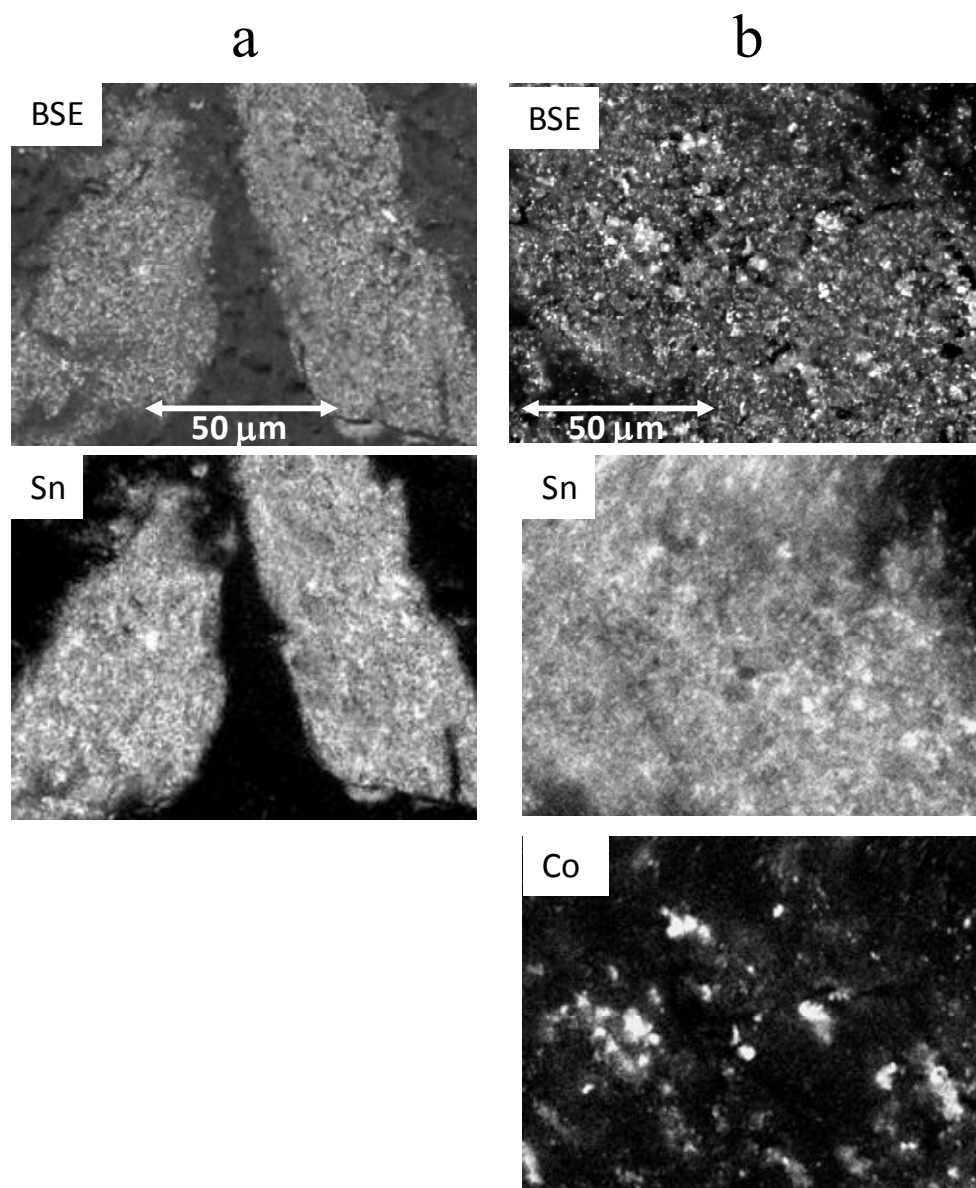

Figure 4. Quantitative EDS maps, after ZAF correction, of (a) FOPSn30 and (b) FOPSn30Co15 for the element Co (based on K lines) and Sn (based on the L line). The backscattered electrons image is also shown for reference.

The EDS maps reveal a homogeneous distribution of tin atoms in the particles. On the other hand, the images for FOPSn30Co15 reveal that cobalt is located in specific areas of variable brightness, whereas tin was widely distributed (Figure 4b). This is the expected result of the presence of various Co-Sn phases which concentrate the transition metals in located areas for those phases with low Sn/Co ratios.

Electrochemical behavior

Figure 5 shows the differential capacity plots for the first and fifteenth cycle of lithium test cells using the composites. The first discharge profile significantly differs from subsequent discharges. It is ascribed to irreversible structural and morphological changes occurring upon Li-Sn alloy formation that cannot be completely recovered after the first charge. Therefore, the new sites for the lithium reaction have different energy on the second discharge leading to a distinct profile. The bands observed at 0.3 and 0.6 V during the first discharge and their corresponding counterparts at 0.6, 0.72 and 0.8 V are ascribable to the electrochemical formation/decomposition of Li-Sn alloys. A progressive broadening of the main band at 0.3 V occurs on introducing cobalt in the composite. It can be assigned to an increasingly disorder in cobalt content samples that average the energy of the sites at which the incoming lithium ions are linked. This effect can be considered advantageous according to previous reports [25]. The electroactivity of the carbon matrix is restricted to a broadened band at voltage values near to 0 V. On cycling, a different behavior is detected for each studied sample. FOPSn30 showed a drastic decrease of the reduction and oxidation bands intensities as compared to cobalt-containing composites. Contrarily, FOPSn30Co15 and FOPSn50Co25 evidenced a significant increase of the main reduction signal intensity. Most probably, the continuous cycling may lead to the aggregation and recrystallization of the intermetallic particles. All these effects will be undoubtedly reflected on the capacity retention of the lithium cells. Extended galvanostatic cycling tests were carried out at voltages from 0.002 to 1.5 V (Figure 6). This upper cut-off voltage used was imposed by the need to balance capacity values and their retention over a large number of cycles [26]. The formation of Li-Sn intermetallic compounds, allowed to the Sn-C composite to reach a capacity value of 505 mA h g^{-1} after the first discharge. This value is larger than that

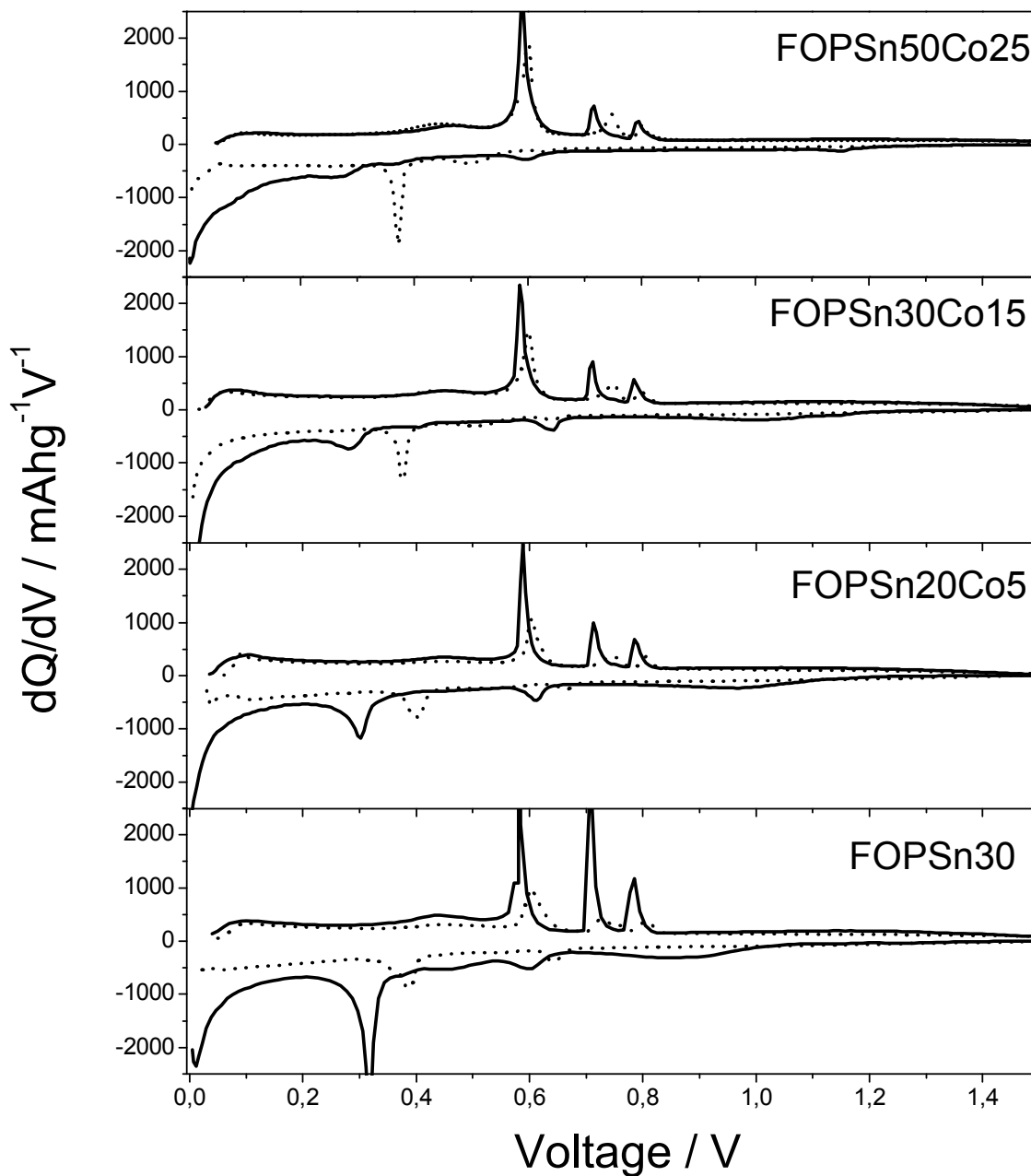recorded for the free metal coke. However, FOPSn30 failed to retain high capacity values over a long cycling.

Figure 5. Differential capacity plots recorded from galvanostatic experiments at 35 mAg^{-1}. First cycle (solid line) and fifteenth cycle (dash line).

The discharge capacity of the first cycle decreased when cobalt was introduced in the composite. Cobalt atoms are electrochemically inactive against the electrochemical reaction of lithium and its content must therefore be limited in the electrode composition. By contrast, capacity retention was substantially improved for a large number of cycles. Previous studies on metal-carbon composites by our group revealed irreversible capacities of ca. 250 mA h g^{-1} [9] and 400 mA h g^{-1} [27] for Sn-C and Sn-Co-C composites, respectively. Interestingly, the Sn-Co-C composites studied here provided irreversible capacity values of 100 mA h g^{-1}. The best electrochemical performance corresponded to FOPSn50Co25.
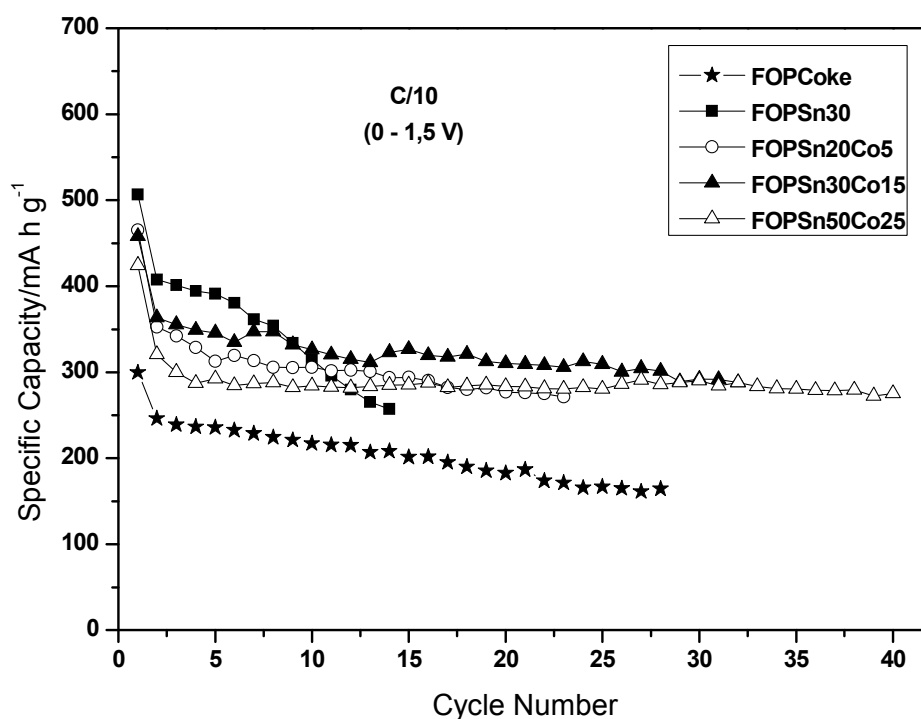

Figure 6. Galvanostatic cycling of metal free coke, Sn–C and Sn–Co–C composites. Kinetic rate: 35 mAg^{-1}.

This result confirms the beneficial effect of cobalt. The presence of this transition metal favors structural disordering on the electrode material and therefore delays the deleterious formation of crystalline phases of Li$_x$Sn [10]. A significant decrease in capacity from 424 to yield 287 mA h g^{-1} was recorded after the first five cycles. Then, the cycling stability allowed preserving a capacity value of 277 mA h g^{-1}

after 40 cycles. Contrarily, 456 mA h g^{-1} were recorded for FOPSn30Co15 but a more enhanced capacity fading was observed after a large number of cycles.

The kinetic response of the working electrodes over a number of cycles is usually evaluated by impedance spectroscopy (Figure 7a). The gradual deterioration of the electrode can be monitored via the increase in cell impedance, which hinders the efficient lithium diffusion across the electrolyte/electrode interface.
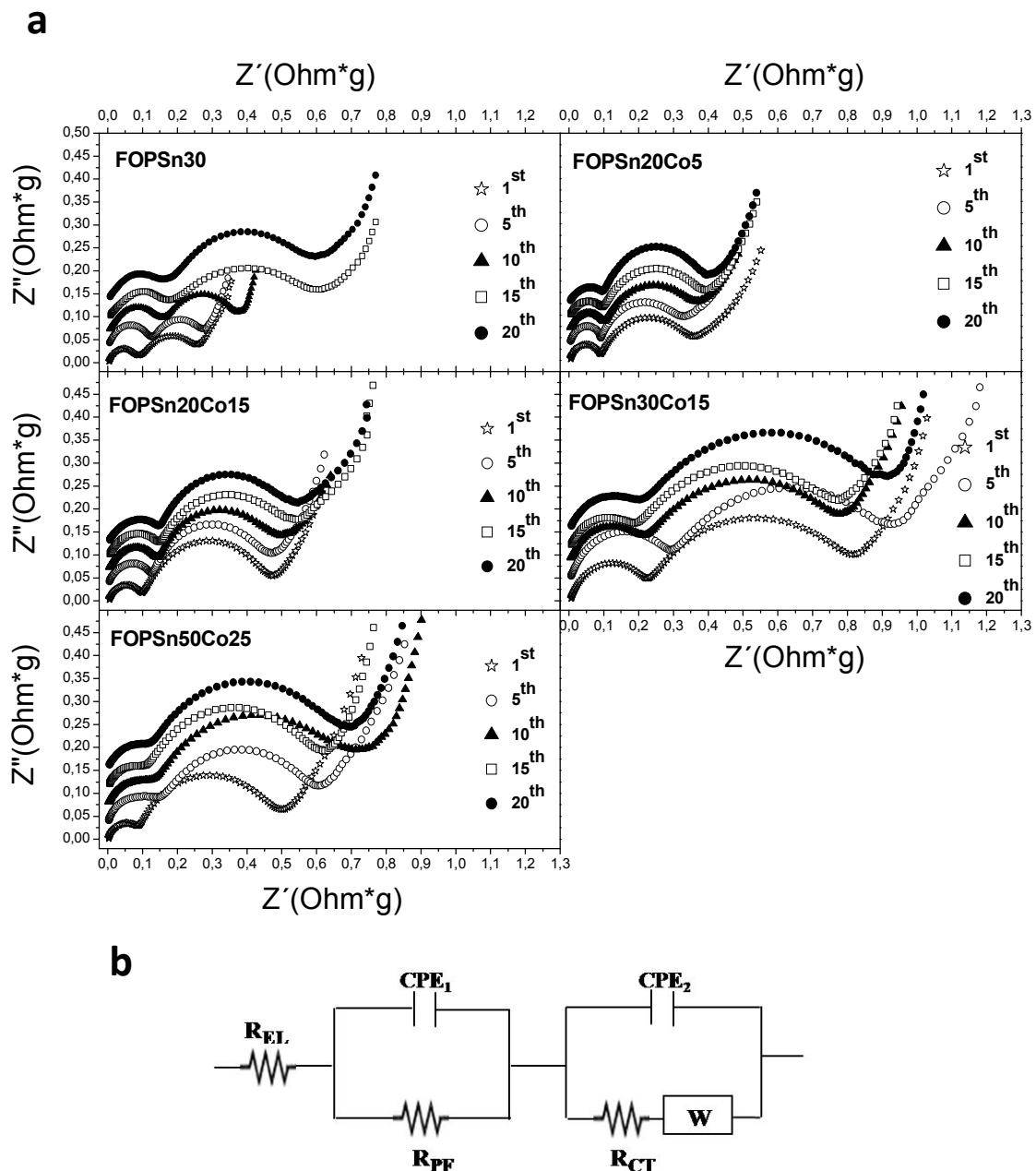

Figure 7. a) Nyquist plots for fully discharged electrodes after the first, fifth, tenth, fifteenth and twentieth cycle, b) Analogue circuit for the fitting of the impedance response.

The two depressed semicircles at high and medium frequencies in the impedance spectra are usually assigned to lithium migration across the passivating film and the charge transfer reaction, respectively. The semicircle depression is provoked by the presence of inhomogeneities in polycrystalline materials such as roughness and porosity that hinder the frequency dispersion at the interface [28]. The constant phase elements (CPE) included in the equivalent circuit take into account the depression of the semicircles. A further straight line is usually observed that is commonly assigned to lithium diffusion into the composite particles. A Warburg component (W) is introduced to describe the system response to the Li^+ diffusion through the composite electrode. The impedance spectra were fitted to an equivalent circuit involving the above-described lithium migration phenomena (Figure 7b). The electrical resistance values of these interfaces (R_{PF} and R_{CT}) are shown in Table 3. R_{PF} values increased on cycling.

Table 3. Electrical resistance of selected Sn–C and Sn–Co–C composites as calculated by fitting their impedance spectra.

Sample name	R ($\Omega \times g$)	1st	5th	10th	15th	20th
				n^{th} discharge		
FOPSn30	R_{PF}	0.087	0.128	0.172	0.201	0.224
	R_{CT}	0.153	0.121	0.173	0.233	0.483
FOPSn20Co5	R_{PF}	0.099	0.128	0.145	0.155	0.193
	R_{CT}	0.345	0.306	0.323	0.34	0.466
FOPSn30Co15	R_{PF}	0.225	0.296	0.219	0.194	0.212
	R_{CT}	0.543	0.581	0.520	0.541	0.653
FOPSn50Co25	R_{PF}	0.087	0.142	0.130	0.117	0.137
	R_{CT}	0.375	0.430	0.538	0.452	0.494

A recent report has shown that the chemical contact between tin and electrolyte caused electrolyte decomposition products on tin anode surface. Based on infrared spectra of anode surface, the formation of P-F containing inorganic species and new organic species were detected on the electrode surface [29]. As can be seen, the presence of large cobalt contents in FOPSn50Co25 and FOPSn30Co15 involved a significant increase of the cell impedance as compared to FOPSn30 and FOPSn20Co5.

In fact, the highest resistance values recorded for FOPSn30Co15 may explain the capacity fading observed upon cycling which eventually mollify the higher capacity values recorded during the first cycles. In a previous report on Sn-Co-C composites, we concluded a good electrochemical behavior could be achieved with only minor cobalt contents [27]. However, the absence of cobalt in FOPSn30 revealed an increase in the cell impedance on cycling.

Post-mortem analysis

In order to determine the role played by cobalt-tin phase on cycling, the XRD patterns of cycled electrodes for FOPSn50Co25 are shown in Figure 8. The electrodes subjected to the first discharge are characterized by an enhanced loss of crystallinity, though peaks ascribable to the departing material remain visible. Most likely, isolated metal particles could not be reached by lithium ions and converted to Li-Sn alloys upon discharging. Among the different phases present in the starting sample, $Co_3SnC_{0.7}$ and CoSn seem to be the most resilient phases to react with lithium during the first discharge. $Co_3SnC_{0.7}$ is electrochemically inactive as the reflections remain clearly visible after ten cycles, while CoSn fully reacts after the second discharge. These observations indicate that the electrochemical activity of cobalt-tin phases largely differs and the presence of $Co_3SnC_{0.7}$ would prevent good electrode reversibility. Nevertheless, the quantification of the amorphous intermetallic Co-Sn phases upon cycling cannot be properly inferred from XRD patterns. In order to complete the limited information provided by X-ray diffraction on the characterization of tin-containing phases retrieved after cycling, [119]Sn Mössbauer spectra for FOPSn30Co15 and FOPSn50Co25 electrodes charged after several cycles were recorded (Figure 9).
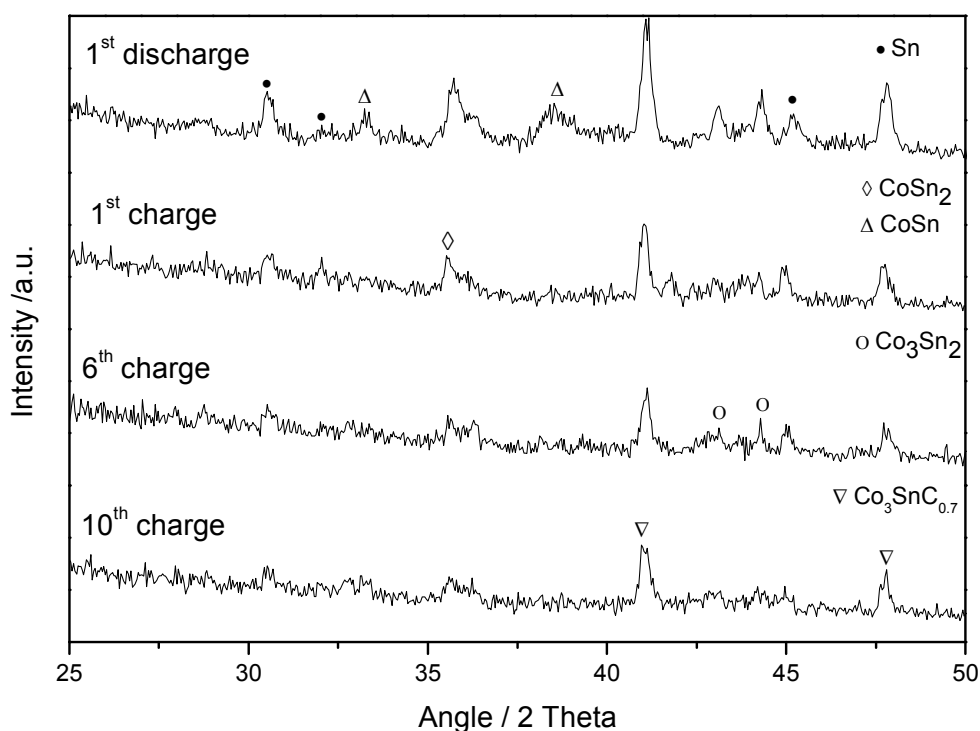
Figure 8. XRD patterns of discharged and subsequently charged electrodes of FOPSn50Co25 after the first discharged and 1st, 6th and 10th charged cycles.

Changes in the spectra profiles were ascribed to variations in the relative contribution of the initial phases upon cycling. The invariability of X-ray diffraction patterns of $Sn_{31}Co_{28}C_{41}$ electrodes before and after cycling have been taken as a proof of the good performance of this composite [30]. As can be seen from Table 4, the contribution of the singlet attributed to $Co_3SnC_{0.7}$ was significantly increased for FOPSn30Co15 upon cycling. Contrarily, the doublet assigned to the tin-rich phase $CoSn_2$ continuously decreased. Instead, the contribution of $Co_3SnC_{0.7}$, rich in cobalt, remained almost constant in the whole range for FOPSn50Co25, while the contribution of $CoSn_2$ significantly increased. Thus, the prevalence of $Co_3SnC_{0.7}$, with a high content in the non-electroactive cobalt element, in subsequent cycles could be also responsible for the high cell impedance and capacity fading observed in the cycling of FOPSn30Co15 electrodes. Probably the formation of cobalt rich inactive phases such as $Co_3SnC_{0.7}$ during cycling would hinder the access to Sn atoms at the core of large particles [31].
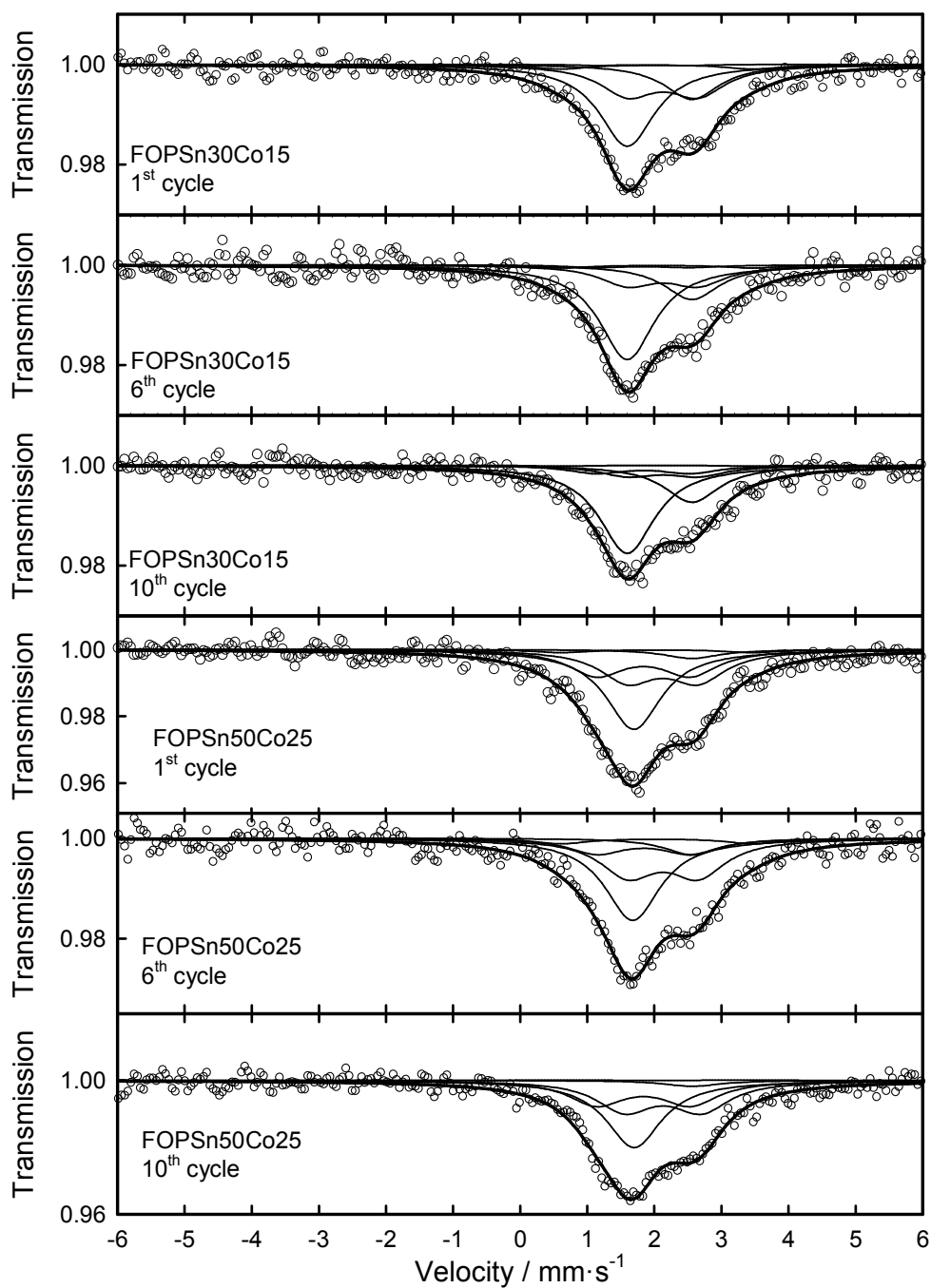
Figure 9. **^{119}Sn Mössbauer spectra of FOPSn30Co15 and FOPSn50Co25 after 1st, 6th and 10th charged cycles.**

Tables 4. Relative contributions of tin phases identified by ^{119}Sn Mössbauer spectroscopy cycled electrodes.

FOPSn30Co15	β-Sn (%)	CoSn$_2$ (%)	CoSn (%)	Co$_3$SnC$_{0.7}$ (%)
Original	14.6	32.55	19.68	33.17
1st cycle	18.82	30.94	6.19	44.05
6th cycle	19.42	21.26	6.23	53.08
10th cycle	22.87	12.35	10.14	54.63
FOPSn50Co25				
Original	20.88	11.67	30.63	36.81
1st cycle	4.38	29.33	27.31	38.99
6th cycle	7.92	33.69	19.29	39.1
10th cycle	3.29	32.6	26.7	37.4

2.3.4 Conclusions

We propose a simple, cost-effective method for preparing Sn-Co-C composites. The fluidized state of the carbon precursor during the copyrolysis process and the carbothermal reduction of the metal oxide precursors ensure the formation of finely powdered intermetallic particles homogeneously embedded in the carbon matrix. The XRD patterns for the composites are consistent with an efficient reduction of the precursor oxides and the formation of metallic phases, mainly β-Sn, CoSn, CoSn$_2$ and Co$_3$SnC$_{0.7}$. ^{119}Sn Mössbauer spectra exhibited asymmetric profiles that were fitted according to the tin phases identified by X-ray diffraction. The relative contribution of β-Sn is underestimated due to the low Lamb-Mössbauer factor as compared to the cobalt-tin phases. Electron microscopy revealed a homogeneous dispersion of metallic-containing particles while cobalt was more localized, probably in the cobalt-rich phase.

The presence of cobalt was effective towards stabilizing cyclability. For example, FOPSn50Co25 exhibited a capacity of 277 mA h g^{-1} after 40 cycles. The impedance spectra revealed an increase of the overall resistance in cobalt-containing samples. On the other hand, the constancy of resistance on cycling reveals that cobalt effectively contributes to the electrode preservation after a number of cycles.

The ^{119}Sn Mössbauer spectra of cycled electrodes revealed the prevalence of the cobalt-rich phase Co$_3$SnC$_{0.7}$ for FOPSn30Co15 which was associated to the capacity fading observed during the first cycles. These results reveal the important role of cobalt

in the reversible reaction with tin, but also the detrimental effect of the presence phases with high cobalt content. Moreover, the irreversibility in the first discharge was significantly lower than in previously reported tin-carbon composites. Although the delivered capacity was lower than the theoretical capacity of graphite, one should bear in mind the safety problems caused by the extremely low operating voltage of graphite anodes.

Acknowledgements

References

1. M. Winter, J. O. Besenhard, Electrochim. Acta 45 (1999), 31-50.

2. P. Lavela, J. L.Tirado, J. Power Sources 172 (2007) 379-387.

3. H. Huang, L.F. Nazar, Angew. Chem. Int. Ed. 40 (2001) 3880-3884.

4. H. Inoue, International Meeting on Lithium Batteries, Biarritz, France, 2006.

5. T. Prem Kumar, R. Ramesh, Y.Y. Lin, G. Ting-Kuo Fey, Electrochem. Commun. 6 (2004) 520–525.

6. X. Sun, X. Wang, L. Qiao, D. Hu, N. Feng, X. Li, Y. Liu, D. He, Electrochimica Acta 66 (2012) 204– 209.

7. J-S. Chen, Y-L. Cheah, Y-Ti. Chen, N. Jayaprakash, S. Madhavi, Y-H. Yang, X-W. Lou, J. Phys. Chem. C 113 (2009) 20504–20508.

8. A. Trifonova, M .Winter, J.O. Besenhard, J. Power Sources 174 (2007) 800–804.

9. J.L. Tirado, R. Santamaría, G.F. Ortiz, R. Menéndez, P. Lavela, J.M. Jiménez-Mateos, F. J. Gómez García, A. Concheso, R. Alcantara, Carbon 45 (2007) 1396-1409.

10. J.R. Dahn, R.E. Mar, A. Abouzeid, J. Electrochem. Soc. 153 (2006) A361-A365.

11. P.P. Ferguson, R.A. Dunlap, J.R. Dahn, J. Electrochem. Soc. 157(2010) A326-A332.

12. J.S. Thorne, P.P. Ferguson, R.A. Dunlap, J.R. Dahn, J. Alloys Compd. 472 (2009) 390.

13. Z. Edfouf, F. Cuevas, M. Latroche, C. Georges, C. Jordy, T. Hezeque, G. Caillon, J.C. Jumas, M.T. Sougrati, J. Power Sources 196 (2011) 4762–4768.

14. P.E. Lippens, M. El Khalifi, M. Chamas, A. Perea, M.-T. Sougrati, C. Ionica-Bousquet, L. Aldon, J. Olivier-Fourcade, J.C. Jumas, Hyperfine Interact. 206 (2012) 35.

15. S. Naille, J.-C. Jumas, P.-E. Lippens, J. Olivier-Fourcade, J Power Sources 189 (2009) 814–817.

16. F. Nacimiento, P. Lavela, J. L. Tirado, J. M. Jiménez-Mateos, J. Solid State Electrochem. 16 (2012) 953–962.

17. H.H. Standelmaier, L.J. Huetter, Acta Metall. 7 (1959) 415-419.

18. A.D.W. Todd, R.A. Dunlap, J.R. Dahn, J. Alloys Compd. 443(2007) 114-120.

19. J. Jaén, M.L. Varsányi, E. Kovács, I. Czakó-Nagy, A. Buzás, A. Vértes, L. Kiss Electrochim. Acta 29 (1984) 1119-1122.

20. G.F. Ortiz, R. Alcántara, I. Rodríguez, J.L. Tirado, J. Electroanal. Chem 605 (2007) 98–108.

21. C.M. Ionica-Bousquet, P.E. Lippens, L. Aldon, J. Olivier-Fourcade, J.C. Jumas Chem. Mater. 18 (2006) 6442-6447.

22. S.I. Lee, S. Yoon, C.M. Park, J.M. Lee, H. Kim, D. Im, S.G. Doo, H.J. Sohn, Electrochim. Acta 54 (2008) 364–369.

23. R. Alcántara, P. Lavela, G. Ortiz, I. Rodríguez, J.L. Tirado, Hyperfine Interact. 187 (2008) 13–17.

24. N.N. Greenwood, T.C. Gibb, Mössbauer spectroscopy. Chapman & Hall, London, 1971.

25. R. Zhang, M.S.Whittingham, Electrochem. Solid-State Lett. 13 (2010) A184-A187.

26. I.A. Courtney, J.R. Dahn, J. Electrochem. Soc. 144 (1997) 2943-2948.

27. J.L.Tirado, G. F. Ortiz, P. Lavela, F. Nacimiento, J. Solid State Electrochem. 14 (2010) 139-148.

28. J.R. McDonald, Impedance Spectroscopy, Emphasizing Solid Materials and Systems, John Wiley & Sons, USA, 1987.

29. S.W Song, S.W. Baek. Electrochim. Acta 54 (2009) 1312–1318.

30. J. Hassoun, S. Panero, B. Scrosati, Fuel Cells 09 (2009) 277–283.

31. P.P. Ferguson, A.D.W. Todd, J.R. Dahn, Electrochem. Commun. 10 (2008) 25–31.

Capítulo 3.-

Materiales híbridos de cobalto-estaño y poliacrilonitrilo

3.1 Cobalt and tin oxalates and PAN mixture as a new electrode material for lithium ion batteries

Francisco Nacimiento, Ricardo Alcántara, José L. Tirado

Abstract

A mixture between cobalt oxalate, tin oxalate and dispersed polyacrylonitrile (PAN) molecules has been used as a new electrode active material for lithium ion batteries. The electrode shows good capacity retention in the case that the imposed potential limit is below 2.0 V. The mechanism of the reaction with lithium was studied by using XRD and ^{119}Sn Mössbauer spectroscopy. The electrode materials become irreversibly amorphous at the beginning of the reaction, when tin oxalate is decomposed and Sn(IV) is detected. Then, the metallic ions are reduced and amorphous tin–cobalt phases are formed. Finally, previously unknown Li-Co-Sn phases are reversibly formed near 0.0 V. The oxalate groups and the PAN form an electrochemically inert matrix. Due to the matrix, the aggregation of the amorphous particles into crystalline particles upon cycling is avoided. The extraction of lithium at the potential values near 2.0 V yields to tin–oxygen interactions and this feature disturbs the matrix and yields to capacity fade.

ELSEVIER

3.1.1   Introduction

Tin-containing intermetallic are very promising materials for lithium ion batteries electrodes. Pure tin possesses great ability to react reversibly with lithium. The use of multi-component systems or composites can be advantageous over pure metals. The presence of transition metal elements and carbon is useful to maintain the integrity of the tin-based electrode after charge– discharge cycling [1, 2]. The electrochemical reaction of the tin based electrodes with lithium may yield amorphous particles of meta stable phases. These new phases have a natural tendency to crystallize into larger particles of more stable phases upon charge–discharge cycling. The processes of crystallization and grain growth lead to electrode failure. The preparation of high performance composite electrode materials containing small particles of tin and other elements is not always easy. The organic polymer may contribute to disaggregating the small metallic particles. The use of organic polymers such as polyacrylonitrile (PAN) in composite electrodes has been proposed [3, 4]. The use of PAN ($-[CH_2-CH(CN)]_n-$) can be advantageous because of its ability to interact with metallic surfaces, electronic conductivity and easy denitrogenation that yields to carbon [5].

Several oxysalts have been explored as electrode materials in the last decade. Tin oxalate was shown to be able to react with 11 Li per formula yielding to reversible capacities of around 600 mAh g^{-1} in the first cycles [6]. Recently, the use of iron oxalate nano-ribbons [7] and cobalt oxalate nano-ribbons [8] as electrode active materials for lithium ion batteries has been reported.

In this work, the use of tin and cobalt oxalates and PAN mixture as an inorganic–organic electrode for lithium ion batteries is explored by first time. The aim of this work is to form in situ a Co-Sn-organic phase composite electrode. X-ray diffraction (XRD) and ^{119}Sn Mössbauer spectroscopy are used to study the electrode reaction with lithium.

3.1.2   Experimental

The composite material was prepared by mixing tin and cobalt oxalates and PAN. These chemicals were supplied by Aldrich. The starting Co:Sn atomic ratio was equals to 1:2. First, 2.150 g of tin oxalate were added to 200 ml of absolute ethanol with

continuous high-speed stirring. Ethanol was used as a solvent because of its ability to dissolve both inorganic and organic compounds and its easy evaporation. Then, 0.633 g of cobalt oxalate and 1.0 g of PAN were added. The resulting suspension was gently heated at 50 ºC in air atmosphere until solvent evaporation while continuous stirring. Further heating at 120 ºC was carried out in a Buchi oven under dynamic vacuum.

The elemental analysis of the samples was carried out in a scanning electron microscope (SEM) JSM6300 instrument equipped with an energy dispersive spectrometer (EDS). In addition, C-N analysis was carried out by using an elemental analyzer Eurovector EA3000. The FTIR spectra were recorded in a Bruker Tensor27 instrument equipped with a beam splitter of CsI in transmission mode and 4 cm^{-1} of resolution. Thermal analysis experiments were carried out in a Shimadzu DTG-60 instrument at a heating rate of 1 ºC/min.

X-ray diffraction (XRD) diagrams were recorded on a Siemens D5000 instrument with CuKα radiation. Ex situ XRD diagrams of the electrodes were recorded after recuperating the electrodes from the electrochemical cells in a dry box, and protecting them with a plastic tape to avoid any reaction with air. ^{119}Sn Mössbauer spectra were registered at room temperature in a Wissel instrument and using a Ba^{119}SnO$_3$ source. The isomer shifts were referenced to BaSnO$_3$ (δ = 0.0 mm s^{-1}). The ex situ spectra of the electrodes were recorded after putting them into polybag (supplied by Aldrich) under inert atmosphere and hermetically closed with a commercial heat-sealer.

The galvanostatic experiments were carried out in an Arbin instrument and using Li test cells. In order to prepare the electrodes, carbon black (20 wt.%) and binder (polyvinylidene fluoride, 10 wt.%) were added to the mixture of oxalates and PAN (70 wt.%) in the presence of methyl-pyrrolidone. The resulting slurry was spread out onto a high-purity Cu foil, dried at 120 ºC under vacuum overnight, and finally pressed. LiPF$_6$ 1 M in ethylene carbonate: diethyl carbonate (EC:DEC = 50:50 in weight) was used as electrolyte solution. Mass-normalized current intensities between 30 and 80 mA/g were used for the electrochemical cycling experiments.

3.1.3   Results and discussion

The chemical composition of the sample consisting of a mixture of cobalt and tin oxalates and PAN is shown in Table 1. For the sake of comparison, another sample was prepared by the same method but without adding PAN and the resulting elemental analysis is included in Table 1.

Table 1. EDAX microanalysis and C-N analysis results expressed as weight percentage

ELEMENT	EDAX			C-N			
	Cobalt and tin oxalates at 50ºC	Cobalt and tin oxalates and PAN at 50ºC	Cobalt and tin oxalates and PAN at 120ºC	Cobalt oxalate	Tin oxalate	Cobalt and tin oxalates and PAN	PAN
Sn	29.3(3)	21.5(4)	17.8(5)				
Co	8.5(2)	4.3(1)	6.0(2)				
O	52.4(5)	31.3(6)	27.0(8)				
C	9.8(3)	33.0(6)	39(1)	13.2	11.5	28.1	67.4
N	-	10(1)	10(2)	-	-	7.0	24.7

The contribution of the carbon atoms in the tape used to support the sample may influence on the carbon content. The amount of tin in the samples was within the 17–22 % mass range.

The FTIR spectra of the PAN-oxalates mixture and reference materials are shown in Figure. 1. In the PAN spectrum (Figure 1a), the band located at 2240 cm^{-1} is ascribed to the -C≡N stretching [9]. The spectrum of tin oxalate (Figure 1b) shows two characteristic doublets placed at 1600–1670 and 1290–1350 cm^{-1} that are ascribable to asymmetric and symmetric stretching of carboxylate groups, respectively [6]. The peak at 790 cm^{-1} is due to O-C=O deformation. The peak at 480 cm^{-1} is ascribable to Sn-O stretching. Adsorbed water molecules give a broad band near 3530 cm^{-1}. The intense band at 3365 cm^{-1} is ascribed to crystallization water in cobalt oxalate (Figure 1c). The spectrum of tin oxalate does not show vibrations of water molecules. The bands

corresponding to PAN, tin oxalate and cobalt oxalate are observed in the electrode material obtained at 50 °C (Figure 1d). After heating to 120 °C under vacuum (Figure 1e), the peaks of water are not observed, and the position of the peaks in the region at around 1600 cm^{-1} is slightly changed. The peak at 790 cm^{-1} is still observed. The peak at 2240 cm^{-1} exhibits low intensity. In consequence, the treatment at 120 °C removes most of the crystallization water molecules from cobalt oxalate and the adsorbed water, and the carboxylate groups and the PAN vibrations are preserved.
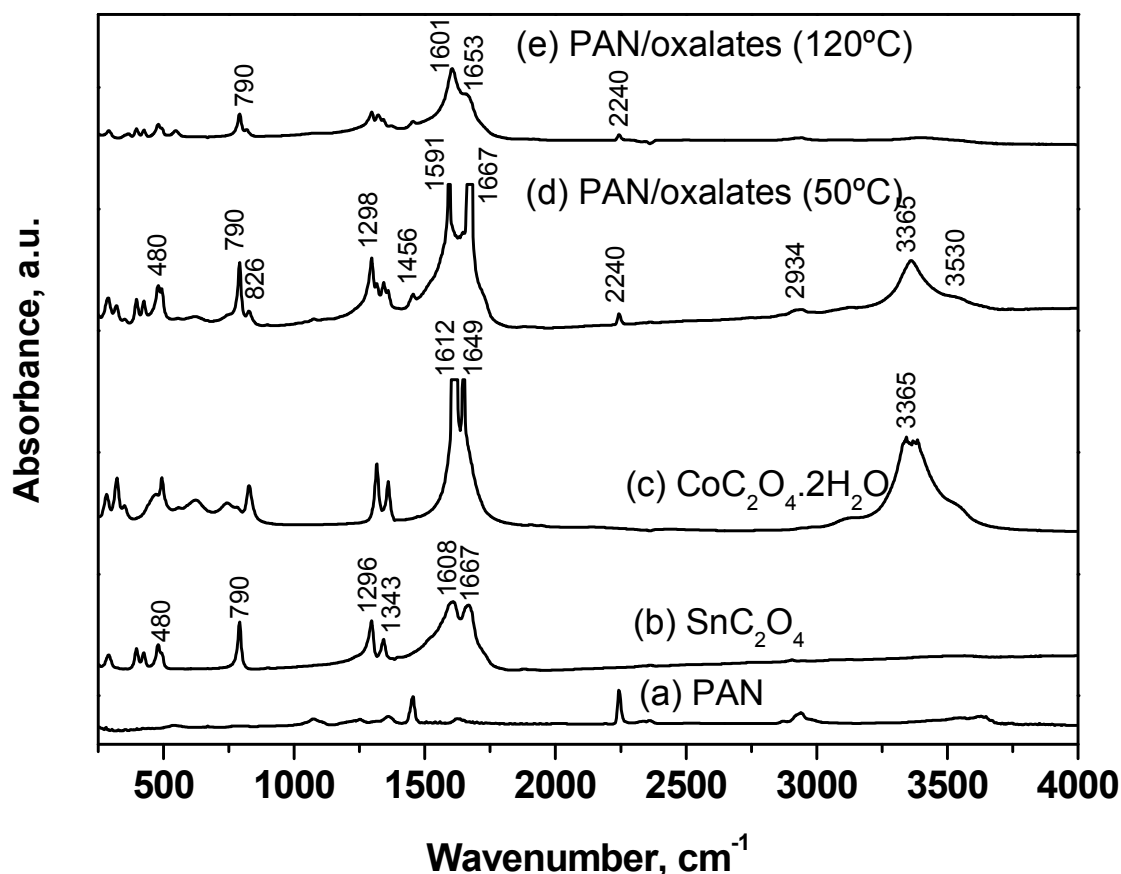

Figure 1. FTIR spectra for: (a) pure PAN, (b) anhydrous tin oxalate, (c) hydrated cobalt oxalate, (d) mixture of PAN and tin and cobalt oxalates obtained at 50°C and (e) the same mixture dried at 120°C under vacuum.

The thermogravimetric curves (not shown) of pure $CoC_2O_4.2H_2O$ reveal that the loss of crystallization water stars at 160 °C in air atmosphere. Under an Ar-flow, the dehydration stars at 145 °C. The decomposition of the anhydrous oxalates MC_2O_4 was observed between 243 °C and 297 °C, depending on the metallic element and the atmosphere. These results are consistent with the observation of XRD reflections of

SnC_2O_4 (XRD file no 14-0743) and CoC_2O_4-$2H_2O$ (XRD file no 25-0251) at 50 ºC (Figure 2d). The smaller intensity of the lines of the cobalt compound is a result of the lower scattering of the lighter metal atoms in the composite. The XRD pattern of the composite electrode material dried at 120 ºC under vacuum (Figure 2e) shows that the reflections of CoC_2O_4-$2H_2O$ have virtually disappeared. It is known that the dehydration of CoC_2O_4-$2H_2O$ below 250 ºC leads to a poorly crystallized CoC_2O_4 product [10]. The broad band at ca. 24º/2θ is consistent with previously reported data on the dehydrated product [8]. Dry PAN exhibits a XRD peak centered at ca. 16.8º/2θ ascribed to hexagonally packed assembly of rod-like polymer chains [9]. This peak virtually disappears in the composite sample. In summary, the XRD pattern of the composite sample prepared at 50 ºC (Figure 2d) exhibits reflections corresponding exclusively to tin (II) oxalate and cobalt oxalate hydrate. These results agree well with a high dispersion of the PAN molecules in the oxalates mixture, and this feature is further corroborated by the TEM micrographs.
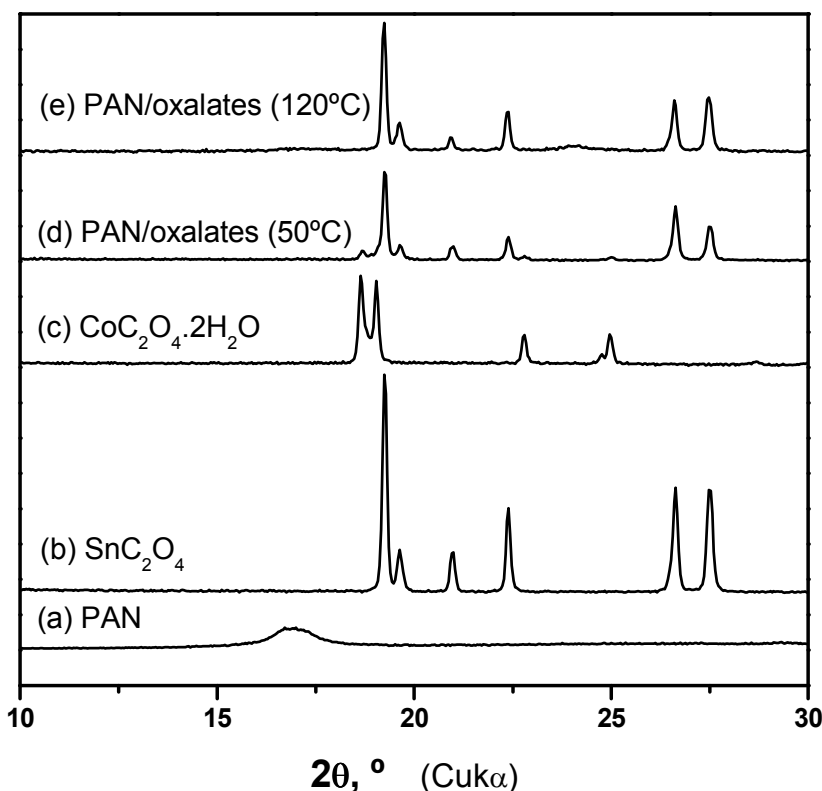

Figure 2. A detailed view of the XRD patterns for: for: (a) pure PAN, (b) anhydrous tin oxalate, (c) hydrated cobalt oxalate, (d) mixture of PAN and tin and cobalt oxalates obtained at 50ºC and (e) the same mixture dried at 120ºC under vacuum.

The electrodes containing cobalt oxalate, tin oxalate and PAN show great ability to react reversibly with Li. The potential–capacity plot of the first cycles is shown in Figure 3. The whole mass of the electrode comprising Co, Sn, C, N and O atoms, except the binder and carbon black additives, is taken into account to calculate the gravimetric capacity. If only the mass of tin atoms is taken into account (Table 1), the resulting specific capacity would exceed the maximum theoretical capacity of tin (993 mAh g^{-1} for the composition limit $Li_{22}Sn_5$). Thus, it can be concluded that other atoms contribute to the redox reactions. The large irreversible capacity of the first discharge–charge cycle would be detrimental for a commercial use. Irreversible lithium consumption due to reaction with carboxylic groups and consequent formation of $Li_2C_2O_4$ is expected for SnC_2O_4 [6]. To study the possible reaction of PAN with Li, an electrode containing PAN, and carbon black and PVDF as additives, was prepared. The observed capacity of the first discharge was 20 mAh g^{-1} as referred to the mass of PAN. In consequence, the contribution of PAN to the lithium consumption in the composite electrode would be negligible.
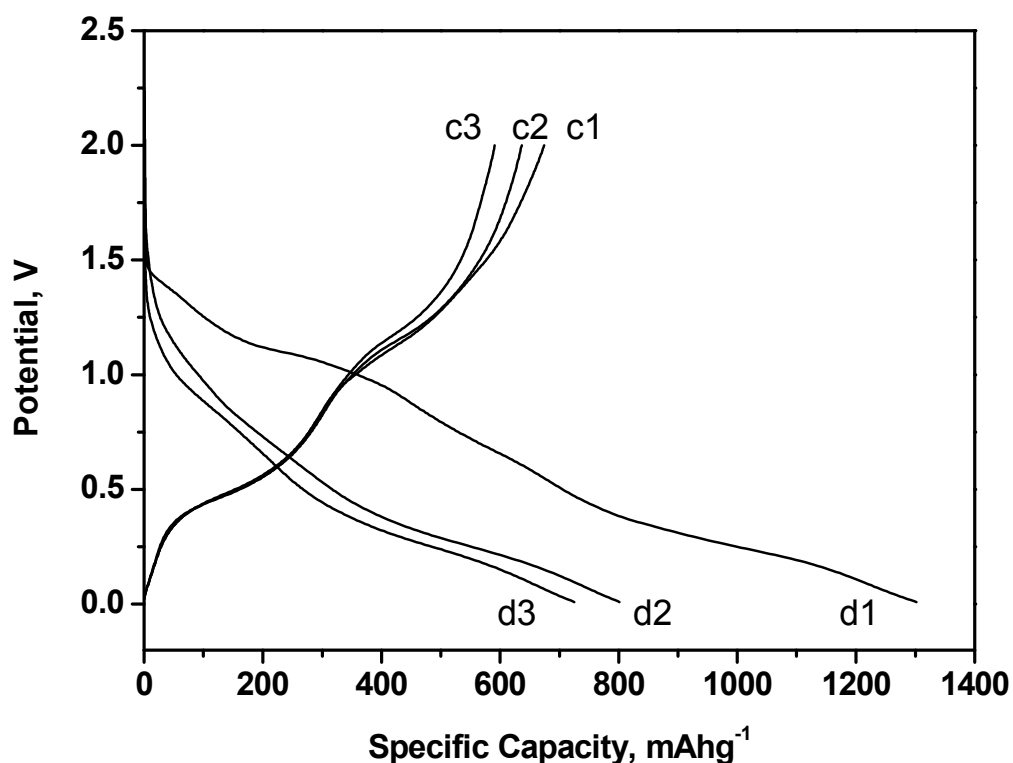

Figure 3. **Potential-capacity plot for the first cycles. The   number (n) of the discharge (dn) and charge (cn) are marked.**

The electrochemical performance upon cycling of the oxalates-based composite electrode is much better than the previously observed for pure tin oxalate [6].
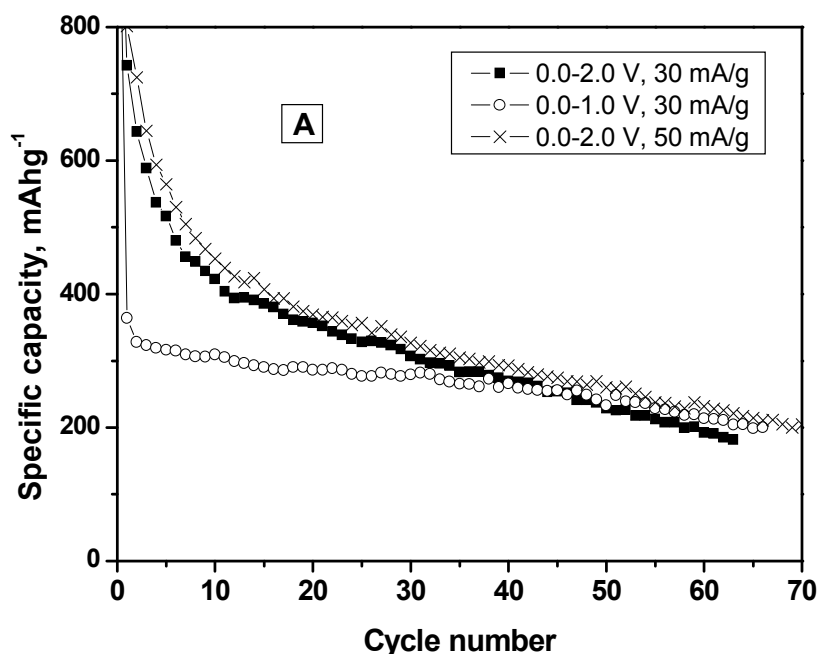

Figure 4-A. Specific capacity as a function of cycle number in lithium test cells. Current intensity values of 30-50 mA/g.
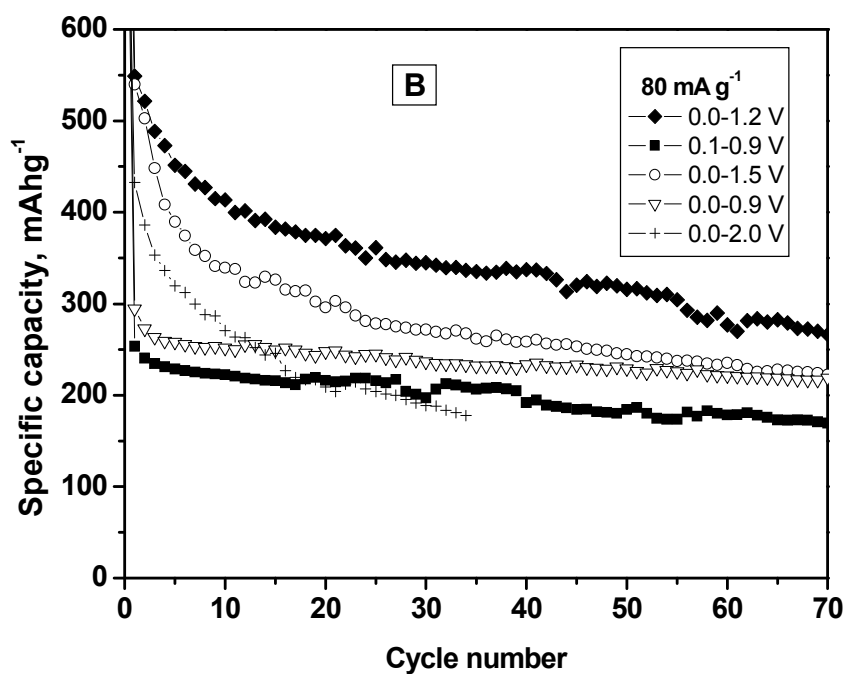

Figure 4-B. Specific capacity as a function of cycle number in lithium test cells. Current intensity value of 80 mA/g.
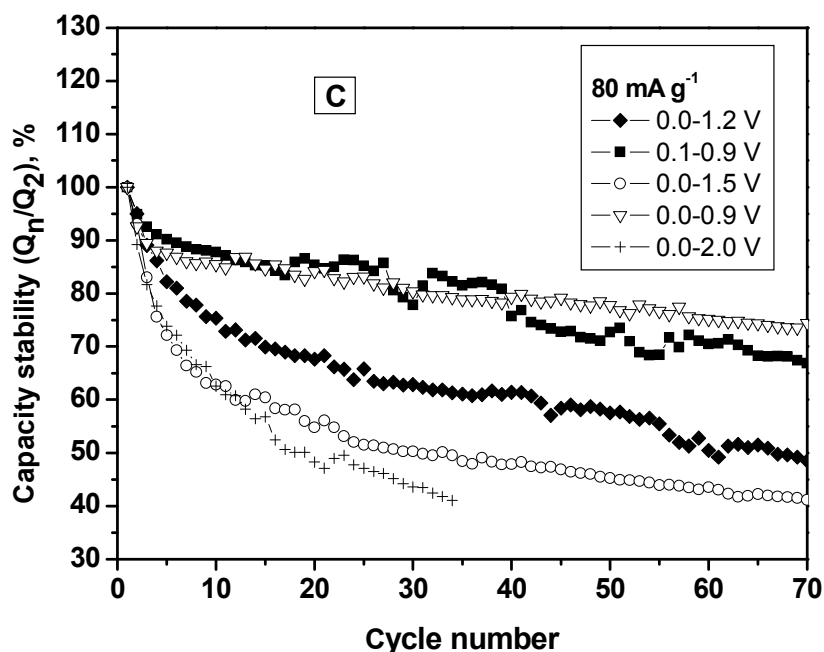
Figure 4-C. Specific capacity as a function of cycle number in lithium test cells. Capacity stability plot view as discharge capacity of the n-cycle divided into the capacity of the second cycle.

Strong influence of the cycling conditions on the electrochemical performance is observed (Figure 4 A–C). When the upper potential limit is equals to 2.0 V, the capacity retention is poorer, irrespectively of the imposed current intensity in the range between 30 and 80 mA/g. The electrochemical cycling is improved when imposing the upper potential limit below 1.5 V.

In Fig. 4B and C, it is observed that the capacity stability upon cycling continuously is improved by decreasing the upper potential limit from 2.0 to 0.9 V. After 70 cycles, the highest capacity is observed for the 0.0–1.2 V potential window (Figure 4B), but the best stability is observed for the 0.0–0.9 V potential window (Figure 4C). The presence of a relatively inert matrix can decrease the surface energy of the tin-based particles, avoiding their aggregation and maintaining the electrode integrity upon cycling. This matrix is affected by the high potential limits, as evidenced in the evolution of the capacity (Figure 4). In this way, several authors reported that in the case of tin oxide electrodes the Li_2O matrix holding the Sn atoms may be destroyed if the cutoff potential is high [11,12].

Irrespectively of the same initial oxidation state of the tin atoms, the potential–capacity curves (Figure 3) and the corresponding derivative plots (Figure 5) differ from the previously reported for SnO [13] and are rather similar to the previously reported for pure tin(II) oxalate [6].

The observed peaks in the derivative curves (differential capacity vs. potential) corresponding to the composite electrode are broadened. This is indicative of the poor crystallinity of the reaction products. The derivative curves corresponding to Sn, SnO_2, SnC_2O_4 and CoC_2O_4 are shown in Figure 5 B–E for comparative purposes.
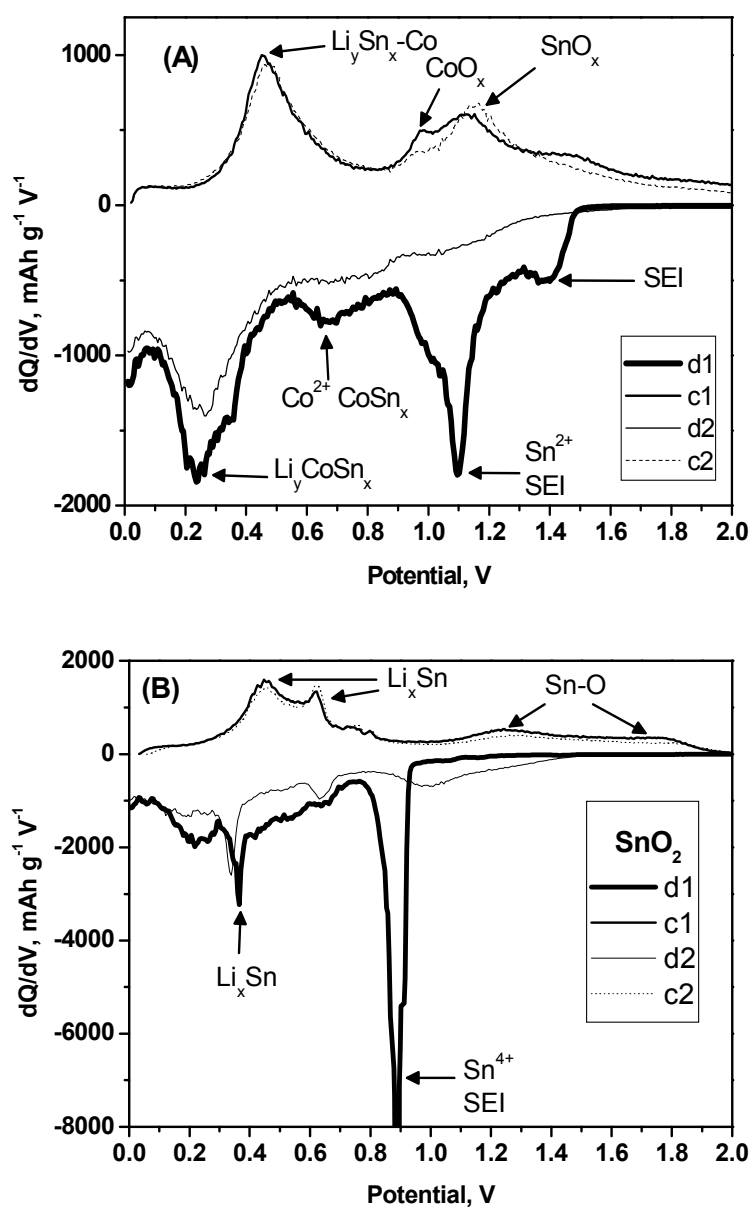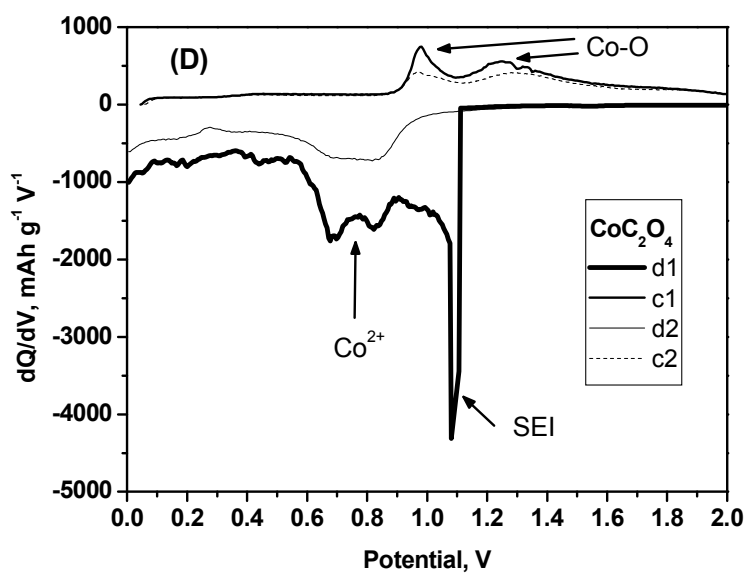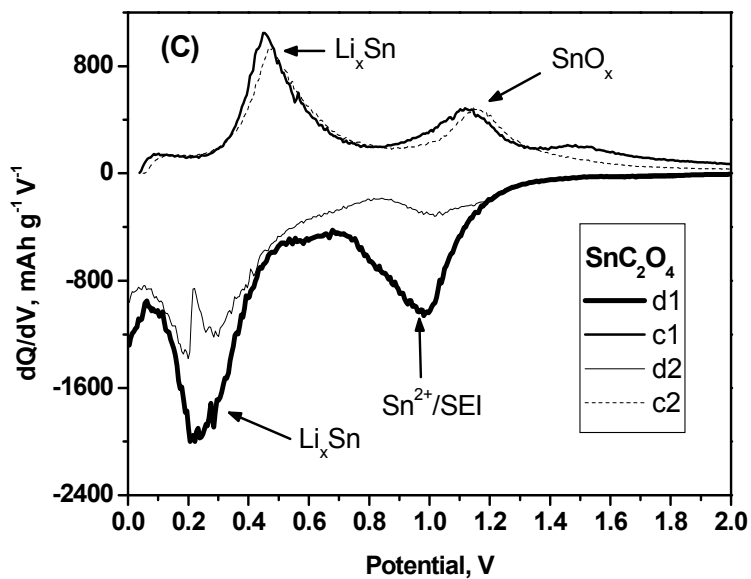

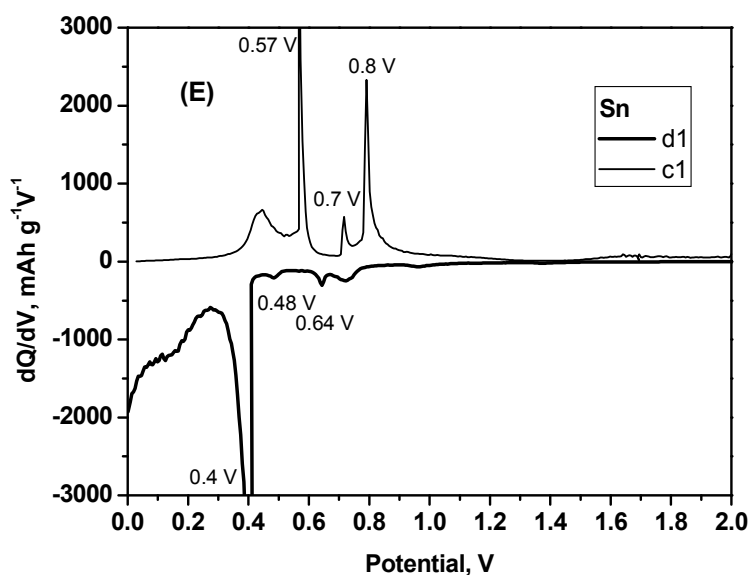**Fig. 5 (continued)**

Fig. 5 (continued)

Figure 5. Differential capacity vs. potential corresponding to the discharge (d) and charge (c) of the first cycles for (A) composite electrode containing oxalates mixture and PAN, (B) tin dioxide, (C) tin oxalate, (D) cobalt oxalate and (E) tin.

According to previous studies [14], the alkyl carbonate solvents are reduced at a potential below 1.5 V, Li_2O is formed below 1 V, and at potential below 0.6 V tin forms alloys with lithium. Pure cobalt oxalate exhibits an intense and irreversible peak at 1.1 V due to electrolyte consumption, and less intense signals in the region between 0.6 and 0.9 V due to the reduction of the cobalt ions. Pure tin(II) oxalate exhibits a broadened and asymmetric peak between 1.2 and 0.7 V due to several reductions processes, and a broadened peak between 0.4 and 0.1 V due to formation of lithium-tin alloys. Crystalline tin exhibits a narrow and very intense peak at 0.4 V. Tin dioxide shows a very intense peak at ca. 0.9 V due to reduction of Sn^{4+} ions and formation of lithia and a solid electrolyte interphase (SEI), while the main signal due to the formation of lithium–tin alloys is centered at 0.36 V. In the derivative curve of the first discharge of the composite electrode (Figure 5A), the peak placed at 1.4 V was previously observed for pure tin oxalate [6] and was tentatively ascribed to the reaction of Li with oxalate groups and formation of lithium oxalate. This peak is not observed in the pure tin oxalate and cobalt oxalate reference materials (Figure 5C and D).

The formation of a SEI and/or reaction between Li and PAN can contribute to this region. Lithium oxalate can be a component of the SEI [15,16]. By comparison of the derivative curves, the peak observed between 1.2 and 0.9 V would be mainly due to the reduction of the tin ions and formation of SEI in the composite electrode. Reduction of Sn(IV) also can contribute to the signal in the region at 0.9 V, as is discussed later. The irreversible peak around 0.7 V, not observed for pure tin oxalate, might be ascribed to the reduction of Co^{2+} ions and the in situ formation of $CoSn_x$ grains. Similarly, an irreversible peak was observed at around 0.5 V in the first discharge of Co_2SnO_4 [17]. It is worth to remember that Co is a fast diffuser in Sn, with great ability to form amorphous alloys. The broadened peak placed at 0.25 V in the discharge process, and at 0.45 V in the charge, is ascribed to the reversible formation of lithium-containing intermetallic with very small grain size. This peak is not observed for pure tin. Tin oxalate also shows a broadened peak at ca. 0.25 V that is also observed at 0.45 V in the charge process. According to Dahn et al., the average potential of the first discharge process shifts to lower values as the cobalt content increases in Co-Sn-C alloys [18]. The shoulder in the derivative curve of the first discharge at 0.35 V might be due to the occurrence of Li_xSn phases in the composite electrode. The derivative curve corresponding to the second discharge of pure tin oxalate shows the splitting of the region at ca. 0.3 V into two peaks and this feature can be related with an increase in particle size. However, the second discharge of the composite electrode is not split. This indicates that the presence of cobalt atoms helps to maintain very small grains of the alloy. On the other hand, it was observed that the thermal decomposition of tin and cobalt oxalates mixture leads to the formation of Co-Sn alloys (not shown). The segregation of tin would lead to peak at ca. 0.6 V in the charge process [19]. Thus, the charge process of tin dioxide shows a peak at 0.62 V in the derivative curve due to Li-Sn dealloying and partial formation of tin oxide at potential values over 1.0 V (Figure 5B). The charge curve of Sn shows narrows peaks at 0.57, 0.7 and 0.8 V due to dealloying processes (Figure 5E). The reoxidation of the cobalt oxalate electrode shows a broadened signal between 0.9 and 1.5 V. The charge process in the tin oxalate electrode leads to a broadened signal at ca. 0.5 V due to extraction of lithium form an alloy with very small particle size, and broadened signals over 1.0 V due to tin–oxygen interactions. Narrow peaks between 0.5 and 0.8 V ascribable to crystalline Li-Sn intermetallics (transition from LiSn to Li_2Sn_5), are not observed during the charge process of the composite electrode. All the results are consistent with the formation

of unknown Li-Sn-Co phases after the first discharge and are incompatible with the segregation of large grains of Sn during the charge. The peaks located at potentials of ca. 1.0 V were also observed for pure tin oxalate. These peaks can be due to tin oxidation and formation of Sn-O species. An extended oxidation of tin between ca. 1.0 and 2.0 V can contribute to destroy of the matrix and electrode failure upon cycling with high potential limit. Cobalt oxidation would take place at around 2 V [20].

The XRD pattern corresponding to the electrode partially discharged to 1.3 V still exhibits low-intensity reflections corresponding to the initial tin oxalate. Irrespectively of the peaks due to the Cu foil and the protective plastic film, all the electrodes that were recuperated between 0.9 V and 0.0 V of the fist discharge exhibit amorphous XRD patterns (Figure 6B b–d). After the first discharge down to 0.0 V and re-charge to 0.7, 1.2 or 2.0 V the XRD patterns remain amorphous. The XRD pattern obtained at 0.0 V after 45 discharge-charge cycles shows that the active material remains amorphous (Figure 6B e45). From the electrochemical point of view, it is preferred that the electrode materials remain amorphous and that the crystallization processes and grain growth are inhibited, resulting in a more stable electrode. The cobalt d-electrons can contribute to stabilize the amorphous tin-based alloys and avoid crystallization processes [21]. The irreversible amorphization process makes difficult the study of the reaction mechanism. We have used the [119]Sn Mössbauer spectroscopy to further study the reaction mechanism. The hyperfine parameters and the barycentre of the whole signal can reveal the occurrence of several oxidation states and alloys. In the case that the unambiguous identification of chemical compounds and specific tin sites is not possible, the barycentre of the whole spectrum can lead to valuable information [22,23].
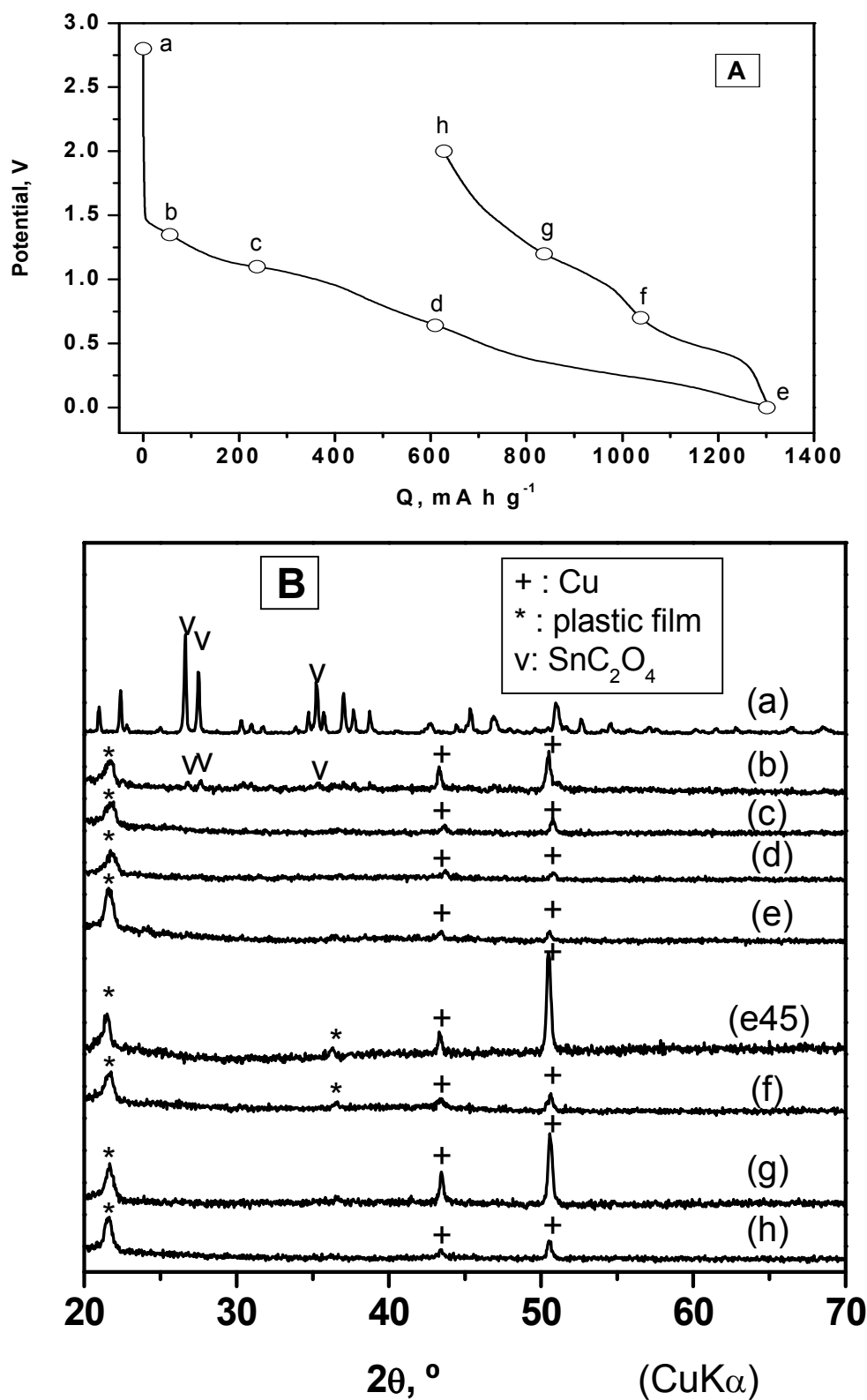
Figure 6-A. Study of the mechanism of the reaction at selected states of discharge (a-e) and charge (f-h). Potential-capacity plot of the first cycle. (B) Study of the mechanism of the reaction at selected states of discharge (a-e) and charge (f-h). Ex-situ XRD patterns.
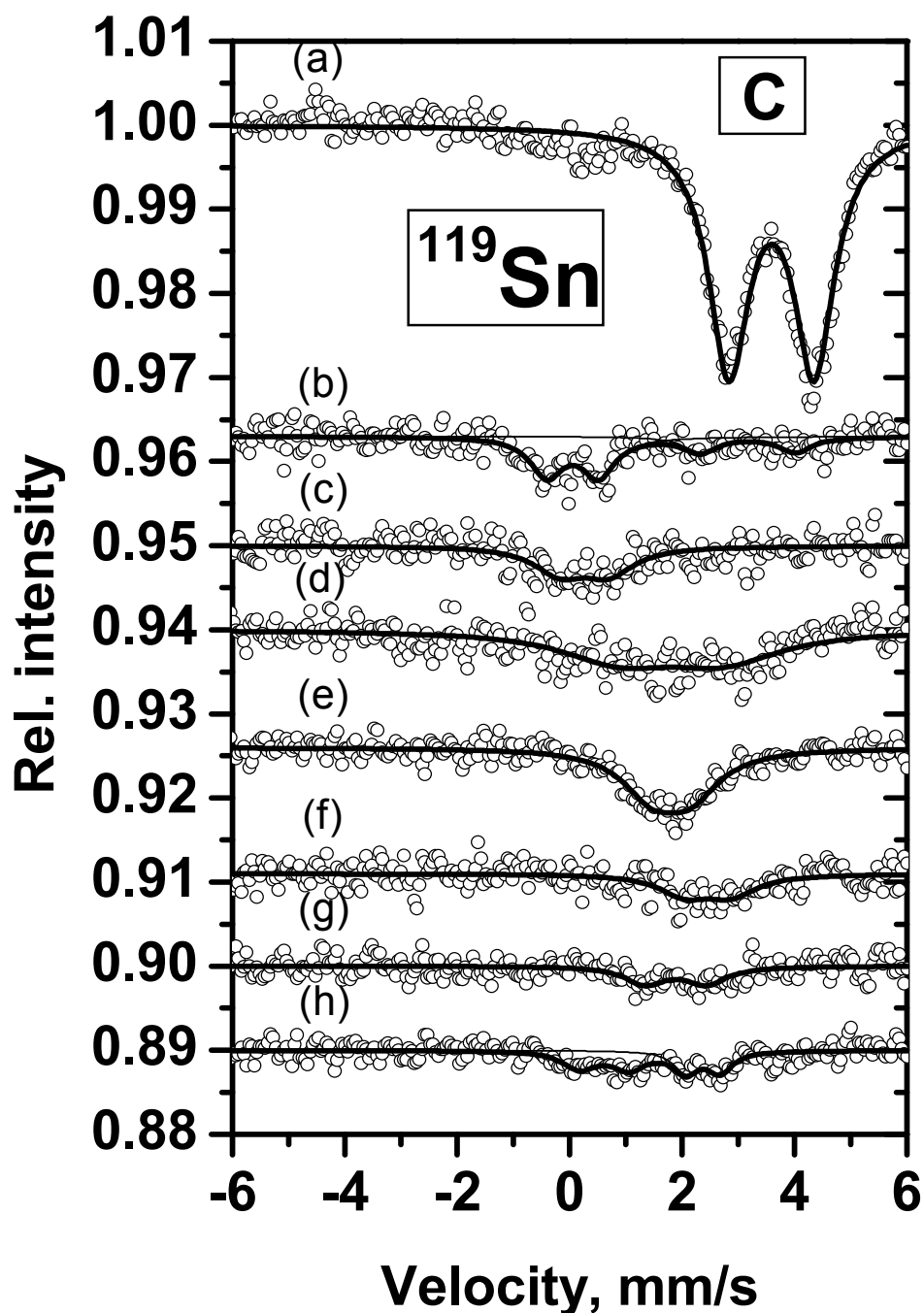
Figure 6-C. Study of the mechanism of the reaction at selected states of discharge (a-e) and charge (f-h). Ex-situ ^{119}Sn Mössbauer spectra.The spectra have been offset vertically for clarity.

The barycentre value does not necessarily represent any chemical compound, but rather represent the average contribution of different tin sites. The ^{119}Sn Mössbauer spectrum is ascribed exclusively to Sn(II) (Figure 6C a, Table 2). After reaction with

Li, the poor crystallinity of the resulting products contributes to the observed low intensity of the spectra. It has been reported that small particles size may lead to lower recoil-free fractions [24]. The reaction of lithium with tin-based electrodes leads to low intensity Mössbauer spectra for electrodes that remain stable and amorphous upon cycling [25]. In the case that the reaction of tin-based electrodes with lithium results in more crystalline phases, the corresponding Mössbauer spectra can be more intense but the electrochemical behavior would be poorer [26,27]. Both Co and Li can contribute to decrease the isomer shift of [119]Sn [28,29,19,30]. This feature can be related with the tendency of the tin atoms to give electrons to the alloy. The electron density at the tin 5s-orbital decreases as a consequence of the electron transfer to the alloy, resulting in a decrease of the isomer shift value for Co-Sn alloys in comparison with pure tin [31]. Alternatively, the decrease of the isomer shift can be seen as due to the decrease of the number of tin–tin interactions that are disrupted by cobalt or lithium atoms [22]. The spectrum obtained at beginning of the first discharge exhibits a main signal that is placed at isomer shifts values that correspond to Sn(IV) (Figure 6C b), but the quadrupole splitting is high ($\Delta = 0.92(5)$ mm/s).

Table 2. Fitting hyperfine parameters of [119]Sn Mössbauer measurements for pristine material (a), and electrodes recuperated from lithium cells in the discharge (b-e) and charge (f-h) states. For further explanation of the notation, see Figure 6.

Notation	δ	Δ	Γ	C	Assignation
(a)	3.593(9)	1.52(1)	0.87(2)	100	Sn(II)
(b)	0.05(4)	0.92(5)	0.71(1)	71	Sn(IV)
	3.2(1)	1.7(2)	0.71(3)	29	Sn(II)
(c)	0.3(1)	0.9(1)	1.1(3)	100	Sn(IV)
(d)	1.8(1)	1.8(2)	2.5(5)	100	$CoSn_x$
(e)	1.80(5)	0.7(1)	1.3(1)	100	Li_yCoSn_x
(f)	2.5(1)	0.8(1)	1.1(3)	100	$CoSn_x$
(g)	1.9(1)	1.1(1)	0.9(2)	100	$CoSn_xO_z$
(h)	0.6(1)	0.9(1)	0.7(2)	54	SnO_x
	2.37(5)	0.6(1)	0.5(1)	46	$CoSn_x$

δ: isomer shift (mm s^{-1}). Δ: quadropole splitting (mm s^{-1}). Γ: line width (mm s^{-1}).
C: relative contribution (%).

It is worth to note that the Sn(IV) atoms in Co_2SnO_4 [17] and cassiterite doped with cobalt [32] show high quadrupole splitting values. Metastable tin–oxygen species might be formed in the electrodes that do not correspond to any pure crystalline and stoichiometric compound. Traces of Sn(II) are also detected. The formation of SnO_2 and $Li_2C_2O_4$ as the only products due only to one stoichiometric reaction between Li and SnC_2O_4 would be impossible. It is known that Sn(II) can disproportionate into Sn(IV) and Sn [13,33]. Thus, tentatively, the reaction of tin oxalate with lithium at around 1.1 V may be written as follows:

$$2SnC_2O_4 + 2Li = Li_2CO_3 + Sn + SnO_2 + 3CO \qquad (1)$$
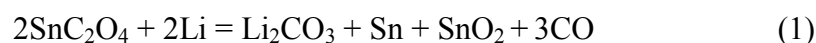
The resulting Sn would remain undetected due to a much lower Lamb-Mössbauer factor than Sn(IV) [34]. The generated lithium carbonate and other lithium oxysalts can contribute to create a SEI. The in situ formed tin dioxide would contribute to the region at 0.9 V in the derivative curve (Figure 5A and C).The reaction of cobalt oxalate with lithium in the range between 1.0 and 1.4 V in the simplest assumption would be:

$$CoC_2O_4 + 2Li = Li_2C_2O_4 + Co \qquad (2)$$
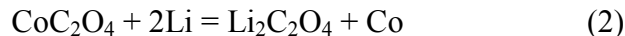
Reaction (2) is supported by previous studies on pure cobalt oxalate that used XAS and showed the formation of Co [8]. Looking at the details of the derivative curve in the galvanostatic experiments, the reduction of cobalt oxalate would be a more complex process with several steps. The [119]Sn Mössbauer spectrum obtained at 1.1 V exhibits a signal corresponding to Sn(IV) atoms in highly distorted environment (Figure 6C c). Interactions of tin atoms with both oxygen and cobalt atoms are expected. Tin dioxide, or cobalt-doped tin dioxide, is expected to be reduced at around 1.1–0.9 V [32] following the next reaction:

$$SnO_2 + 4Li = 2Li_2O + Sn \qquad (3)$$
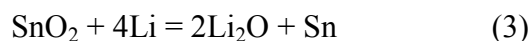
The generated lithia also contributes to create a relatively stable matrix to buffer the volume changes of the electrode. The lithium consumption in the reactions above would be mostly irreversible. At 0.6 V of the first discharge, the resulting spectrum (Figure 6C d) is centered at isomer shifts values corresponding to $CoSn_x$ alloys [28,29]. The spectrum is much broadened and has low intensity due to the formation or
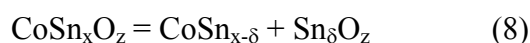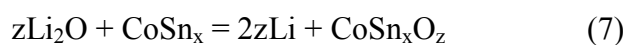
amorphous alloys, and the fitting represents not a single type of tin atoms but the average situation of the tin atoms in variable environments. Since cobalt has a great ability to diffuse into tin and to form amorphous alloys [35], the in situ generated Sn and Co atoms diffuse and form undetermined Co-Sn alloys:

$$Co + xSn = CoSn_x \qquad (4)$$

The spectrum corresponding to the completed discharge state (Figure 6C e) can be fitted with a doublet signal centered at $\delta=1.80(5)$ mm/s. This value is near the expected for $Li_{22}Sn_5$ ($\delta=1.837(3)$ mm/s and $\Delta=0.27(2)$ mm/s) [22]. The higher quadrupole splitting value ($\Delta= 0.7(1)$ mm/s) strongly suggests the presence of cobalt atoms in the vicinity of the tin atoms. The complete lithiation of nanocrystalline $CoSn_3$ also yields to nearly the same hyperfine parameters values ($\delta=1.93(4)$ mm/s, $\Delta=0.50(7)$ mm/s) [36]. The presence of Co tends to increase the isomer shift value. Thus, the discharged electrode contains amorphous Li_yCoSn_x with cobalt content lower than the observed for lithiated $CoSn_3$, in agreement with this reaction:

$$yLi + CoSn_x = Li_yCoSn_x \qquad (5)$$

After the charge up to 0.7 V, the isomer shift value is increased ($\delta=2.5(1)$ mm/s) as a result of lithium extraction. From 0.7 to 2.0 V the spectra are split into two signals. After the re-charge process up to 2.0 V, the spectrum is fitted with two doublet signals. One of these signals is placed at $\delta=2.37(5)$ mm/s and this value is within the region expected for tin alloy with a small amount of Co or Li. The other signal is located at $\delta=0.6(1)$ mm/s, and can correspond to "unusual" tin-oxygen phases or, otherwise, tin atoms that have residual interactions with oxygen atoms. The origin of the oxygen atoms can be the carboxylic groups of the oxalates and the in-situ generated tin dioxide. The occurrences of these tin-oxygen interactions are related with the capacity fade upon cycling due to the destruction of the $Li_2C_2O_4$-Li_2O matrix. The reactions of the charge process can be written as:

$$Li_yCoSn_x = Li + CoSn_x \qquad (6)$$

$$zLi_2O + CoSn_x = 2zLi + CoSn_xO_z \qquad (7)$$

$$CoSn_xO_z = CoSn_{x-\delta} + Sn_\delta O_z \qquad (8)$$

The mechanism of the reaction is followed by the change of the average isomer shift in the ^{119}Sn Mössbauer spectra (Figure 7).

Due to the occurrence of Sn(IV), the average isomer shit decreases at the beginning of the first discharge (reaction (1)), while the Sn(0) atoms are not detected. At further discharge depth (reactions (3) and (4)), the formation of Sn(0) and CoSn$_x$ increases the average isomer shift as referred to Sn(IV). The reaction of CoSn$_x$ with Li would tend to slightly decrease the isomer shift value (reaction (5)), but the resulting values are within the experimental fluctuation. Due to the partial extraction of lithium, the isomer shift is increased (reaction (6)). With further lithium extraction, at the end of the charge process, the isomer shifts decreases due to partial oxidation of tin atoms and the occurrence of tin-oxygen interactions (reaction (7)). Further lithium extraction induces the extraction of lithium from the Li$_2$O component of the Li$_2$C$_2$O$_4$-Li$_2$O matrix, segregation of the tin phases (reaction (8)) and tin-oxygen interactions, and consequently the average isomer shift decreases.
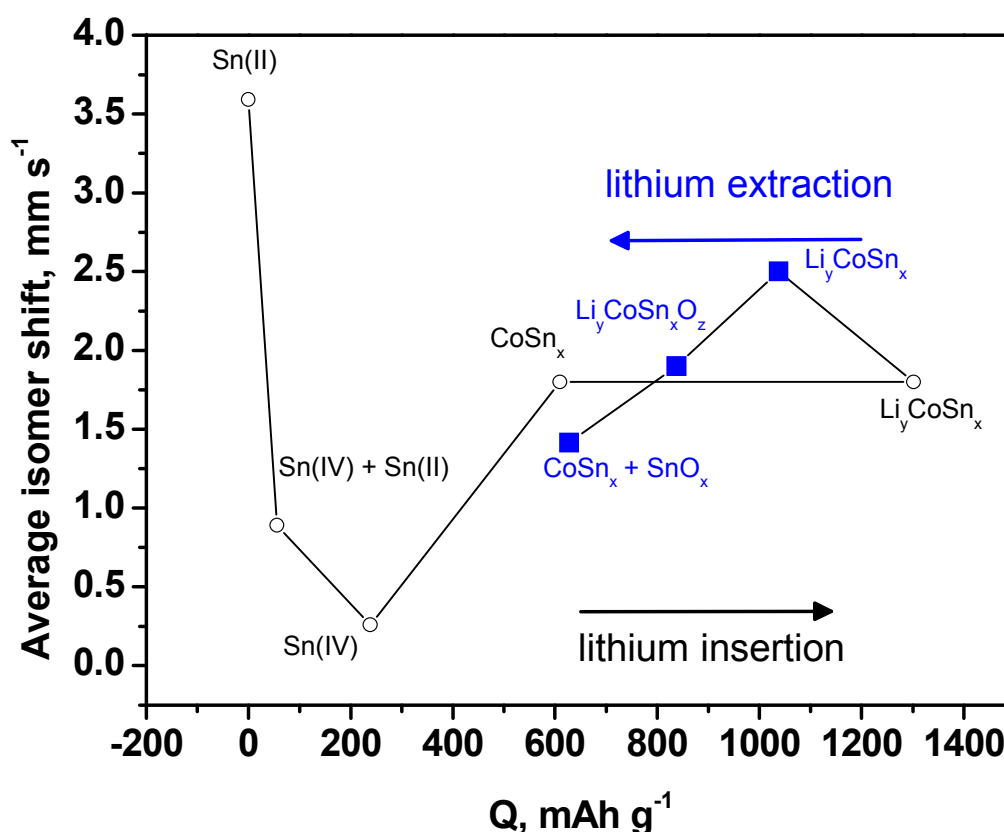

Figure 7. Average isomer shift of the ^{119}Sn Mössbauer spectra as a function of the first discharge (open circles) and charge (closed squares) depth.

3.1.4 Conclusions

Electrodes containing a mixture of cobalt and tin oxalates and dispersed PAN molecules have been prepared. In contrast with electrochemical behaviour that was unambiguously described for pure cobalt oxalate and tin oxalate, the interactions between these solids in the composite electrodes lead to the formation of amorphous Li_yCoSn_x after reaction with Li. The cobalt-tin grains are the electrochemically active particles in a matrix containing inorganic (lithia and lithium oxysalts) and organic (PAN) compounds. The matrix hinders the thermodynamic tendency to decrease the surface energy, increase the particle size and crystallize and, consequently, the matrix can improve the electrochemical cycling. The high irreversibility of the first cycle and the instability of the $Li_2C_2O_4$-Li_2O matrix in the charge process would be the main drawbacks for a commercial use of these systems.

Acknowledgements

References

1. http://www.sony.net/SonyInfo/News/Press/200502/05-006E/index.html

2. Q. Fan, P.J. Chupas, M.S. Whittingham, Electrochem. Solid-State Lett. 10 (2007) A274-A278.

3. X. He, W. Pu, L. Wang, J. Ren, C. Jiang, C. Wan, Solid State Ionics 178 (2007) 833-836.

4. F. Nacimiento, R. Alcántara, J.L. Tirado, J. Alloys Compd. 485 (2009) 385-390.

5. C. Reynaud, C. Boiziau, C. Juret, S. Leroy, J. Perreau, Synthetic Metals 11 (1985) 159-165.

6. R. Alcántara, F.J. Fernández-Madrigal, P. Lavela, C. Pérez-Vicente, J.L. Tirado, J. Solid State Electrochem. 6 (2001) 55-62.

7. M.J. Aragón, B. León, C. Pérez-Vicente, J.L. Tirado, Inorg. Chem. 47 (2008) 10366-10371.

8. M.J. Aragón, B. León, C.P. Pérez Vicente, J.L. Tirado, A. Chadwick, A. Berko, S.Y. Beh, Chem. Mater. 21 (2009) 1834-1840.

9. Z. Bashir, S.P. Church, D. Waldron, Polymer 35 (1994) 967-976.

10. A.K. Nikumbh, A.E. Athare, V.B. Raut, Thermochimica Acta 186 (1991) 217-233.

11. A. Courtney, J.R. Dahn, J. Electrochem. Soc. 144 (1997) 2045-2948

12. J. Chouvin, C. Branci, J. Sarradin, J. Olivier-Fourcade, J.C. Jumas, B. Simon, Ph. Biensan, J. Power Sources 81-82 (1999) 277-281.

13. D. Aurbach, A. Nimberger, B. Markovsky, E. Levi, E. Sominski, A. Gedanken, Chem. Mater. 14 (2002) 4155.

14. J. Zhu, Z. Lu, S.T. Aruna, D. Aurbach, A. Gedanken, Chem. Mater. 12 (2000) 2557-2566

15. G.F. Ortiz, R. Alcántara, P. Lavela, J.L. Tirado, J. Electrochem. Soc. 152 (2005) A1797-A1803.

16. C.M. Lee, B.J. Mun, P.N. Ross, Electrochem. Solid State Lett. 149 (2002) A1286-A1292.

17. R. Alcántara, G.F. Ortiz, P. Lavela, J.L. Tirado, Electrochem. Comm. 8 (2006) 731-736.

18. J.R. Dahn, R.E. Mar, A. Abouzeid, J. Electrochem. Soc. 153 (2006) A361-A365.

19. P.P. Ferguson, M.L. Martine, R.A. Dunlap, J.R. Dahn, Electrochim. Acta 54 (2009) 4534-4539

20. P. Poizot, S. Laurelle, S. Grugeon, L. Dupont, J.M. Tarascon, J. Power Sources 97–98 (2001) 235-239.

21. J.G. Geny, D. Malterre, M. Vergnat, M. Piecuch, G. Marchal, J. Non-Cryst. Solids 62 (1984) 1243-1248.

22. R.A. Dunlap, R.A. Small, D.D. MacNeil, M.N. Obrovac, J.R. Dahn, J. Alloys Compds. 289 (1999) 135-142.

23. I. Sandu, T. Brousse, D.M. Schleich, M. Danot, J. Solid State Chem. 177 (2004) 4332-43340.

24. R. Alcántara, P. Lavela, G. Ortiz, I. Rodríguez, J.L. Tirado, Hyperfine Interact. 187 (2008) 13-17.

25. I. A. Courtney, R.A. Dunlap, J.R. Dahn, Electrochim. Acta 45 (1999) 51-58.

26. C.M. Burba, R. Frech, A.Seidel, L. Häggström, A. Nytén, J.O. Thomas, J Solid State Electrochem 13 (2009) 1267–1272.

27. M. Mouyanea, L. Aldon,, M. Womes, B. Ducourant, J.C. Jumas, J. Olivier-Fourcade, J. Power Sources 189 (2009) 818-822.

28. R. Alcántara, G. Ortiz, I. Rodríguez, J.L. Tirado, J. Power Sources 189 (2009) 309-314.

29. G.F. Ortiz, R. Alcántara, I. Rodríguez, J.L. Tirado, J. Electroanal. Chem. 605 (2007) 98-108.

30. F. Robert, P.E. Lippens, J. Olivier-Fourcade, J.C. Jumas, F. Gillot, M. Morcrette, J.M. Tarascon, J. Solid State Chem. 180 (2007) 339-348.

31. A. Vertes, J. Jaén, M.L. Varsanyi, J. Radioanal. Nucl. Chem. 90 (1985) 383-393.

32. R. Alcántara, G.F. Ortiz, J.L. Tirado, ChemPhysChem 8 (2007) 80-86.

33. J. Chouvin, J. Olivier-Fourcade, J.C. Jumas, B. Simon, P. Biensan, F.J. Fernández-Madrigal, J.L. Tirado, C. Pérez-Vicente, J. Electroanal. Chem. 494 (2000) 136-146.

34. A. Hightower, P. Delcroix, G. Le CaRr, C. K. Huang, B. V. Ratnakumar, C. C. Ahn, B. Fultz, J. Electrochem. Soc. 147 (2000) 1–8.

35. P. Guilmin, P. Guyot, G. Marchal, Phys. Lett. 109 (1985) 174-178.

36. R. Alcántara, U. Nwokeke, I. Rodríguez, J.L. Tirado, Electrochem. Solid-State Lett. 11 (2008) A209-A213.

3.2 Comparative study of composite electrodes containing tin, polyacrylonitrile and cobalt or iron

Francisco Nacimiento, Ricardo Alcántara, José L. Tirado

Abstract

Composite materials containing Co-Sn alloys and polyacrylonitrile (PAN) have been prepared by reduction of Co(II) and Sn(II) in dimethylformamide with $NaBH_4$. The resulting cobalt and tin form an amorphous alloy and the PAN molecules hinder the growth and crystallization of the metallic grains. After heating the composite material obtained at 300ºC in Ar-atmosphere, the amorphous alloy leads to poorly crystallized $CoSn_2$, and the PAN molecules are partially pyrolyzed. In contrast, the reduction of Fe(II) and Sn(II) leads to crystalline Sn. The electrode containing nanosized $CoSn_2$ and PAN shows an excellent electrochemical behavior in lithium cells due to the structural stability of the PAN matrix and the small size of the metallic grains.

ELSEVIER

3.2.1 Introduction

Tin possesses the chemical property to alloy extensively with lithium. This feature makes tin and tin compounds very promising for lithium ion batteries electrodes. However, pure tin commonly exhibits very rapid capacity fade in a few charge-discharge cycles. Several intermetallic compounds and alloys containing tin and cobalt seem to be particularly useful [1, 2]. Thus, CoSn [3], $CoSn_2$ [4, 5], Co_3Sn_2 [5,7] and $CoSn_3$ [8] compounds, and Co-Sn-C alloys [2, 9] have been studied as electrode materials. It seems that the cobalt atoms stabilize tin-based electrodes upon cycling, by buffering volume changes and avoiding grain growth. The theoretical specific capacity decreases when cobalt is added, as compared with pure tin. The substitution of cobalt by iron can be advantageous from toxicological and economic perspectives. Interestingly, $CoSn_2$ and $FeSn_2$ are isostructural (space group I4/mcm). It has been proposed that the structure of $CoSn_2$ (and $FeSn_2$) has tunnels among the Sn atoms where Li might penetrate to initiate the reaction and, however, neither CoSn nor Co_3Sn_2 have such tunnels [1]. Carbon is another relevant component of the tin-based electrodes, which can enhance the connectivity between the metallic particles and stabilize the whole composite electrode [1]. Graphite, disordered carbon or organic polymers may be used as a source of carbon for the tin-based electrode. The use of small particles, amorphous alloys or nanocrystalline compounds is apparently an important prerequisite to achieve excellent electrochemical behavior. The large particles drive to breakage of the grains, swelling of the electrode and electrolyte consumption.

The reaction between lithium and Co-Sn compounds has been the subject of several studies that highlight the influence of grain size on the electrochemical reactions. Fan et al. proposed that amorphous CoSn forms Li-Co-Sn alloys [10]. The reaction between crystalline $CoSn_2$ and Li was studied by Ionica et al. [4]. Recently, Fergusson et al. concluded that fully lithiated $Co_3Sn_3C_4$ prepared by mechanical attrition is composed of nanoscale regions of $Li_{22}Sn_5$, nanoscale Co and lithiated carbon, while CoSn grains form after lithium extraction [11].

Polyacrylonitrile (PAN) is a very versatile polymer of formula (-[CH_2-CH(CN)]$_n$-), having several applications in the field of batteries. Thus, PAN molecules, together a plasticizer and a lithium salt can be used to prepare a solid electrolyte for lithium batteries [12]. PAN molecules can also be used as precursor to prepare carbon

fibers [13] and hard-carbons [14] that can be used as electrode active materials for lithium ion batteries. After pyrolysis at moderate temperatures [15], PAN molecules can form a conductive matrix of carbon that surrounds Sn particles [16]. PAN molecules have also been used to encapsulate $CoSn_2$ nanoparticles, and the TEM images showed that the metallic particles with nanometric size were surrounded by a carbonaceous film [17, 18]. The use of PAN to create Si-filled carbon fibers for lithium ion batteries also has been reported [19].

In this work, a comparative study on the preparation and properties of Co-Sn-PAN and Fe-Sn-PAN composites, and the role that is played by the PAN molecules is carried out. The effect of annealing at 300ºC the PAN-containing electrode materials is also studied.

3.2.2   Experimental

For the preparation of Co-Sn-PAN composite, first 4.0 g of $SnCl_2.2H_2O$, 2.1 g of $CoCl_2.6H_2O$ and 0.6 g of polyacrylonitrile (PAN, with M_W=150.000) were added into 250 mL of n,n-dimethylformamide (DMF) with continuous stirring. Second, an aqueous solution of $NaBH_4$ was added. Then, further water was added. It is worth noting that PAN is highly soluble in DMF and scarcely soluble in water. The resulting precipitate was separated by centrifugation, rinsed several times and dried under vacuum at 120ºC overnight. For the sake of comparison, a sample was prepared by using an equivalent procedure but without addition of PAN. Alternatively, iron(II) chloride was used instead of cobalt chloride to prepare Fe-Sn-PAN composites. All the reagents were supplied by Aldrich. The Co-Sn-PAN composite sample was further annealed at 300ºC during 3 h under an Ar-flow of 90 mL/min.

X-ray diffraction patterns were recorded in a Siemens D5000 instrument and using 0.04º-2 s steps. The average grain size was calculated by applying the Scherrer equation ($Lc=0.9\lambda/\beta cos\theta$) to the most intense Bragg reflection. Carbon and nitrogen contents were determined in an elemental analyzer Eurovector EA3000. Differential thermal analysis (DTA) experiments were carried out by using a Shimadzu DTG-60 instrument, alumina pans, 10ºC/min of heating rate and 50 mL/min of Ar-flow.

To study the pyrolysis of PAN, pure PAN was heated in an alumina crucible under Ar-flow (90 mL/min) at temperatures between 300 and 600ºC, with a heating rate of 1.5ºC/min and the imposed temperature was hold during 3 h. The NMR spectra of the resulting residua were recorded. Solid state ^{13}C NMR spectra were recorded in a BrukerAvance 400 WB instrument.

The electrochemical behavior of the prepared materials was studied in lithium test cells. A piece of Li was used as negative electrode. The positive electrode contained active material (70%), carbon black (20%) and polyvinylidene fluoride (PVDF) like binder (10%). A 1 M solution of $LiPF_6$ in an ethylene carbonate:diethyl carbonate solvents mixture (EC:DEC=50:50) was used as electrolyte. The instrument to carry out the discharge-charge cycling experiments was as a VMP. Typically, a mass-normalized constant current of 50 mA/g and 0.0-0.9 volts of potential window were imposed for the cycling experiments. Experiments were also performed at variable current intensities. Co, Sn and PAN were considered in the calculation of the specific capacity.

3.2.3   Results and discussion

The sample obtained by reduction of cobalt and tin ions in DMF without PAN shows a XRD pattern (Figure 1) with intense Bragg reflections corresponding to well crystallized $CoSn_2$ (main phase) and β-Sn (minor phase). The calculated grain size of $CoSn_2$ is Lc= 36 nm. In contrast, the sample obtained with PAN possesses an amorphous character. The dispersed molecules of PAN do not drive to any XRD diffraction. After annealing this amorphous sample at 300ºC under Ar-flow, a low-intensity reflection emerges which can be ascribed to $CoSn_2$ (ICDD file nº 25-0256), although the possible presence of amorphous alloys cannot be ignored. The calculated grain size value for $CoSn_2$ is Lc= 18 nm. These samples, that contain intermetallic particles surrounded by PAN [17], can be named like $CoSn_2$@PAN. The XRD patterns of the samples obtained by reduction of iron and tin ions in the presence of PAN, or without PAN, show in both cases intense reflections corresponding to crystalline β-Sn with Lc= 30 nm (Figure 2). Only traces of $FeSn_2$ are found. These samples, that contain crystalline tin, PAN and iron with no apparent interaction between them, can be named like Fe-Sn-PAN. In principle, it would be easier to reduce Fe(II) ions than Co(II) ions. Nanocrystalline Fe would lead to a low-intensity reflection placed at ca. 44.7º2θ

overlapping with Sn reflections. The Fe-Sn-PAN sample showed a strong tendency to react exothermally with the air atmosphere when it was manually ground in an agate mortar, yielding to iron and tin oxides (XRD not shown).
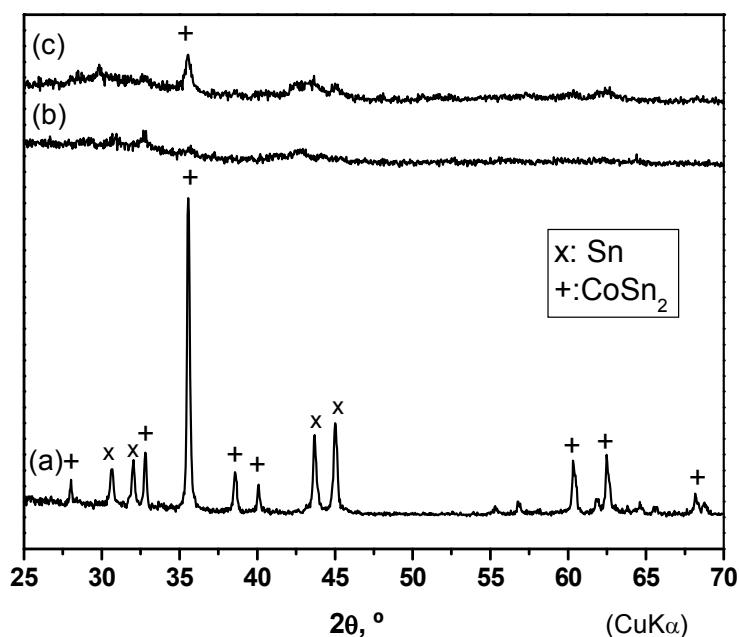
Figure 1. XRD patterns of (a) CoSn$_2$, (b) CoSn$_2$@PAN and (c) CoSn$_2$@PAN annealed at 300ºC under Ar-flow. The samples corresponding to (a) and (b) were heated up to 120^{a}C under vacuum.

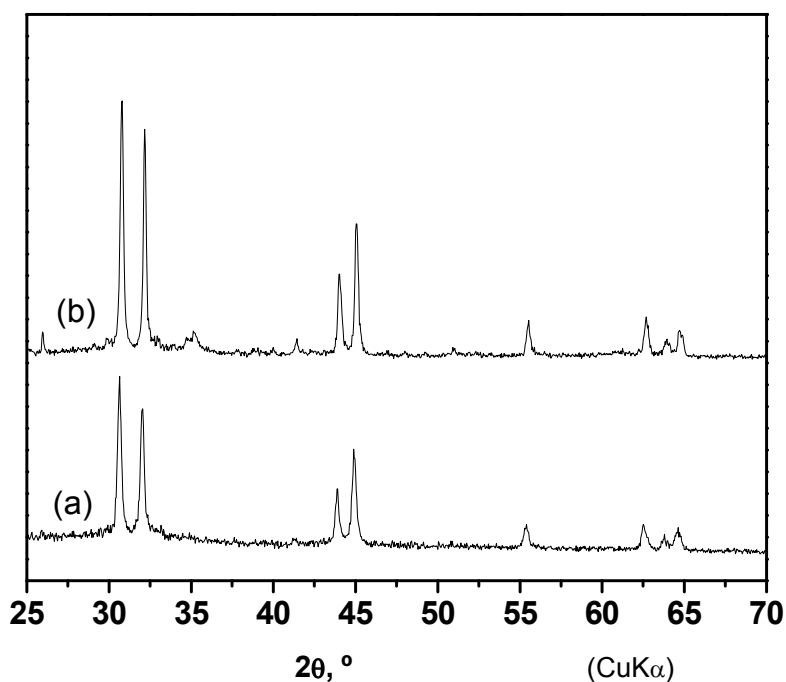**Figure 2. XRD patterns of (a) Fe-Sn and (b) Fe-Sn-PAN samples heated up to 120ºC under vacuum.**

The DTA curve of $CoSn_2$@PAN does not show the endothermal peak corresponding to the melting point of tin. The exothermal peak observed at 295ºC (Figure 3) may be due to grain growth and crystallization of the amorphous alloy and/or PAN pyrolysis. This peak is not observed after cooling down and recording the DTA curve during a second heating process. The $CoSn_2$ sample obtained without adding PAN does show neither the melting point of tin nor the exothermal peak at 295 º C.
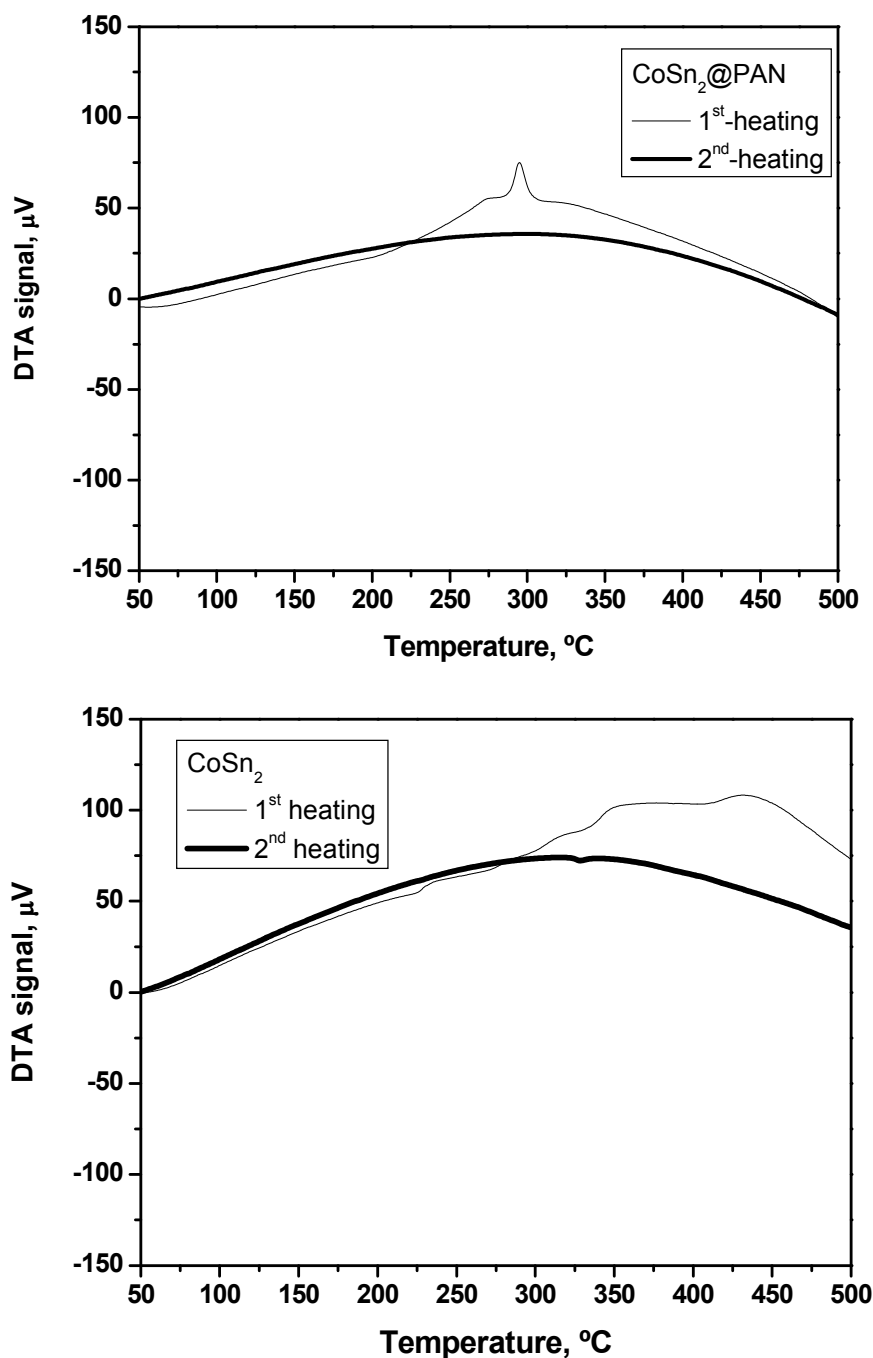

Figure 3. DTA curves for CoSn₂@PAN and CoSn₂ prepared without adding PAN.

In contrast, the DTA curve of the sample prepared with iron instead of cobalt shows an endothermal peak at the melting point of Sn (232°C) besides endothermal peaks al 115-133°C due to solvent evaporation (Figure 4). The melting point of Sn is not observed after cooling the sample and recording the DTA, suggesting that tin reacts to form other compounds during the first heating.

All these XRD and DTA results evidence the two following features: (i) the easier tin/cobalt diffusion to form alloys and intermetallics in comparison with tin/iron, and (ii) the addition of polymer PAN hinders the grain growth of $CoSn_2$. It is known that cobalt and tin have great ability to form amorphous alloys [20-22].
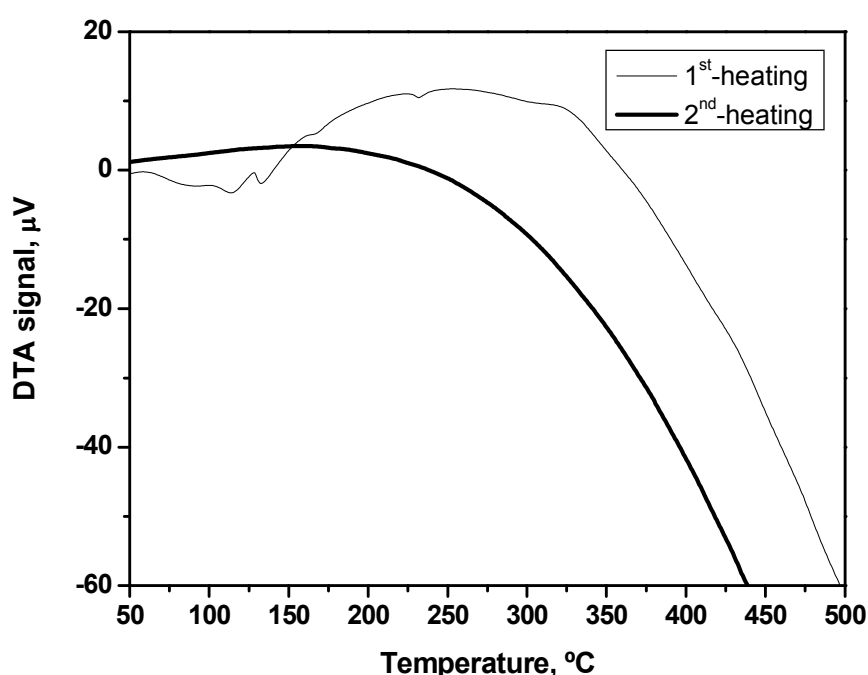

Figure 4. DTA curves for Fe-Sn-PAN.

The experimental contents in carbon and nitrogen for $CoSn_2$@PAN-120°C are 10.0 and 3.5% by mass, respectively. After annealing at 300°C, the carbon and nitrogen contents decrease to 8.8 and 2.7%, respectively. These data reflect an incomplete pyrolysis and denitrogenation of the PAN molecules. It is expected that the thermal treatment of PAN modifies the polymer chains and increasesits electrical conductivity [15]. The presence of PAN molecules and the effect of the thermal treatment on the PAN molecules can be observed by using NMR. The ^{13}C CP/MAS NMR spectrum of pristine PAN (Figure 5) shows a peak at about 30-35 ppm ascribable to sp^3 carbon in the polymer chain (CH and CH_2), another peak at 121 ppm ascribable to unsaturated

carbon in C≡N [23, 24], and spinning side bands. The treatment of PAN with $NaBH_4$ solution did not modify the ^{13}C NMR spectra (not shown).
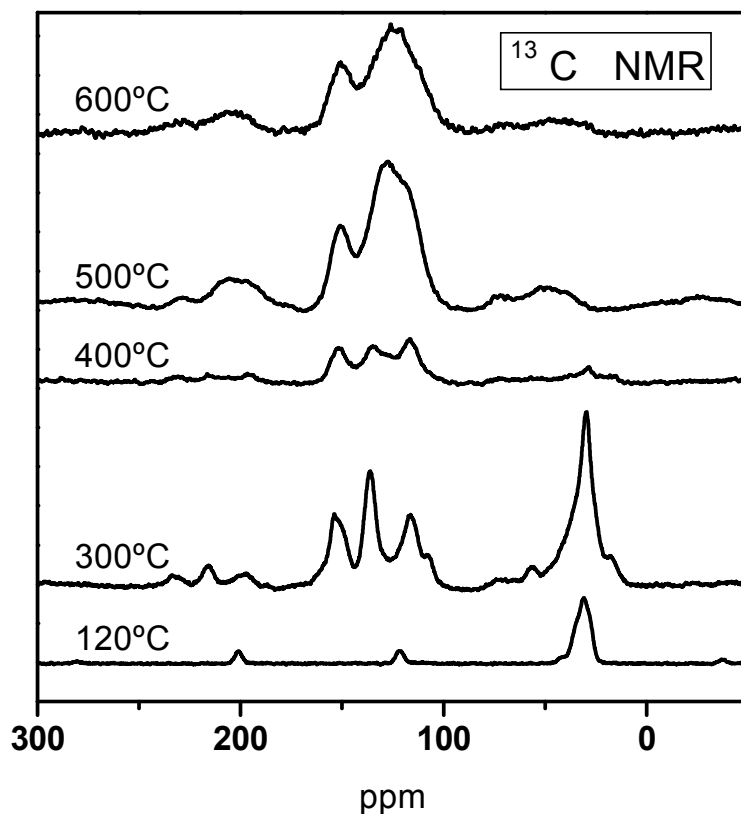

Figure 5. ^{13}C CP/MAS NMR spectra for PAN dried at 120ºC under vacuum and annealed in inert atmosphere between 300 and 600ºC.

After heating PAN to 300ºC, the peak at 30 ppm is maintained, the peak at 121 ppm disappears and new peaks emerge. The most intense of these new peaks is located at 135 ppm. Most probably, the peaks at 116 and 135 ppm correspond to the formation of C=C double bonds in the polymer backbone. A peak at 153 ppm can be ascribed to conjugated C=N species [24]. After annealing at 400-600ºC, the peak at 30 ppm disappears and two broadened peaks at observed at 151 and 125 ppm. The ^{13}C CP/MAS NMR spectra of $CoSn_2$@PAN are equivalent to those of pristine PAN (Figure 6), and this result corroborates the presence of PAN molecules in the $CoSn_2$@PAN sample. The relative intensity of the peak at ca. 30 ppm due to sp[3] carbon indicates that the partial

pyrolysis is more extended for CoSn$_2$@PAN-300ºC in comparison with pure PAN heated to 300ºC. It is known that PAN can interact with metallic surfaces and have an easy pyrolysis [15]. From the results of C-N analysis and NMR, it can be concluded that the sample CoSn$_2$@PAN-120ºC contains PAN molecules and CoSn$_2$@PAN-300ºC contains partially pyrolyzed PAN.
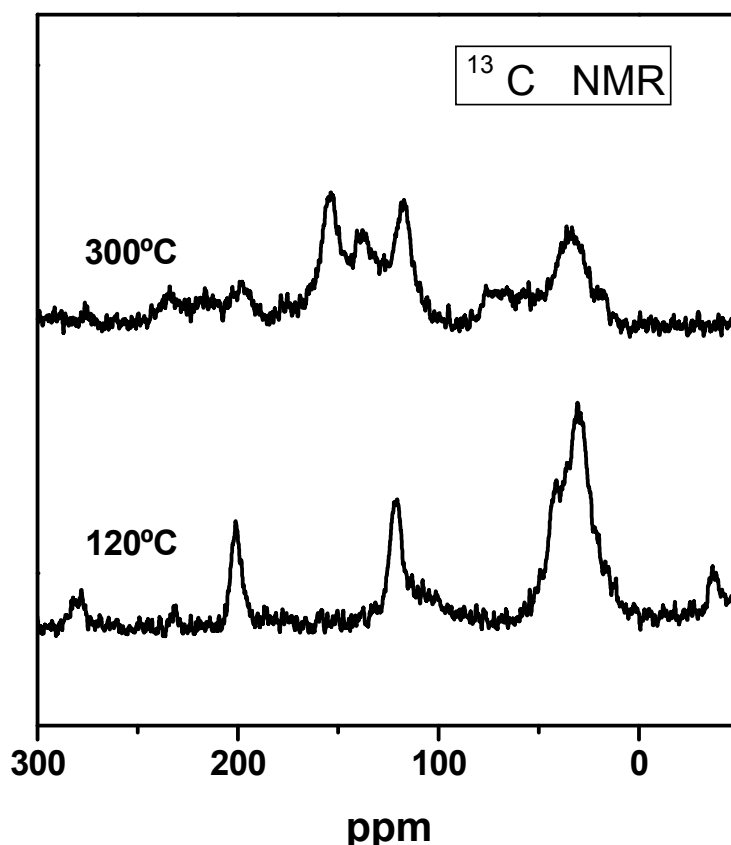
Figure 6. ^{13}C CP/MAS NMR spectra for CoSn$_2$@PAN dried at 120ºC and annealed in inert atmosphere at 300ºC.

The specific capacity is shown in Figure 7 as a function of cycle number. The carbonaceous residua that results from the annealing of PAN at 300ºC can slightly contribute to the capacity [17]. It is worth noting that pure microcrystalline CoSn$_2$ shows high efficiency in the first cycle (85%) but poor capacity retention [1] and that nanocrystalline FeSn$_2$ shows better capacity retention than microstalline FeSn$_2$ [25].

The resulting capacity retention of $CoSn_2$@PAN-120ºC and $CoSn_2$@PAN-300ºC is very good. It is expected that the PAN polymer conforms to the volume changes of the metallic particles that occur during the charge/discharge cycling. PAN is a matrix of structural stability that holds the metallic particle together and allows the migration of the lithium ions. The observed specific capacity of the amorphous $CoSn_2$@PAN-120ºC sample at 50 mA/g is about 480 mAh/g. After annealing at 300ºC, the capacity is slightly lower (around 400 mAh/g), most probably due to the crystallization and grain growth processes and longer lithium ion diffusion path length. A main drawback for the commercial use of these electrode materials would be the high irreversible capacity observed in the first cycle. Hassoun et al. reported an initial irreversible capacity of about 28% for Co-Sn-C alloy [9].

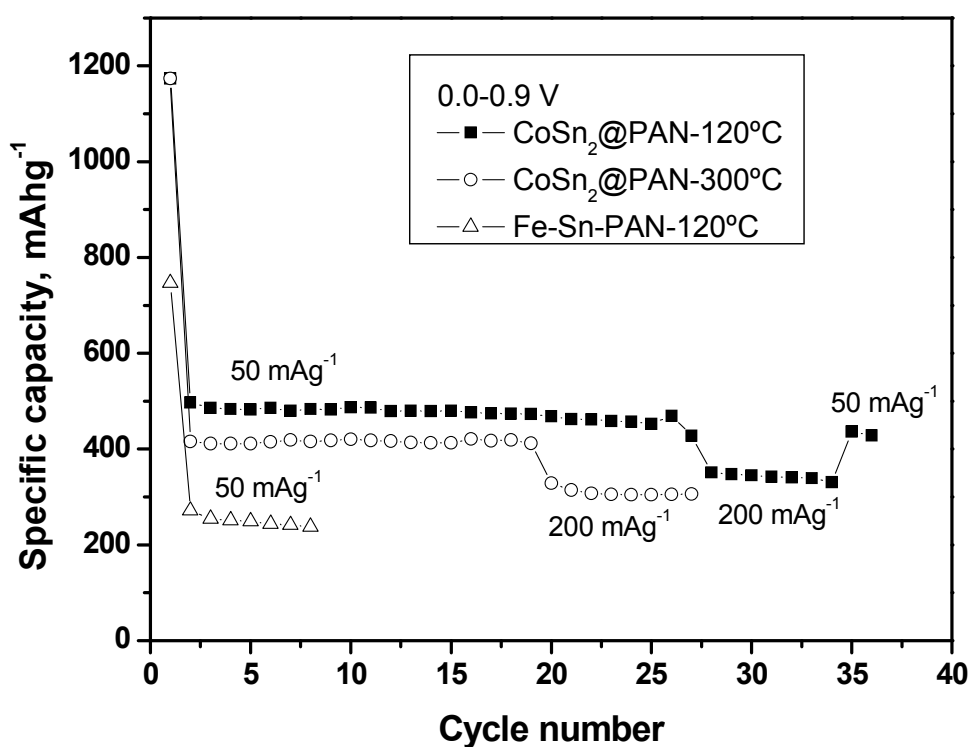**Figure 7. Specific capacity as a function of cycle number for $CoSn_2$@PAN obtained at 120 and 300ºC, and Fe-Sn-PAN obtained at 120ºC. Initial gravimetric current intensity: 50 mA/g. Potential window: 0.0-0.9 V. After several cycles, the imposed current was increased to 200 mA/g.**

Ionica-Bousquet et al. reported an initial capacity loss for pure $CoSn_2$ of 27% [4]. The $CoSn_2$@PAN electrode shows higher irreverisibility in the first cycle (efficiency of about 43%). The reasons for the observed low initial efficiency can be due to the high reactivity of the surface of the nanoparticles and the low upper potential limit that is imposed. In this context, recently Li et al. found very poor capacity retention and high irreversibility for Co-Sn-C electrodes when PVDF binder is used (60% of capacity loss after 5 cycles), while sodium carboxymethyl cellulose (CMC) binder yields to better electrochemical performance (500 mAh/g after 90 cycles) [26]. The rate capability of the electrode is another important issue [9]. These PAN-containing materials exhibit a relatively good response to the imposing of higher current intensities, with capacity values of about 350 mAh/g at 200 mA/g. The electrochemical behavior of the sample prepared with iron instead of cobalt exhibits poorer electrochemical behavior, as expected due to the presence of crystalline Sn. However, the capacity retention of this electrode material is better than the generally expected for pure Sn.

The galvanostatic cycling results for $CoSn_2$@PAN are shown as potential-capacity plots and derivative curves in Figure 8. The shape of these derivative curves is rather similar to the cyclic voltammetry reported for Co-Sn-C alloys obtained by mechanical-milling [9]. The derivative plot (dQ/dV vs. potential) of $CoSn_2$@PAN shows an irreversible peak at 1.5 V in the first discharge that can be ascribed to surface films formation and passivation (solid electrolyte interface). The reaction of lithium with XRD-undetected oxides in the surface of the metallic particles can also contribute to the irreversible capacity of the first discharge. Then, other peaks are observed at ca. 0.6 and 0.2 V. The main peak due to the reaction between Li and pure Sn would occur at 0.4 V [27], but it is not observed. This result suggests the occurrence of a Li-Co-Sn alloy. By definition, the alloy contains metallic grains with different compositions. During the first charge process, a broadened peak is observed with relative maxima at 0.47 and 0.6 V that corresponds to the extraction of lithium from the alloy. The extraction of lithium from crystalline Li_xSn would drive to a narrow peak at 0.8 V in the charge that is not observed here. Additional peaks are observedin the second cycle, at 0.2 V during discharge and 0.47/0.6 V during charge. All these results discard the formation of large and crystalline grains of Li_xSn compounds.
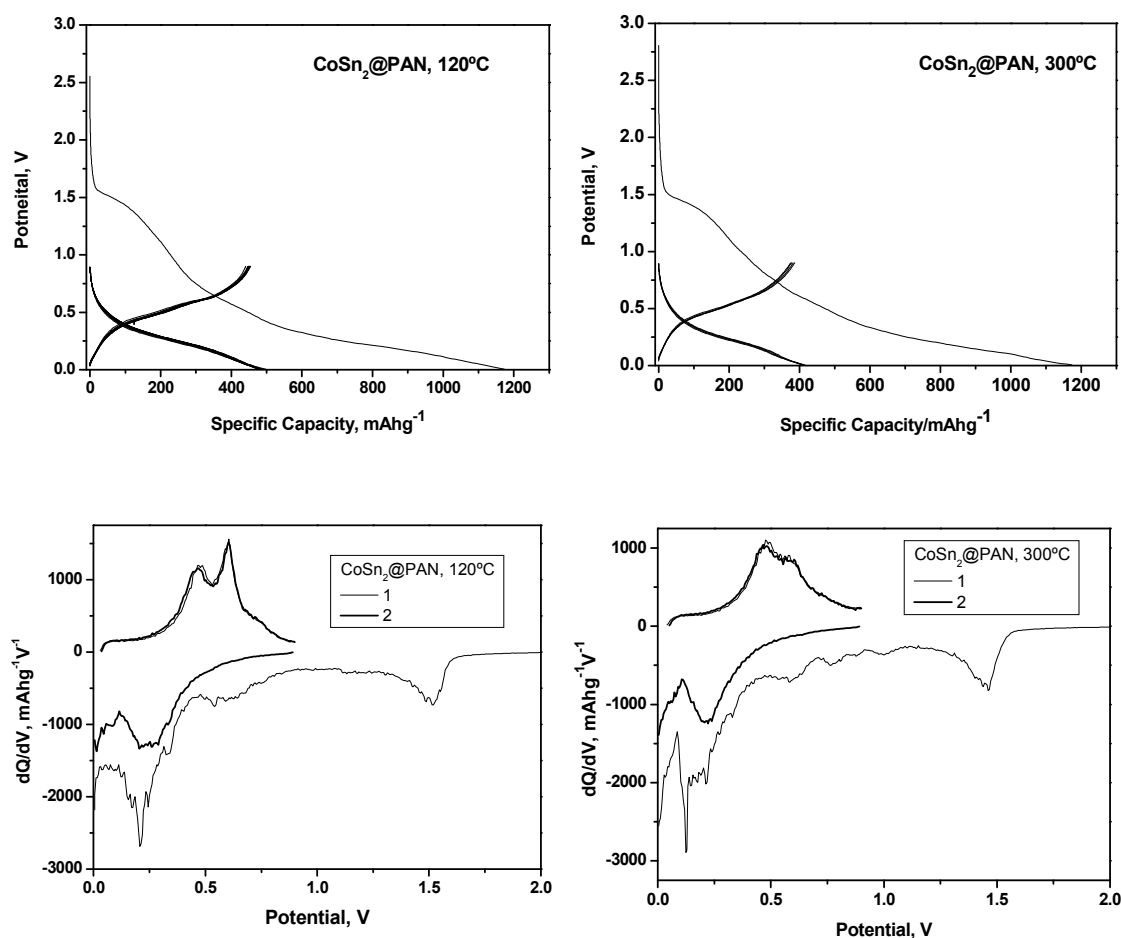
Figure 8. Potential-capacity curves and differential capacity curves for CoSn₂@PAN obtained at 120 and 300ºC. Current intensity: 50 mA/g. Potential window: 0.0-0.9 V.

These results are in line with a reversible extraction of lithium from an amorphous or poorly-crystallized lithium-cobalt-tin alloy. After annealing at 300ºC, the resulting derivative plot exhibits little changes, except a more broadened region in the charge process. The derivative plots of the sample prepared with iron differs from the sample prepared with cobalt. The Fe-Sn-PAN composite electrode shows peaks at 1.1, 0.6, 0.5 and 0.4 V in the first discharge and at 0.5, 0.6, 0.7 and 0.8 V in the first charge (Figure 9). The irreversible peak at 1.1 V is due to reduction of amorphous oxides and formation of surface films, while the other peaks are ascribed to the reversible formation of Li_xSn phases. Apparently, the iron atoms remain electrochemically inactive.

157

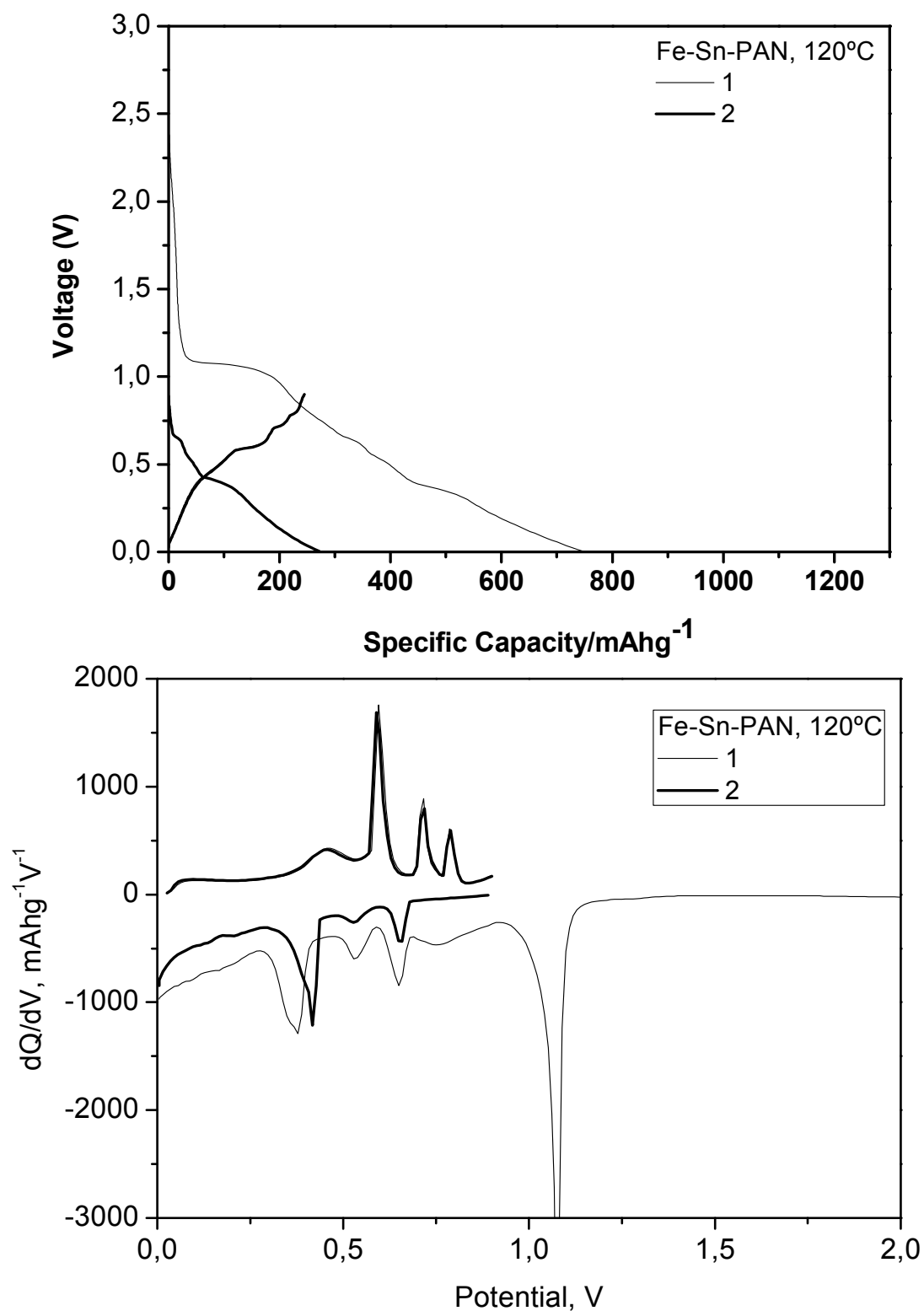**Figure 9. Potential-capacity curves and derivative plots for Fe-Sn-PAN obtained at 120ºC. Current intensity: 50 mA/g. Potential window: 0.0-0.9 V.**

3.2.4 Conclusions

The addition of PAN polymer stabilizes the formation of amorphous Co-Sn alloys throughout reduction of Co(II) and Sn(II) with $NaBH_4$. In contrast, the reduction of Fe(II) and Sn(II) leads to the occurrence of crystalline β-Sn. Amorphous $CoSn_2$@PAN delivers a specific capacity of ca. 480 mAh/g, which is superior to the maximum capacity of graphite. The PAN molecules stabilize the metallic grains and improve the discharge-charge properties. PAN or pyrolyzed PAN may be a component of future commercial lithium ion batteries based on Co-Sn alloys. However, a major drawback of these electrode materials is the initial irreversible capacity. PAN is studied here because it is a versatile polymer that shows a certain tendency to establish interactions with metallic particles and relatively easy denitrogenation when heated, but other polymers may be used in future works.

Acknowledgements

References

1. J.J. Zhang, Y.Y. Xia, J. Electrochem. Soc. 153 (2006) A1466.
2. A.D.W. Todd, R.E. Mar, J.R. Dahn, J. Electrochem. Soc. 154 (2007) A597.
3. R. Alcántara, I. Rodríguez, J.L. Tirado, ChemPhysChem 9 (2008) 1171.
4. C.M. Ionica-Bousquet, P.E. Lippens, L. Aldon, J. Olivier-Fourcada, J.C. Jumas, Chem. Mater 18 (2006) 6442.
5. R. Alcántara, G. Ortiz, I. Rodríguez, J.L. Tirado, J. PowerSources 189 (2009) 309.
6. J. Xie, X.B. Zhao, G.S. Cao, J.P. Tu, J. Power Sources 164 (2007) 386.
7. J.R. Dahn, R.E. Mar, A. Abouzeid, J. Electrochem. Soc. 153 (2006) A361.

8. R. Alcántara, U. Nwokeke, I. Rodríguez, J.L. Tirado, Electrochem. Solid-State Lett. 11 (2008) A209

9. J. Hassoun, S. Panero, G. Mulas, B. Scrosati, J. Power Sources 171 (2007) 928.

10. Q. Fan, P. J. Chupas, M.S. Whittingham, Electrochem. Solid-State Lett. 10 (2007) A274.

11. P.P. Ferguson, R.A. Dunlap, J.R. Dahn, J. Electrochem. Soc. 157 (2010) A326.

12. J.Y. Song, Y.Y. Wang, C.C. Wan, J. Power Sources 77 (1999) 183.

13. J.F. Snyder, E.L. Wong, C.W. Hubbard, J. Electrochem. Soc. 156 (2009) A215.

14. Y.J. Kim, H.J. Lee, S.W. Lee, B.W. Cho, C.R. Park, Carbon 43 (2005) 163.

15. C. Reynaud, C. Boiziau, C.Juret, S. Leroy, J. Perreau, G. Lecayon, Synthetic Metals 11 (1985) 159.

16. Y. Yu, L. Gu, C.B. Zhu, P.A. van Aken, J. Maier, J. Am. Chem. Soc. 131 (2009) 15894.

17. F. Nacimiento, R. Alcántara, J.L. Tirado, J. Electrochem. Soc. 157 (2010) A666.

18. F. Nacimiento, R. Alcántara, J.L. Tirado, J. AlloysCompd. 289 (2009) 135.

19. L.W. Ji, K.H. Jung, A.J. Medford, X.W. Zhang, J. Mater. Chem. 19 (2009) 4992.

20. N. Tamura, M. Fujimoto, M. Kamino, S. Fujitani, Electrochim. Acta 49 (2004) 1949.

21. P. Guilmin, P. Guyot, G. Marchal, Phys. Lett. 109 (1985) 174.

22. J. Jaén, M.L. Varsányl, E. Kovács, I. Czakó-Nagy, A. Buzás, A. Vértes, L. Kiss, Electrochim. Acta 29 (1984) 1119.

23. S. Dalton, F. Heatley, P. M. Budd, Polymer 40 (1999) 5531.

24. S.C. Martin, J.L. Liggat, C.E. Snape, Polymer Degradation and Stability 74 (2001) 407.

25. U.G. Nwokeke, R. Alcántara, J.L. Tirado, R. Stoyanova, M. Yoncheva, E. Zhecheva, Chem. Mater. 22 (2010) 2268.

26. J. Li, D.B. Le, P.P. Ferguson, J.R. Dahn, Electrochim. Acta 55 (2010) 2991.

27. F. Nacimiento, R. Alcántara, J.L. Tirado, J. Electroanal. Chem. 642 (2010) 143.

3.3 Polyacrylonitrile and cobalt-tin compounds based composite and its electrochemical properties in lithium ion batteries

Ricardo Alcántara, Francisco Nacimiento, José L. Tirado

Abstract

A novel composite electrode material has been prepared by an easy and inexpensive route. Nanocrystalline grains of the tin-based phases $CoSn_2$, $CoSn$ and SnO_2 are embedded in an amorphous layer based on the polyacrylonitrile (PAN) polymer. Maximum reversible capacities around 600 mAhg^{-1} are observed. The PAN-based layer and the oxygen atoms contribute to stabilize the intermetallic phases upon electrochemical cycling, thus improving capacity retention. The mechanisms of the reactions are explored by using X-ray diffraction (XRD) and Mössbauer spectroscopy. In the first discharge process, the cassiterite phase is destroyed and amorphous Li_yCoSn_x phases are formed, while some grains of $CoSn$ and $CoSn_2$ remained unaffected. Lithium-tin intermetallic phases are not detected. In the charge process, the segregation of tin-based phases into Co-rich and Co-poor regions takes place.

3.3.1 Introduction

The natural tendency of nanosize particles to agglomerate in order to reduce their surface energy can jeopardize the electrochemical behavior of some electrode materials. The addition of elements, such as oxygen, 3*d*-series transition elements and carbon, to the tin-containing material can be used to improve the electrochemical behavior of the negative electrode for lithium ion batteries. Thus, the elements other than tin are added mainly to try to avoid the formation of large grains of Li_xSn phases and then to help to maintain the electrode integrity upon charge-discharge cycling. Great attention has been addressed towards the Co-Sn-C system, and the role of the carbon and cobalt has been studied [1, 2]. The simultaneous presence of cobalt and carbon seems to be particularly efficient to improve the stability of the tin-based electrodes. The Co-Sn-O system also has deserved certain studies [3]. A great advantage of the tin oxide electrode materials is that very large first discharge capacities might be achieved when the cell operates going from Sn(IV) to Sn(0).

In addition to the chemical composition, the control of the microstructure is another key point. Amorphous or nanocrystalline materials seem to be more adequate as starting compounds than microcrystalline ones. However, the *in-situ* formation of amorphous compounds in the first electrochemical cycle when starting from microcrystalline phases may also lead to improved results. The intimate nanostructure of the particles of the different phases in the composite material should be controlled. An interesting approach is to encapsulate or to form a shell surrounding the particles of the tin-based phase [4-7]. Thus, carbonaceous materials and organic polymers might form a shell or coating that protects the intermetallic grains against the irreversible electrolyte consumption and avoid particle aggregation during cycling.

Due to the different parameters described above, the preparation of composite materials for electrodes with optimized electrochemical behavior can be more difficult than the preparation of pure single phases. The development of easy and economic preparative routes is an important and difficult task. The use of organic polymers and intermetallic phases might be an adequate option. In this work, the preparation of tin-based compounds by chemical reduction and their encapsulation with polyacrilonitrile (PAN) are explored.

3.3.2   Experimental

To obtain tin-based composite electrodes, a Co:Sn=1:2 nominal atomic ratio was used, and the following procedure was carried out. Firstly, 0.1 g of PAN 1 g of $SnCl_2$ and 0.53 g of $CoCl_2.6H_2O$ were added to 50 mL of N,N-dimethylformamide (DMF). All the reagents were supplied by Aldrich. According to the supplier information, the used PAN polymer with formula $[-CH_2CH(CN)-]_n$ has an average molecular weight $M_W=$ 150,000, melting point $T_m=317ºC$, and is soluble in DMF. After stirring for 1 h, 0.8 g of $NaBH_4$ previously dissolved in 5 mL of water were added. Then, 75 mL of water were added. After stirring during one hour, the resulting precipitate was separated by centrifugation and washed with water and absolute ethanol, and finally dried at 120ºC during 1 h under dynamic vacuum. For industrial purposes, the possible toxicity of powdered PAN by inhalation and the toxic gases formed by its combustions (HCN, CO and NH_3) should be taken into account. The solvent DMF also can involve toxicological and environmental risks.

The XRD patterns were recorded in a Siemens D5000 instrument, using 0.04º/2θ –2 s. steps. Transmission electron microscopy (TEM) images of the intermetallic particles were recorded on a JEM-2010 apparatus equipped with a probe for chemical analysis. ^{119}Sn Mössbauer spectra recorded at room temperature in a Wissel instrument and $Ba^{119m}SnO_3$ as a radiation source. The isomer shifts were referenced to $BaSnO_3$ ($δ=$ 0.0 mm s^{-1}). The goodness of the fit was controlled by the classical $χ^2$ test. For the *ex-situ* recording of the XRD patterns and Mössbauer spectra of the electrodes after reaction with lithium, the electrode materials were recuperated from the electrochemical cells and special care was taken to avoid the reaction with air.

The electrochemical experiments were carried out in Swagelok^{TM} lithium test cells and using an Arbin instrument. A piece of Li was used as negative electrode. The positive electrode was constituted by 70% of active material, 10 % of binder (PVDF) and 20% of conductive agent (carbon black). A copper foil was used to support the electrode material. Lithium hexafluorophosphate dissolved in ethylene carbonate:dimethyl carbonate (1:1 wt.) solvents mixture was used as the electrolyte solution. The used current density was 30 mAg^{-1} or, alternatively, 50 mAg^{-1}.

3.3.3   Results and discussion

The XRD pattern of the prepared composite sample (Figure 1c) exhibits broadened reflections that can be ascribed to $CoSn_2$ (ICDD file nº 25-0256), CoSn (ICDD file nº 02-0559) and SnO_2 (ICDD file nº 41-1445). The most intense reflections correspond to $CoSn_2$. The reflections corresponding to the cassiterite phase have the lowest relative intensities, and the reflections corresponding to the hexagonal CoSn phase have intermediate intensities. Pure tin is not observed. Since the starting atomic ratio was Co:Sn=1:2, it seems that a small fraction of the tin atoms are oxidized to tin dioxide.
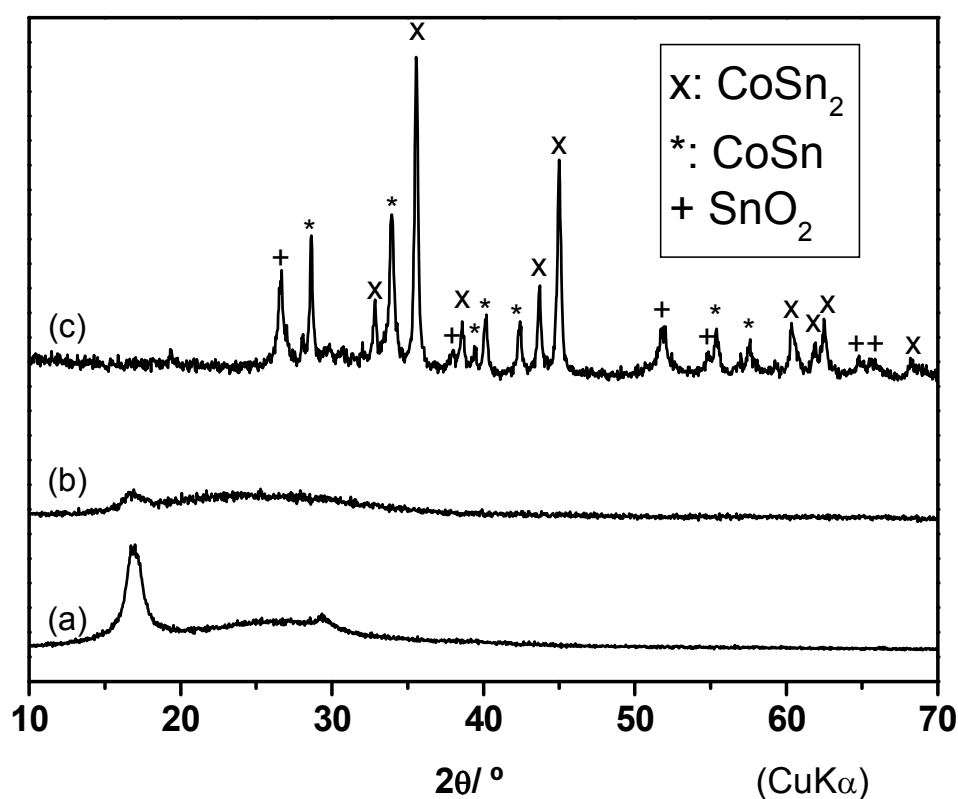
Figure 1. XRD patterns for original PAN (a), PAN treated with NaBH₄ (b) and electrode composite material (c). The significant XRD peaks are indentified.

The crystallite sizes calculated by using the Scherrer equation are the following: $Lc(SnO_2)$= 19 nm, $Lc(CoSn)$= 26 nm and $Lc(CoSn_2)$=29 nm. The reflection that is observed at 16.8º/2θ in the original PAN polymer (Figure 1a) might be due to a poor structural ordering (glass transition temperature T_g=85ºC), and this reflections is no more observed in the composite material (Figure 1c). It was checked that the XRD

pattern of pure PAN was not affected by the thermal treatment under the same conditions (120ºC under vacuum) as expected and, however, the reflection exhibits very low intensity after treatment of pure PAN with great excess of boronhydride (Figure 1b). The broad band at ca. 25º/2θ is typical of amorphous materials. Moreover, the treatment of pure PAN with $NaBH_4$ aqueous solution results in a change of the solid from white to yellowish color. These results clearly show that the PAN polymer suffers a transformation process when treated with boronhydride. The reduction of nitriles can be achieved by reduction with $NaBH_4$ and transition metal chlorides can act as catalyst [8].

In this sense, it has been reported that polyacrylonitrile molecules can be adhered onto metal surface and yield to a pyrolitic carbon film [9]. It was reported that the denitrogenation of PAN due to thermal treatment starts at only 200ºC [10].
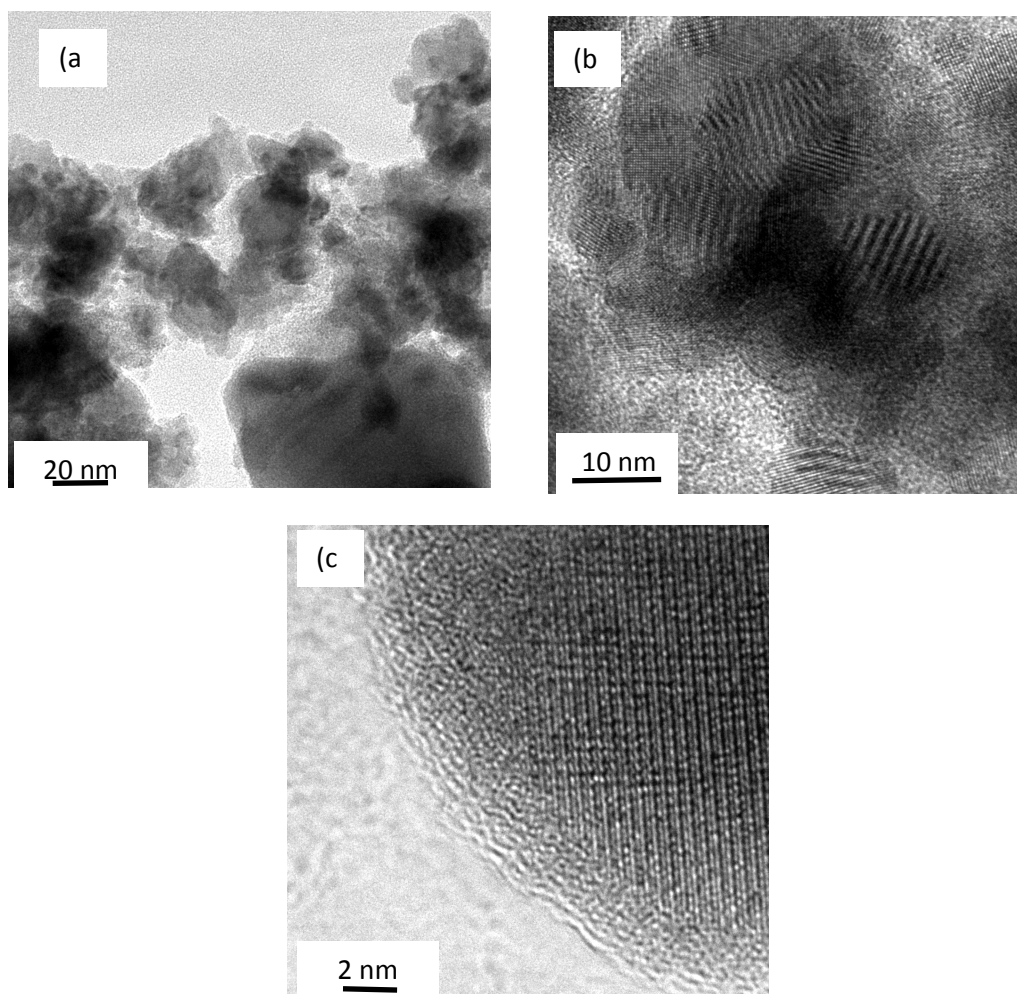

Figure 2. TEM micrographs for electrode composite material.

The chemical transformation of the original PAN polymer due to the treatment with boronhydride and heating under vacuum at 120ªC and the consequent formation of an undetermined amorphous carbonaceous or organic phase is the most probable. On the other hand, other syntheses performed with different relative amounts of the reagents and preparation conditions yielded to composite electrodes that contained no SnO_2. However, the sample that is studied in this work was selected on the basis that a better electrochemical behavior was observed if a small amount of tin oxide was present in the composite electrode. The TEM micrographs (Figure 2a-c) show that the composite sample is mainly constituted by nanocrystalline grains of around 10 nm. These grains contain cobalt and tin atoms which form agglomerates and are embedded in a non-crystalline matrix that does not contain any metallic elements. An amorphous layer with thickness of around 1 nm can be observed in some particles (Figure 2c).
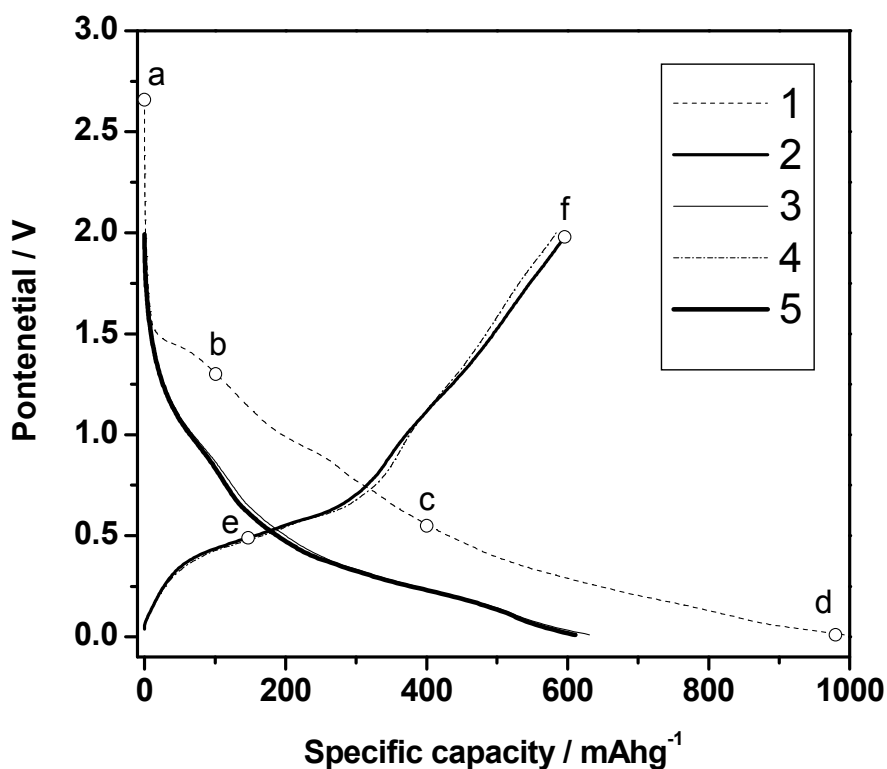

Figure 3. Potential-capacity curves obtained in lithium test cells. The first consecutive sweeps are numbered 1-5 (one discharge-charge cycle corresponds to 2 sweeps). The selected states of discharge (a-d) and charge (e,f) for Mössbauer and XRD studies are labeled.

The electrochemical performance of the composite material constituted by nanocrystalline particles $CoSn_2$, $CoSn$, SnO_2 embedded in a polymer matrix is shown in Figures 3-5. The masses of all the tin-based phases and the PAN polymer are taken into account to calculate the gravimetric capacity. The ability of $CoSn_2$ to react with lithium is quite high and its maximum reported reversible capacity is just below 600 mAh/g [11,12]. The capacity of CoSn is more limited and strongly depends on the grain size [12,13]. The capacity and capacity retention of the cassiterite and other tin oxides is strongly influenced by the imposed potential limits and the grain size [7]. The presence of the PAN-based matrix and the oxygen atoms of the cassiterite might contribute to stabilize the tin phases after reaction with lithium. More specifically, PAN might enhance the stability against the irreversible side reactions in the electrolyte solution and buffer the volume changes upon cycling. The oxygen atoms also can contribute to buffer the volume changes upon charge-discharge cycling. The irreversible part of the first cycle is equals to 395 mAh/g, and is mainly due to the reaction of Li with tin dioxide and with the PAN-based layer. This value would be unacceptable for a commercial use.

In the derivative curve of the first discharge process (Figure 4), irreversible peaks are observed at 1.45, 0.9 and 0.75 V. The irreversible process at 1.45 V is more probably due to the decomposition of the PAN-based matrix after reaction with lithium and/or the formation of a SEI. The peak at 0.9 V can be ascribed to the reduction of Sn(IV) atoms and formation of lithia ($4Li + SnO_2 = 2Li_2O + Sn$). The signals observed in the first discharge process in the ranges between 0.10 and 0.35 V and between 0.0 and 0.1 V are indicative of the presence of cobalt and tin atoms that react with lithium [14]. These signals are also observed in the successive discharges, but are slightly shifted to higher potential. Signals corresponding to large grains of Li_xSn phases at 0.7-0.8 V in the first and successive charge processes are not observed, suggesting that nanoscopic grains of unknown intermetallic phases in the Li-Co-Sn system are reversibly formed. The two broadened peaks observed at 0.45 and 0.6 V in the charge process were previously reported for electrodes containing cobalt and tin [2, 3, 6, 14].
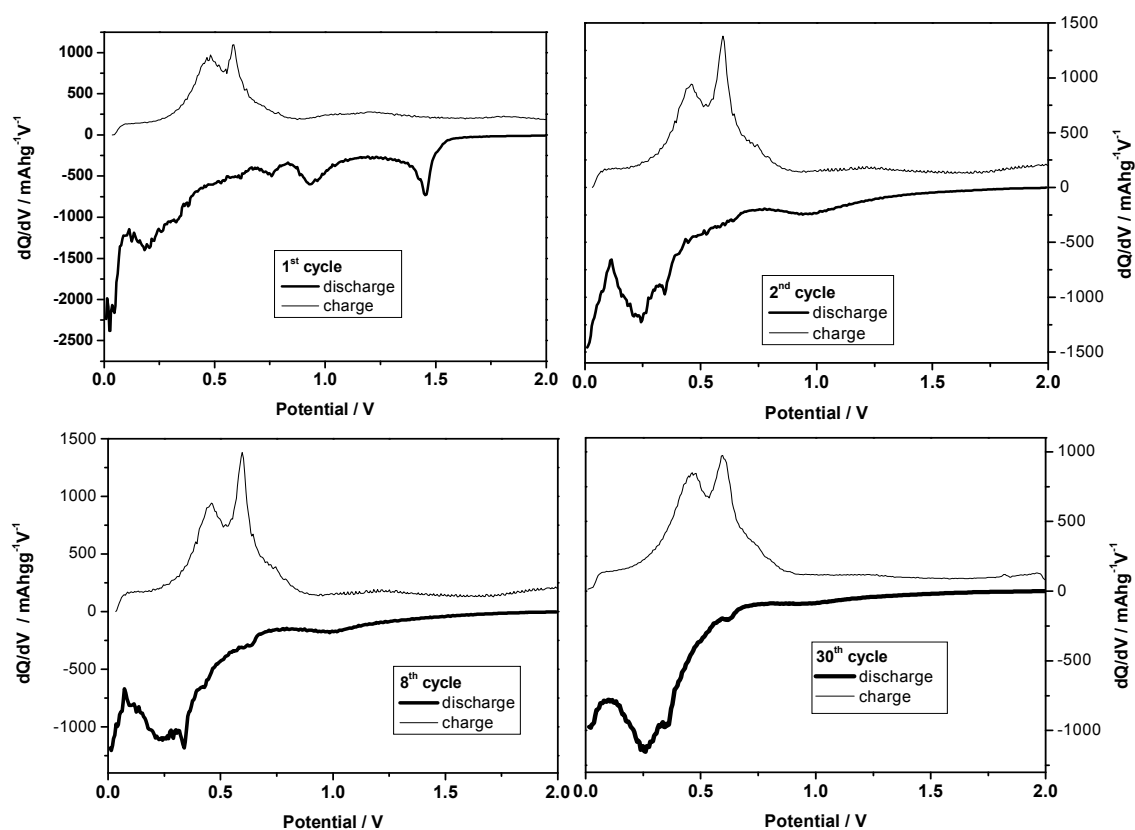
Figure 4. Derivative discharge-charge curves for the cycle number 1, 2, 8 and 30.

These peaks can be due to phase transitions in nanoscopic lithium-tin grains. These features suggest the formation of grains that are poor in cobalt that come from the original tin oxide phase or, alternatively, from the original $CoSn_x$ phase that generates cobalt-poor grains after reaction with Li. The observed behavior for the composite electrode is better than the commonly observed for pure crystalline tin or tin oxide phases. To study the cycling performance, several potential limits were tested (Figure 5A).
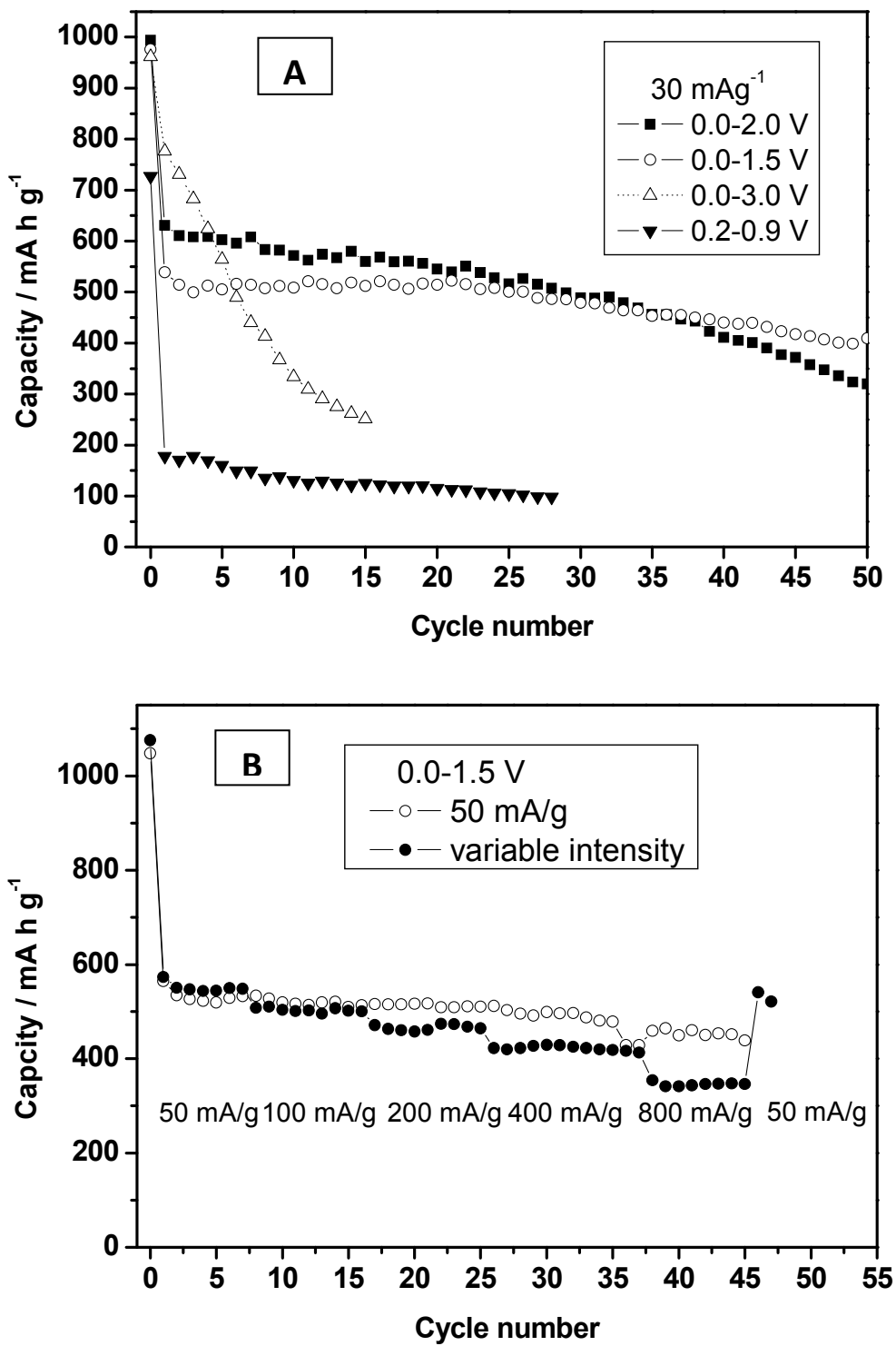
Figure 5. (A) Specific capacity as a function of cycle number at selected potential limits and 30 mA/g of current. (B) Specific capacity as a function of cycle number at 50 mA/g of current, and at variable intensities and 0.0-1.5 V of potential window.

A very low capacity is observed by using a potential window between 0.2 and 0.9 V. The capacity fade is very strong for the largest potential limits of 0.0 and 3.0 V, and the efficiency of the discharge/charge processes is only 90% after 10 cycles. In contrast, the efficiency is 96% at the same cycle number for the 0.0-1.5 potential window. The electrode loses its stability after charging up to 3 V, and we think that this feature can be related with the integrity of the lithia matrix that is formed upon reaction of the SnO_2 minor phase. In fact, we observed that composites electrodes containing exclusively intermetallic phases and PAN, without tin oxide, showed poorer electrochemical performance and rapid capacity fade. Previous studies on Co_2SnO_4 showed that the lithia matrix in this composite electrode disappears above 1.0 V, [3] and this feature can contribute to the capacity fade upon cycling. For the sample studied here, the optimum potential limits are 0.0 V for the lower limit, and 1.5-2.0 V for the upper limit, and reversible capacities between 500 and 630 mAhg^{-1} are observed in the first cycles with quite acceptable stability and efficiencies or around 95-97%.

The values of maximum capacities are superior to the values previously reported for $CoSn_2$ and CoSn single phases [11-13]. The capacity falls down after 30 cycles, while the efficiencies values change from around 97% to 90%, probably due to electrolyte consumption. The observed reversible capacities at higher rates are acceptable (Figure 5B), and the capacity retention is improved.

The *ex-situ* XRD patterns of the electrodes at different levels of the discharge (a-d) and charge (e, f) process are shown in Figure 6A. The diffractions of the relevant phases are marked. Reflections from the copper current collector and the plastic film to avoid any reaction with air are observed. At the beginning of the discharge process (Figure 6Ab) all the phases in the original phase are still detected, and any change of the relative intensity is not detected. Tin dioxide reflections are not observed at 0.0 V (Figure 6Ad).

Figure 6-A XRD of pristine electrode active material (a) and after reaction with Li at selected potentials of the first discharge (b-d) and charge (f). The spectra have been successively shifted in the vertical axis. For further explanation of the notation, see Fig. 2. The XRD pattern labeled as d55 corresponds to an electrode material grafted from the copper support at 0.0 V after 55 cycles.
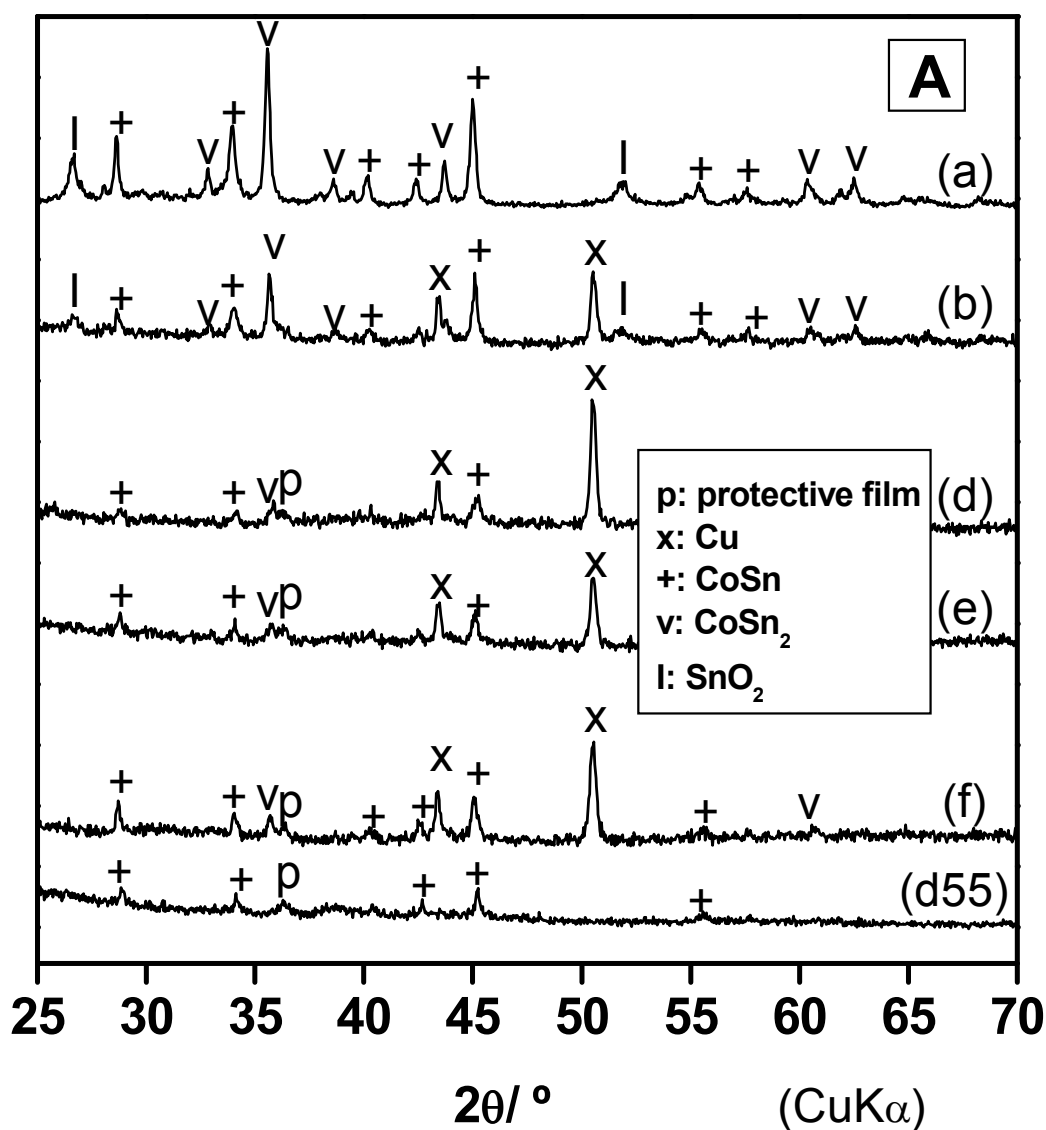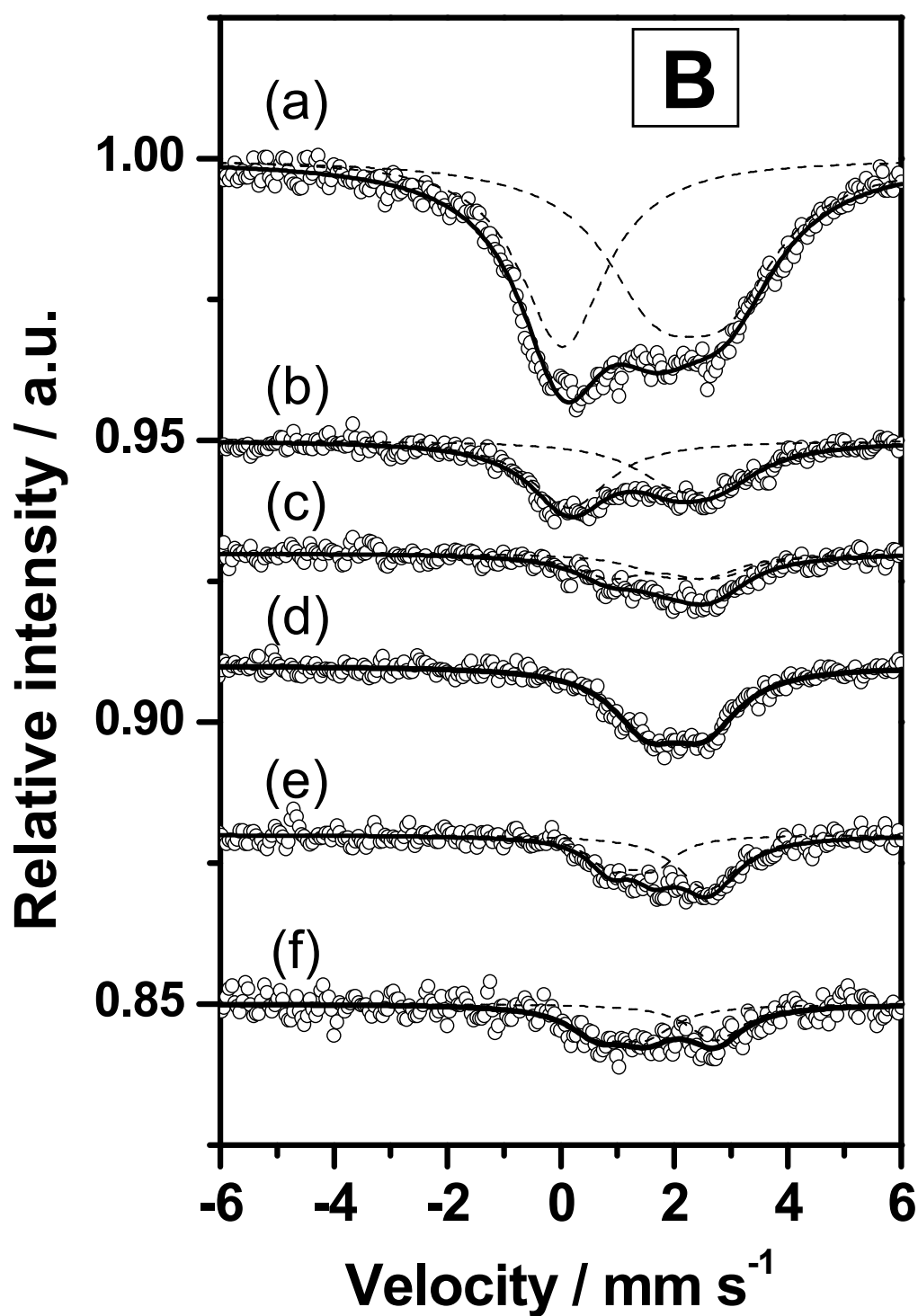
Figure 6-B [119]**Sn Mössbauer spectra of pristine electrode active material (a) and after reaction with Li at selected potentials of the first discharge (b-d) and charge (f).**

Reflections corresponding to CoSn and $CoSn_2$ are still observed at 0.0 V, but the loss of relative intensity is more abrupt for $CoSn_2$. It was previously reported that the coarse particles of hexagonal CoSn exhibit low reactivity towards lithium [13]. Although $CoSn_2$ is more reactive than CoSn towards lithium, some grains of $CoSn_2$ might also remain unreacted, particularly in the case that other phases form an impenetrable skin. Any tin oxide, pure tin or Li_xSn phases are not observed. Henceforth, the products of the reaction of the composite electrode with lithium are XRD-undetectable. Very probably, unknown Li_yCoSn_x phases are formed. After 55 cycles in the range between 0.0 and 2.0 V, the electrode recuperated at 0.0 V (Figure 5A d55) only shows reflections corresponding to CoSn. This involves that all the grains of $CoSn_2$ have reacted with lithium, and that Li_xSn grains do not appear in the discharge state. After a discharge-charge process up to 0.5 or 2 V, the resulting XRD patterns (Figure 6A e,f) still exhibit low-intensity reflections corresponding to CoSn and $CoSn_2$, while tin oxides, lithium-tin intermetallic phases and pure tin are not observed. The relative contribution of the CoSn phase is higher after a complete discharge-charge cycle, indicating the stability of this phase.

We have used the [119]Sn Mössbauer spectroscopy to further study the mechanism of the electrochemical reaction. The spectra are shown in Figure 6B and the fitting results are shown in Table 1. The spectrum of the original composite material before reaction with lithium is much broadened. The contribution of XRD-undetectable $CoSn_x$ phases with x<1 cannot be discarded. Two signals were used for the fitting. However, the use of more signals for the fitting may artificially lower the apparent goodness of fit without a real physical meaning.

Due to the higher Lamb-factor of the SnO_2 in comparison with the intermetallic phases, the relative contribution to the spectrum of the minor phase SnO_2 is enhanced in the region near 0.0 mm/s. The region of the spectrum centered at 2.3 mm/s represents the situation of several tin atoms in the $CoSn_x$ compounds. Irrespectively of the low intensity, after discharging down to 1.3 V (Figure 6Bb), the broadened spectrum has suffered little changes. This confirms that the electrochemical capacity from 3 to 1.3 V is mainly due to reaction of the PAN-based amorphous phase and formation of a SEI, although some contribution of lithium reaction with $CoSn_2$ cannot be completely

discarded. After the reaction with lithium at lower potential, the contribution of Sn(IV) atoms disappears. At 0.5 V of the first discharge process, the contribution of Sn(IV) is not detected, while two signals probably due to unknown Li_yCoSn_x phases with different amounts of lithium [2] are observed. Henceforth, the reduction of Sn(IV) to Sn(0) stars below 1.3 V, and is completed at 0.5 V. These results confirm that the peak at 0.9 V in the derivative discharge curve can be due to the reduction of tin dioxide. The spectrum corresponding to the electrode discharged down to 0.0 V can be fitted with a doublet signal centered at 2.04 mm/s that represents the average situation of amorphous Li_yCoSn_x and unreacted crystalline phases. This former isomer shift value is significantly lower than the corresponding to β-Sn (δ=2.55 mm/s), but higher than the corresponding to fully lithiated tin [12].

Table 1. **Fitting hyperfine parameters of ^{119}Sn Mössbauer measurements for pristine material (a), and electrodes recuperated from lithium cells in the discharge (b-d) and re-charge (e,f) states. For further explanation of the notation, see Fig. 3. As a reference, the parameters reported in the literature for pure phases are given.**

Notation	^{119}Sn Mössbauer						
	δ	Δ	Γ	C	χ^2	A	
	2.559(3)	0.0	1.022(9)				β-Sn [15]
	2.25(2)	1.12(3)	1.38(5)	67			nano-CoSn₃ [16]
	1.21(4)	2.03(5)	1.382(3)	33			
	2.14(5)	0.77(9)	0.96(2)	100			CoSn₂ [8]
	1.854(6)	1.60(1)	0.99(1)	67			CoSn [10]
	2.03(1)	3.14(2)	0.94(2)	33			
a	0.04(3)	0.00	1.85(8)	40	0.5	4.5	SnO₂
	2.29(5)	1.24(6)	2.3(1)	60			CoSn$_x$
b	0.16(3)	0.00	1.67(1)	50	0.5	1.7	SnO₂
	2.38(8)	0.8(1)	1.8(2)	50			CoSn$_x$
c	1.7(1)	1.6(2)	1.5(2)	56	0.5	1.3	Li$_y$CoSn$_x$
	2.3(2)	0.9(2)	1.5(4)	44			CoSn$_x$
d	2.04(3)	1.02(4)	1.49(8)	100	0.5	2.0	Li$_y$CoSn$_x$
e	2.59(4)	0.00	1.3(1)	57	0.6	1.6	Sn
	1.3(1)	0.8(1)	0.9(1)	43			CoSn$_x$O$_y$
f	2.73(7)	0.00	1.2(2)	39	0.6	1.5	CoSn$_x$ (Co-poor)
	1.1(1)	0.8(1)	1.2(2)	61			CoSn$_x$O$_y$

δ: isomer shift (mm s⁻¹). Δ: quadropole splitting (mm s⁻¹). Γ: line width (mm s⁻¹).
C: relative contribution (%). χ^2: goodness of the fit. A: absorption (%).

No segregation of the composite electrode into distinguishable phases at 0.0 V is detected in the Mössbauer spectrum. All these observations agree well with the simultaneous interaction of the tin atoms with more electropositive elements such as cobalt and lithium [2, 12]. The results evidence the formation of a stable Li_yCoSn_x metallic glass (or amorphous alloy). After complete discharge to 0.0 V and partial re-charge to 0.5 V, the resulting spectrum (Figure 6Be) shows an asymmetric broadening and can be fitted with two signals. The signal located at lower isomer shift increases its relative intensity when the charge voltage increases from 0.5 to 2.0 V. Irrespectively that the spectrum which results after re-charge up to 2 V exhibits low intensity, it is observed that the original spectrum is not recuperated. In contrast to the corresponding XRD patterns, the resulting Mössbauer parameters at 0 (discharge state) and 2 V (re-charge state) are different. This clearly shows that unknown phases that remain XRD-undetected are formed at 2 V, and thus the fitting of the Mössbauer spectrum cannot be unique. In this case, the useful information can be obtained from the average isomer shift of the whole spectrum. In the charge state at 2 V, the average isomer shift is lower than the corresponding to pure tin [15], Li_xSn phases [15], hexagonal CoSn [13], $CoSn_3$ [16] and $CoSn_2$ [11], and this can indicate some interaction between tin and oxygen atoms. To support this hypothesis, it is worth to note that some authors reported that prior to the maximum extraction of lithium from previously lithiated tin oxide, unusual species of tin-oxygen were found by using Mössbauer spectroscopy [17, 18]. Alternatively, interactions between tin and carbon atoms can slightly reduce the isomer shift [2]. The spectrum at 2 V was fitted with two signals. One doublet signal at 1.1 mm/s is ascribed to a mixture of unknown amorphous $CoSn_x$ phases that interact with oxygen atoms (named as $CoSn_xO_y$) and unreacted CoSn and $CoSn_2$ phases. The interactions of tin atoms with oxygen atoms decrease the isomer shift. One singlet signal at around 2.7 mm/s is due to XRD-undetectable tin, probably containing some dissolved cobalt atoms that induce the amorphous character. These tin atoms are represented as "$CoSn_x$ (Co-poor)" in Table 1. Since the signal from Sn (IV) is not observed, it is expected that the lithia matrix be partially preserved at this voltage. Henceforth, the recuperation of Sn (IV) is discarded for the composite electrode charged at 2 V, but it seems that tin atoms interact with cobalt and oxygen atoms and form amorphous $CoSn_x$-O_y particles, and that Co-poor tin grains have been segregated during the charge process. The PAN-based matrix can contribute to stabilize these $CoSn_x$-O_y particles.

3.3.4   Conclusions

A composite electrode constituted by nanosize particles of tin intermetallics (mayor phases) and tin dioxide (minor phase) embedded in a PAN polymer matrix has been prepared. Maximum reversible capacities of around 600 mAh/g can be achieved with this electrode in lithium cells. In the first steps of the discharge, electrons are consumed for irreversible reactions such SEI formation. Secondly, tin dioxide is reduced and lithia is formed. Finally, further lithium reacts with tin and tin-cobalt phases to form a metallic glass (amorphous alloy). After a discharge-charge cycle, Sn(IV) atoms do not reappear at 2 V, but interactions of tin atoms with cobalt and oxygen are envisaged, and segregation into different phases is detected. The polymer and oxide phases can contribute to stabilize the intermetallic phases.

References

1. P.P. Fergusson, J.R. Dahn, Electrochem. Solid State Lett. 11 (2008) A187.

2. G.F. Ortiz, R. Alcántara, I. Rodríguez, J.L. Tirado, J. Electroanal. Chem. 605 (2007) 98.

3. R. Alcántara, G.F. Ortiz, P. Lavela, J.L. Tirado, Electrochem. Comun. 8 (2006) 731.

4. K.T. Lee, Y.S. Jung, S.M. Oh, J. Am. Chem. Soc. 125 (2003) 5652.

5. X. He, W. Pu, L. Wang, J. Ren, C. Jiang, C. Wan, Solid State Ionics 178 (2007) 833.

6. H. Kim, J. Cho. Electrochim. Acta 52 (2007) 4197.

7. G.F. Ortiz, R. Alcántara, J.L. Tirado, Electrochem. Solid State Lett. 10 (2007) A286.

8. S. Caddick, D.B. Judd, A.K. de K. Lewis, M.T. Reicha, M.R.V. Williams, Tetrahedron 59 (2003) 5417.

9. S. Leroy, C. Boiziau, G. Lécayon, G. Le Gressus, M. Makram, J.P. Vigouroux, Materials Letters 3 (1985) 239.

10. C. Reynaud, C. Boiziau, C. Juret, S. Leroy, J. Perreau, G. Lecayon, Synthetic Metals 11 (1985) 159.

11. C.M. Ionica-Bousquet, P.E. Lippens, L. Aldon, J. Olivier-Fourcade, J.C. Jumas, Chem. Mater. 18 (2006) 6442.

12. R. Alcántara, G. Ortiz, I. Rodríguez, J.L Tirado, J. Power Sources 189 (2009) 309.

13. R. Alcántara, I. Rodríguez, J.L. Tirado, ChemPhysChem 9 (2008) 1171.

14. J.R. Dahn, R.E. Mar, A. Abouzeid, J. Electrochem. Soc. 153 (2006) A361.

15. R.A. Dunlap, R.A. Small, D.D. MacNeil, M.N. Obrovac, J.R. Dahn, J. Alloys Compd. 289 (1999) 135.

16. R. Alcántara, U. Nwokeke, I. Rodríguez, J.L. Tirado, Electrochem. Solid-State Lett. 11 (2008) A209.

17. I. Sandu, T. Brousse, D.M. Schleich, M. Danot, J. Solid State Chem. 179 (2006) 476.

18. J. Chouvin, C. Branci, J. Sarradin, J. Olivier-Fourcade, J.C. Jumas, B. Simon, Ph. Biensan, J. Power Sources 81-82 (1999) 277.

3.4 PAN-encapsulated nanocrystalline CoSn$_2$ particles as negative electrode active material for lithium-ion batteries

Francisco Nacimiento, Ricardo Alcántara, José L. Tirado

Abstract

Composite electrodes have been prepared throughout the reduction of tin and cobalt ions in the presence of polyacrylonitrile (PAN). The resulting product consists of tin-cobalt intermetallic nanoparticles surrounded by a PAN-based shell, the main intermetallic phase being nanocrystalline CoSn$_2$. The organic molecules prevented the growth of the intermetallic grains upon annealing and formed an amorphous carbon layer. The observed maximum reversible capacities are around 600 mAh/g. Excellent capacity retention has been achieved for PAN-CoSn$_2$ composite electrodes.

3.4.1 Introduction

The addition of different elements, such as 3*d*-series transition metals and carbon to the tin-containing electrode, has been found useful to improve the electrochemical behavior in lithium ion batteries. The system Co-Sn-C is particularly promising [1, 2]. Cobalt has great ability to form small particles and amorphous phases with tin [3]. Carbon-containing composites show improved particle connectivity [4], buffer the volume change upon cycling [4] and avoid particle growth upon cycling [5]. On the other hand, nanostructuring also buffers the abrupt volume changes of the electrode due to reaction with Li [6], reduces cracking within the electrode [7] and Li-ion diffusion lengths [8], and improves of the electrochemical performance of the alloys [7, 9, 10]. For tin-coated graphite ("core-shell" structures), the graphite phase acts as a lithium intercalation site and also plays the role of a buffer to the metal volume expansion [11]. Besides composition and particle size, a strict control over the space distribution of the different phases is also relevant for the electrochemical performance. The encapsulation of Li-alloying element within a carbonaceous or organic phase might be an adequate option, and many efforts have been done in this field [12-17]. In turn, a non-metallic shell might contribute to stabilize the particle of the tin-based phase. Very recently, endohedral tin nanoparticles encapsulated in bamboo-like hollow carbon nanofibers prepared by using pyrolysis of coaxially electrospun nanofibers were studied [4].

In this work, the encapsulation of nanocrystalline $CoSn_2$ with an organic polymer is studied. For this purpose, polyacrylonitrile (PAN) has been selected.

3.4.2 Experimental

The Co-Sn-PAN composites were prepared as follows. Firstly, 4.0 g of $SnCl_2 \cdot 2H_2O$, 1.0 g of polyacrylonitrile (PAN) and 2.1 g of $CoCl_2 \cdot 6H_2O$ were added into 250 mL of n,n-dimethylformamide (DMF) with continue stirring. Secondly, 3.6 g of $NaBH_4$ previously dissolved in 25mL of H_2O were added. Then, 350 mL of water were added. The resulting Co-Sn-PAN precipitate was separated by centrifugation and rinsed with water. The composite was annealed at 120ºC under vacuum, and between 300 and 600ºC under Ar flow (60 mL/min). In addition, another sample with a lower initial PAN-content (0.6 g) was prepared by following the same experimental procedure.

For comparison, $CoSn_2$ was prepared by using the same procedure but without addition of PAN. X-ray diffraction (XRD) diagrams were recorded in a Siemens D5000 instrument with CuKα radiation. Elemental analysis was carried out in a Scanning Electron Microscope (SEM) JSM-6300 instrument equipped with an energy dispersive x-ray analyzer (EDAX). The carbon and nitrogen content was determined by using an elemental analyzer Eurovector EA3000. Transmission electron microscopy (TEM) images were recorded on a JEM-2010 apparatus equipped with elemental analysis device. ^{119}Sn Mössbauer spectra were registered at room temperature in a Wissel instrument, using a Ba^{119}SnSO$_3$ source, and BaSnO$_3$ as a reference (isomer shift δ=0.0 mm/s).

The electrochemical experiments were carried out in lithium test cells, using a piece of Li as negative electrode. The positive electrode contained the Co-Sn-PAN composite (80%), and polyvinylidene (PVDF, 15%) and carbon black (5%) as additives. Alternatively, 70% of active material, 15% of PVDF and 15% of carbon were used. A copper foil supplied by Goodfellow was used to support the electrode. The electrolyte was 1 M LiPF$_6$ in ethylene carbonate:diethyl carbonate solvents mixture. An Arbin instrument was used in the galvanostatic discharge-charge cycles.

Electrochemical impedance spectroscopy (EIS) measurements of the electrodes were carried out at 5 mV ac amplitude using an Autolab instrument and three-electrode cells. A Li-piece was used as counter electrode and another piece of Li was used as reference-electrode. The tin-containing electrode was used as working electrode. The spectra were recorded at different cycle numbers in the discharge state (0.0 V) and after a relaxation period. The impedance values were normalized by multiplying them by the electrode active mass, and the spectra were represented in Ohm·g units.

3.4.3　Results and discussion

The XRD pattern of the composite sample annealed at 120ºC exhibits broadened reflections (Figure 1-A). Reflections corresponding to PAN, Co, SnO$_2$, SnO and Sn are not detected. Reflections that can be ascribed to nanocrystalline $CoSn_2$ (XRD file nº 25-0256) and CoSn (XRD file nº 2-559) intermetallic phases are observed. Most probably, poorly crystallized or amorphous Co-Sn alloys are also formed that remain XRD-

undetected. Cobalt and tin have a great ability to form $CoSn_x$ amorphous alloys. In addition, the presence of XRD-amorphous oxides cannot be discarded.
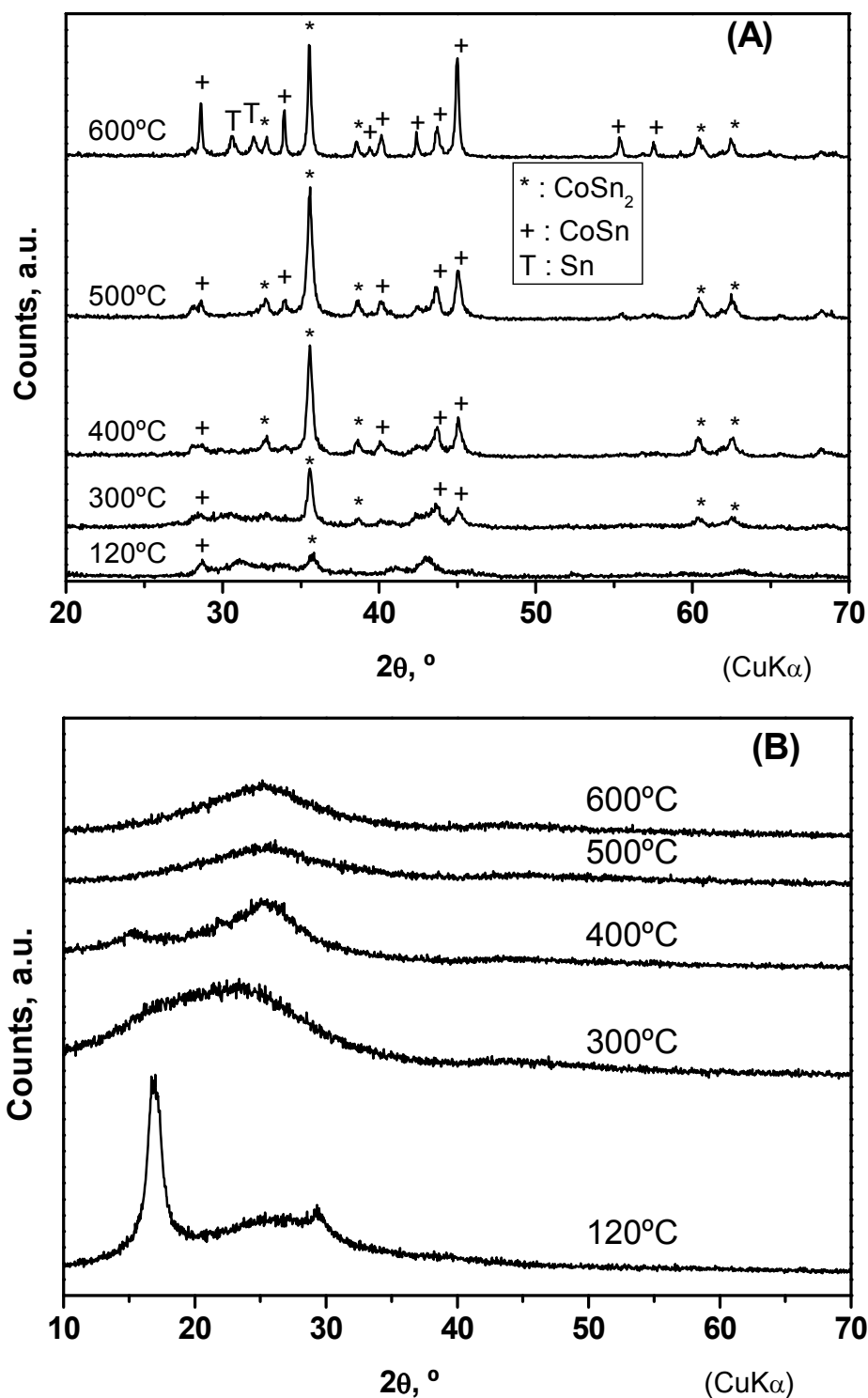

Figure 1. (A) XRD patterns of $CoSn_2$@PAN samples annealed in the range between 120 and 600ºC. (B) XRD patterns of PAN samples annealed in the range between 120 and 600ºC.

The peak at ca. 17º/2θ corresponding to the packing arrangement of the PAN chains [18] is not observed, probably due to the dispersion of the organic molecules caused by the chemical treatment with $NaBH_4$ solution. The annealing of pure PAN at 300ºC under Ar-flow leads to the formation of an amorphous carbonaceous phase that exhibits a broad band between ca. 15 and 30º/2θ in the XRD pattern (Figure 1-B). The pyrolysis of PAN has been studied by many authors, and temperatures between 200 and 300ºC were reported for the denitrogenation process [19, 20]. PAN exhibits the ability to interact with metallic surfaces, together with an easy denitrogenation [19]. After annealing at 400ºC, the observed broad signals centered at ca. 15 and 24º/2θ are typical of carbon materials containing unorganized carbon and turbostratic carbon [21, 22]. The samples pyrolysed at 500-600ºC show a broad band at ca. 24º/2θ. This region corresponds to the (002) Bragg peak of graphite, and the diagrams are typical of non-graphitized or turbostratic materials. The XRD reflections of the tin-based phases become narrower and more intense after annealing at 300ºC (Figure 1-A). This feature supports the hypothesis that non-crystalline Co-Sn alloys are formed at 120ºC. The main reflection corresponds to the $CoSn_2$ phase, and the average crystallites size calculated by using the Scherrer equation is 50 nm at a preparation temperature of 300ºC.

Increasing the annealing temperature up to 600ºC leads to the occurrence of reflections ascribable to pure β-Sn, while the reflections of hexagonal CoSn become relatively more intense. This involves that $CoSn_2$ is thermally decomposed into CoSn and Sn, this being in agreement with the phase diagram of the Co-Sn system [23]. The relative amounts of the crystalline phases were quantified by using the XRD patterns and the method of controlled additions [24]. For this purpose, a reference material (commercial Sn or prepared CoSn) is added to the sample in known proportion and the relative intensities of the XRD reflections are measured. By repeating the procedure with different amounts of the reference material (S-internal standard), the concentration of the S-phase in the original sample is extrapolated. Thus, in the sample obtained at 600ºC the relative masses are: $CoSn_2$ 68%, CoSn 20% and Sn 12%. The poor crystallinity of the phases makes difficult the quantification in the samples prepared at lower temperatures. The carbonaceous-based layer obtained from the PAN

molecules remains XRD-undetectable. On the other hand, the preparation of samples with a lower relative amount of PAN leads to the occurrence of XRD-detectable tin dioxide, as described elsewhere [17]. It seems that the encapsulation with a high concentration of PAN prevents against an extended oxidation of the intermetallic phases in air or, alternatively, the tin dioxide particles remain very small. The very broadened [119]Sn Mössbauer spectra (not shown) in the range of isomer shift values between -1.0 and +4 mm/s are in agreement with the occurrence of Sn(IV) atoms and several intermetallic tin phases [17, 25]. In addition, the PAN molecules surrounding the intermetallic particles prevent grain growth in some extension, and the XRD-reflections tend to remain relatively broadened after annealing (Figure 1A).

The elemental analysis carried out in a SEM apparatus equipped with EDS detector showed a Sn/Co atomic ratio of 2.0(3) for the samples obtained between 120 and 600ºC. The relative amount of carbon and nitrogen was determined by using a C-N analyzer instrument and the results are shown in Table 1. As a reference, the results for pure PAN treated at several temperatures and $CoSn_2$ obtained without PAN are also shown.

Table 1. Results of the elemental analysis expressed as percentage in mass.

	C-N analysis					
	$CoSn_2$@PAN					$CoSn_2$
	120ºC	300ºC	400ºC	500ºC	600ºC	120ºC
C	11.7	12.4	11.6	13.4	12.3	0.1
N	4.0	3.7	3.1	3.8	3.4	-
	PAN					
C	67.5	65.0	65.5	60.4	71.1	
N	24.7	20.4	17.4	14.7	-	

PAN content in the composite sample obtained at 120ºC is around 16.5 % by mass. Tin content is ca. 67 %. The PAN-containing samples annealed at higher temperatures exhibit higher carbon to nitrogen ration, due to the pyrolysis process, although the carbonization process is not completed in the samples prepared in the range between 120 and 600ºC. Selected TEM micrographs of the Co-Sn-PAN

composite after annealing at 300ºC and the X-ray spectra at selected regions are shown in Figure 2. It is observed that an amorphous carbon-based layer, which is free of Co and Sn, encapsulates nanocrystalline grains of $CoSn_2$. Henceforth, these samples can be represented as $CoSn_2@PAN$. Copper peaks from the TEM grid are also observed
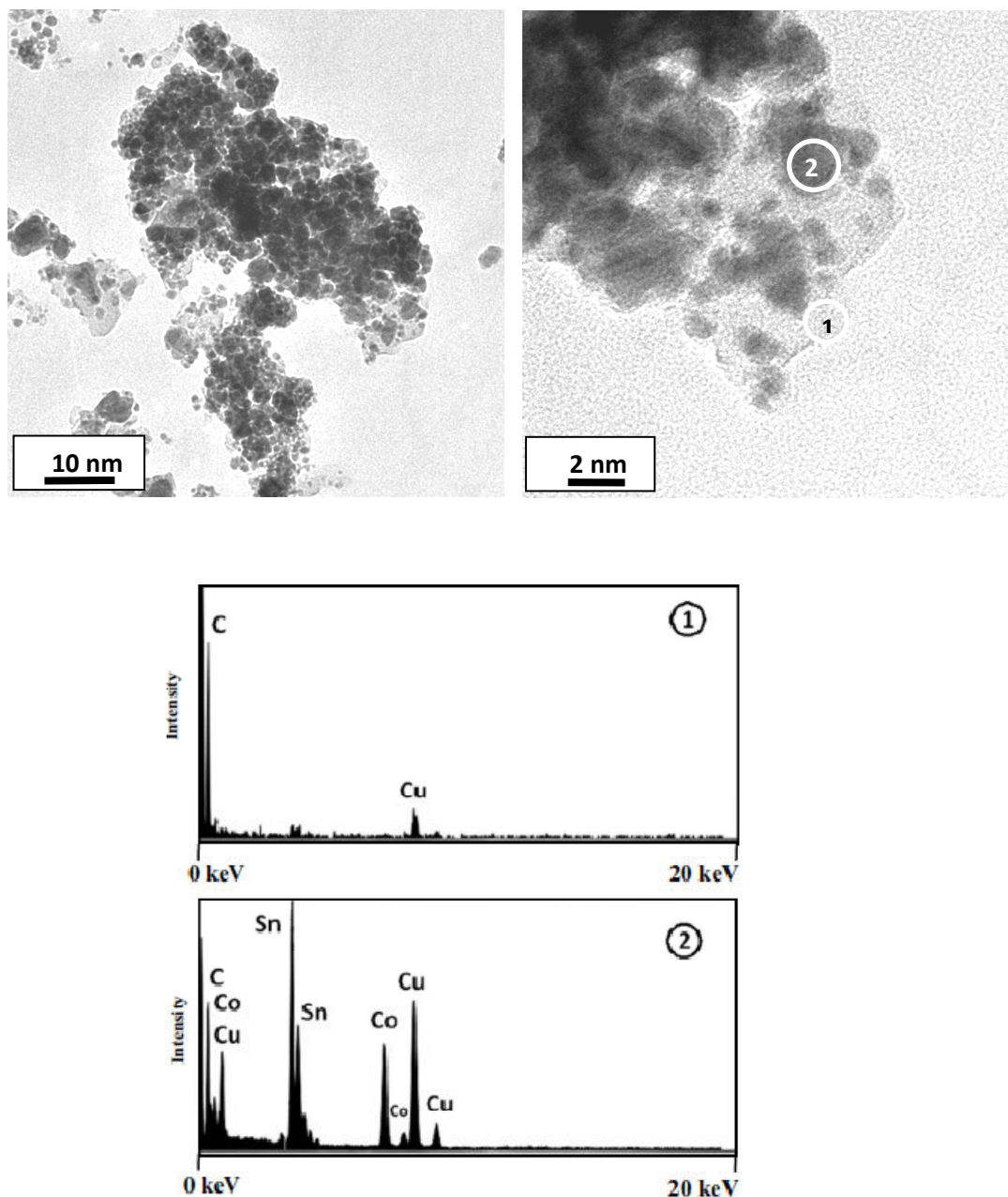

Figure 2. TEM images of $CoSn_2@PAN$ annealed at 300ºC. The corresponding X-ray spectra are shown for the marked regions 1 (carbonaceous layer) and 2 (Co-Sn core).

The CoSn$_2$@PAN active electrode materials prepared at 120 and 300ºC exhibit maximum specific capacities values around 600 mAhg^{-1} in the first few cycles (Figure 3).
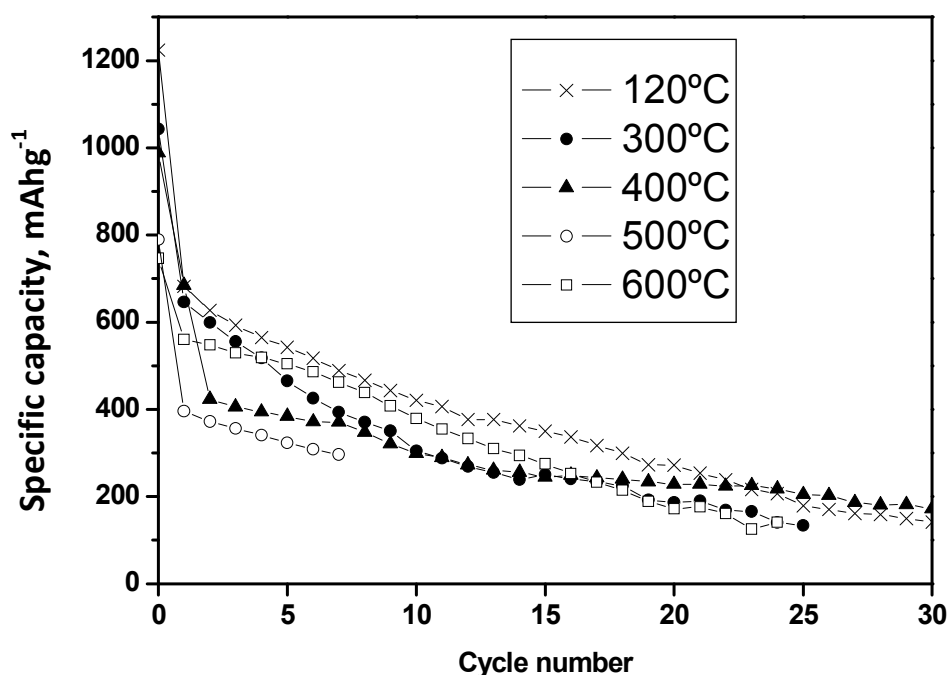

Figure 3. Specific capacity as a function of cycle number for CoSn2@PAN prepapred in the range between 120 and 600ºC. Active material: 80%. Potential range: 0.0-2.0 V. Intensity: 50 mA/g.

All the atoms in PAN and the intermetallic phase are taken into account to calculate the specific capacity. This capacity value is equivalent to ca. 900 mAhg^{-1} as refereed only to the mass of tin atoms, and this value is slightly below the maximum theoretical capacity for a pure tin electrode (993 mAhg^{-1} for a Li$_{22}$Sn$_5$ limit composition). When the annealing temperature is increased from 120 to 500ºC, the initial capacity is decreased, most probably due to the crystallization process of the CoSn$_x$ alloys. The bad cycle performance of the sample obtained at 300ºC in comparison with the sample obtained at 120ºC (Figure 3) would be related to the increase of the grain size of the intermetallic phases, as can be seen in the XRD pattern (Figure 1A). After further annealing up to 600ºC, the capacity slightly increases due to the occurrence of pure β-Sn. The capacity retention is poor in all the cases when 80 % of active material and 0-2.0 V of potential range are used. Much better electrochemical cycling is observed when using electrodes with 70 % of active material and 0-1.5 V of

potential range (Figure 4-top). Most probably, the 5 % of added carbon black is below the percolation limit. As expected, the potential-capacity curves (Figure 4-bottom) differ from those previously observed for pure $CoSn_2$ with micrometric particle size [26, 27], and the reversible capacity is higher for $CoSn_2$@PAN.

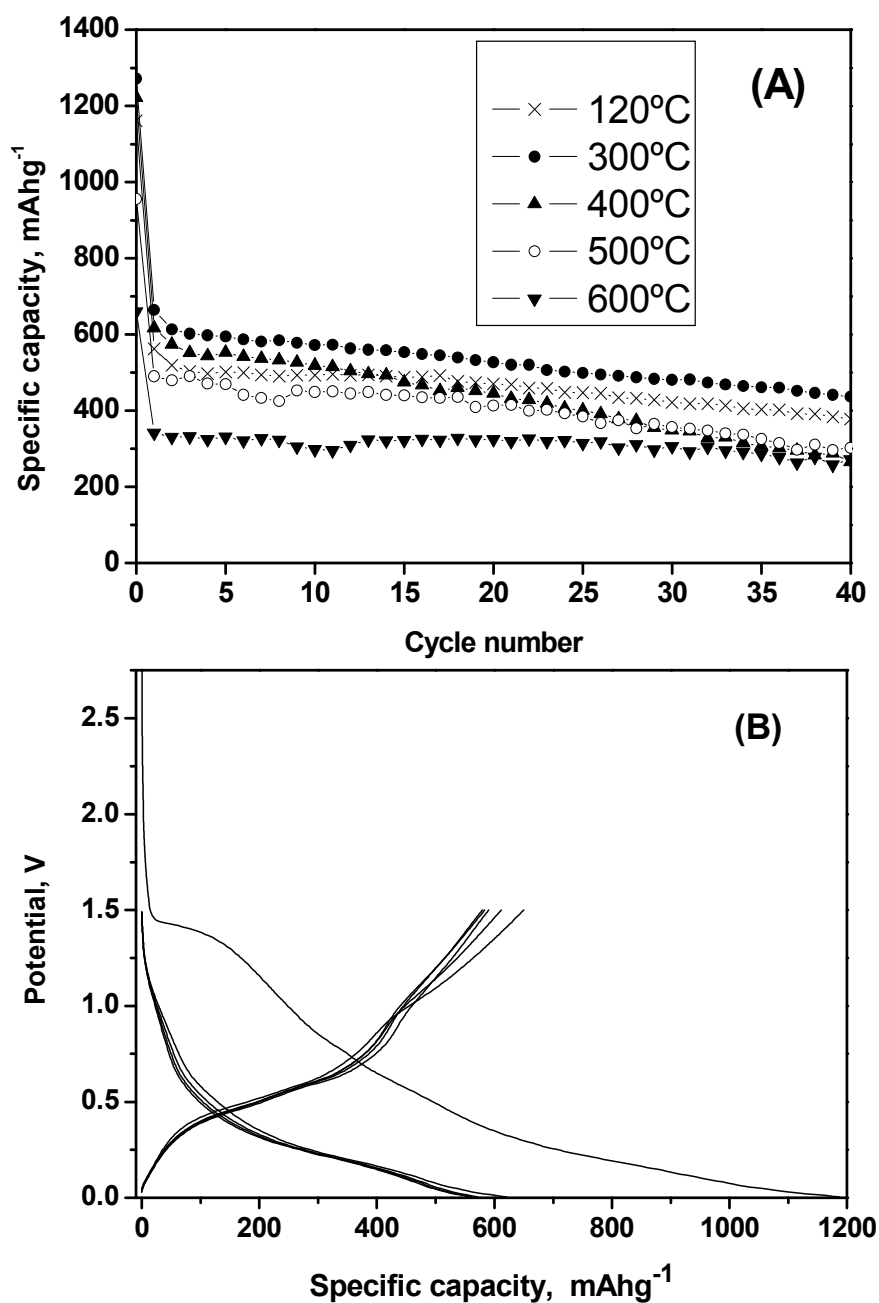**Figure 4. (A) Specific capacity as a function of cycle number for $CoSn_2$@PAN prepared at 120-600ºC. (B) potential vs. specific capacity for $CoSn_2$@PAN prepared at 300ºC. Active material: 70%. Potential range: 0-1.5 V. Intensity: 50 mA/g .**

The nanometric character of the $CoSn_x$ intermetallic phases, and the occurrence of tin dioxide can contribute the high capacity values. In this way, it was reported that nanosized CoSn particles exhibit higher capacity than microsized CoSn particles [28], and that amorphous Co_3Sn_2 particles show high capacities while crystalline Co_3Sn_2 is inactive against lithium [29, 30]. According to Yu et al., the nanostructured metallic particles shorten the transport lengths for both electrons and lithium ions [4]. On the other hand, a nanoscopic phase leads to intensified surface reactions and high irreversible capacity [31]. Below 1.2 V, most of the lithium would be extracted from Li_yCoSn_x and Li_xSn phases [8, 9]. The capacity observed at around 1.2 V in the charge process is mostly due to the extraction of lithium from the Li_2O matrix, which is previously formed by reaction of XRD-undetected tin oxide with lithium [31]. The $CoSn_2$@PAN electrode shows much better capacity retention than the usually observed for pure SnO_2 [32]. The carbonaceous phase (ex-PAN) may contribute to create a more stable electrode/electrolyte interphase. The intermetallic particles may suffer swelling, cracking and formation of new surfaces that form new solid electrolyte interphase upon cycling [33]. In the case of carbon materials, these are almost dimensionally stable during Li uptake and release. A dense surface film is formed, which experiences only little mechanical strain and is more or less mechanically stable [33]. In this sense, Noh et al. reported that tin nanoparticles encapsulated in a carbonaceous phase obtained from glucose showed superior electrochemical behavior than pure tin, and this feature was associated with the stability of the amorphous carbon-coated Sn [15]. Zhao et al., observed that pyrolyzed PAN improves the electrochemical behavior of Si-SnSb and decreases the polarization of the cell, the electrochemical behavior was better in the case of pyrolysis at 600ºC than at 400ºC, and this was associated to an efficient dispersing of the alloy and enhanced conductivity [20].

In order to study the possible reaction of PAN with Li, the resulting potential-capacity curves of an electrochemical test cell using PAN as main component of the electrode (70% wt.) and PVDF (10% wt.) and carbon black (20% wt.) as additives are shown in Figure 5A. The resulting capacity is negligible for PAN dried at 120ºC. In contrast, the carbonaceous product resulting from the annealing of PAN at 300ºC exhibits reversible capacities of around 400 mAh/g in the first cycles, but the capacity retention is poor (Figure 5B). A large initial amount of PAN can result in an excess of amorphous carbon (ex-PAN) and capacity fade in the $CoSn_2$@PAN composite
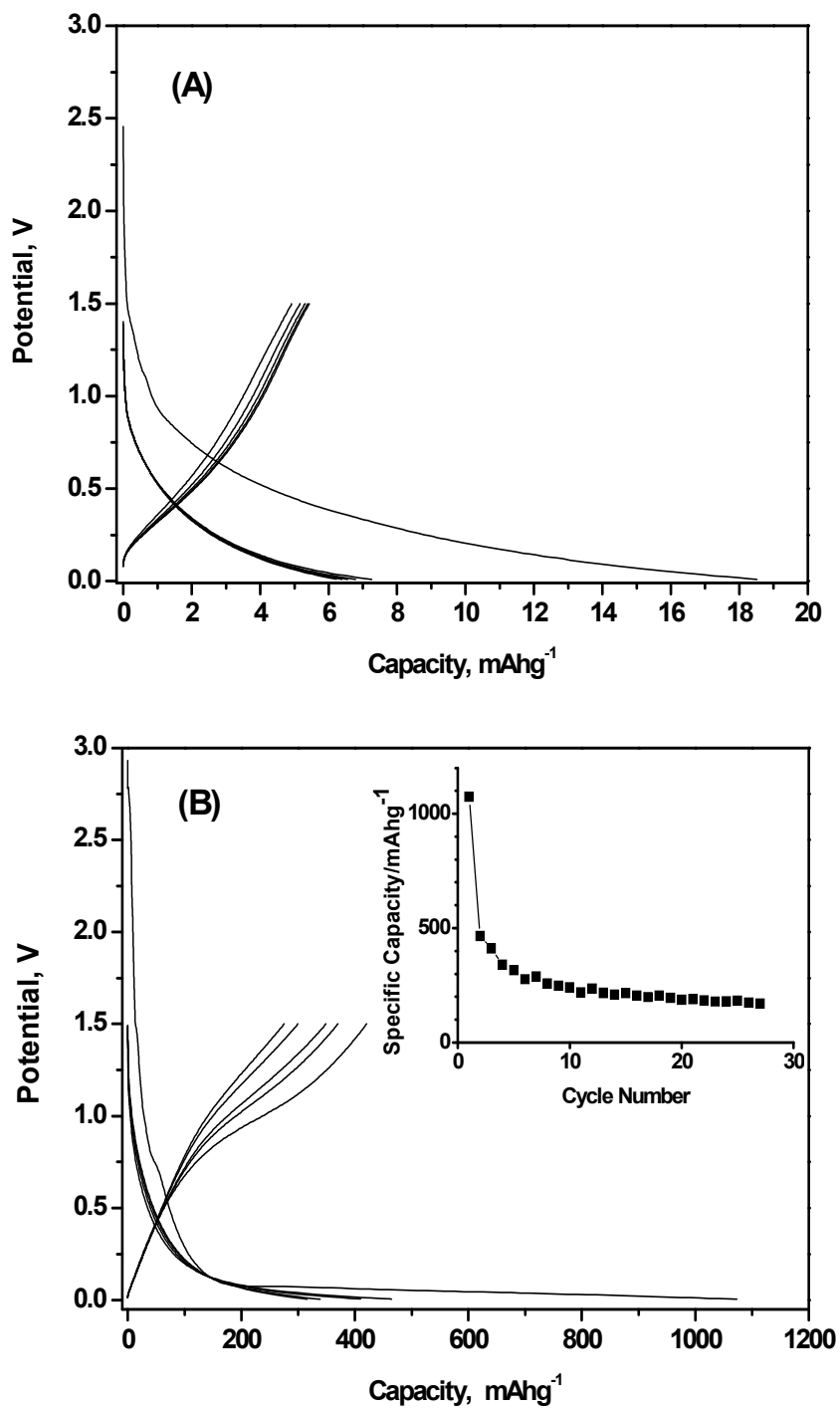
electrodes obtained at 300-600ºC.

Figure 5. Potential vs. specific capacity curves for (A) PAN dried at 120ºC under vacuum and (B) PAN annealed under Ar-flow at 300ºC. The capacity evolution is shown as an inset. Intensity: 50 mA/g.

For the sake of comparison, the specific capacity as a function of the cycle number in lithium test cell is shown for $CoSn_2$, obtained at 120ºC with and without whithout PAN (Figure 6). The resulting behavior for PAN-free $CoSn_2$ is similar to the previously found by other authors [26]. The capacity strongly decreases in the first ten cycles from 800 to around 300 m Ah/g. In the case of the $CoSn_2$@PAN sample in this figure, a relatively low amount of PAN was used in the preparation method (0.6 g of PAN by 4.0 g of $SnCl_2.2H_2O$). The capacity after ten cycles is around 550 mAh/g for the samples prepared with PAN. Thus, the electrochemical cycling experiments show that the electrochemical behavior of $CoSn_2$@PAN is much better than that of $CoSn_2$. For the $CoSn_2$@PAN sample obtained at 300ºC, the observed bad cycle performance may be due to the formation of higher grain size of metallic particles and/or the contribution of the carbonaceous phase formed from partial denitrogenation of PAN.
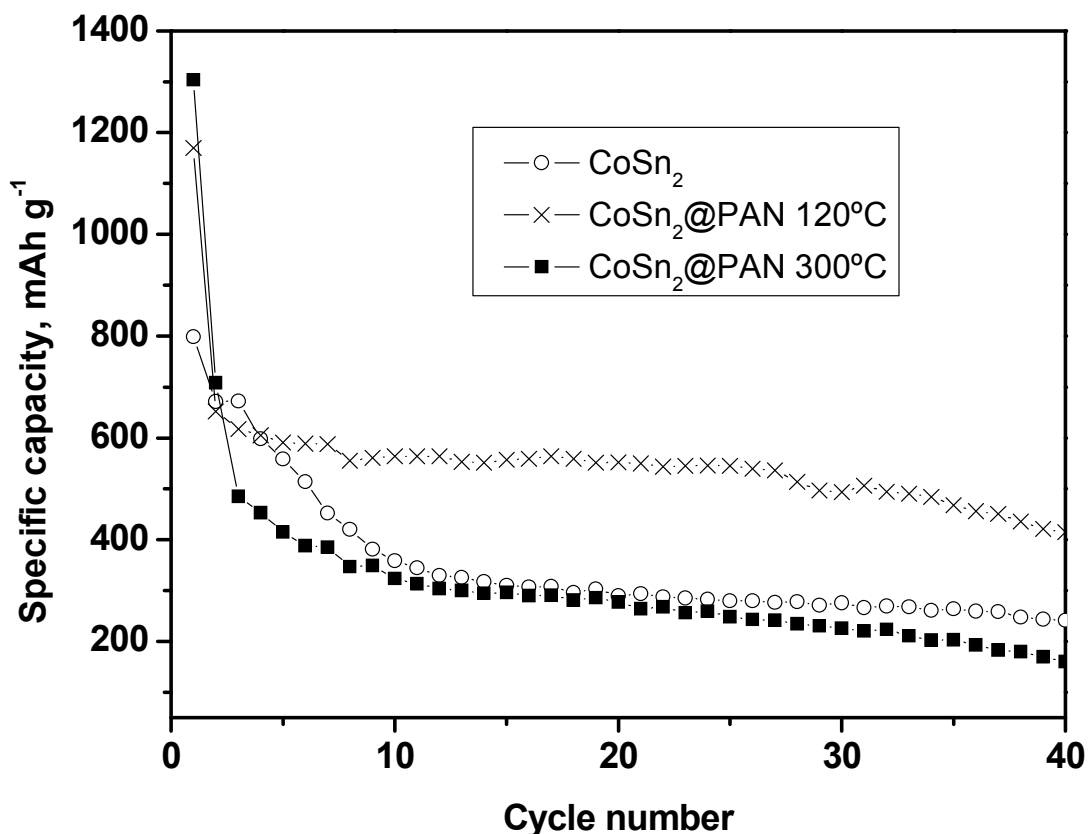

Figure 6. Specific capacity as a function of cycle number for $CoSn_2$ and $CoSn_2$@PAN prepared at 120 and 300ºC. Active material: 70%. Potential range: 0-1.5 V. Intensity: 50 mA/g.

The relative amount of PAN used in the preparation affects the resulting behavior of the $CoSn_2$@PAN samples obtained at 120ºC, as discussed below. We have previously reported that composite electrodes based on Co, Sn and PAN and containing SnO_2 lead to better capacity retention [17]. The presence of a subtle PAN-coating was also observed in the TEM micrographs resulting when the relative amount of PAN was very low, as published in elsewhere [17].

The mechanism of the electrochemical reaction of lithium with this sample was studied by using XRD and [119]Sn Mössbauer spectroscopy. It was shown that both tin dioxide and the intermetallic phases react with lithium in the composite electrode [17]. The improved electrochemical behavior of a $CoSn_2$@PAN sample prepared at 120ºC by using a lower relative amount of PAN (2.4 %, according to elemental analysis), as described elsewhere [17] is clear from in Figure 7. Although the irreversible capacity of the first cycle could jeopardize the practical application of this material, excellent capacity retention is observed. For a very low PAN-content [17], the presence of nanocrystalline tin dioxide leads to the formation of a lithia matrix that remains stable in the potential range between 0.0 and 0.9 V. The small size of the tin dioxide particles (19 nm) and the PAN-based coating can enhance the electrode stability as was previously observed for nano-SnO_2 coated with tin phosphate [32].
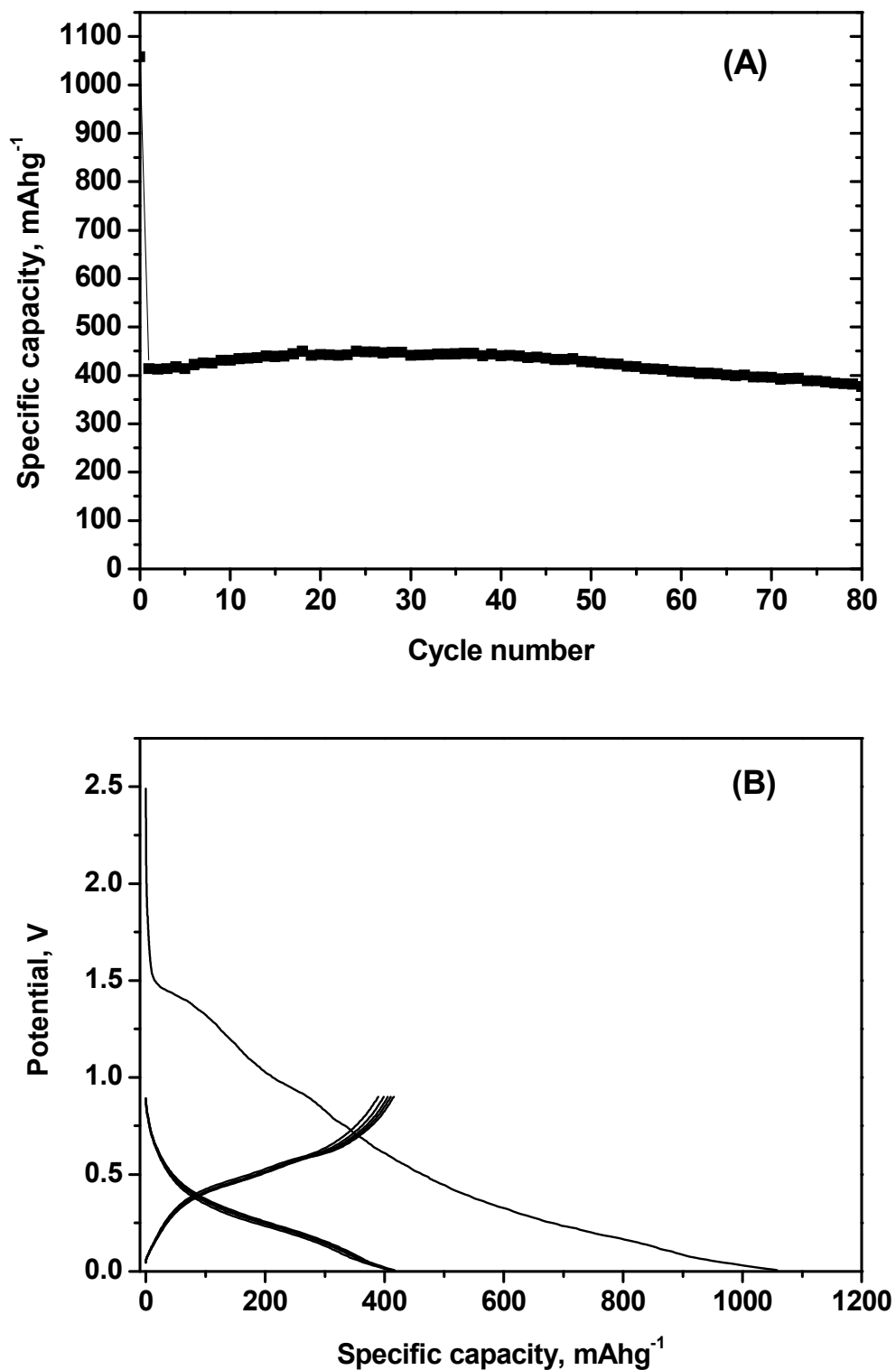
Figure 7. Potential vs. specific capacity (A) and specific capacity as a function of cycle number (B) for CoSn$_2$@PAN prepared at 120ºC. Active material: 80%. Potential range: 0-0.9 V. Intensity: 50 mA/g.

In order to further study the influence of PAN in the electrode behavior, impedance spectra were recorded (Figure 8).

Figure 8. (A) Impedance spectra of electrodes at 0.0 V vs. Li⁺/Li for different cycle numbers (1, 2, 5 and 20). (a) CoSn₂@PAN obtained at 120ºC, (b) CoSn₂@PAN obtained at 300ºC and (c) PAN-free CoSn₂. (B) Equivalent circuit used for the fitting of the spectra. Q represents a constant phase element, R a resistor, and W represents a Warbug element.

All the spectra exhibit two depressed semicircles in the region of high and medium frequencies, and a sloped line at low frequencies. The impedance spectroscopy usually provides only an indirect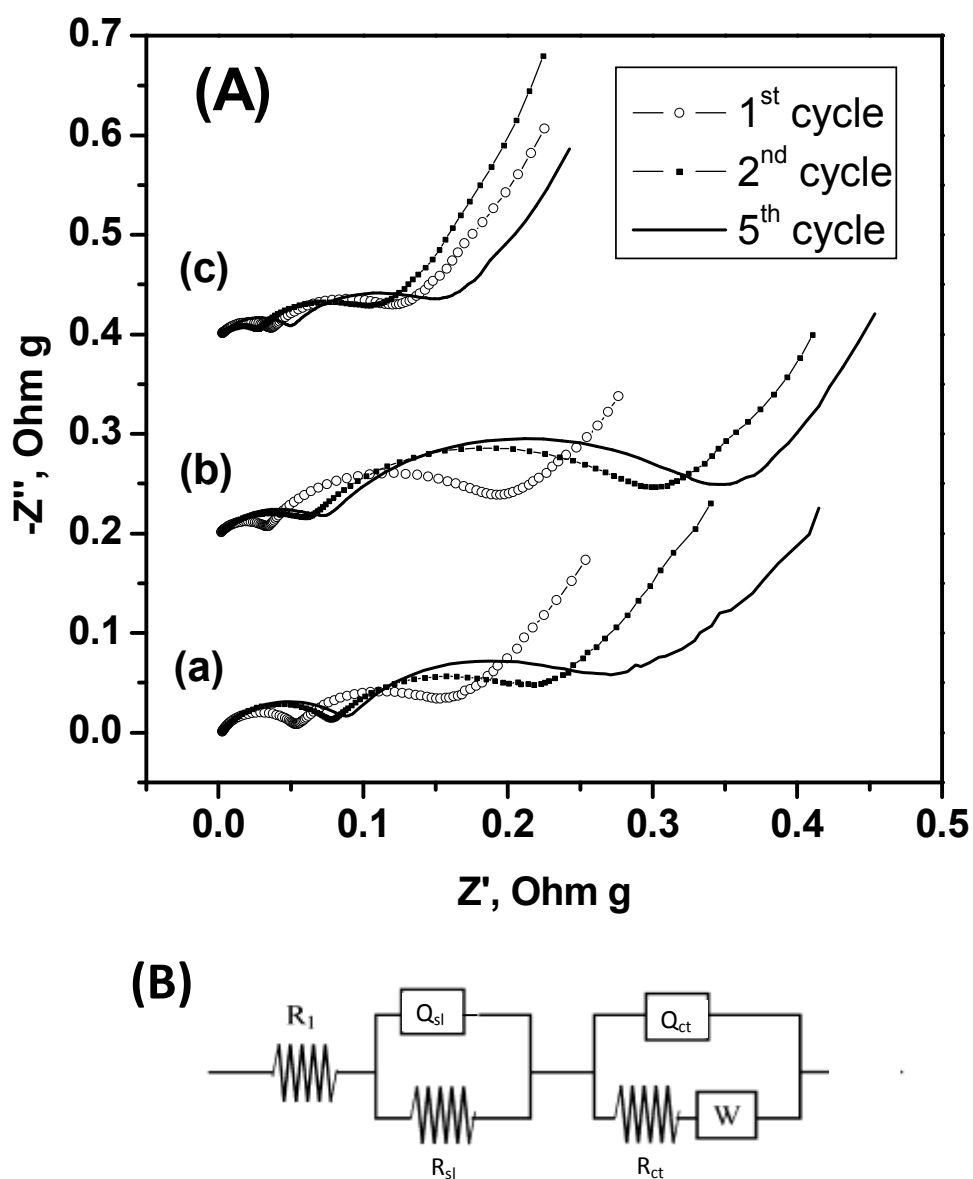 characterization of a given system, the interpretation of the impedance spectra is not always unambiguous and other observations are required to validate a given interpretation of the impedance spectra [34]. Having this in mind, we have tentatively interpreted the impedance spectra based on the results shown above and on the literature [35-38]. Usually, it is accepted that the semicircles represent ion transport resistances and interfacial capacitances. It has been reported that a film is formed by electrolyte decomposition in the surface of tin electrodes [35, 36]. For impedance spectra of electrodes containing CoSn, $CoSn_2$ and carbon phases, Hassoun et al. deduced the formation of complex films on the surface of tin and carbon phases [37]. The semicircle at high frequencies is ascribed to transfer of lithium through the surface film that covers the electrochemically active electrode particles. The semicircle at medium frequencies is assigned to the charge-transfer and lithium transfer at the film/active mass interface [31]. The sloped line is assigned to the lithium diffusion in the electrode particles (Warburg type element). The spectra were fitted with the equivalent circuit shown in Figure 8B, and the resulting resistance values are shown in Table 2. After the first discharge (cycle 1 in Table 2), charge transfer resistance is higher for the electrodes that contain PAN in comparison with an electrode constituted by nanometric particles of PAN-free $CoSn_2$. This feature can be explained as being due to a less electrochemically active surface area for lithium intercalation in the composite electrode and/or a low conductivity of the incompletely pyrolyzed PAN-based matrix. The increase of the annealing temperature from 120 to 300ºC results in an increase of the charge transfer resistance for $CoSn_2$@PAN. The resistance values increase with the cycle number. The electrodes containing PAN-free $CoSn_2$ are less affected by the cycling process.

Other authors found that the charge transfer resistance of CoSn-$CoSn_2$-carbon electrodes does not change upon cycling [37]. The rise of the impedance for the composite electrodes between cycles 1 and 5 is indicative of a modification of the electrode. Probably, the PAN-based surface films are modified upon cycling and contribute to the impedance rise, while the encapsulated tin-based particles remain nearly stable. As a result, charge transfer impedance increases at the surface film/active mass interface. A certain loss of electrical contact in the metallic particles of

the composite electrode cannot be completely ruled out. On the other hand, it may be possible that the surface film in the metallic particles formed by electrolyte decomposition may redissolve in the electrolyte [33], these films would never become very thick, and this would lead to capacity fade in the first ten cycles of PAN-free $CoSn_2$. Most probably, the PAN-derived films may contribute to form a thicker passivating layer and then to modify the charge transfer value. In contrast, the PAN-free metallic particles continuously consume electrolyte and a thick surface film is not formed.

Table 2. Mass-normalized resistances (in Ohm*g units) obtained from impedance spectra of electrodes at different cycle numbers.

cycle	$CoSn_2$@PAN 120ºC		$CoSn_2$@PAN 300ºC		$CoSn_2$ 120ºC	
	R_{sl}	R_{ct}	R_{sl}	R_{ct}	R_{sl}	R_{ct}
1	0.05	0.08	0.03	0.14	0.04	0.06
2	0.08	0.10	0.06	0.21	0.03	0.06
5	0.09	0.15	0.08	0.24	0.05	0.07

R_{sl} = surface-layer resistance; R_{ct} = charge-transfer resistance.

3.4.4   Conclusions

Composite electrodes containing $CoSn_2$ in a PAN-based matrix have been prepared. After thermal treatment, the PAN is partially decomposed into carbon and forms a shell that surrounds the metallic phases. The presence of the PAN-based matrix contributes to the stabilization of the tin-based electrode upon cycling. The encapsulation of tin-based intermetallics with carbonaceous or organic materials is very promising alternative for lithium ion batteries. The main problem of these materials is the high irreversibility of lithium consumption in the first cycle. Research to minimize this effect by surface modification and/or previous lithiation is now in course.

Acknowledgements

References

1. P.P. Fergusson and J.R. Dahn, *Electrochem. Solid State Lett.* **11**, A187 (2008).

2. G.F. Ortiz, R. Alcántara, I. Rodríguez and J.L. Tirado, *J. Electroanal. Chem.*, **605**, 98 (2007).

3. J.G. Geny, D. Malterre, M. Vergnat, M. Piecuch and G. Marchal, *J. Non-Cryst. Solids* **62**, 1243 (1984).

4. Y. Yu, L. Gu, C. Wang, A. Dhanabalan, P. A. van Aken and J. Maier, *Angew. Chem.* **48**, 6485 (2009).

5. L. Huang, J.S. Cai, Y. He, F.S. Ke and S.G. Sun, *Electrochem. Commun.* **11**, 950 (2009).

6. Q. Fan, P.J. Chupas, M.S. Whittingham, *Electrochem. Solid-State Lett.* **10**, A274 (2007).

7. P. G. Bruce, B. Scrosati and J.M. Tarascon, *Angew. Chem. Int. Ed.* **47**, 2930 (2008).

8. M. Armand and J.M. Tarascon, *Nature* **451**, 652 (2008).

9. A.S. Arico, P. Bruce, B. Scrosati, J.M. Tarascon and W. van Schalkwijk, *Nature* **4**, 366 (2005).

10. C. Kim, M. Noh, M. Choi, J. Cho and B. Park, *Chem. Mater.* **17**, 3297 (2005).

11. Trifonova, M. Winter and J.O. Besenhard, *J. Power Sources* **174**, 800 (2007).

12. H. Kim and J. Cho, *J. Electrochem. Soc.*, **154**, A462 (2007).

13. X. He, W. Pu, L. Wang, J. Ren, C. Jiang and C. Wan, *Solid State Ionics*, **178**, 833 (2007).

14. K.T. Lee, Y.S. Jung and S.M. Oh, *J. Am. Chem. Soc.* **125**, 5652 (2003).

15. M. Noh, Y. Kwon, H. Lee, J. Cho, Y. Kim and M.G. Kim, *Chem. Mater.* **17**, 1926 (2005).

16. H. Kim and J. Cho, *Electrochim. Acta* **52**, 4197 (2007).

17. F. Nacimiento, R. Alcántara and J.L. Tirado, *J. Alloys Compd.* **289**, 135 (2009).

18. Z. Bashir, S.P. Church and D. Waldron, *Polymer*, **35**, 968 (1994).

19. C. Raynaud, C. Boiziau, C. Juret, S. Leroy, J. Perreau and G. Lecayon, *Synthetic Metals* **11**, 159 (1985).

20. J. Zhao, L. Wang, X He, C. Wan and C. Jiang, *Electrochim. Acta* **53**, 7048 (2008).

21. R.E. Franklin, Proc R Soc (London) A, 209, 196 (1951).

22. R. Alcántara, F.J. Fernández-Madrigal, P. Lavela, J.L. Tirado, C. Gómez de Salazar, R. Stoyanova and E. Zhecheva, *Carbon* **38**, 1031 (2000).

23. K. Ishida and T. Nishizawa, *J. Phase Equilib.*, **12**, 88 (1991).

24. H. Deng and J.M. Hossenlopp, *J. Phys. Chem. B* **109**, 66 (2005).

25. A. Aboulaich, F. Robert, P.E. Lippens, L. Aldon, J. Olivier-Fourcade, P. Willmann and J.C. Jumas, *Hyperf. Interac.* **167**, 733 (2006).

26. C. M. Ionica-Bousquet, P. E. Lippens, L. Aldon, J. Olivier-Fourcade and J. C. Jumas, *Chem. Mater.* **18**, 6442 (2006).

27. R. Alcántara, G. Ortiz, I. Rodríguez and J.L. Tirado, *J. Power Sources* **189**, 309 (2009).

28. R. Alcántara, I. Rodríguez and J.L. Tirado, *ChemPhysChem* **8**, 1171 (2008).

29. J.R. Dahn, R.E. Mar and A. Abouzeid*, J. Electrochem. Soc.* **153**, A361 (2006).

30. M.Z. Xie, X.B. Zhao, G.S. Cao and J.P. Tu, *J. Power Sources* **164**, 386 (2007).

31. D. Aurbach, A. Nimberger, B. Markovsky, E. Levi, E. Sominski and A. Gedanken, *Chem. Mater.* **14**, 4155 (2002).

32. G.F. Ortiz, R. Alcántara and J.L. Tirado, *Electrochem. Solid State Lett.* **10**, A286 (2007).

33. M. Wachtler, J.O. Besenhard and M. Winter, *J. Power Sources* **94**, 189 (2001).

34. M.E. Orazem, P. Argawal and L.H. Garcia-Rubio, *J. Electroanal. Chem.* **378**, 51 (1994).

35. D. Aurbach, *J. Power Sources* **89**, 206 (2000).

36. J. Hassoun, P. Reale and S. Panero, *J. Power Sources* **174**, 321 (2007).

37. J. Hassoun, P. Ochal, G. Mulas, C. Bonatto, B. Scrosati, *J. Power Sources* **187**, 568 (2008).

38. R. Alcántara, G.F. Ortiz, P. Lavela, J.L. Tirado, R. Stoyanova and E. Zhecheva, *Chem. Mater.* **18**, 2293 (2006).
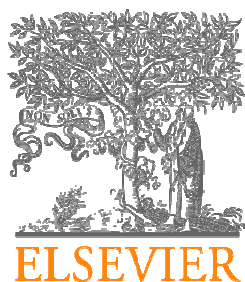
3.5 Nanocrystalline CoSn₂-carbon composite electrode prepared by using sonochemistry

Francisco Nacimiento, Ricardo Alcántara, Uche G. Nwokeke, José R. González, José L. Tirado

Abstract

A sonochemical method has been used to prepare negative electrode materials containing intermetallic nanoparticles and polyacrylonitrile (PAN). The ultrasound irradiation is applied to achieve small particle size. After annealing at 490°C under Ar-flow, the polymer PAN is partially carbonized and the metallic nanoparticles are surrounded by a carbonaceous matrix. The main metallic phase is $CoSn_2$. The carbonaceous coating and the surface oxides have been explored by using XPS. The resulting $CoSn_2$-carbonaceous phase electrode ($CoSn_2@C$) shows improved electrochemical behavior (ca. 450 mAh/g after 50 cycles) in comparison with previous reports on pure crystalline $CoSn_2$. The reaction between $CoSn_2@C$ and Li has been studied by using XRD and ^{119}Sn Mössbauer spectroscopy. The formation of large grains of crystalline Li_xSn phases after the first discharge is discarded. The small particle size which is achieved by using ultrasonication and the carbonaceous matrix contribute to maintain the Co-Sn interactions during the electrochemical cycling. The aggregation of the nanosized metallic particles upon electrochemical cycling can be suppressed by the carbonaceous matrix (pyrolytic PAN).

ELSEVIER

3.5.1   Introduction

The lithium ion batteries developed in the 1990's contain $LiCoO_2$ as the positive electrode, carbon (e.g. graphite or coke) as the negative electrode and the electrolyte is a liquid solution containing organic solvents (e.g. ethylene carbonate (EC) and dimethyl carbonate (DMC)) and lithium salt (e.g. $LiPF_6$) [1]. More recent lithium ion batteries can contain alloys in the negative electrode [2]. The presence of cobalt and other metallic elements, gives an additional value to the recycling of these batteries. Although, the maximum theoretical capacity of graphite is 372 mAh/g, several Li-alloying elements, such as Sn, Sb and Al, exhibit much higher capacity values. After a few charge-dicharge cycles of the pure metals electrodes, the changes of the unit cell volume and/or the irreversible reactions between the metallic particles and the liquid electrolyte solution drives to fade of capacity and battery failure. The use of nanoparticulate alloys as negative electrode material can let to achieve higher capacities and good cycling behavior in lithium ion batteries [3, 4].

The sonochemical method can be used to obtain nanoparticles. The high-intensity ultrasound irradiation in liquid solutions produces the acoustic cavitation effect, collapse of bubbles and high temperatures and pressures in small regions of the solution. Chen et al. reported the preparation of Sn-Bi nanoparticles by applying ultrasonication to Sn and Bi melted together [5]. Tin nanorods were synthesized by using a sonochemical method combined with a polyol process [6]. Ultrasound irradiation and hydrazine as reducing agent were used to prepare Ni and Co particles, and a dramatic effect of the solvent in the particle size was observed [7]. According to the theory developed by Derjaguin, Landau, Verway and Overbeek (DLVO theory), the presence of polymer chains can influence on the stability of the colloidal particles and prevent their aggregation, modifying the viscosity of the dispersion medium [7]. The preparation of electrode materials for lithium ion batteries by using sonochemistry has been little explored [8-10].

Polyacrylonitrile (PAN) can be been used as a component of solid composite electrolyte lithium battery [11]. The lithium ions transport by hopping through the PAN chains. The polymer chains can improve the mechanical properties and the stability of the electrolyte/electrode interface. In addition, PAN has been used to form a matrix that

protects the tin-containing metallic nanoparticles for the negative electrode of lithium ion batteries containing liquid electrolyte solution [12, 13]. The annealing of the PAN-containing composites yielded to rather poor cycling behaviors [12, 13]

The current work describes by the first time the preparation of composite materials containing nanoparticles of Co-Sn alloys encapsulated in a carbonaceous matrix throughout using the sonochemical method. PAN is used like the source of carbon. The electrochemical behavior of this electrode material in lithium test cells is evaluated and the results are very promising.

3.5.2   Materials and methods

For the preparation of the composite electrode material, 2.0 g of $SnCl_2.2H_2O$, 1.06 g of $CoCl_2.6H_2O$ and 0.63 of PAN (molecular weight=150.000) were added into 125 mL of n,n-dimethylformamide (DMF) and ultrasound irradiation was applied with a high intensity ultrasonic probe with Ti-horn (Sonics VCX750 sonicator). All the reagents were supplied by Aldrich. Then, an excess amount of a freshly prepared alkaline solution of $NaBH_4$ in water was added while the ultrasound irradiation was continuously applied. PAN is highly soluble in DMF and poorly soluble in water. After reduction of the metallic ions, the surface of the metallic particles interacts with the PAN molecules and the metal-PAN particles precipitate out. The resulting solid was separated by ultracentrifugation, washed and the solvent was evaporated under vacuum at 120ºC. Then, the resulting solid was annealed at 490°C under Ar-flow. The imposed temperature was chosen in order to avoid an extensive decomposition of the intermetallic compound ($CoSn_2$) into other phases at higher temperatures. For the sake of comparison, samples with nominal compositions CoSn and $CoSn_2$ were also obtained by using ultrasound irradiation and no PAN was added.

X-ray diffraction (XRD) patterns were recorded by using a Siemens D5000 instrument with CuKα radiation and 0.04°2θ-6 s steps. The C-N content was determined with an elemental analyzer Eurovector EA3000. The cobalt and tin cobalt content was determined by using a Scanning Electron Microscopy equipped with an EDS analyzer.[119]Sn Mössbauer spectra were registered at room temperature by using a Wissel instrument and a Ba[119]SnO$_3$ source of radiation. In order to record ex-situ XRD

and Mössbauer spectra of the electrochemically cycled electrode materials, special cares were taken to avoid any undesired reaction with the air atmosphere [4].

X-ray Photoelectron Spectroscopy (XPS) measurements were carried out in a SPECS Phobios 150MCD instrument by using Al Kα radiation (1486.6 eV). The C1s peak at 284.8 eV was used for correcting the binding energies. A Shirley-type baseline and the CasaXPS program were applied for the fitting of the spectra. Peak areas and sensitivity factors provided by the instrument producer were applied to quantify the atomic surface concentrations.

The electrochemical experiments were carried out by using an Arbin instrument. The electrochemical test cells contained a piece of lithium as negative electrode and Co-Sn-PAN (70%), polyvinylidene fluoride PVDF (15%) and carbon (15%) as positive electrode. The electrolyte solution was 1 M LiPF$_6$ in ethylene carbonate:diethyl carbonate solvent mixture. The imposed current intensity was 50 mA/g. The total mass of cobalt, tin and PAN is used to calculate the specific capacity values.

3.5.3   Results and discussion

Selected TEM images of the composite material containing cobalt, tin and PAN are shown in Figure 1-top. Nanometric particles between 5 and 50 nm embedded in a carbonaceous amorphous phase are observed. Lattice fringes are also visible in the metallic particles, evidencing the nanocrystalline nature of the product. Agglomerates of around 200 nm containing single metallic particles and the encapsulating carbonaceous phase are observed. The XRD reflections (Figure 1-bottom) have low intensity and are broadened due to size effects. The most intense reflection corresponds to CoSn$_2$ (XRD file 25-0256), while very low-intensity reflections corresponding to CoSn (XRD file number 02-0559) and SnO$_2$ (XRD file 41-1445) are also observed. The formation of tin oxide can be related to the high surface reactivity of metallic particles with very small size. The average grain size (Lc) values calculated from the broadening of the (121) reflection of CoSn$_2$ at 35.5°/2θ and applying the Scherrer equation is Lc=26 nm, in agreement with the TEM images. The grain sizes previously reported for samples obtained without ultrasonication are larger [12]. The carbonaceous phase and/or other

non-crystalline phase such as amorphous Co-Sn alloy can contribute to the broadened band observed between ca. 15 and 35°/2θ.
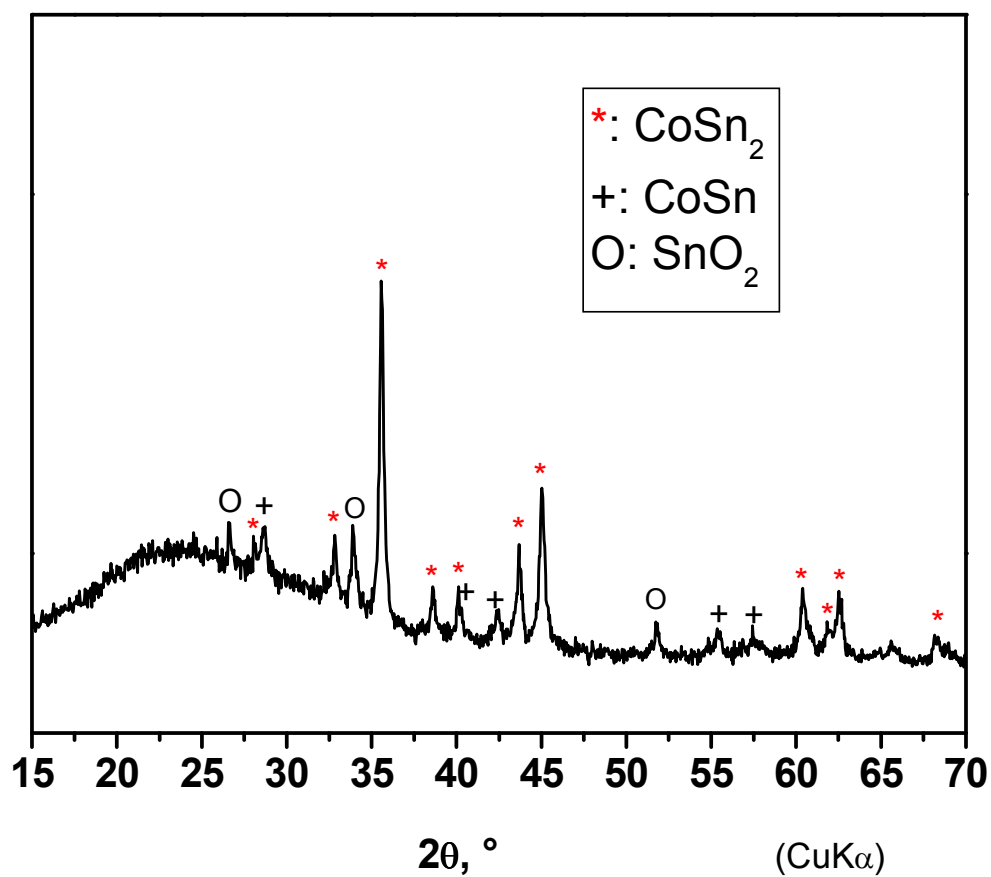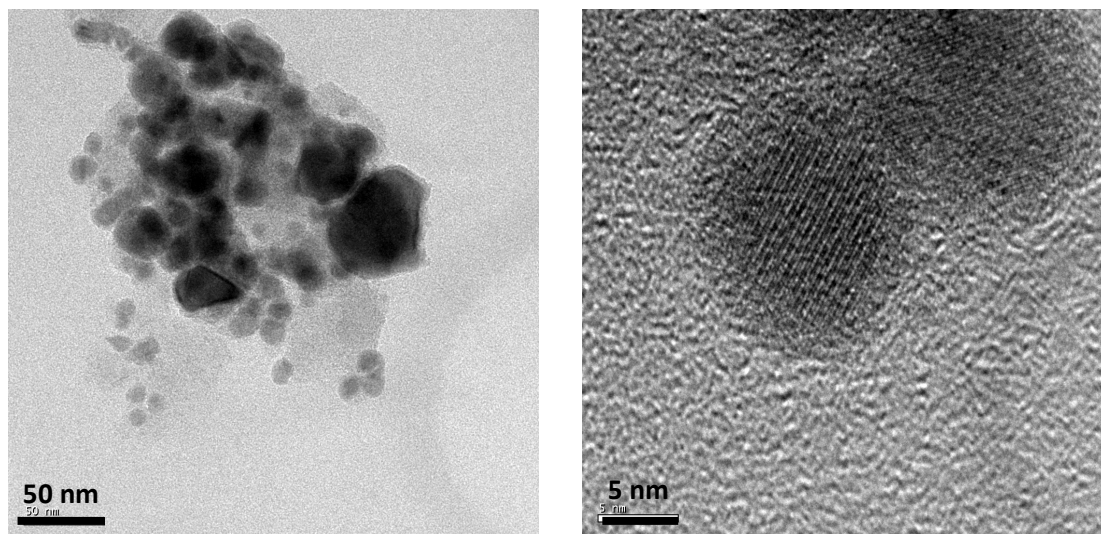

Figure 1. TEM images and XRD for CoSn₂@C.

The results show that the ultrasound irradiation can help to control the particle size and the crystallinity of the composite material. The results also illustrate the great tendency of cobalt atoms to form nanocrystalline compounds with tin. The ultrasonic radiation may help to prepare the very small metallic particles and to paste the PAN molecules to those metallic nanoparticles. The carbonaceous-based matrix (ex-PAN) may hinder the metallic grain growth after heating up to 490°C. The obtained sample can be referred as $CoSn_2@C$.

The carbon and nitrogen content was determined by using a C-N analyzer. The PAN content before annealing at 490°C is around 14% by mass. The ratio Sn/Co=2.0 was checked by EDS analysis. A partial denitrogenation and carbonization of PAN molecules can be inferred from the observed increase of the experimental ratio between the carbon and nitrogen contents (C/N) from C/N=3.2 at 120°C to C/N=4.1 at 490°C. It is worth to note that an increase of the annealing temperature or time used during the carbonization process may promote crystallization and growth of the metallic particles resulting in a poorer electrochemical cycling [12]. Figure 2 shows selected regions of the XP spectra for $CoSn_2@C$. The fitting results are shown in Table 1.

Table 1. Binding energies (B.E.) and atomic concentrations (C) of the $Sn3d_{5/2}$, $Co2p_{3/2}$, C1s, O1s and N1s peaks .

	B.E., eV	C, %
C1s	284.6	23.4
C1s	285.8	10.7
C1s	286.8	12.2
O1s	531.5	27.3
O1s	530.4	8.0
$Co2p_{3/2}$	781.0	1.3
$Co2p_{3/2}$	785.6	0.6
$Co2p_{3/2}$	777.5	0.3
$Sn3d_{3/2}$	495.0	10.5
$Sn3d_{3/2}$	493.0	0.5
N1s	398.9	5.3

The C1s core level peak was fitted with three components. The C1s peak at 284.6 eV is ascribed to carbon (mayor component), the C1s peak at 285.8 eV is ascribed to C bonded to H and the C1s peak at 286.8 eV is ascribed to C bonded to N. The total

carbon and nitrogen concentrations derived from the C1s and N1s signals were 46.3% and 5.3%, respectively. These results are in good agreement with the coating formation by the uncompleted carbonization of PAN. The main component of the $Sn3d_{5/2}$ region with binding energy of 495.0 eV is assigned to Sn(IV), while the peak at 493.0 eV is a minor component of Sn(0). The $Co2p_{3/2}$ peak exhibits very low intensity and was fitted to a peak at 781 eV that is ascribed to Co(II), another peak at 777.5 eV that is ascribed to Co(0) and satellite peak that result from different final state accessible through the band structure of CoO [14].
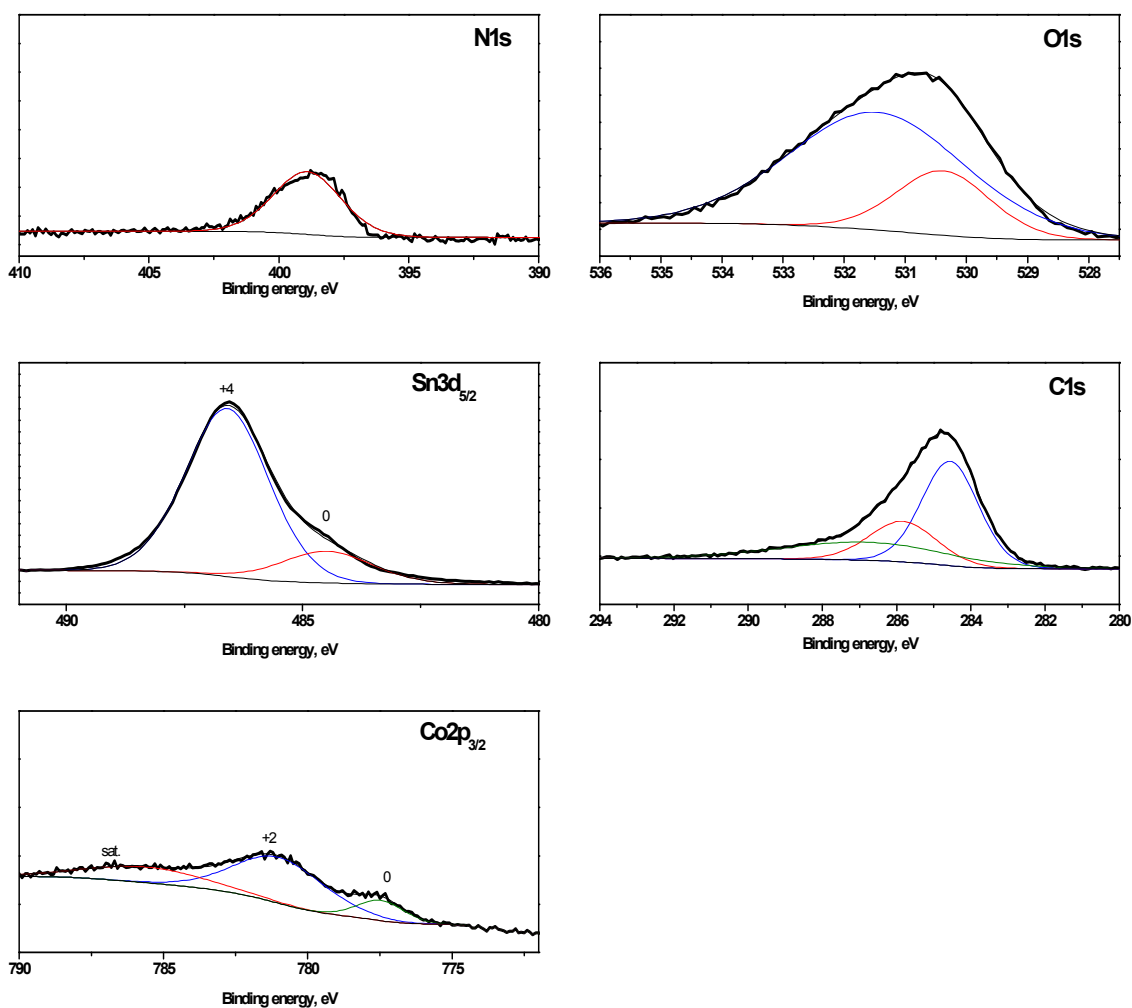
Figure 2. XPS spectra of $Sn3d_{3/2}$, $Co2p_{3/2}$, O1s, C1s and N1s regions.
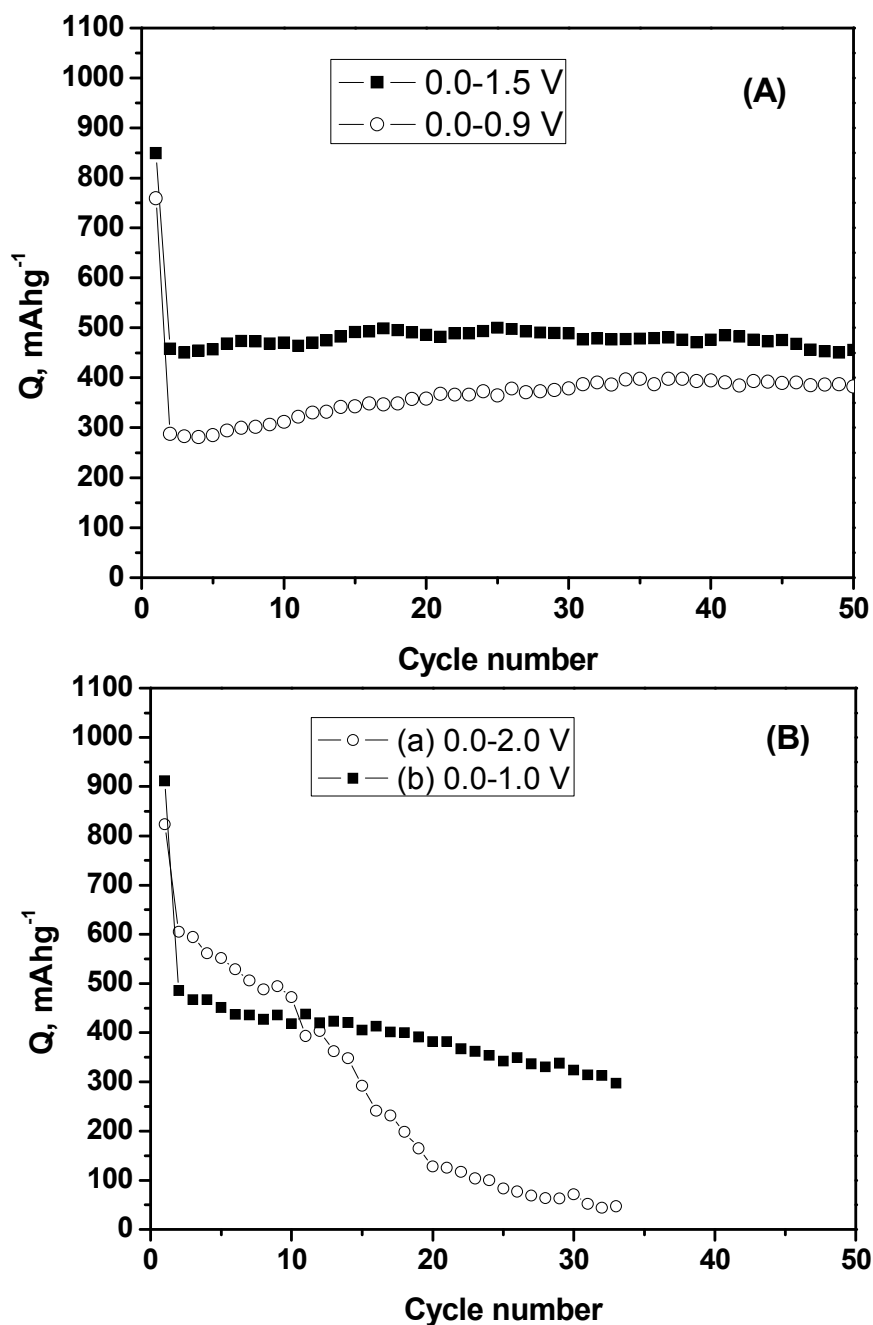
Figure 3. Specific capacity as a function of cycle number for samples obtained by using high intensity ultrasonication. (A) CoSn$_2$@C cycled at different potential limits. (B) Specific capacity as a function of cycle number for samples obtained by using high intensity ultrasonication. PAN-free samples for (a) CoSn at 0.0-2.0 V and (b) CoSn$_2$ at 0.0-1.0 V.

The broadened O1s emission was fitted with a major peak located at 531.5 eV and a minor peak located at 530.4 eV that are ascribed to oxygen ions in metal oxides. The above observations and the relatively high intensities of the O1s and Sn3d peaks in comparison with Co2p evidence that a layer based mainly on SnO_2 covers the surface of the intermetallic particles. Li et al. also reported by using XPS that the surface of electrodeposited CoSn alloy is covered by a thin oxide layer resulting from the exposure of sample to air and preferential oxidation of tin [15].

The specific capacity as a function of cycle number for $CoSn_2@C$ is shown in Figure 3A. The electrochemical performance is better than the previously reported for pure $CoSn_2$ [14] and the equivalent Co-Sn-PAN samples obtained without ultrasonication [12]. For the sake of comparison, the samples with stoichiometries CoSn and $CoSn_2$ that were obtained without PAN and applying ultrasonication also show poorer electrochemical behavior (Figure 3B).

The small grain size of the intermetallic particles and the properties of the carbonaceous matrix contribute to the stability of the electrode. The presence of cobalt atoms also helps to maintain the integrity of the electrode material. The narrower potential window (0.0-0.9 V) leads to lower initial reversible capacity. The potential-capacity curves and derivative curves for $CoSn_2@C$ are shown in Figure 4. The efficiency value of the first discharge-charge cycle is only 51%. This sample shows an irreversible peak at 1.5 V in the first discharge due to solid electrolyte interface (SEI) and lithia formation (main reaction product) due to reaction of SnO_2 with Li. The carbonaceous phase may contribute extensively to the SEI formation and irreversible lithium consume in the first cycle. The derivative curves show good electrode stability upon cycling. After 30 cycles, a peak is observed at 0.26 V in the discharge and two peaks at 0.45 and 0.6 V at observed in the charge that strongly suggest the formation of amorphous Li-Co-Sn alloys [3, 4]. Due to the absence of sharp peaks in the derivative curves, the occurrence of large grains of crystalline Li_xSn phases after the first cycle is discarded and the formation of a Li-Co-Sn alloy is inferred.
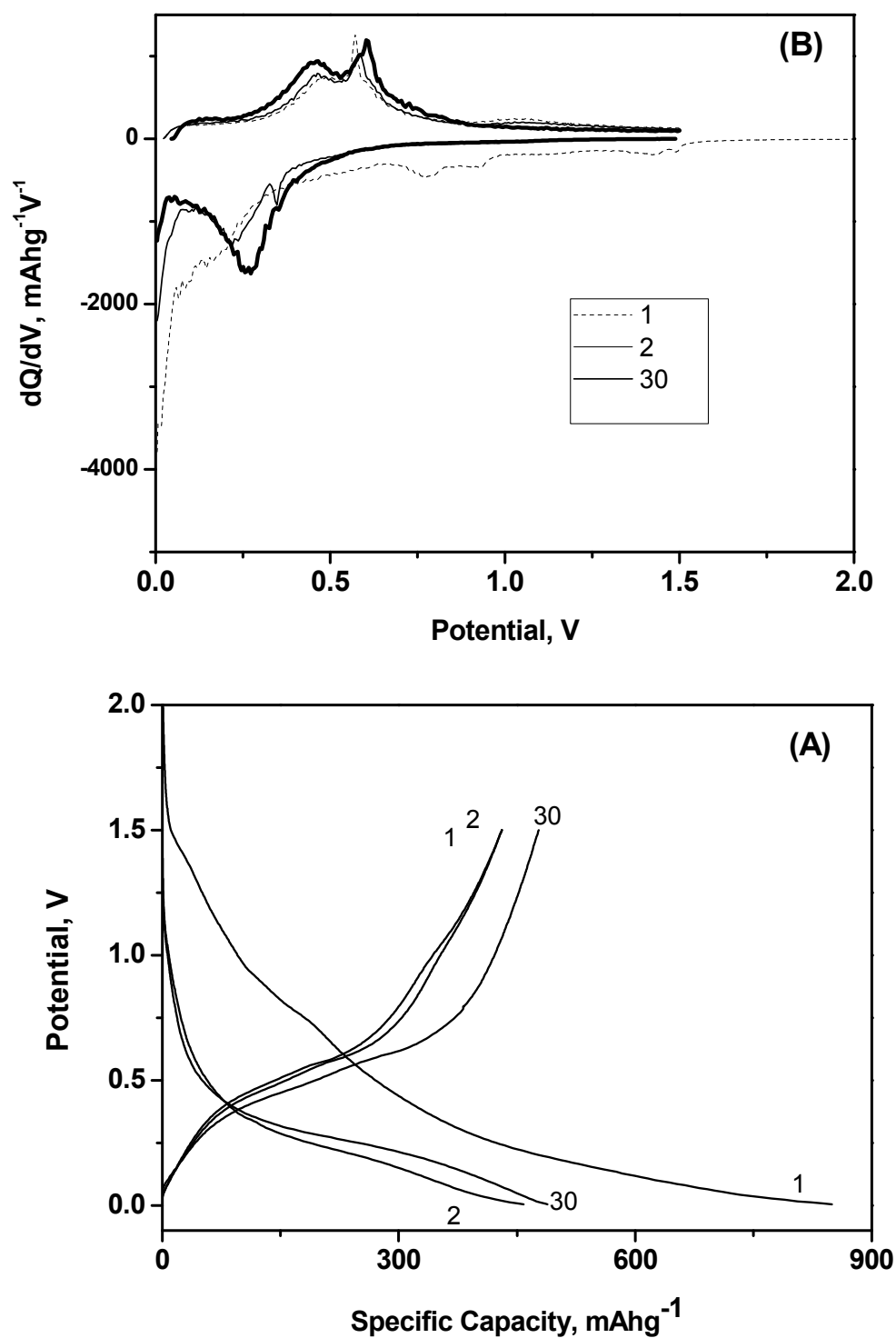
Figure 4. Potential-capacity plot (A) and corresponding derivatives curves (B) for the cycles numbers 1, 2 and 30 of $CoSn_2@C$.

In order to further explore the mechanism of the reaction between $CoSn_2@C$ and Li, the electrochemical experiments were interrupted at selected states of discharge-charge. Then the electrode materials were recovered in the dry-box and XRD patterns and ^{119}Sn Mössbauer spectra were recorded (Figure 5). The ex-situ XRD and in-situ ^{119}Sn Mössbauer spectroscopy study of the reaction between pure and crystalline $CoSn_2$ and Li was reported by Ionica-Bousquet et al. [16]. Irrespectively of the state of discharge-charge, all the electrode materials show Bragg reflections corresponding to $CoSn_2$. The reflections corresponding to tin oxide irreversibly disappear as it is expected due to the formation of amorphous Li_2O and Li_xSn. A reflection placed at 22.7°2θ in Figure 5Bb is ascribed to the initial formation of $Li_{13}Sn_5$ (XRD file number 29-0838), which may be produced by the lithiation of the minor phase SnO_2 or, alternatively, of the Sn extruded from $CoSn_2$. After further depth of discharge the Bragg reflection of $Li_{13}Sn_5$ is not observed (Figure 5Bc). Neither crystalline Sn nor Li_xSn are not observed in the full discharge (Figure 5Bd) and charge (Figure 5Be) states. It means that Sn atoms do not aggregate into large cluster of pure and crystalline tin. The XRD results are in good agreement with the formation of amorphous Li-Co-Sn alloy after the first discharge. The Co atoms extruded from $CoSn_2$ can diffuse into the initially formed Li_xSn grains and to form amorphous Li-Co-Sn alloys, and this process may be enhanced by the small particle size and large surface area of the particles obtained by ultrasonication. During the whole lithiation of crystalline and pure $CoSn_2$, Ionica et al. found a broadened Bragg peak at 38.5-40.2°2θ that was ascribed to the occurrence of crystalline Li_xSn phase while the extruded Co was not detected [16]. The interactions between tin and cobalt atoms can contribute to maintain the small grain size and the amorphous character [17].
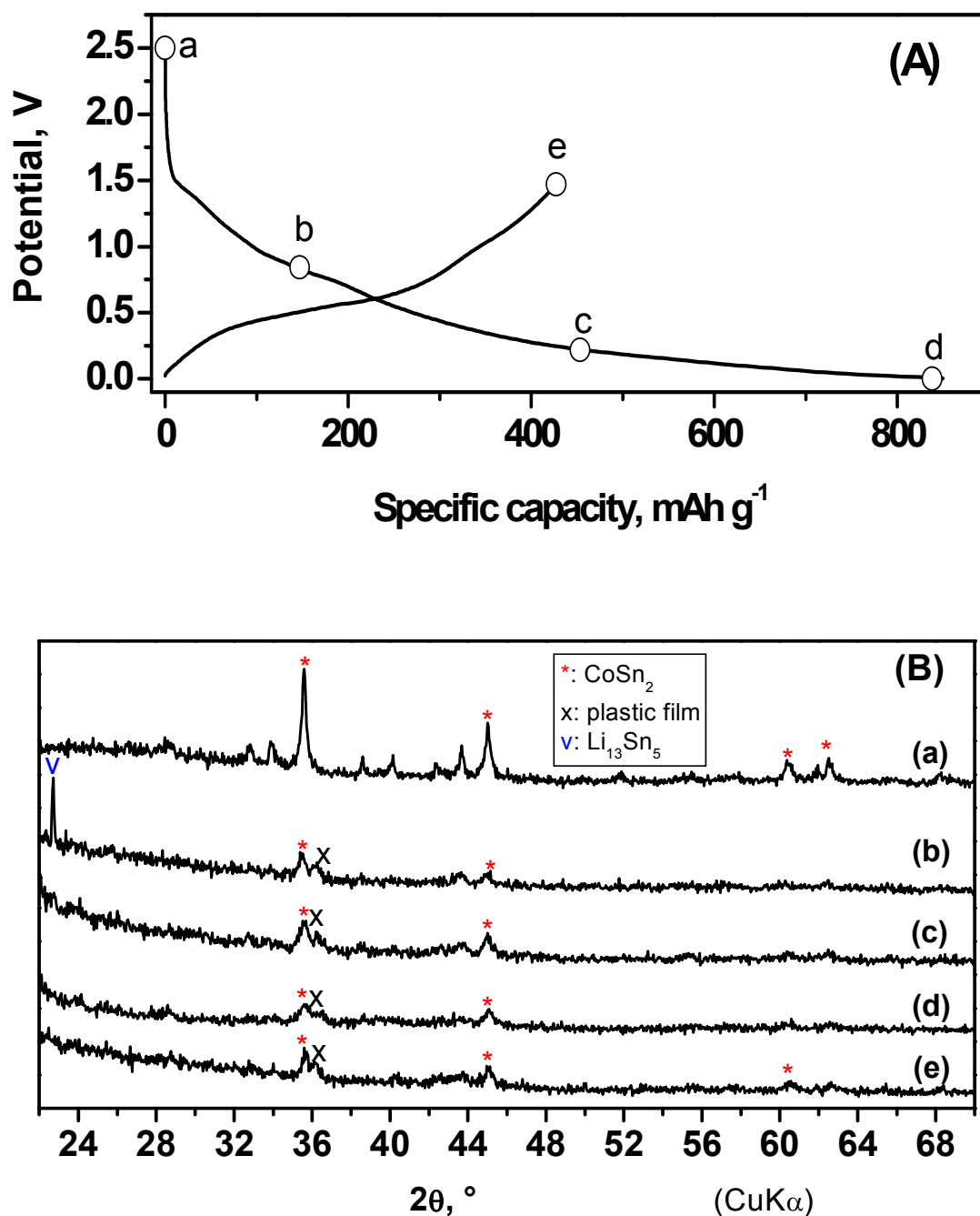
Figure 5. Analysis of the reaction mechanism at selected states of first discharge (a-e) and following charge (f). (A) Potential-capacity plot of the first cycle showing the selected points. (B) Ex-situ XRD patterns, where the major peaks of the phases are indicated.
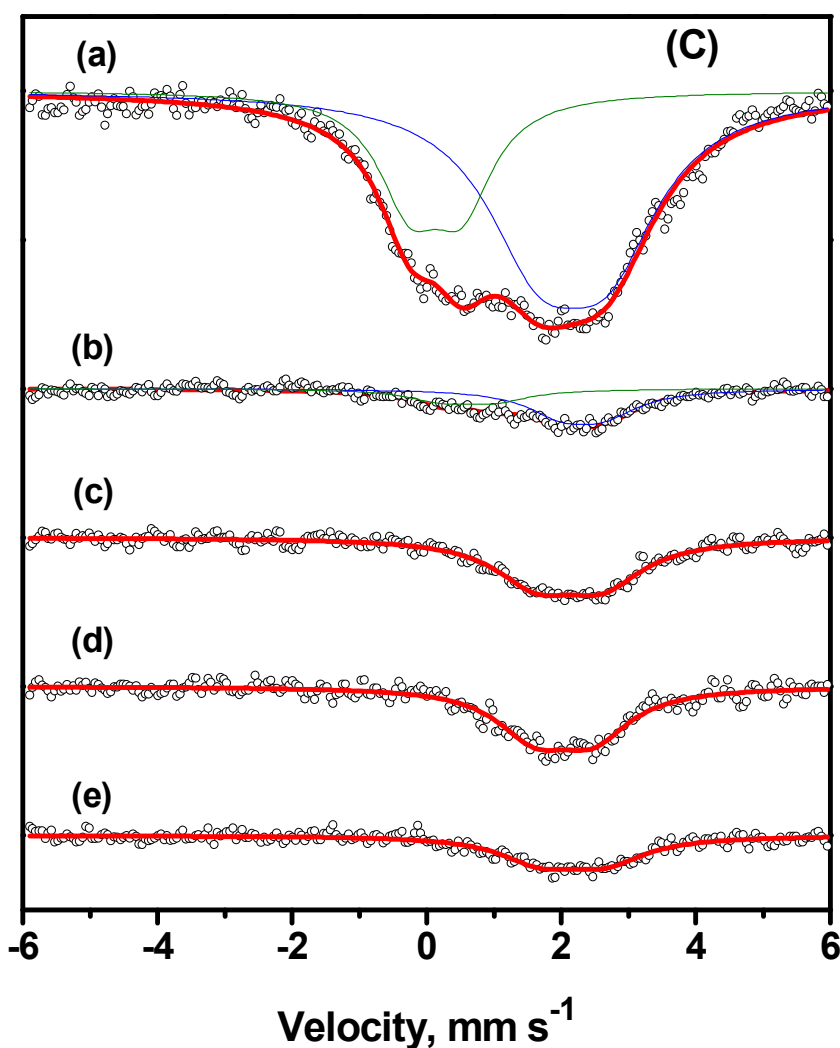
Figure 5-C. Analysis of the reaction mechanism at selected states of first discharge (a-e) and following charge (f). Ex-situ ^{119}Sn Mössbauer spectra.

    The interactions with the Co atoms decrease the potential of the reaction as refereed to pure Li_xSn as it is observed in the derivative curves shown above [3]. Thus, the initial small particle size of the metallic particles that is achieved by using the ultrasound irradiation and the presence of the carbonaceous matrix can contribute to maintain the small particle size and the Co-Sn interactions after the reaction with Li. On the other hand, it is worth recalling that the lithiation of nanoparticulate $FeSn_2$ (isostructural with $CoSn_2$) leads to the occurrence of XRD-detectable $Li_{22}Sn_5$ phase because of the more difficult Fe/Sn alloying process in comparison with the easier Co/Sn alloying [18]. The capacity of the discharge process (Figure 4A-Be, f) would be

212

sufficient to complete the reaction of the $CoSn_2$ phase with Li and the $CoSn_2$ phase would be destroyed. However, low-intersity Bragg reflections of $CoSn_2$ are still visible.

Most probably, the $CoSn_2$ structure is partially reconstructed, although the existence of non reacted $CoSn_2$ grains that remain electrically disconnected cannot be completely discarded. In this way, Ferguson et al. reported that during the first charge of previously lithiated $Sn_{30}Co_{30}C_{40}$ (nanostructured and obtained by mechanical attrition) the nanoscale regions of $Li_{22}Sn_5$ and Co react and CoSn is reconstructed [19]. The presence of PAN also can contribute to maintain the small particle size and to hinder the occurrence of large crystalline grains.

[119]Sn Mössbauer spectra are shown in Figure 5C. For the pristine sample (Figure 4Ba), the spectrum was fitted with two quadrupole split doublets. Irrespectively of the higher Lamb-Mössbauer factor of Sn(IV) that increases its relative contribution to the spectra, the peak at isomer shift $\delta=0.14(4)$ mm/s is ascribed to Sn(IV). The peak at $\delta=2.17(3)$ mm/s and quadrupole splitting $\Delta= 1.02(4)$ mm/s represents the average situation of the tin atoms in the metallic alloy and it is nearby the values corresponding to $CoSn_2$ ($\delta=2.14$ mm/s and $\Delta=0.78$ mm/s) [20]. The relative contribution of Sn(IV) irreversibly decreases at the beginning of the first discharge (Figure 5Cb), as expected due the formation of Li_2O and Sn. After the discharge to ca. 0.2 V, the signal from Sn(IV) is not observed and the observed doublet at $\delta=2.12(3)$ with $\Delta=0.98(4)$ mm/s represents the average situation of the tin atoms in the alloy (Figure 4Cc). After the complete discharge down to 0.0 V (Figure 4Cd), the observed spectrum has been fitted with one quadrupole split doublet peak with $\delta=2.04(3)$ mm/s and $\Delta= 0.87(5)$ mm/s. Thus, the average isomer shift of the tin atoms in the alloys slightly decreases from 2.17 to 2.04 when the discharge depth increases. This isomer shift decreasing for Li_xSn-Co alloys is less abrupt than the corresponding to Co-free Li_xSn phases as it was discussed in elsewhere [20, 21]. The contribution of the Sn(IV) atoms is not recovered after the discharge-charge cycle, indicating that the formation of Li_2O is irreversible within the imposed potential window. The hyperfine parameters resulting from fitting of the spectrum obtained after the first discharge-charge cycle (Figure 5Ce), $\delta=2.17(4)$ mm/s and $\Delta= 0.96(7)$ mm/s, nearly corresponds to $CoSn_2$ and this feature is in good agreement with the partial reconstruction of the $CoSn_2$ structure while the occurrence of β-Sn is inhibited. The TEM micrographs of the electrode material recovered after

electrochemical cycling reveals that nanometric metallic particles smaller than 50 nm are still dispersed in a non-metallic matrix of pyrolytic PAN (Figure 6).
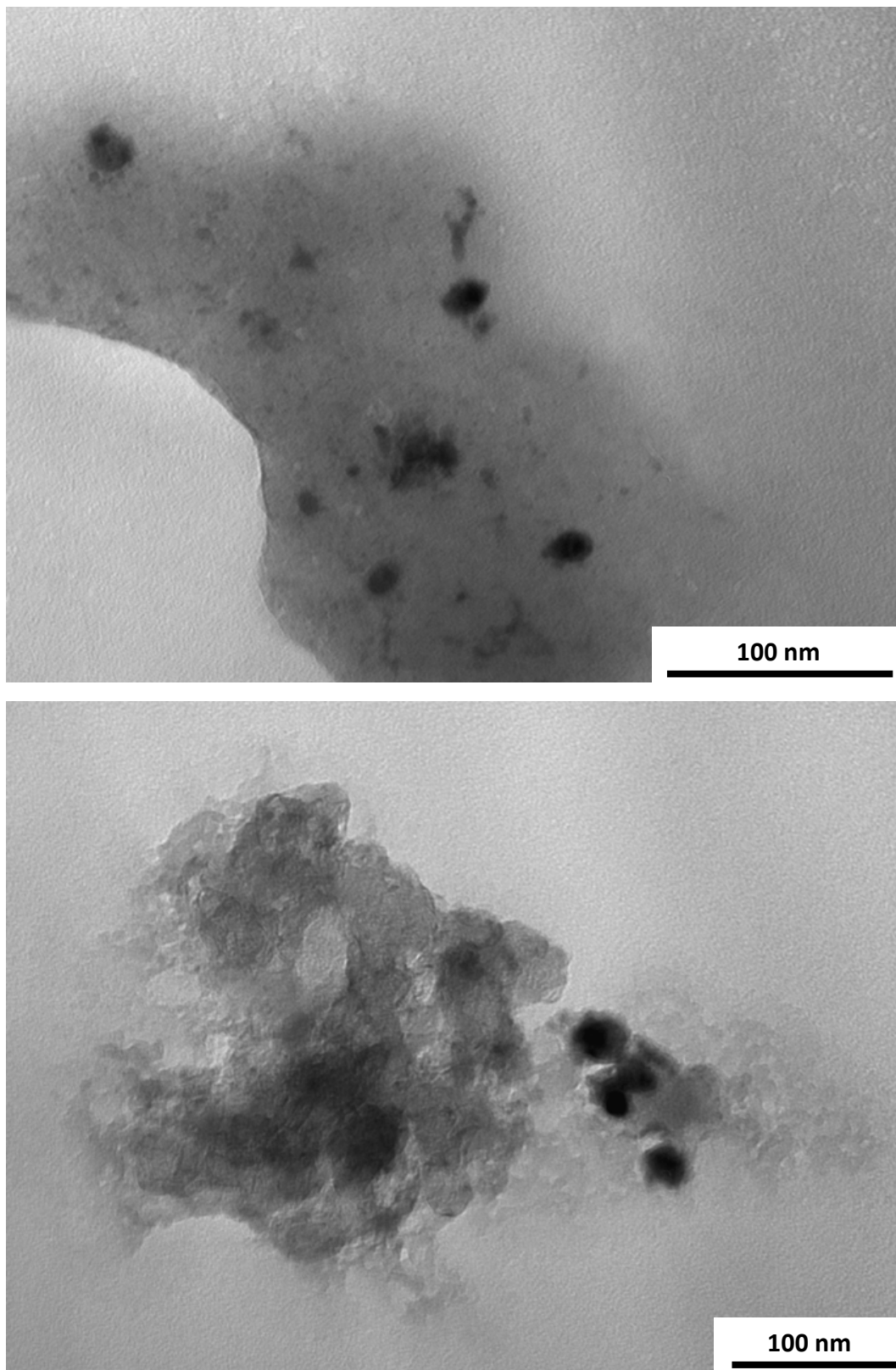

Figure 6. TEM micrographs of the CoSn$_2$@C. electrode material after ten discharge-charge cycles.

3.5.4   Conclusions

The sonochemical method has been successfully used here to encapsulate $CoSn_2$ in a carbonaceous matrix. The resulting electrode material show good stability upon cycling. The use of the ultrasonication allows achieving very small particles of $CoSn_2$ which favors the formation of amorphous Li-Co-Sn and $CoSn_2$ alloys, the carbonaceous matrix helps to maintain the small particle size and consequently the occurrence of large grains of crystalline Li_xSn is avoided. A main problem is the initial capacity loss due to irreversible reactions. The use of the sonochemical method to prepare nanosized intermetallics-carbonaceous materials for batteries electrodes is very promising. Others intermetallics and sources of carbon should be explored.

Acknowledgments

References

1. Y. Nishi, The development of lithium ion secondary batteries, Chemical Record 1 (2001) 406-413.

2. Q. Fan, P.J. Chupas, M. S. Whittingham, Characterization of amorphous and crystalline tin-cobalt anodes, Electrochem. Solid-State Lett. 10 (2007) A274-A278.

3. J.R. Dahn, R.E. Mar, A. Abouzeid, Combinatorial study of $Sn_{1-x}Co_x$ (0 < x < 0.6) and $[Sn_{0.55}Co_{0.45}]_{(1-y)}C_y$ (0 < y < 0.5) alloy negative electrode materials for Li-ion batteries, J. Electrochem. Soc. 153 (2006) A361-A365.

4. R. Alcántara, U. Nwokeke, I. Rodríguez, J.L. Tirado, Electrochemical reaction of lithium with nanocrystalline $CoSn_3$, Electrochem. Solid-State Lett. 11 (2008) A209-A213.

5. H. Chen, Z. Li, Z. Wu, Z. Zhang, A novel route to prepare and characterize Sn-Bi nanoparticles, J. All. Comp. 394 (2005) 282-285.

6. L. Qiu, V.G. Pol, J. Calderon-Moreno, A. Gedanken, Synthesis of tin nanorods via a sonochemical method combined with a polyol process, Ultrason. Sonochem. 12 (2005) 243-247.

7. R. Abu-Much, A. Gedanken, Sonochemical Synthesis under a Magnetic Field: Fabrication of Nickel and Cobalt Particles and Variation of Their Physical Properties, Chem. Eur. J. 14 (2008) 10115-10122.

8. A. Odani, A. Nimberger, B. Markovsky, E. Sominski, E. Levi, V.G. Kumar, M. Motiei, A. Gedanken, P. Dan, D. Aurbach, Development and testing of nanomaterials for rechargeable lithium batteries, J. Power Sources 119-121 (2003) 517-521.

9. D. Jugovic, M. Mitric, N. Cvjeticanin, B. Jancar, S. Mentus, D. Uskokovic, Synthesis and characterization of LiFePO4/C composite obtained by sonochemical method, Solid State Ionics 179 (2008) 415-419.

10. H. Mukaibo, A. Yoshizawa, T. Momma, T. Osaka, Particle size and performance of SnS_2 anodes for rechargeable lithium batteries, J. Power Sources 119-121 (2003) 60-63.

11. Y.T. Chen, Y.C. Chuang, J.H. Su, H.C. Yu, Y.W. Chen-Yang, High discharge capacity solid composite polymer electrolyte lithium battery, J. Power Sources 196 (2011) 2802-2809.

12. F. Nacimiento, R. Alcántara, J.L. Tirado, PAN-encapsulated nanocrystalline $CoSn_2$ particles as negative electrode active material for lithium-ion batteries, J. Electrochem. Soc. 157 (2010) A666-A671.

13. F. Nacimiento, R. Alcántara, J.L. Tirado, Comparative study of composite electrodes containing tin, polyacrylonitrile and cobalt or iron, J. Power Sources 196 (2011) 2893-2898.

14. A. Thissen, D. Ensling, F.J. Fernéndez-Madrigal, W. Jaegermann, R. Alcántara, P. Lavela, J.L. Tirado, Photoelectron Spectroscopy study of the reaction of Li and Na with $NiCo_2O_4$, Chem. Mater. 17 (2005) 5202-5208.

15. J.T. Li, J. Swiatowska, A. Seyeux, L. Huang, V. Maurice, S.G. Sun, P. Marcus, XPS and ToF-SIMS study of Sn-Co alloy thin films as anode for lithium ion battery, J. Power Sources 195 (2010) 8251-8257.

16. C.M. Ionica-Bousquet, P.E. Lippens, L. Aldon, J. Olivier-Fourcade, J.C. Jumas, In situ Sn-119 Mossbauer effect study of Li-$CoSn_2$ electrochemical system, Chem. Mater. 18 (2006) 6442-6447.

17. J.F. Geny, D. Malterre, M. Vergnat, M. Piecuch, G. Marchal, Forming ability and stability of amorphous M_xSn_{1-x} alloys (M= V, Cr, Mn, Fe, Co, Ni, Cu), J. Non-Cryst. Solids 61-62 (1984) 1243-1248.

18. U.G. Nwokeke, R. Alcántara, J.L. Tirado, R. Stoyanova, M. Yoncheva, E. Zhecheva, Electron Paramagnetic Resonance, X-ray diffraction, Mössbauer spectroscopy, and electrochemical studies on nanocrystalline $FeSn_2$ obtained by reduction of salts in tetraethylene glycol, Chem. Mater. 22 (2010) 2268-2275.

19. P.P. Ferguson, R.A. Dunlap, J.R. Dahn, An in situ study of the electrochemical reaction of Li with nanostructured $Sn_{30}Co_{30}C_{40}$, J. Electrochem. Soc. 157 (2010) A326-A332.

20. G.F. Ortiz, R. Alcántara, I. Rodríguez, J.L. Tirado, New tin-based materials containing cobalt and carbon for lithium-ion batteries, J. Electroanal. Chem. 605 (2007) 98-108.

21. R. Alcántara, G. Ortiz, I. Rodríguez, J.L. Tirado, Effects of heteroatoms and nanosize on tin-based electrodes, J. Power Sources 189 (2009) 309-314.

Capítulo 4.-

Películas finas electrodepositadas

4.1 Electrodeposited polyacrylonitrile and cobalt-tin composite thin film on titanium substrate

Francisco Nacimiento, Ricardo Alcántara, José R. González, José L. Tirado

Abstract

Organic-inorganic films have been prepared. Electrodeposited polyacrylonitrile (PAN) and cobalt-tin films on titanium substrate are studied as a new electrode for lithium ion batteries. For the preparation of the electrode, firstly, cobalt and tin are electrodeposited on titanium substrate and an amorphous and metastable Co-Sn alloy is the main product. Secondly, PAN is deposited on the Co-Sn/Ti substrate through electropolymerization of the monomer (acrylonitrile). The interfacial properties of tin-based electrochemically active material are modified via electrodeposition of PAN, as is observed by using electrochemical impedance spectroscopy. Areal capacities in the order of mAh/cm^2 have been achieved.

4.1.1 Introduction

The deposition of tin or Co-Sn composite alloys on two- or three-dimensional substrates has been envisaged as a promising way to improve the electrochemical cycling of tin-based electrodes, mainly due to the good electrical contact between the active material and the current collector and the ability to buffer the electrode volume changes [1-12]. The resulting electrodes show higher initial Coulombic efficiency, excellent capability at high rates, and good cycling stability. Consequently, these electrodes can be highly advantageous for the development of lithium ion batteries for electric vehicles.

The deposition of Sn on several substrates is being extensively studied in the last few years. Thus, Wang et al. have recently reported the sputtering of Sn on Cu nanowire arrays [5], Jiang et al. electrodeposited Sn on Cu nanorods [6] and Bazin et al. electroplated Sn on Cu nanopillars [7]. Du et al. electrodeposited Sn on Ni nanocone-arrays and observed that annealing led to the formation of Ni-Sn alloys [8]. Metal foams [9, 10] and carbon paper [11] have also been used as substrates for Sn alloys. Particularly, Co-Sn alloys also can be electrodeposited on metallic substrates such as porous copper [12]. The metallic substrates act as current collector and favor a good adhesion and electrical contact of the active material. While no binder was used in the electrodes mentioned above, liquid solutions were employed as the electrolyte in all of them.

Promising alternatives to the use of liquid electrolytes can be found among inorganic solids, organic polymers and gels. Polyacrylonitrile (PAN) containing a lithium salt can be a suitable electrolyte for solid state batteries [13-15]. In fact, the solutions of $LiPF_6$ in organic solvents such as ethylene carbonate (EC) act as plasticizers of PAN [13, 14]. The -C≡N groups of PAN ($-[CH_2-CH(CN)]_n-$) can be coordinated to Li^+ ions and allow the ionic conductivity. On the other hand, the electrodeposition of a PAN film onto electrodes such and MnO_2 and carbon for lithium microbatteries has been reported [16].

In this work we report for the first time the electrodeposition of PAN on tin-based films previously electrodeposited on a metallic substrate. For this purpose, titanium foil has been used as the substrate and current collector. The interface properties are explored by using electrochemical impedance spectroscopy.

4.1.2   Experimental

Firstly, Co-Sn films were prepared by co-electroplating method. For the electrodeposition of Co-Sn films, a smooth surface of titanium foil was used and a constant current intensity of 75 mA/cm^2 was imposed during 5 or 20 min to an aqueous solution (plating bath) containing 0.05 M CoCl$_2$, 0.03 M SnCl$_2$ and 0.7 M K$_4$P$_2$O$_7$. The pyrophosphate ion was used as a complexing agent of cobalt(II) and tin(II) to improve the Co-Sn codeposition.   The reference electrode was Ag/AgCl and the counter electrode was Pt.

Polyacrylonitrile (PAN) films were in-situ grown on the metallic substrates by electropolymerisation of acrylonitrile (AN) solution in acetonitrile (ACN), following a procedure equivalent to that reported elsewhere for using carbon substrate [16, 17]. The electrolyte solution was 2 M AN as monomer and 0.05 M tetrabutylammonium perchlorate as supporting salt in ACN solvent. Five voltammetric cycles were carried out in the potential window between -0.5 and -3.5 V vs. Ag/AgCl reference electrode and Pt counterelectrode, at 100 mV/s of rate and using a VMP instrument. The application of successive voltage pulses lets to obtain the grafting and the reduction of the monomer on the cathode, while the potential is maintained lower than the potential able to reduce the supporting salt [16, 17]. On the other hand, tetraalkylammonium salts are very suitable as supporting electrolytes and are extensively employed in electrochemistry because of excellent solubility characteristics in most organic solvents and the absence of impurities that lead to undesirable residual currents. Then, the electrode was dried under vacuum at 60°C overnight. A drop of dimethyl formamide (DMF) was added to the surface of the electrode for achieving a more homogeneous dispersion of PAN, and then DMF was evaporated at 60°C during one hour [16]. The resulting electrode was immersed in 1 M LiPF$_6$ in ethylene carbonate:diethyl carbonate (EC:DEC) electrolyte solution during one hour prior to the assembly of the lithium test cells.

For FTIR analysis, the PAN film grown in a Ti foil by the procedure described above was scraped off as a powder, and a Bruker FTIR Tensor 27 instrument was used. A Siemens D5000 instrument was used for X-Ray Diffraction (XRD) measurements. Elemental composition determinations and morphological analysis were carried out in a

Scanning Electron Microscope (SEM) JSM-6300 equipped with secondary electron detector (Everhart-Thornley type) and X-ray detector (EDAX-type).

The lithium cells were assembled using a piece of Ti foil with geometrical area of 0.2 cm^2 previously electrodeposited with tin-cobalt alloy and PAN, as the working electrode, one Li piece as counter electrode, and a second Li piece as reference electrode. A VMP instrument was used as galvanostat and for electrochemical impedance spectroscopy (EIS) measurements. The electrolyte was 1 M LiPF$_6$ in EC:DEC solvent mixture supplied by Merck. Electrochemical impedance spectra were recorded by using three-electrode T-type cells in the frequency range from 200 kHz to 10 mHz, 0.01 V of open circuit voltage and 10 mV of amplitude. The impedance spectra in all the range of frequencies were simulated by using an equivalent circuit and fitted by using the EC-Lab software provided by Biologic.

4.1.3   Results and discussion

Electrodeposited cobalt-tin alloy film

After electrodeposition of tin-cobalt alloy film on a titanium foil, the resulting XRD pattern (Figure 1) shows low-intensity and broadened reflections corresponding to Sn (ICDD file number 4-673) and CoSn (ICDD file number 2-559). Cobalt and tin atoms were detected by using SEM equipped with composition microanalysis, and the resulting average atomic ratio Co:Sn is equals to 1:2.4. Carbon atoms were not detected. Amorphous tin can contribute to the broadened band at around 20-30°2θ. The cobalt atoms in the X-ray amorphous Co-Sn alloy can be incorporated into the structure of crystalline Sn by annealing while the XRD pattern of Sn emerges, as was found by other authors [18]. After annealing at 200°C the electrodeposited Co-Sn electrode, the reflections of CoSn$_2$ (ICDD file number 25-256) emerge (Figure 1). This feature confirms the occurrence of amorphous and metastable Co-Sn alloy as a main phase prior to annealing. The reflections of the metallic phases were not masked by the electrodeposition of PAN film on pure Ti or CoSn film-Ti.
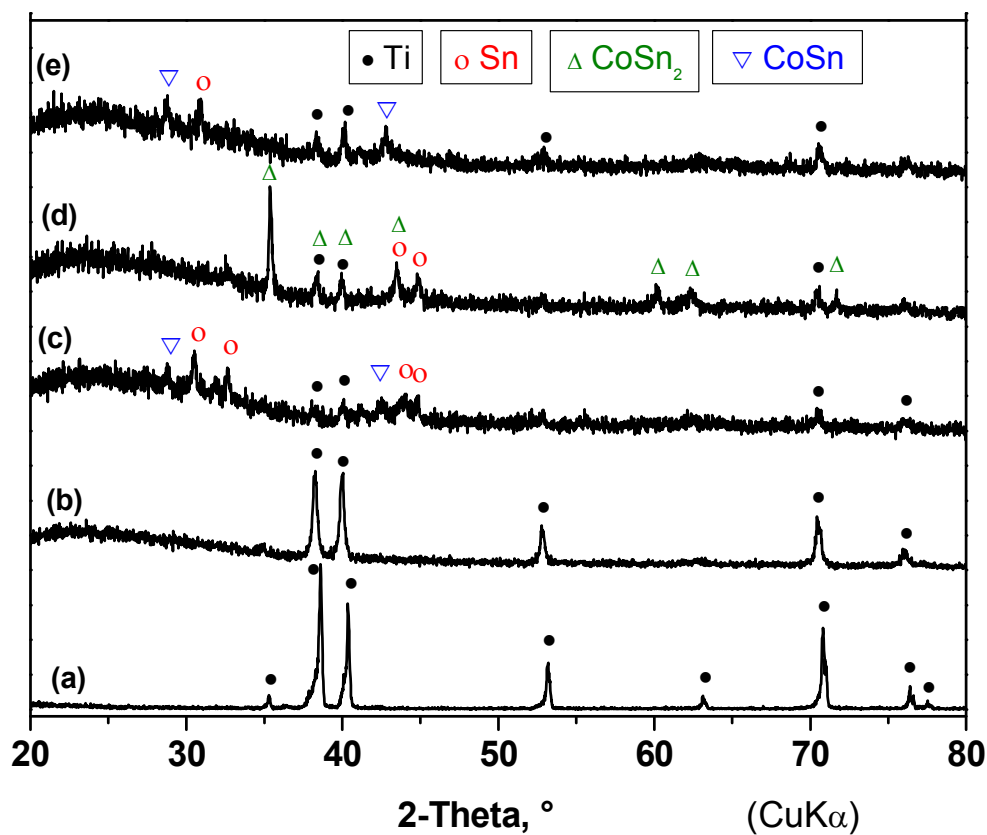
Figure 1. XRD patterns of (a) Ti foil, (b) PAN electrodeposited on Ti foil, (c) Co-Sn electrodeposited on Ti foil, (d) Co-Sn electrodeposited on Ti foil and then annealed at 200°C and (e) PAN electrodeposited on previously electrodeposited Co-Sn on Ti foil.

After the electrodeposition of Co-Sn alloy on Ti foil by applying 75 mA/cm^2 during 5-20 min, the SEM images and composition mapping revealed that a film of Co-Sn alloy with a thickness of ca. 1 μm is deposited on the Ti surface and particles of around 0.5 μm of diameter are deposited on the Co-Sn film (Figure 2). Tabuchi et al. also found particles and agglomerates on the surface of all co-electrodeposited films [2]. In order to observe the well-adhered film, the electrode was cracked and thus the film was partially scraped out. The SEM-EDAX microanalysis and composition mapping revealed that the lower metallic film deposited on Ti exhibits a lower cobalt/tin atomic ratio (Co:Sn=1:3) in comparison with the upper submicrometric particles (Co:Sn=1:1.9)

placed on the film. This feature would involve that the kinetics of electrodeposition is more rapid for tin than cobalt. In fact, the reduction potentials of Sn (-0.136 V) and Co (-0.277 V) are different. Jung et al. also found a higher tin-content with increasing distance away from the substrate for Ni-Sn electrodeposited on copper [19].
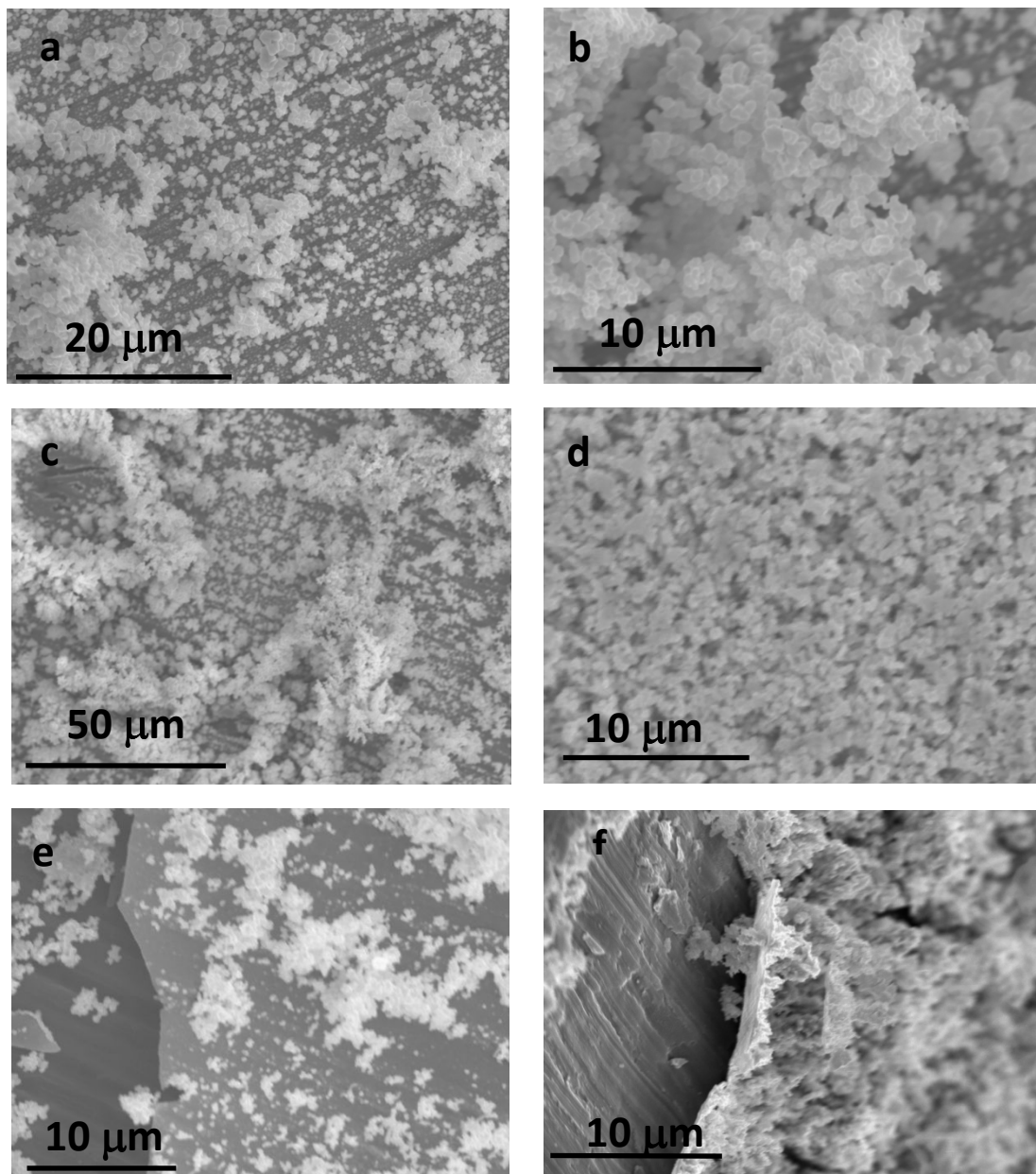

Figure 2. SEM micrographs of Co-Sn electrodeposited on Ti foil (a,b) during 5 minutes and (c-e) 20 minutes, and (f) 20 minutes followed by annealing at 200°C.

Throughout increasing the electrodeposition time from 5 to 20 minutes, the submicrometric particles tend to form aggregates of micrometric dimensions. After annealing the electrode at 200°C under vacuum, cracks are produced in the metallic film, being partially scraped out.

Electrodeposited PAN film

PAN was electrodeposited on a Co-Sn alloy film that was previously electrodeposited on Ti. The voltammograms of AN solutions at 100 mV/s show that the cathodic reaction and the consequent PAN deposition starts at around -2.0 V (Figure 3).

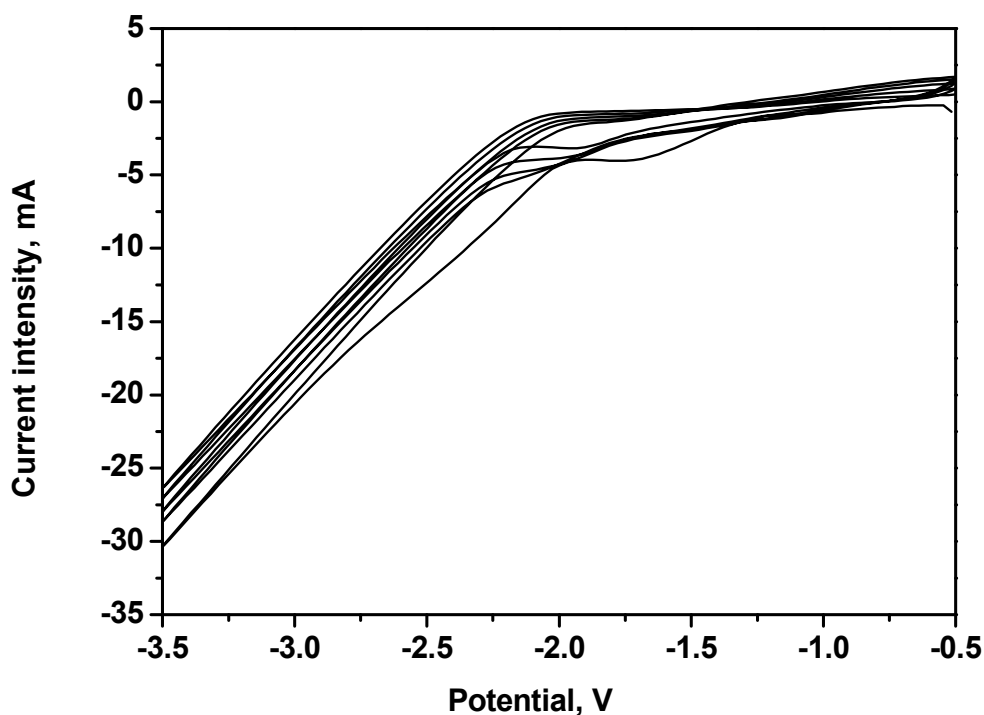**Figure 3. Five voltammetry cycles for PAN electrodeposition in the potential window between -3.5 and -0.5 V. Rate = 100 mV/s. Reference electrode = Ag/AgCl. Counterelectrode = Pt.**

The electrodeposited PAN film is amorphous to XRD. The presence of PAN was checked by using FTIR and SEM-EDAX microanalysis. The PAN powder was removed from a Ti support in which an excess of PAN was previously electrodeposited, and the

FTIR spectrum was recorded (Figure 4). The C≡N stretching mode is located at 2247 cm^{-1} for electrodeposited PAN. The –CH$_2$ group is observed at 1455 cm^{-1}. The peak at 1421 cm^{-1} may indicate the formation of cyclic structures during the electropolimerization. The band at around 3500 cm^{-1} is due to water. The interaction between the organic molecules and the metallic particles was described as a chemisorption process in the case of PAN grafted in metallic surfaces [17, 20].
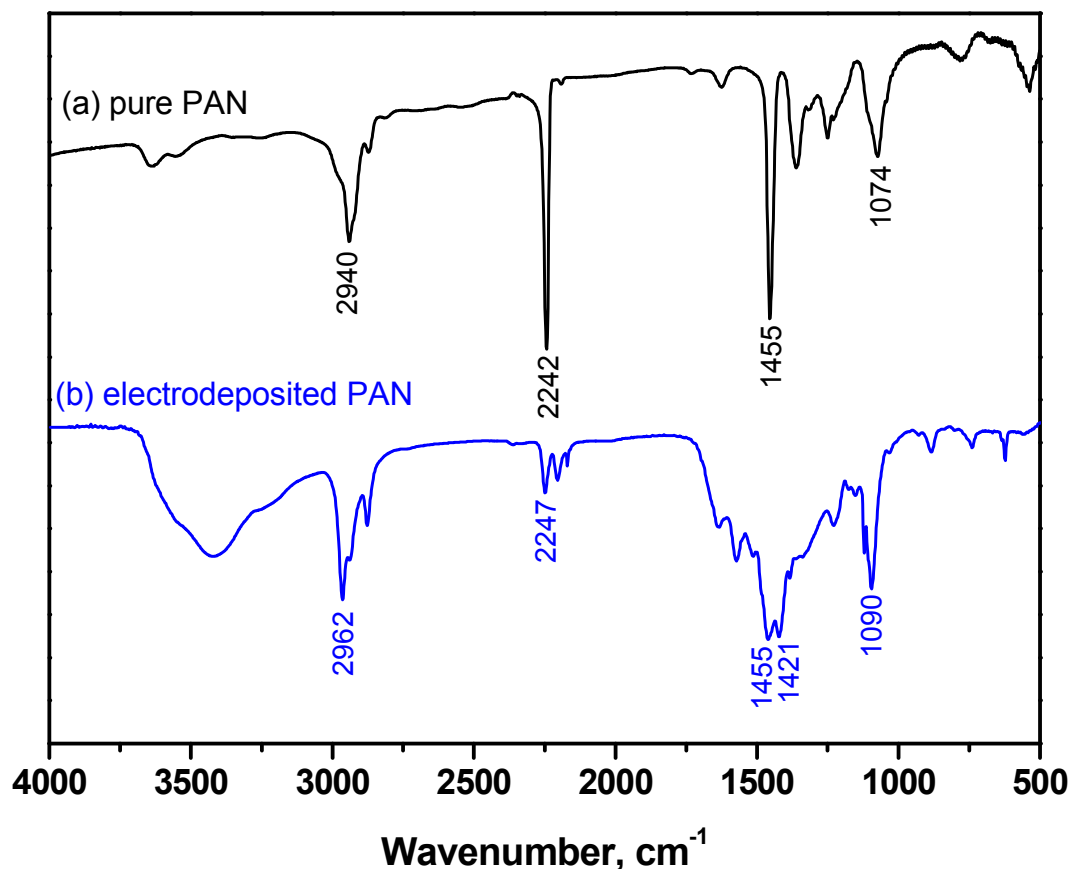
Figure 4. FTIR spectra of (a) commercial PAN and (b) PAN previously electrodeposited on titanium by using a solution of the monomer AN.

Selected SEM micrographs of PAN-containing electrodes are shown in Figure 5. According to EDAX microanalysis and composition mapping, the electrodeposition of PAN on the Co-Sn alloy resulted in the occurrence of carbon atoms homogenously distributed with an atomic ratio (Co+Sn):C=1:1.1, while carbon atoms were not detected in electrodes prepared without PAN. Microparticles deposited on the surface film can be observed in the electrode selected areas with cracks, as shown in Figure 5a,c. The

electrodeposition of an excess amount of PAN by applying 10 voltammetric cycles at slower rate (35 mV/s) resulted in the occurrence of spherical microparticles of PAN and a thick electrode material in the SEM images (Figure 5d), with poor adherence properties, and consequently not suitable for lithium batteries.
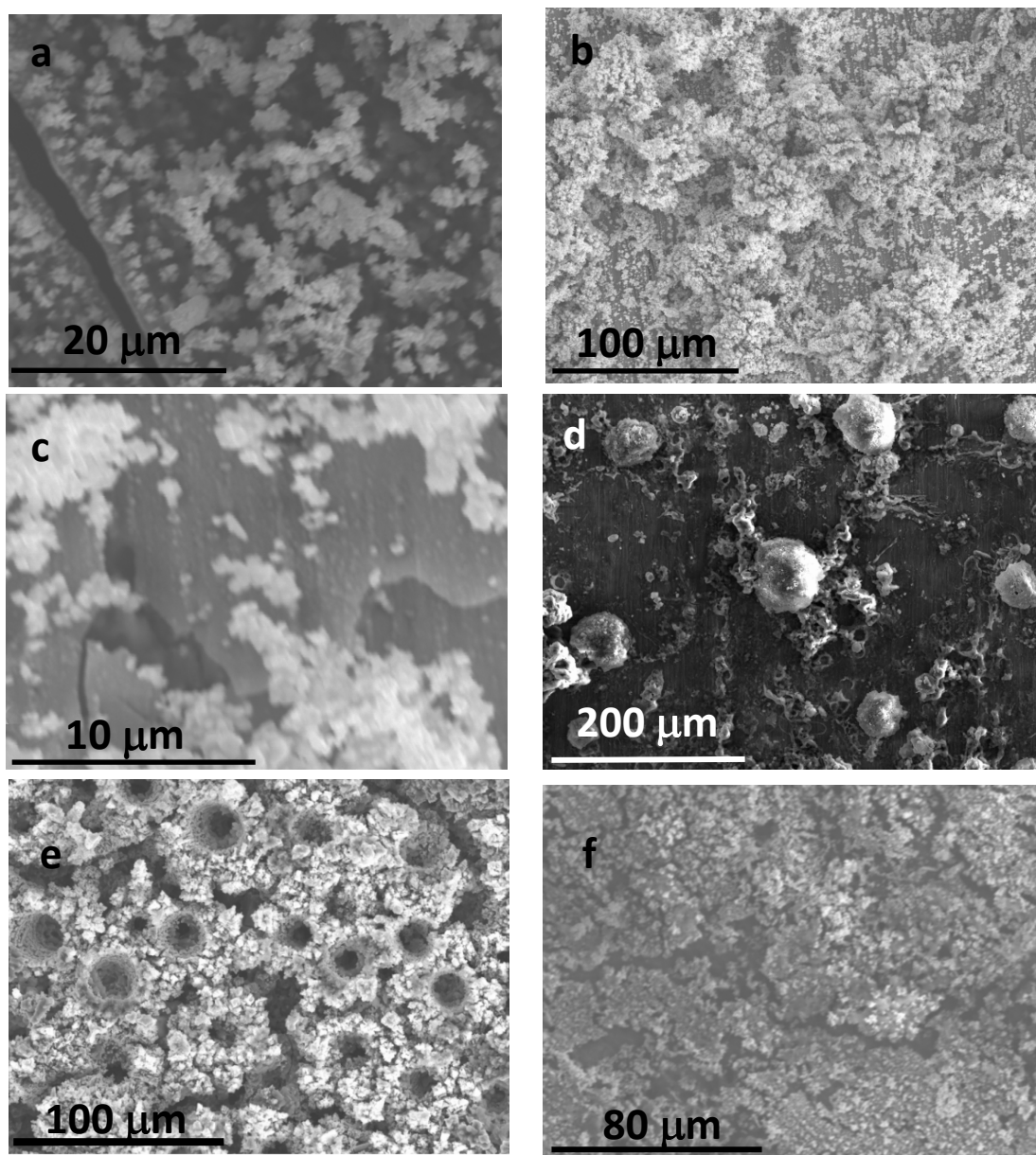

Figure 5. SEM micrographs of Co-Sn film/Ti electrodes after electrodeposition of PAN. The Co-Sn alloy was electrodeposited on Ti foil during (a) 5 minutes and (b-f) 20 minutes. (d) Same that b-c but with excess of electrodeposited PAN. (e) Same that b-c but the electrode was treated with LiPF$_6$ EC:DEC solution. (f) Same that b-c but the electrode was annealed at 200°C.

After electrodeposition of PAN on the electrode, a drop of DMF was added in order to improve the plasticization and gel formation properties of the PAN film. Then, the DMF solvent was removed by heating under vacuum. In order to obtain a PAN-Li$^+$ gel, the electrode was soaked into 1 M LiPF$_6$ in EC:DEC solution in the Ar-filled glove-box. After treatment with LiPF$_6$ EC:DEC, the topography of the electrode exhibits many microsized pores or cavities of ca. 25 μm diameters, and the walls of these microsized pores are made of agglomerated particles of a few micrometers that contain Co, Sn and C atoms according to the mapping of composition (Figure 5e). The morphology of this electrode is rather similar to the nickel-tin foam electrodeposited on copper that was reported by Jung et al [19]. These authors use the in-situ formed hydrogen bubbles for building the foams. In our case, the plasticizers and the evaporation of the solvent EC:DEC may build the peculiar morphology of the electrode particles. Many cracks of the metallic film are produced after annealing at 200°C (Figure 5f).

From the XRD, SEM, EDAX and FTIR results, the electrode containing PAN and Co-Sn film electrodeposited on a metallic support can be schematically represented as shown in Figure 6.
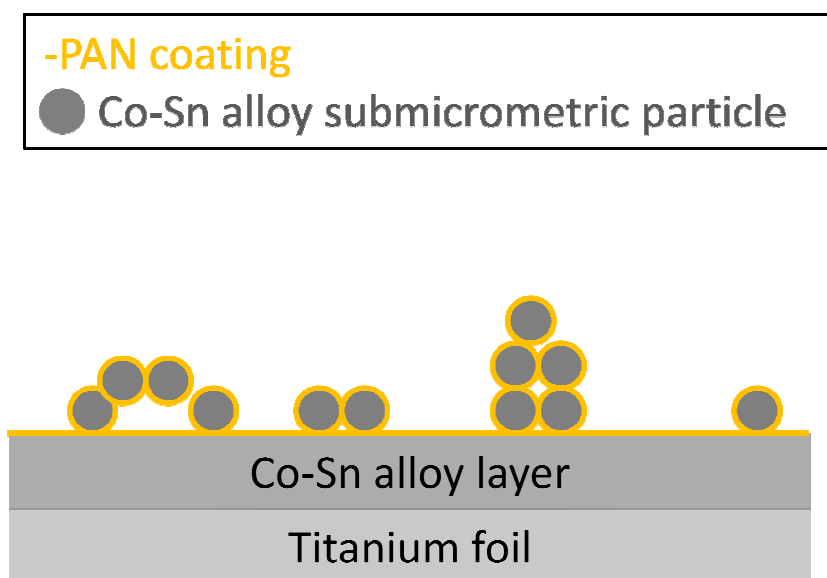
Figure 6. **Schematic representation of the electrode resulting of PAN electrodeposition on Co-Sn alloy film previously electrodeposited on Ti.**
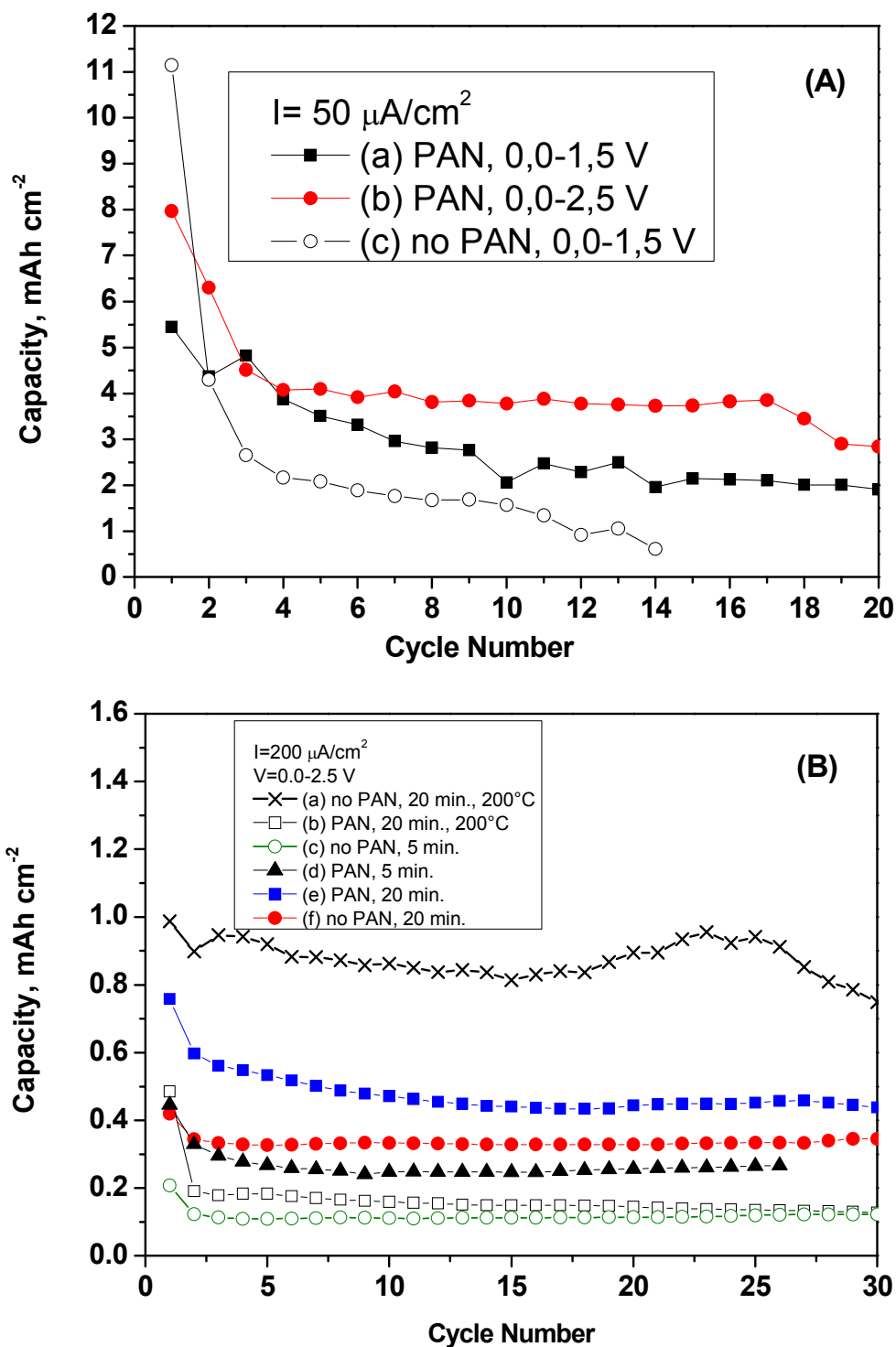
Figure 7. Areal capacities as a function of cycle number for electrodes of Co-Sn alloy electrodeposited on Ti with or without PAN. (A) Imposed current density I= 50 μA/cm² and electrodeposition time of alloy t= 20 minutes. (B) Imposed current density I= 200 μA/cm², potential window V=0.0-2.5 V and electrodeposition time of alloy t= 5 or 20 minutes.

Electrochemistry

The electrochemical cycling performance and efficiency under low cycling rate (Figure 7A) are poorer for the PAN-free sample.

Most probably the low kinetics enhances the irreversible processes such as electrolyte consumption and particle decrepitation. Reversible capacities of ca. 4 mAh/cm^2 and a coulombic efficiency of 80% in the first cycle are achieved for PAN-containing electrodes (Figure 7A a,b). This value is much higher than the previously reported for pure Sn deposited on Cu [7]. It seems that the PAN layer has some protective effect on the electrochemically active alloy. The morphology of the alloy is particularly adequate for achieving good cycling stability. The free space (voids) between the metallic particles can help to buffer the volume changes, while the adherence between the PAN and the metallic surfaces can contribute to preserve the integrity of the electrode. Under faster kinetics, the capacities are lower (Figure 7B).

The electrodes that contain Co-Sn alloy electrodeposited during 5 minutes (Figure 7B c,d) exhibit lower areal capacities than the electrodes containing Co-Sn alloy electrodeposited during 20 minutes (Figure 7B a,b,e,f), as expected from the different tin-content. The PAN-free electrode that was annealed at 200°C and contained the crystalline CoSn$_2$ phase has capacities of ca. 0.8 mAh/cm^2 in the first twenty cycles and then the capacity fades rapidly (Figure 7B a). The PAN-containing electrode annealed at 200°C shows lower capacities, probably due to the formation of cracks in the electrode and loss of electrical contact between the CoSn active material and the titanium substrate (Figure 7B b), and to the poorer electrochemical behavior of crystalline tin based materials in comparison to amorphous tin-cobalt electrode materials [21].

The potential-capacity (E vs. Q) and derivative (dQ/dV vs. E) plots are typical of the lithium alloying-dealloying processes in Co-Sn alloys (Figure 8). The reduction

peaks (lithium insertion) are observed at 0.44, 0.33, 0.24 and 0.04 V in the first discharge. The oxidation peaks (lithium extraction) are located at 0.45, 0.57, 0.60, 0.70 and 0.77 V. After five cycles, the peaks become more broadened. This indicates that tin atoms do not aggregate into larger particles.
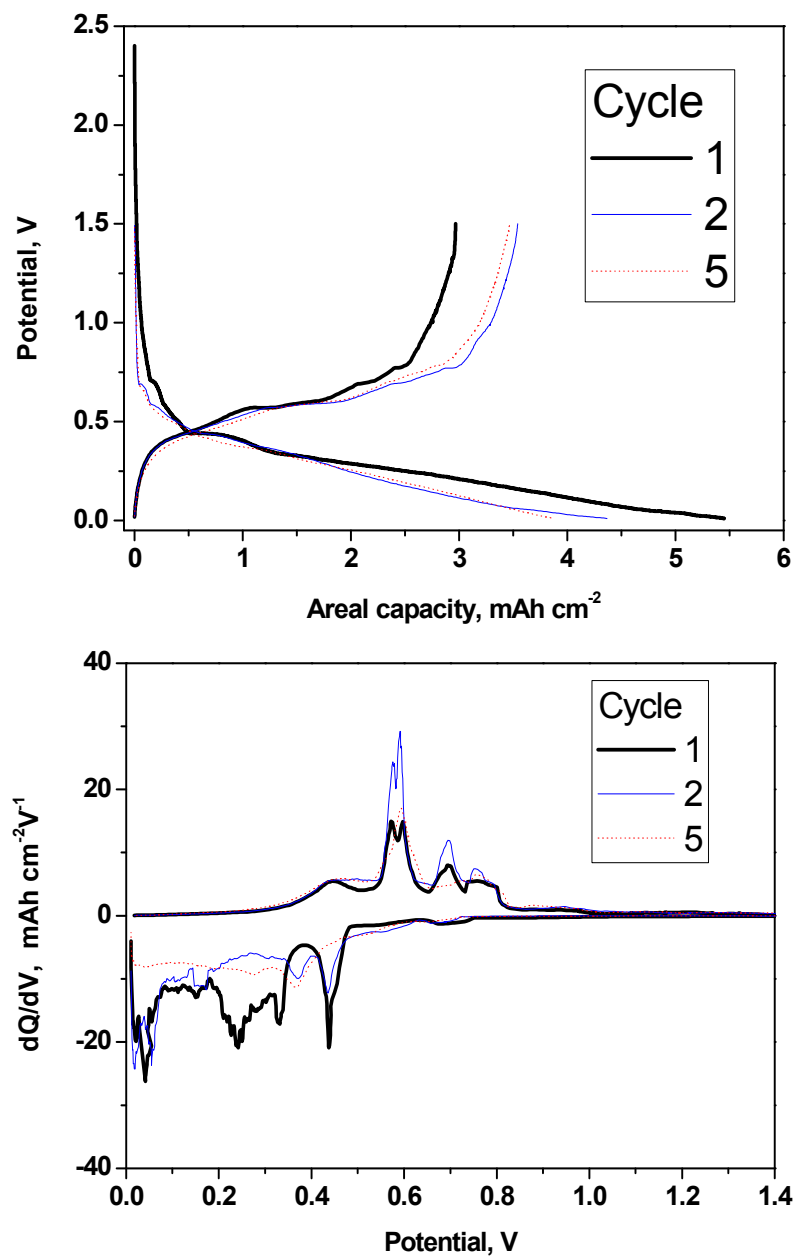

Figure 8. Potential-capacity and derivative plots for the cycle number 1, 2 and 5 of PAN/Co-Sn electrode (electrodeposition time t= 20 minutes). Imposed current density I=50 μA/cm^2.

Post-mortem analysis

The changes in volume of tin particles and the consequent strains generated during the electrochemical cycling is known to be a deleterious effect that can lead to electrode failure. In order to observe possible microstructural changes of the electrodes, the electrodes were recuperated after cycling and SEM micrographs were obtained. The PAN-free electrode has Co-Sn alloy particles with ca. 60 μm length and ca. 10 μm thickness deposited on the Ti support (Figure 9a), evidencing that the electrochemical cycling induces significant changes in the electrode microstructure.
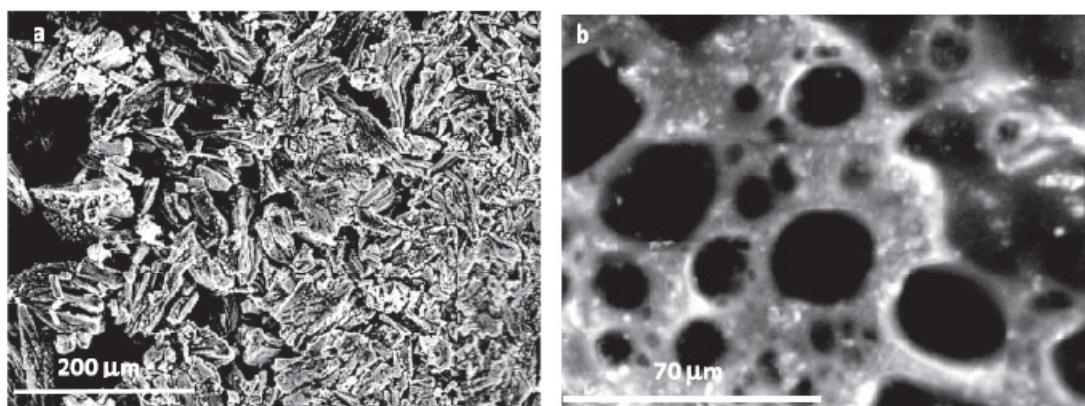
Figure 9. SEM micrographs for electrodes of Co-Sn alloy on Ti after 100 discharge-charge cycle in lithium cells for: (a) PAN-free electrode and (b) PAN-containing electrode.

After cycling, the electrode of PAN/Co-Sn alloy exhibits a more homogenous and continue morphology, with pores of ca. 10-25 μm diameter (Figure 9b) that resemble the electrode prior to cycling, shown in Figure 5.e. These results illustrate that the PAN film modifies the morpohological responde of the electrode during lithium insertion/extraction.

Impedance spectra

To further study the electrochemical behavior of the electrode materials and their interfacial phenomena, impedance spectra were recorded after discharge to 0.0 V vs. Li^+/Li at selected cycles (Figure 10). These spectra exhibit a depressed semicircle at high frequencies, another depressed semicircle at intermediate frequencies and a sloped line at low frequencies. According to generally accepted interpretations, these features are ascribed to transfer of lithium through the surface film that covers the electrochemically active material, charge transfer and lithium transfer across the surface film and the active mass, and lithium diffusion in the electrode active material (Warbug element) or cell capacitance, respectively [12, 22-25]. The formation of surface film on tin alloy has been reported by other authors [22, 26]. The semicircle at intermediate frequencies may involve several processes such as a combination of film resistance and charge transfer [27].

The spectra were fitted following the equivalent circuit [R_e +R_{sl}/Q_{sl} + (R_{ct}+W)/Q_{ct}] that is shown in Figure 10, which contains resistors (R), constant phase elements (Q) and a Warbug element (W). The resulting low resistance values are in good agreement with the thin film character of the electrodes. The impedance spectra of the PAN-containing electrode are little affected by the charge-discharge cycling.

The intersection of the impedance spectra with the horizontal axis (real part of the impedance) at 200 kHz represents the ionic resistance of the electrolyte (R_e). For the PAN-free electrode, the R_e values are in the 0.31-0.48 Ohm cm^2 range (Figure 11). The values of R_e are higher in the case of the PAN-containing electrode, occurring in the 0.88-1.22 Ohm cm^2 range. It is worth noting that the solid PAN layer would form a thicker and softer layer of PAN-Li^+ gel after being in contact with the liquid electrolyte $LiPF_6$ in EC:DEC. El-Enany et al. recently reported an ionic resistance of 1.4 Ohm cm^2 for PAN film grown on vitreous carbon after addition of 1 M $LiPF_6$ in propylene carbonate [16], in good agreement with our results. If we consider a value of ionic conductivity of $\sigma=4.8\times10^{-5}$ S cm^{-1} for PAN-Li^+ [28], and that the value of R_e=1.0 Ohm cm^2 is exclusively due to the conductivity of Li^+ through the PAN layer, the calculated thickness of the PAN-Li^+ gel layer is d=0.48 μm, which is a reasonable value.
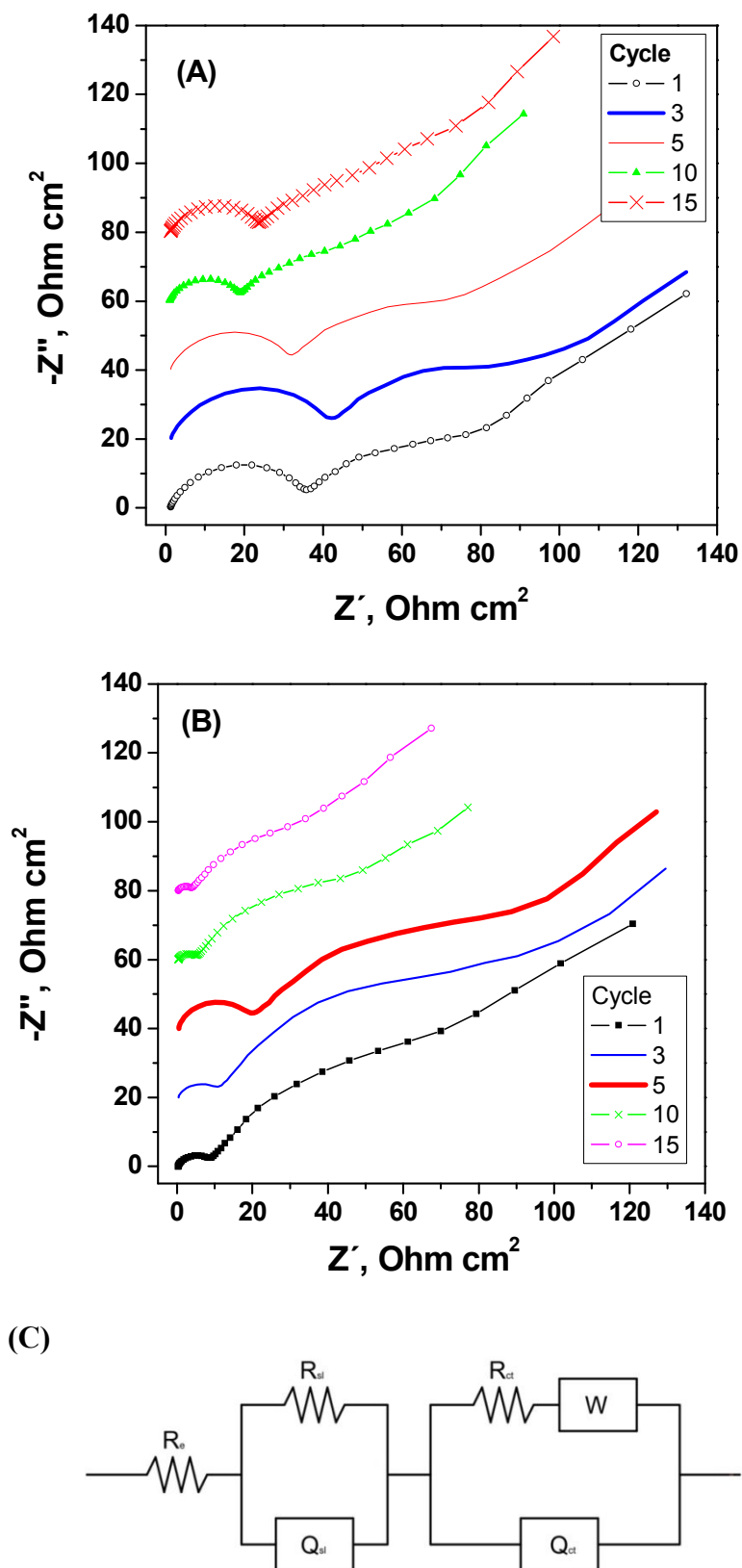
Figure 10. Impedance spectra (Nyquist plots) for (A) PAN-containing electrode and (B) PAN-free electrode, and (C) equivalent circuit. For the sake of clarity, the spectra have been skipped in the vertical axis.

Other studies reported higher values of ionic conductivities for PAN-Li$^+$ polymer electrolyte (σ=2.5x10^{-3} S cm^{-1}) [13, 14], and in this case the thickness of the layer would be d= 25 μm. For the sake of comparison, the film resistance of electrolytic Li$_3$PO$_4$ coating determined from the impedance spectra is in the order of kOhm which is equivalent to a conductivity of around 8x10^{-8} S cm^{-1}, as reported by Liu and Yen [29]. A lithium superionic conductor (Li$_{10}$GeP$_2$S$_{12}$) with 1.2x10^{-3} S cm^{-1} room temperature conductivity has been recently reported by Kamaya et al. and the ionic conductivity of a 1 M LiPF$_6$ liquid solution is around 10^{-2} S cm^{-1} [30].

Using the impedance results reported by Hassoun et al. [22], the initial film resistance corresponding to their tin electrode can be calculated to be around 10-13 Ohm cm^2, which is in good agreement with the experimental results that we obtain for R$_{sl}$ of metallic electrode with no PAN (2.7-21.2 Ohm cm^2 from cycle 1 to 25).

The size of the semicircle at high frequencies and the corresponding resistance of the surface layer (R$_{sl}$) are higher for the PAN-containing electrode (14.3-44.9 Ohm cm^2), suggesting a lower conductivity of the PAN-Li$^+$ gel-tin alloy interphase and/or a thicker surface film in comparison with the liquid electrolyte-tin alloy interphase. After ca. 11 cycles, the amplitude of the semicircle at high frequencies and R$_{sl}$ do not change significantly for both electrodes.

For the PAN-free electrode, a strong decrease of the charge transfer resistance (R$_{ct}$) is observed when the cycle number increases from 1 to 14. This feature involves the modification of the active material, suggesting an increase in effective active area, most probably due to the cracking of the particles due to the strain associated to insertion-deinsertion processes as was previously observed during the first five cycles for tin-based alloys [27]. In the same sense, Du et al. observed little changes in the surface film resistance while the charge transfer resistance changed in the first 30 cycles for Sn electrodeposited on Cu foam [31]. From cycle 16 to 25, the charge transfer of the PAN-free electrode tends to increases. The charge transfer resistance of the PAN-containing electrode exhibited little change from cycle 1 to 17. From all these impedance spectroscopy results shown above, we can conclude that PAN contributes to buffer the volume changes, while the active material/PAN interface and electrical contacts within the active material are maintained on cycling.
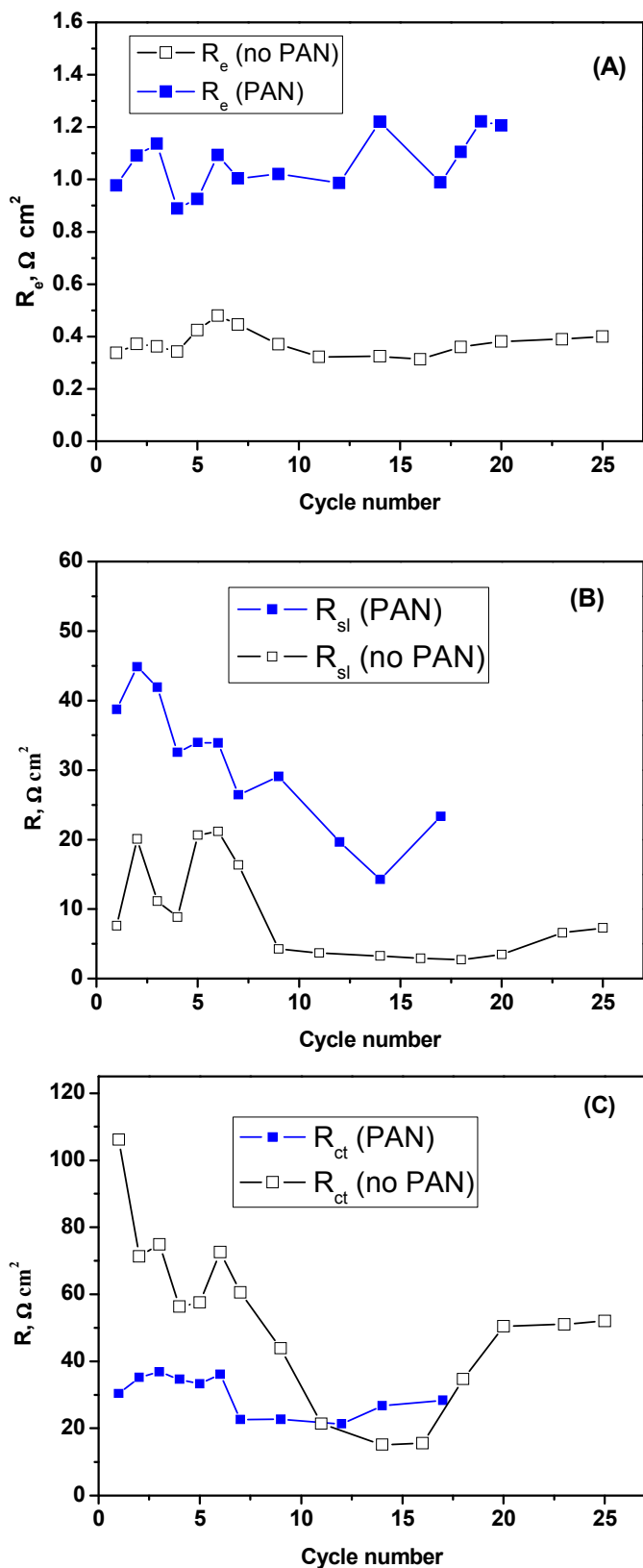
Figure 11. Resistance values obtained from the fitting of the EIS results. (A) Electrolyte resistance (R_e). (B) Surface layer resistance (R_{sl}). (C) Charge transfer resistance (R_{ct}).

4.1.4 Conclusions

The electrodeposition of Co-Sn films on a flat Ti substrate can yield to high areal capacities electrodes. The observed electrodeposited metallic film contains Sn, amorphous Co-Sn alloy and intermetallic phases distributed in a thin film and submicrometric particles. The electropolymerization of PAN on the tin-cobalt electrodes results in electrodes with more stable interfaces. Consequently, the resulting electrode can be described as a composite material containing metallic and organic phases. The composition and thickness of the Co-Sn alloy film and the PAN film may be optimized with further future studies.

Acknowledgements

References

1. N. Tamura, M. Fujimoto, M. Kamino and S. Fujitani, *Electrochim. Acta*, **49**, 1949 (2004).

2. T. Tabuchi, N. Hochgatterer, Z. Ogumi and M. Winter, *J. Power Sources*, **188**, 552 (2009).

3. K. Ui, S. Kikuchi, Y. Jimba and N. Kumagai, *J. Power Sources*, **196**, 3916 (2011).

4. A.D.W. Todd, P.P. Ferguson, J.G. Barker, M.D. Fleischauer and J.R. Dahn, *J. Electrochem. Soc.*, **156**, A1034 (2009).

5. J. Wang, N. Du, H. Zhang, J. Yu and D. Yang, *J. Phys. Chem. C*, **115**, 23620 (2011).

6. D. Jian, H. Tian, C. Qiu, X. Ma and Y. Fu, *J. Solid State Electrochem.*, **15**, 2639 (2011).

7. L. Bazin, S. Mitra, P.L. Taberna, P. Poizot, M. Gressier, M.J. Menu, A. Barnabé, P. Simon and J.M. Tarascon, *J. Power Sources*, **188**, 578 (2009).

8. Z. Du, S. Zhang, Y. Xing and X. Wu, *J. Power Sources*, **196**, 9780 (2011).

9. C. Yang, D. Zhang, Y. Zhao, Y. Lu, L. Wang and J.B. Goodenough, *J. Power Sources*, **196**, 10673 (2011).

10. L. Xue, Z. Fu, Y. Yao, T. Huang and A. Yu, *Electrochim. Acta*, **55**, 7310 (2010).

11. C. Arbizzani, M. Lazzari and M. Mastragostino, *J. Electrochem. Soc.*, 152, A289 (2005).

12. L.J. Xue, Y.F. Xu, L. Huang, F.S. Ke, Y. He, Y.X. Wang, G.Z. Wei, J.T. Li and S.G. Sun, *Electrochim. Acta*, **56**, 5979 (2011).

13. B. Huang, Z. Wang, L. Chen, R. Xue and F. Wang, *Solid State Ionics*, **91**, 279 (1996).

14. K.M. Abraham, H.S. Choe and D.M. Pasquariello, *Electrochim. Acta*, **43**, 16 (1998).

15. U.G. Nwokeke, F. Nacimiento, R. Alcántara and J.L. Tirado, *Electrochem. Solid-State Lett.*, **14**, A148 (2011).

16. G. El-Enany, M.J. Lacey, P.A. Johns and J.R. Owen, *Electrochem. Commun.*, **11**, 2320 (2009).

17. G. Lecayon, Y. Bouizem, C. Le Gressus, C. Reynaud, C. Boiziau and C. Juret, *Chem. Phys. Lett.*, **91**, 506 (1982).

18. H. Kim and J. P. Cho, *J. Electrochem. Soc.*, **154**, A462 (2007).

19. H.R. Jung, E.J. Kim, Y.J. Park and H.C. Shin, *J. Power Sources*, **196**, 5122 (2011).

20. S. Leroy, C. Boiziau, G. Lécayn, C. Le Gressus, C. Makram and J.P. Vogouroux, *Mater. Lett.*, **3**, 239 (1985).

21. R.G. Zhang and M.S. Whittingham, *Electrochem. Solid-State Lett.*, **13**, A184 (2010).

22. J. Hassoun, P. Reale and S. Panero, *J. Power Sources*, **174**, 321 (2007).

23. D. Aurbach, *J. Power Sources*, **89**, 206 (2000).

24. F. Nacimiento, R. Alcántara and J.L. Tirado, *J. Electrochem. Soc.*, **157**, A666 (2010).

25. M. Chamas, P.E. Lippens, J.C. Jumas, J. Hassoun, S. Panero and B. Scrosati, *Electrochim. Acta*, **56**, 6732 (2011).

26. S.D. Bettie, T. Hatchard, A. Bonakdarpour, K.C. Hewitt and J.R. Dahn, *J. Electrochem. Soc.*, **150**, A701 (2003).

27. J. Hassoun, P. Ochal, S. Panero, G. Mulas, C.B. Minella and B. Scrosati, *J. Power Sources*, **180**, 568 (2008).

28. Y.T. Chen, Y.C. Chuang, J.H. Su, H.C. Yu and Y.W. Chen-Yang, *J. Power Sources*, **196**, 2802 (2011).

29. H.C. Liu and S.K. Yen, *J. Power Sources*, **159**, 245 (2006).

30. N. Kamaya, K. Homma, Y. Yamakawa, M. Hirayama, R. Kanno, M. Yonemura, T. Kamiyama, Y. Kato, S. Hama, K. Kawamoto and A. Mitsui, *Nature Materials*, **10**, 682 (2011).

31. Z. Du, S. Zhang, T. Jiang and Z. Bai, *Electrochim. Acta*, **55**, 3537 (2010).

4.2 Improving the electrochemical properties of self-organized titanium dioxide nanotubes in lithium batteries by surface polyacrylonitrile electropolymerization

Francisco Nacimiento, José R. González, Ricardo Alcántara, Gregorio F. Ortiz, José L. Tirado

Abstract

The surface of the amorphous TiO_2 nanotubes is critical to achieve high capacity, cycling stability and high rate performance. In order to improve the stability of nanotubular titanium dioxide electrodes in lithium batteries, polyacrylonitrile (PAN) has been deposited by electropolymerization. Self-organized TiO_2 nanotubes were prepared by titanium anodization with different aspect ratios. After electropolymerization, electron microscopy, composition mapping and XPS data confirmed that electrododeposited PAN covered the complete surface of open ends of the nanotubes, exclusively. The resulting electrode material was tested in lithium cells, and showed reversible areal capacities in the order of 0.5 $mAhcm^{-2}$ and good cycling behavior and within a wide potential window (0.0–3.0 V). The improvement of the electrochemistry is more evident for the lower aspect ratio nt-TiO_2, with capacity values normalized by the nanotubes length of around 0.25 mAh cm^{-2} μm^{-1} at slow rate. An areal capacity of 0.26 mAh cm^{-2} is delivered at 75C rate. The ion-conducting PAN layer ensures lithium ion access to the nanotubes, protects the open end surface from undesirable reactions with the electrolyte and provides enhanced mechanical stability to the electrode and lower charge transfer resistance.

4.2.1 Introduction

It is well known that self-organized titanium dioxide nanotubes (nt-TiO$_2$) can be grown by anodization of a titanium flat surface without the need of templates [1,2]. In recent years, the use of nt-TiO$_2$ in field of lithium ion batteries was found to be particularly promising [3,4]. Besides the lower theoretical capacity for lithium intercalation into TiO$_2$ (335 mAhg^{-1} for a maximum LiTiO$_2$ stoichiometry) as compared with graphite (372 mAhg^{-1}), the higher voltage for Li intercalation could avoid lithium electroplating processes and thus increase the safety of current lithium-ion batteries. In addition to the insertion of Li into TiO$_2$ by a faradaic-type reaction involving the Ti^{4+}/Ti^{3+} redox pair, lithium ions may also be stored in the surface of the TiO$_2$ nanoparticles and increase the overall capacity by pseudocapacitive reactions and double layer phenomena [5,6]. In this line, Borghols et al. proposed that part of the extra capacity for amorphous TiO$_2$ nanoparticles may be due to the reversible lithium storage in the form of Li$_2$O at the TiO$_2$ surface [7]. For nt-TiO$_2$, a greater proportion of surface sites for reaction with lithium and a smaller proportion of interstitial sites for lithium insertion into bulk TiO$_2$ would be expected.Moreover, the high aspect ratio of nt-TiO$_2$, defined as the nanotube length-to-outer diameter ratio, allows achieving higher areal capacities, which is particularly useful for the development of 3D microbatteries with high power density and fast charge properties [4,8].

On the other hand, some limitations are inherent to the use of TiO$_2$ electrodes. Both the Jahn-Teller effect of Ti^{3+} ions and phase transitions can produce strains in crystalline TiO$_2$ and capacity fade on electrochemical charge-discharge cycling. In contrast, nanoparticles of amorphous or poorly crystalline TiO$_2$ can show better cycling stability.However, since the nanoparticles usually exhibit high specific areas, the irreversible reactions with the electrolyte at the surface of the electrode are favored and commonly lead to poor coulombic efficiencies. In order to avoid these drawbacks, the use of organic polymers such as lithium ion-conducting polymers can increase the electrochemical performance, stability and safety of the electrodes [8, 9]. The polymers also may be used for future all-solid state lithium ion microbatteries [10].

It is known that polyacrylonitrile (PAN) films can be electrodeposited on oxide, carbon and metallic substrates [11,12]. In this work, PAN is deposited by electropolymerization on high-length nt-TiO$_2$ previously obtained by anodization of a

titanium foil, and the electro-chemical behavior of the resulting nt-TiO$_2$/PAN electrode in lithium batteries is studied.

4.2.2   Experimental

nt-TiO$_2$ were grown on a high-purity titanium foil supplied by Aldrich. The anodization process was carried out with an Agilent apparatus by alternatively imposing 60 V for 120 min, or 150 V during 25 min. At 150V, the titanium electrode is completely dissolved after ca. 40 min. A platinum electrode was used as counter electrode. The electrolyte solution was 0.3% wt NH$_4$F in ethylenglycol:water (92:8 vol.) mixture.

The deposition of PAN on the nt-TiO$_2$ films was performed by electropolymerization from a 2 M acrylonitrile (CH$_2$CHCN) and 0.05 M tetrabutylammonium perchlorate solution in acetonytrile submitted to a single voltammetry cycle at 100 mVs^{-1} of sweep rate within the –0.5/–3.5 V potential window. For the sake of comparison a thicker PAN layer was also grown using 10 cyclic voltammetry (CV) sweeps. As reference and counter electrodes, Ag/AgCl and Pt were used, respectively. A Biologic-VMP instrument was used to control the PAN electrodeposition.

X-ray diffraction (XRD) patterns were recorded with a Siemens D5000 instrument with CuKα radiation and 0.02/°2θ steps. The morphology and composition of the prepared electrode materials was examine in a JEOL SM6300 Scanning Electron Microscopy (SEM) instrument equipped with Energy-Dispersive X-ray Spectroscopy (EDS) microanalysis and in a Philips CM10 Transmission Electron Microscopy (TEM) instrument. The X-ray Photoelectrons Spectroscopy (XPS) measurements were performed in a SPECS Phobios 150MCD instrument using Mg Kα source (1253.6 eV) and chamber pressure of 4×10^{-9} mbar. The C1s peak at 284.8 eV of adventitious carbon was used as reference. In-depth profiles were obtained by ionic erosion using ion sputtering performed with 4 kV Ar$^+$ beam raster over a 5×5 mm^2 area. Peak areas and sensitivity factors provided by the instrument producer were applied to quantify the atomic surface concentrations. A Shirley baseline type was applied.

The electrochemical cycling (discharge-charge) was performed with a Biologic-VMP instrument. The lithium cells (Swagelok-type) were mounted in a dry box under Ar atmosphere. A piece of Li was used as negative electrode, and the titanium-based foil was used as positive electrode. The positive electrode was dried at 120∘C under vacuum before mounting the electrochemical cell. The electrolyte solution was 1 M LiPF6 in ethylene carbonate:diethyl carbonate EC:DEC = 1:1 solvent mixture. Impedance spectra in the 200 kHz–10 mHz range were recorded in a Biologic-VMP instrument in the discharge state (0.0 V) and using three-electrode cell (T-geometry cell).

4.2.3   Results and discussion

The XRD patterns of the pristine titanium foil (Figure 1Aa), anodized titanium at 60V (Figure 1Ab) and at 150V (Figure 1Ba) and the corresponding anodized titanium films after PAN electrodeposition (Figure 1Ac, Bb) are shown. After anodizing the titanium metal foil, a hump is observed in the XRD pattern at around 15–35/$^\circ$2-theta, while the reflections of the metallic titanium substrate are preserved. The hump is ascribed to amorphous titanium oxide. The XRD peaks of TiO_2 tetragonal anatase phase emerged after annealing at 300°C and the band of the amorphous phase disappeared, as reported elsewhere [3,4].

The amorphous titania films grown on the titanium substrate were examined in the SEM instrument and mechanical fractures were used for lateral views. The TEM micrographs were obtained on the amorphous nt-TiO_2 scraped from the substrate and dispersed in acetone with ultrasonication. The morphology and microstructure of the titania nanotubes can be tailored by controlling anodization voltage and time, among other parameters [1–4]. The results in Figure 2 show that densely packed TiO_2 nanotubes form a planar array with their axes perpendicular to the surface of the titanium substrate. The anodization at 60 V during 120 min produces the following nanotube dimensions: length of ca. 10 μm, inner diameter in the 42–50 nm range and total diameter of ca. 150 nm, which lead to an aspect ratio around 67. These nanotubes will be henceforth referred to as high aspect ratio nt-TiO_2. For the anodization at 150 V during 25 min, the length is ca. 2 μm, the inner diameter is ca. 55 nm, the outer diameter ca. 150 nm and the aspect ratio around 13 (low aspect ratio nt-TiO_2).
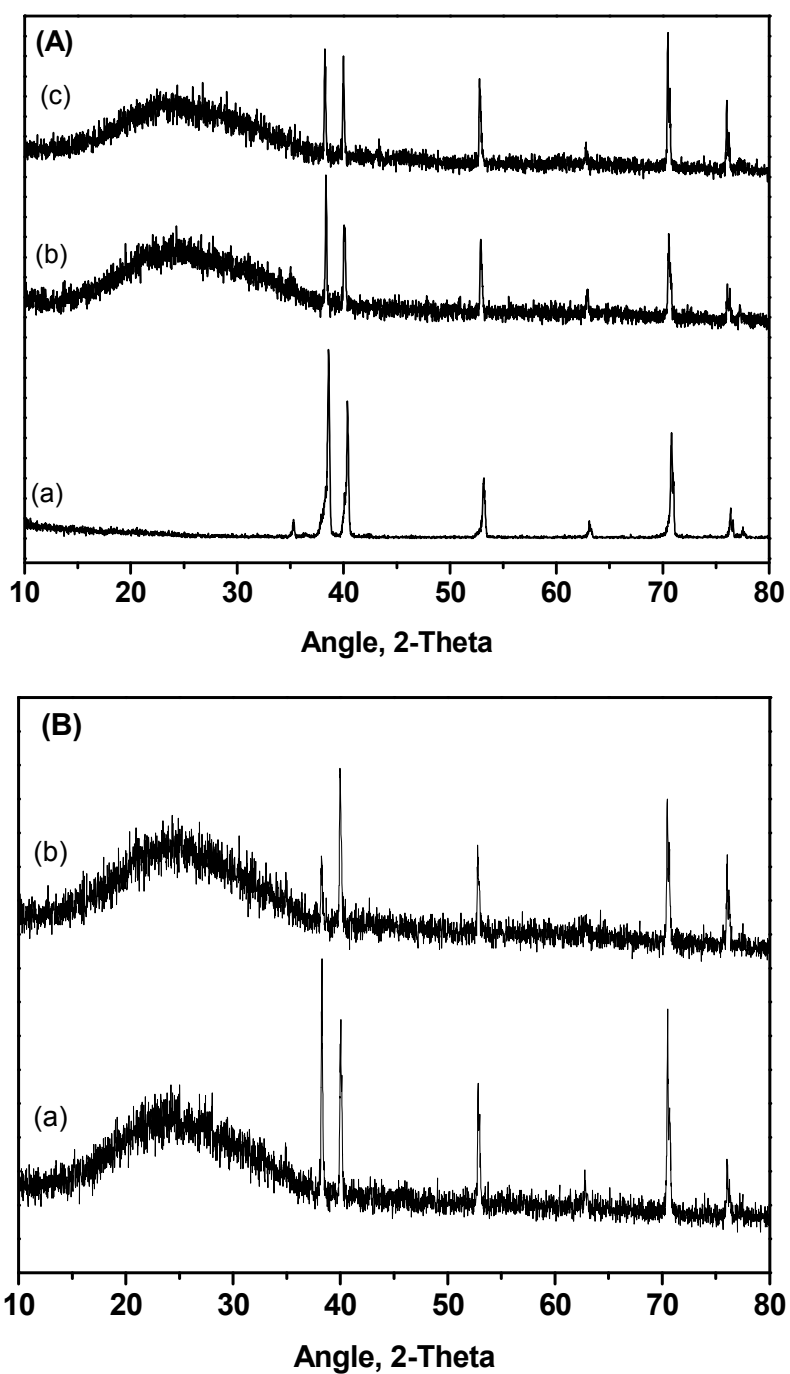
Figure 1. (A) XRD patterns for **(a)** pristine titanium foil, **(b)** anodized titanium foil **(60 V-120 min)** and **(c)** electrodeposited PAN on previously anodized titanium foil. **(B)** XRD patterns for **(a)** anodized titanium foil **(150 V-25 min)** and **(b)** electrodeposited PAN on previously anodized titanium foil.
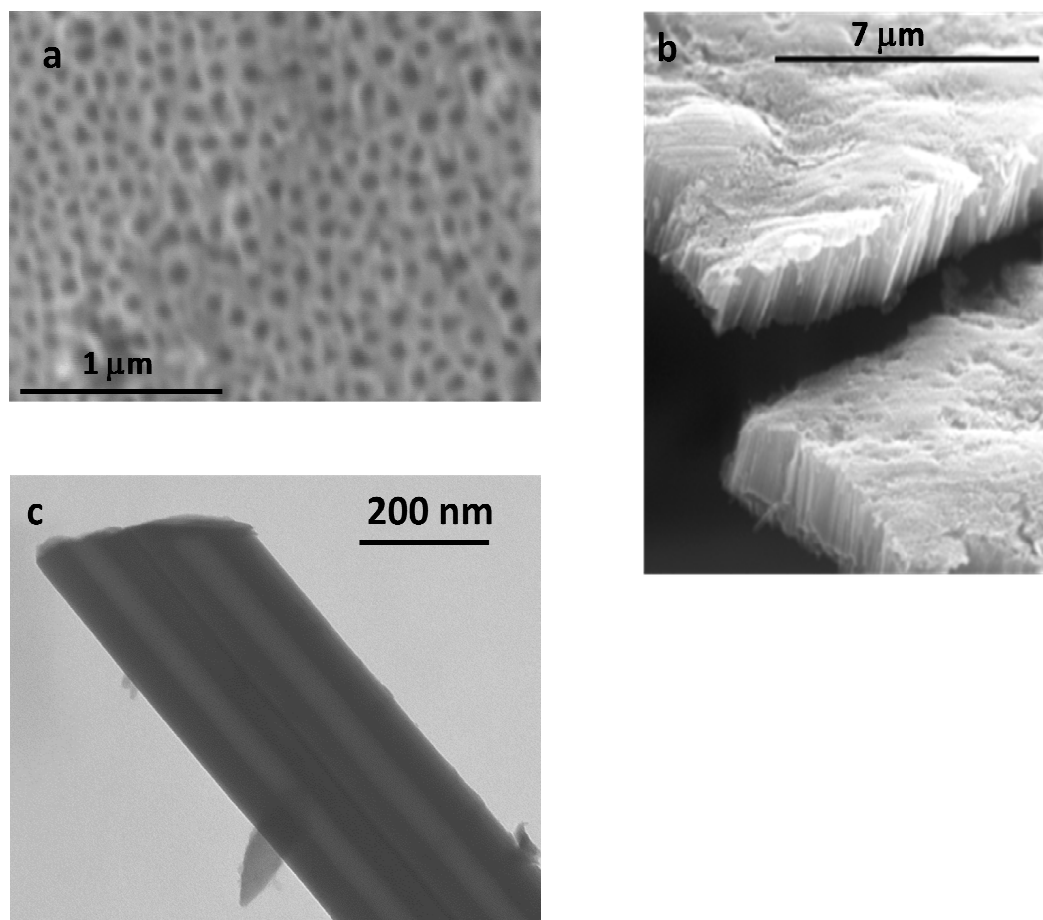
Figure 2. Selected SEM micrographs of nt-TiO$_2$ obtained at (a, b) 150 V-25 min and (c) TEM micrograph of nt-TiO$_2$ obtained at 60 V-120 min.

Although it may seem that anodization time is the main factor that controls nanotube length, further discussion is needed based on previously reported results. Thus, nanotubes obtained by anodization at 42–60 V for 30 min are poorly formed and their length is only ca. 1 μm [4]. In order to obtain well-formed nanotubes after anodization during only 25 min, a very high voltage (150 V) was needed. Well-formed nanotubes mean that individual nanotubes with inner cavity of ca. 40–50 nm and an open end are clearly observed by electron microscopy. However, a very high voltage (e.g. 150 V) limits the maximum anodization time because the solution temperature increases and consequently the titania film is completely dissolved. On the contrary, longer and well-formed nanotubes could be grown at 60 V with longer anodization time (120 minutes). Summarizing, in this study we have compared titania nanotubes that are equivalent in diameter but differ in length. In both cases, the high packing density

decreases the outer surface of nt-TiO$_2$ that can be exposed to the electrolyte in lithium batteries. However, the irreversible reactions at the interface between the nt-TiO$_2$ surface and the electrolyte would be reduced and the mechanical stability would increase by protective coating with a polymeric film.

After PAN electrodeposition on nt-TiO$_2$, the XRD patterns of the electrode materials are not substantially modified (Figure 1). However, the results of SEM, microanalysis, TEM and XPS confirm the presence of PAN. Composition microanalysis and mapping were performed in the SEM equipped with EDS-type detector, working with a 90◦ angle between the electrode surface and the primary electrons beam. The electrodeposition of PAN on the titania surface was revealed by an increase in the C/Ti atomic ratio from 0.0 to 0.64. In addition, the composition maps of tilted nt-TiO$_2$/PAN layers are shown in Figure 3 for carbon (from electrodeposited PAN) and titanium (from nt-TiO$_2$) evidence that PAN molecules are present on only one end of the nanotubes.
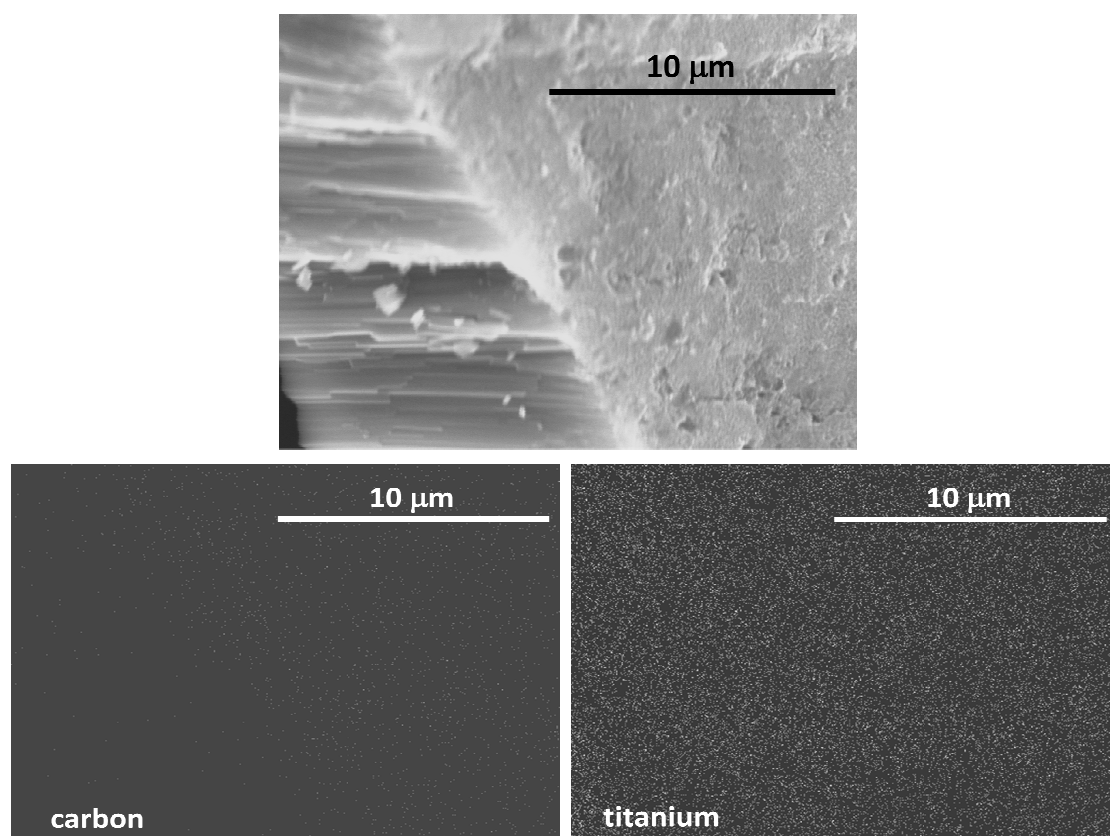

Figure 3. SEM micrograph of nt-TiO$_2$ (60 V-120 min)/PAN (CV1) and the corresponding composition mappings for carbon and titanium.

250

Taking into account that the volume of the sample from which the X-rays are analyzed (sampling volume) is in the order of $2\mu m^3$, we can conclude that a thin film of PAN is deposited on the open ends of the titania nanotubes. In other words, the PAN molecules are not deposited on the inner walls of nt-TiO_2 below a reduced distance from the open end. On the other hand, the TEM micrographs of the nt-TiO_2/PAN powder scraped from the Ti sheet reveal the occurrence of TiO_2 nanotubes and organic material in separate regions (Figure 4). This can be interpreted by assuming that the sample suffers modifications and the PAN film is detached from the nanotubes open ends during the preparation of the specimen for TEM examination by ultrasonication in acetone medium.
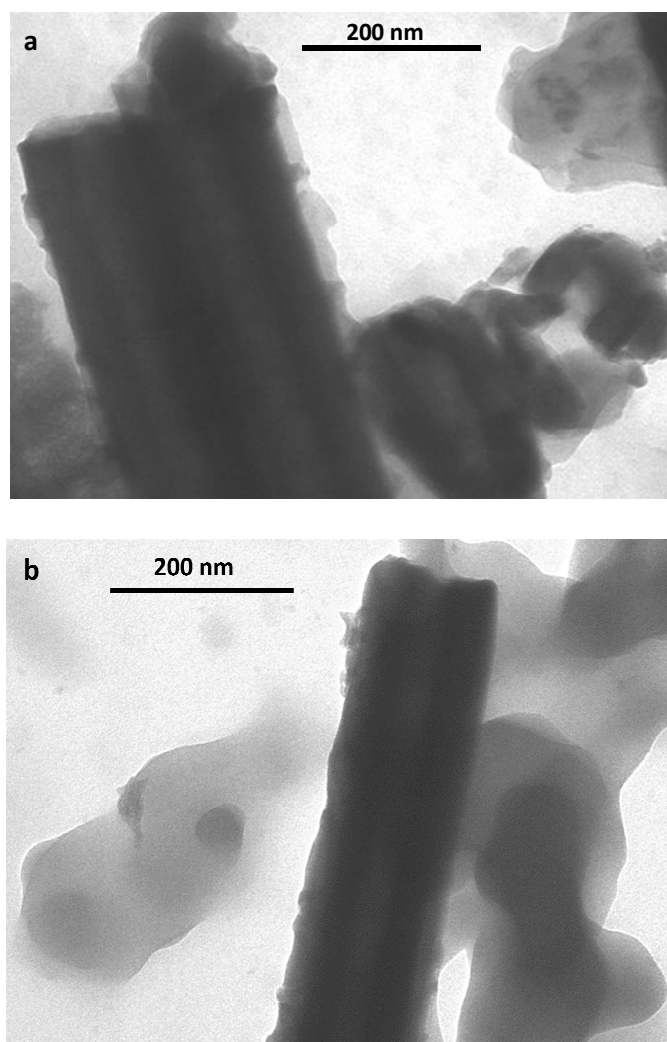

Figure 4. TEM micrographs of nt-TiO_2 (60 V-120 min)/PAN scraped from the Ti sheet for PAN electrodeposited using (a) a single voltammogram cycle and (b) ten voltammogram cycles.

In order to further corroborate the electrodeposition of PAN on nt-TiO$_2$, XPS measurements were performed for the nt-TiO$_2$ (60 V–120 min)/PAN samples obtained by cyclic voltammetry (CV) using 1 cycle (CV1) and 10 cycles (CV10). For the sake of comparison, the XPS spectra of PAN-free nt-TiO$_2$ are shown in Figure 5. For nt-TiO$_2$/PAN electrodes, the XPS spectra for C1s, O1s, N1s and Ti2p binding energies are displayed in Figure 6. One of the most significant features is the observation of the N1s region for nt-TiO$_2$/PANsamples, which does not occur for PAN-free samples, as expected. The C1s region in both Figures 5 and 6 includes the contribution of contaminant surface carbon. It can be decomposed into three components assigned to C–C (284.9 eV), CO or C bonded to N (286.5 eV) and O–C=O (288.6 eV) [13]. The relative contribution of peak 2 increases from Figure 5 and upon increasing the number of CV cycles in Figure 6.
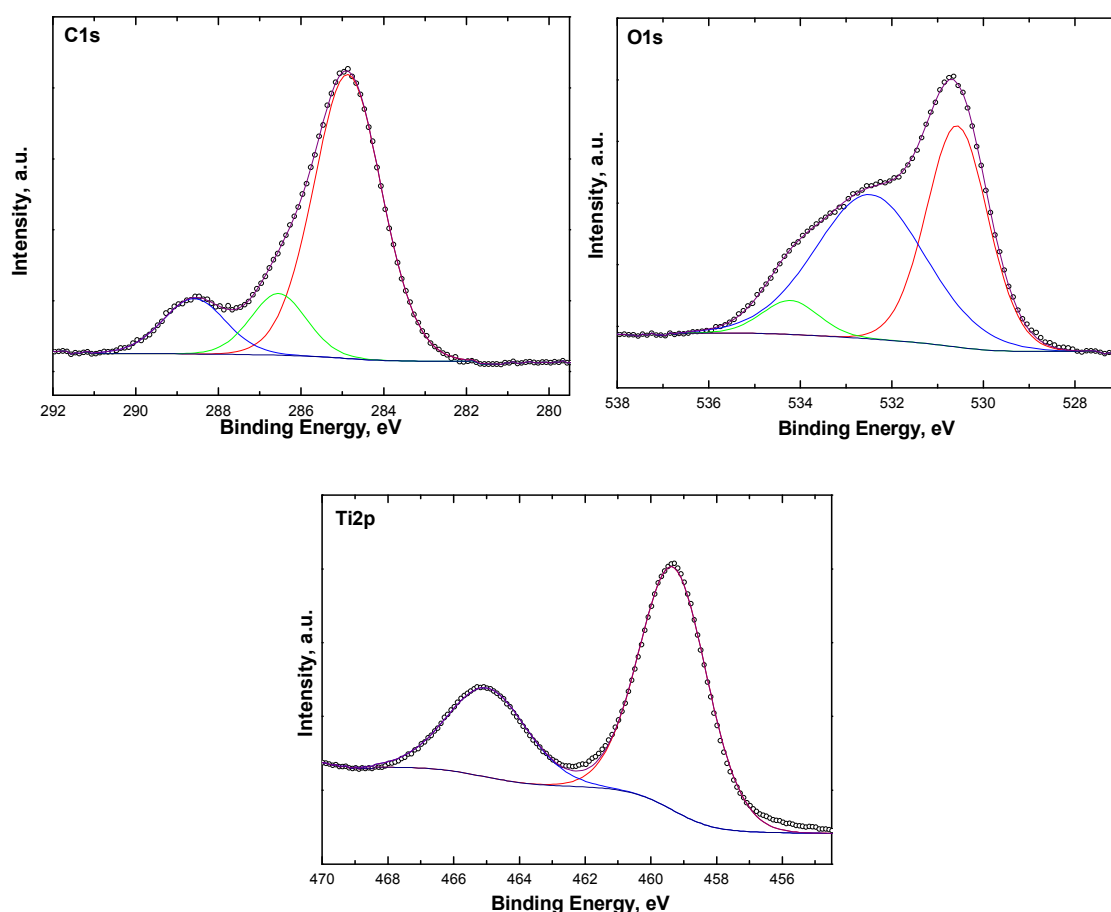

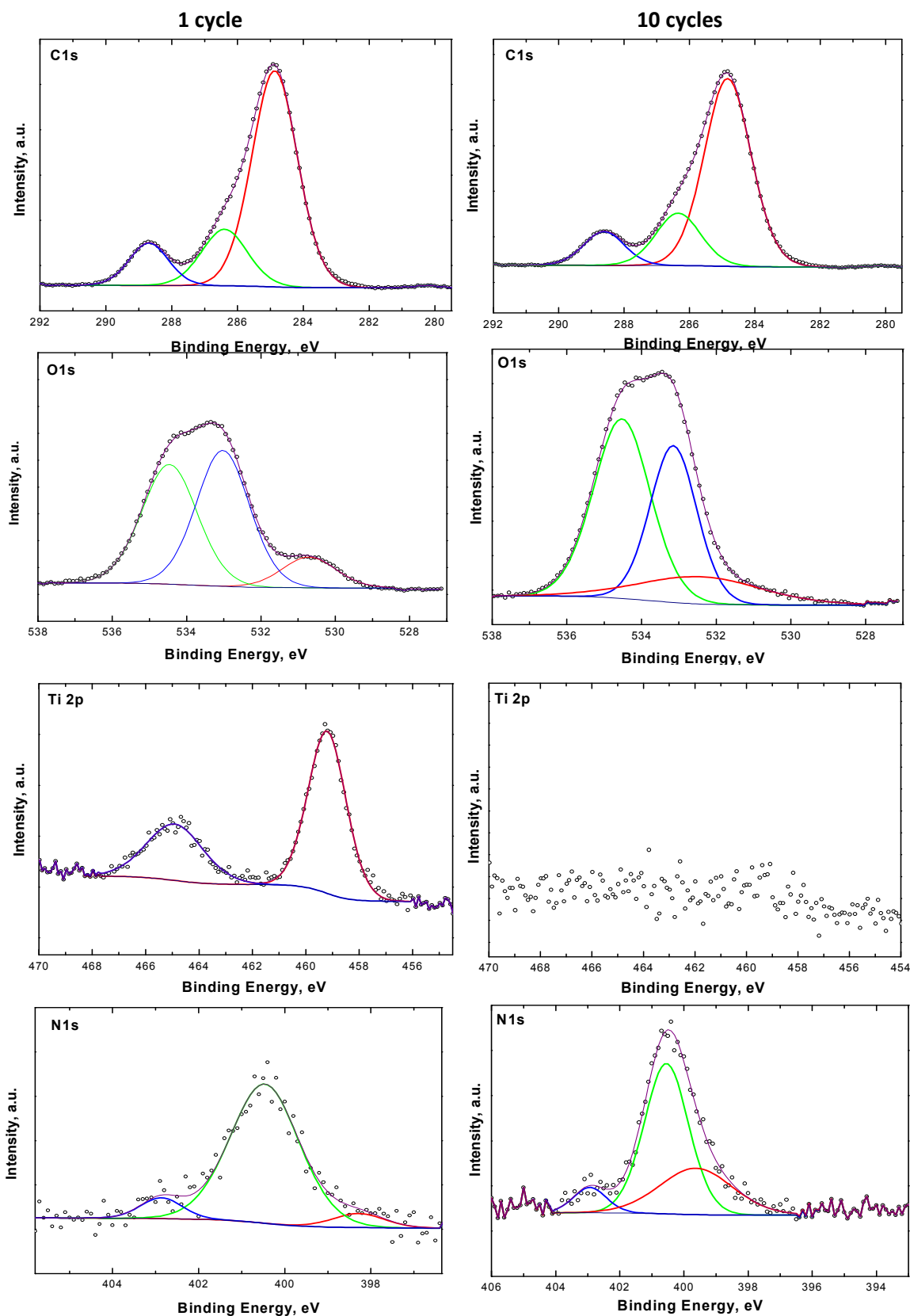**Figure 5. XPS spectra for nt-TiO$_2$ (60 V-120 min).**

1 cycle

10 cycles

Figure 6. XPS spectra for   nt-TiO₂ (60 V- 120 min)/PAN (CV1) (left column) and nt-TiO₂(60 V-120 min)/PAN (CV10) (right column).

Thus, peak 2 contains the contribution of electrodeposited PAN together with contaminant surface carbon. For the O1s spectra, three peaks have been used in the deconvolution. The main O1s peak of nt-TiO_2 at 530.6 eV (Ti-O) is not well observed for the nt-TiO_2/PAN samples. The O1s peaks placed at 534.7 and 532.6 eV are ascribed to hydroxyls groups. Indeed, making depth profile analysis from 0 to 1800 s of argon-etching, the O1s peaks tend to vanish due to reduction. The Ti2p region is well observable for PAN-free nt-TiO_2 and nt-TiO_2/PANCV1 (Figures. 5 and 6), while the absence of Ti2p peaks for CV10 is indicative of the coverage of the all nt-TiO_2 surface with a thicker layer of PAN. This feature was further confirmed when performing a depth profile analysis up to 1800 s of argon bombarding because some peaks ascribable to $Ti2p_{3/2}$ emerged at around 459.2 eV (Figure 7) due to the strip-off effect [14].

The complex N1s region can be deconvoluted into three peaks. The main N1s peak is observed at 400.5 eV and is accompanied by shoulders above and below the binding energy scale (Figure 6). Bradley et al. found similar spectra for surface nitrogen species on PAN carbon fibers [15]. The higher binding energy peak at 402.8 eV is characteristic of ammonium ion [16]. The lower binding energy environments appear to be indicative of aromatic amine ($PhNH_2$) and/or imine (C = NH), which both give peaks at 399 eV, and amide functionalities ($CONH_2$) which would give rise to a peak between 399 to 400 eV [15–18]. The latter signal appeared more favorable for nt-TiO_2/PAN-CV10 (Figure 6).

From SEM, composition mapping, TEM and XPS results, a model of the nt-TiO_2/PAN electrode material can be suggested, which is schematically depicted in Figure 8. Lithium intercalation into these electrodes is expected to take place by lithium ion diffusion through the PAN layer and electron transfer through the titanium substrate to the TiO_2 nanotubes (Figure 8). It is also expected that the EC molecules in the electrolyte solution act like plasticizers of PAN and then a PAN-Li^+ gel be in-situ formed in the lithium cell [8,11,12], which reinforces the electrode architecture while allowing lithium ion diffusion.
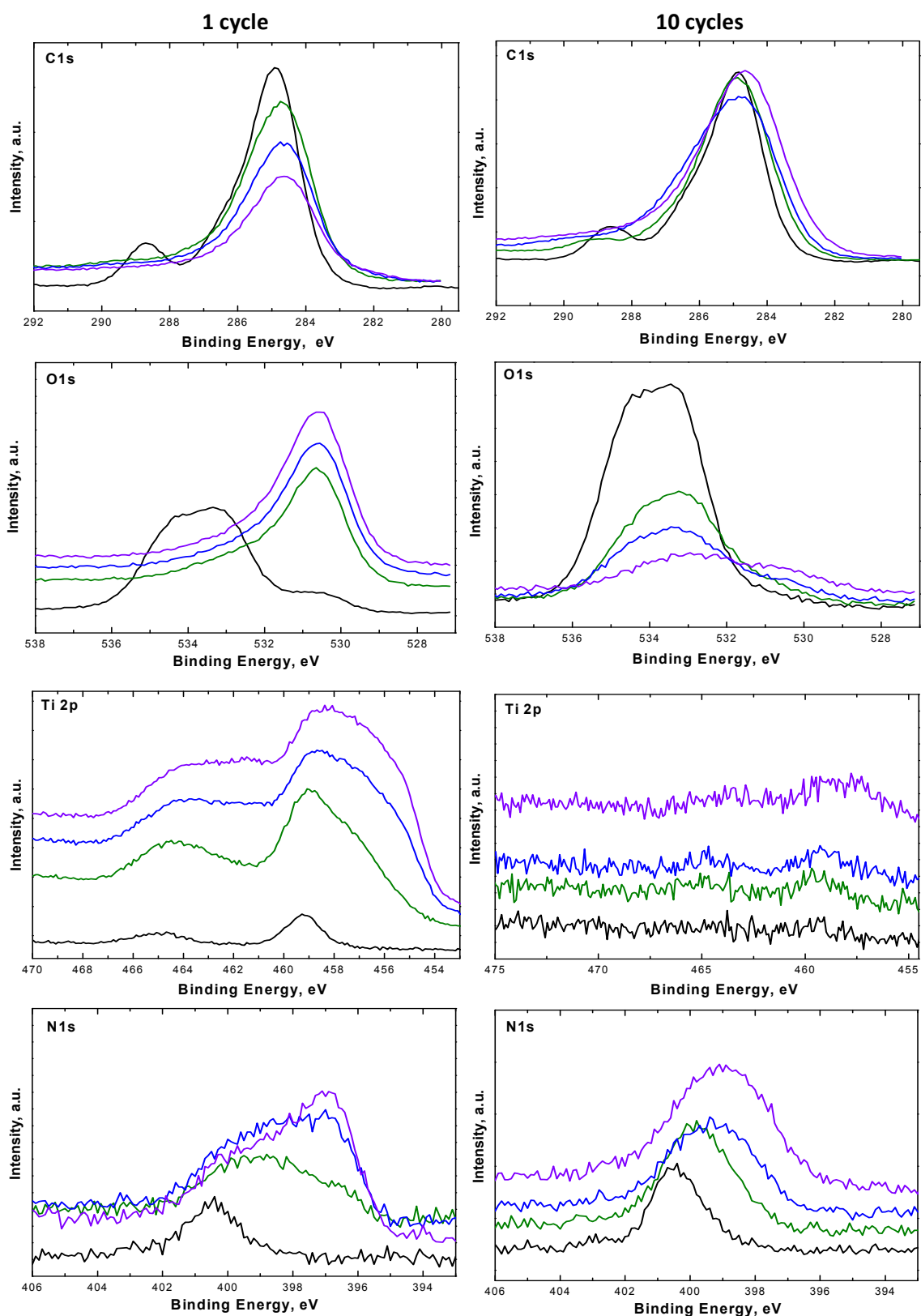
Figure 7. Details of the depth profile for XPS spectra from nt-TiO$_2$ (60 V-120 min)/PAN (CV1) (left column) and nt-TiO$_2$ (60 V-120 min)/PAN (CV10) (right column).

The electrochemical response of lithium test cells using well formed nt-TiO$_2$ of different aspect ratios with and without PAN was studied. The sample with excess of PAN (10 CV cycles), which was prepared for comparison with the single cycle sample, showed poor electrochemical performance (not shown). Figure 9 compares the potential-capacity plots for nt-TiO$_2$ and nt-TiO$_2$/PAN electrodes in lithium cells. It is worth recalling that PAN is not electrochemically active. However, PAN is Li$^+$-conductor. The absence of a well-defined and extended discharge-charge plateaus at around. 1.7–2.1 V is due to the poor crystallinity of titanium dioxide in these samples (Figure 9a and 9b).
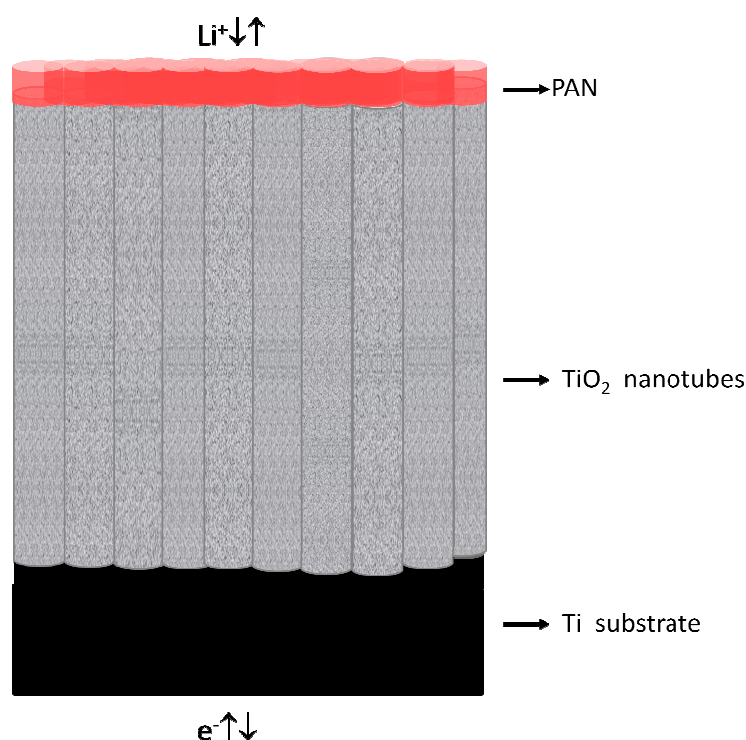
Figure 8. A schematic model for the obtained electrode material.
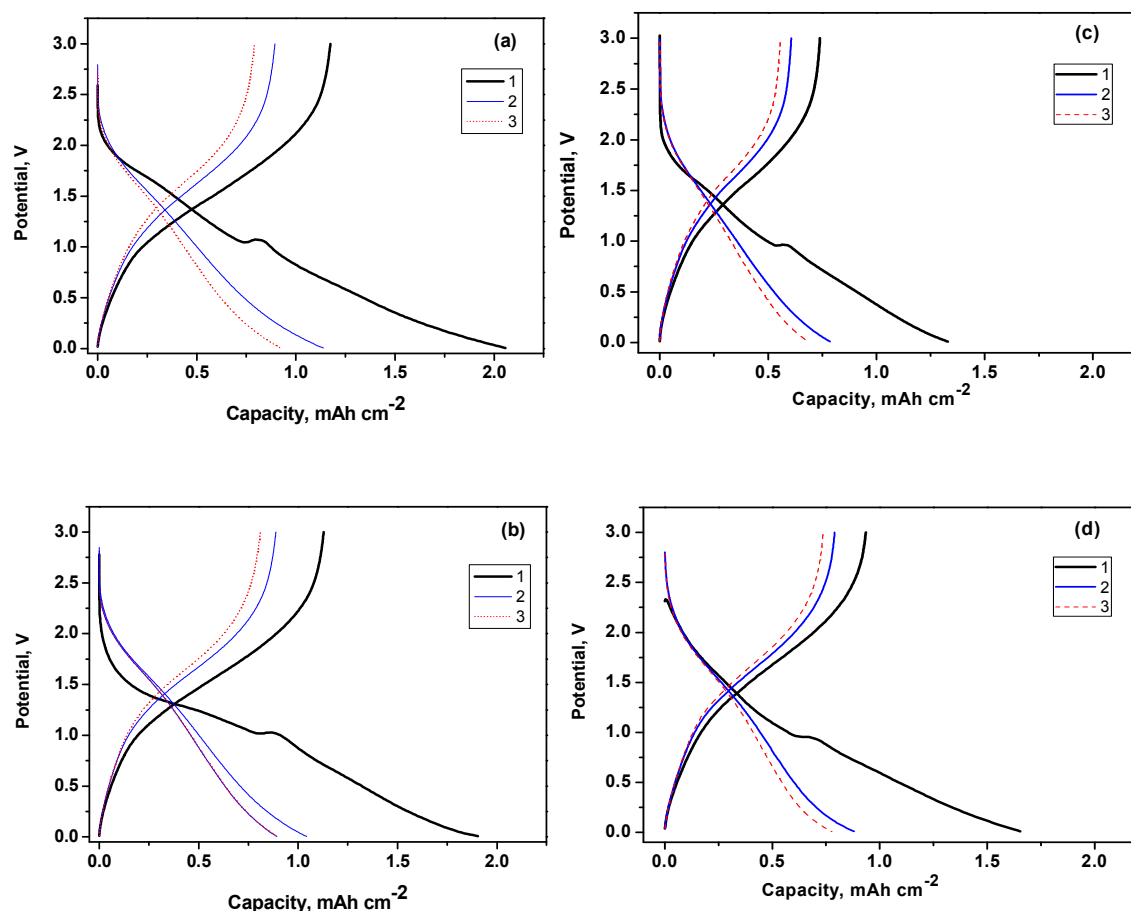
Figure 9. Potential-capacity plots of lithium cells for (a) nt-TiO$_2$ (60 V-120 min), (b) nt-TiO$_2$ (60 V-120 min)/PAN (CV1), (c) nt-TiO$_2$ (150 V-25 min) and (d) nt-TiO$_2$ (150 V-25 min)/PAN (CV1). The cycle number (1-3) is indicated.

Materials with well-defined plateau, characteristic of a two phase mechanism, usually exhibit strains and fast capacity fading during the charge-discharge processes [19]. The absence of a plateau suggests that a wide potential window (0.0–3.0 V) can be used for the cycling of these electrode materials in order to achieve higher reversible capacities. Thus, 0.0 and 1.0 V were imposed as lower potential limits in Figures. 10a, 10b, and 10c, respectively. Regardless of the low potential limit, the formation of Ti in the metallic state through the conversion reaction (TiO$_2$ + 4Li = 2 Li$_2$O + Ti) is not expected [7]. We can estimate from thermodynamics data [20,21] that the Gibbs free energy of the conversion reaction for TiO$_2$ is slightly exoergic, $\Delta G_R = -58.4$ kJ/(mol e$^-$), while for an oxide such as NiO that is well known that suffers conversion reaction

is more clearly spontaneous because $\Delta G_R = -176$ kJ/(mol e$^-$). These values are refereed to one mol of electrons. A main reason for the relative stability of TiO_2 is that its lattice energy is very exoergic (-12961 kJ/mol for anatase vs. -3694 kJ/mol for NiO) [20]. Other reasons for the inertness of TiO_2 are the kinetics of the conversion reaction and the spontaneous formation of a passivating film on titanium.

However, it has been reported that a certain fraction of Li_2O may be formed at the surface of TiO_2 and contribute to the resulting capacity [7]. Yan et al. also used 0.0 V as the lower potential limit for cycling amorphous and anatase nt-TiO_2 and observed that the typical plateau of anatase transformation at around 1.8 V was reversible [22], which is indicative of the preservation of the anatase lattice even cycling at 0.0 V. In fact, the XRD pattern (not shown) of an annealed nt-TiO_2 preserved the anatase structure reflections after cycling in the 3.0– 0.0 V vs. lithium. To further explain the voltage window of nt-TiO_2, we can consider that the main effect of decreasing the grain size is to broaden the energy levels accessible in the materials and thus leading to a broader voltage window at which the electrochemical reaction takes place [23]. For both electrodes, the irreversible feature at around 1 V in the first discharge process is ascribed to consumption of lithium through reaction with impurities such as hydroxyl groups and water trapped in nt-TiO_2 [3,4]. Annealing at high temperatures to achieve complete removal of water traces and to avoid the region at ca. 1 V leads to the crystallization of amorphous TiO_2 into anatase. The subtle changes of the first discharge line in the potential range of 1.8–1.2 V strongly suggest that the electrode/electrolyte interface properties are modified by the PAN film. Three main features can contribute to irreversible lithium consumption and decrease of the coulombic efficiency: irreversible reactions between the nt-TiO_2 surface and the electrolyte (SEI formation), remaining water and hydroxyl groups, and microstrains of the nt-TiO_2 grains due to the lithium insertion that may lead to fracture and loss of electrical contact. The capacity retention of the TiO_2 nanotubes electrode is improved after electrodeposition of PAN for a 0.0–3.0 V potential window (Figures 10a and 10b). However, the difference is negligible for a 1.0–3.0 V cycling range (Figure 10c). As expected, the wider potential range allows higher capacities, and the extended reaction may cause more structural damage, for instance by enhanced Ti^{3+} Jahn-Teller distortion, and undesirable reactions with the electrolyte. Under these conditions, the beneficial effect of the polymer is particularly evident.

As a result of the micrometric length of the nanotubes [4], the observed areal capacities in the order of 0.5 mAhcm^{-2} (Figures 10a and 10b) are much higher than other values previously reported in the literature which are typically below 0.1 mAhcm^{-2} [2,3,8,10,24]. The nt-TiO$_2$/PAN electrodes also show better performance than the equivalent PAN-free nt-TiO$_2$ that we have previously reported elsewhere [4]. Alternatively, the capacity values can be given in mAh cm^{-2} μm^{-1} units, after normalization by dividing areal capacity (mAh cm^{-2}) by nanotube length (μm) [4,5,25]. Thus, for an areal capacity of 0.5 mAh cm^{-2}, the length-normalized capacities are 0.05 mAh cm^{-2} μm^{-1} for high aspect ratio nt-TiO$_2$ and 0.25 mAh cm^{-2} μm^{-1} for low aspect ratio nt-TiO$_2$. The latter value is higher than others reported in the literature, typically below 0.1 mAh cm^{-2} μm^{-1} [4,8,25]. In addition to insertion reactions, the possible contribution of pseudocapacitive surface phenomena on the high-length TiO$_2$ nanotubes to the observed reversible capacity values is not discarded, as was proposed by Choi et al. [26], and the contribution of Li$_2$O surface formation [7]. The interesting feature is that the accessibility of lithium to the complete nanotubes is retained for longer particles. Moreover, the presence of polymer not only preserved the capacities but increased the cycling performance of the nanotubes. The origin of such improvement is probably indicative of good lithium ion mobility in both organic and inorganic components, together with a significant reinforcement of the nanotube array and protection of the nanotube open ends to irreversible reactions with the electrolyte that could deteriorate the lithium transfer from the electrolyte, thus leading to capacity fading. The improvement of the electrochemical cycling is particularly visible after the electrodeposition of PAN on the nt-TiO$_2$ obtained at 150 V (the lower aspect-ratio nanotubes) (Figure 10b).
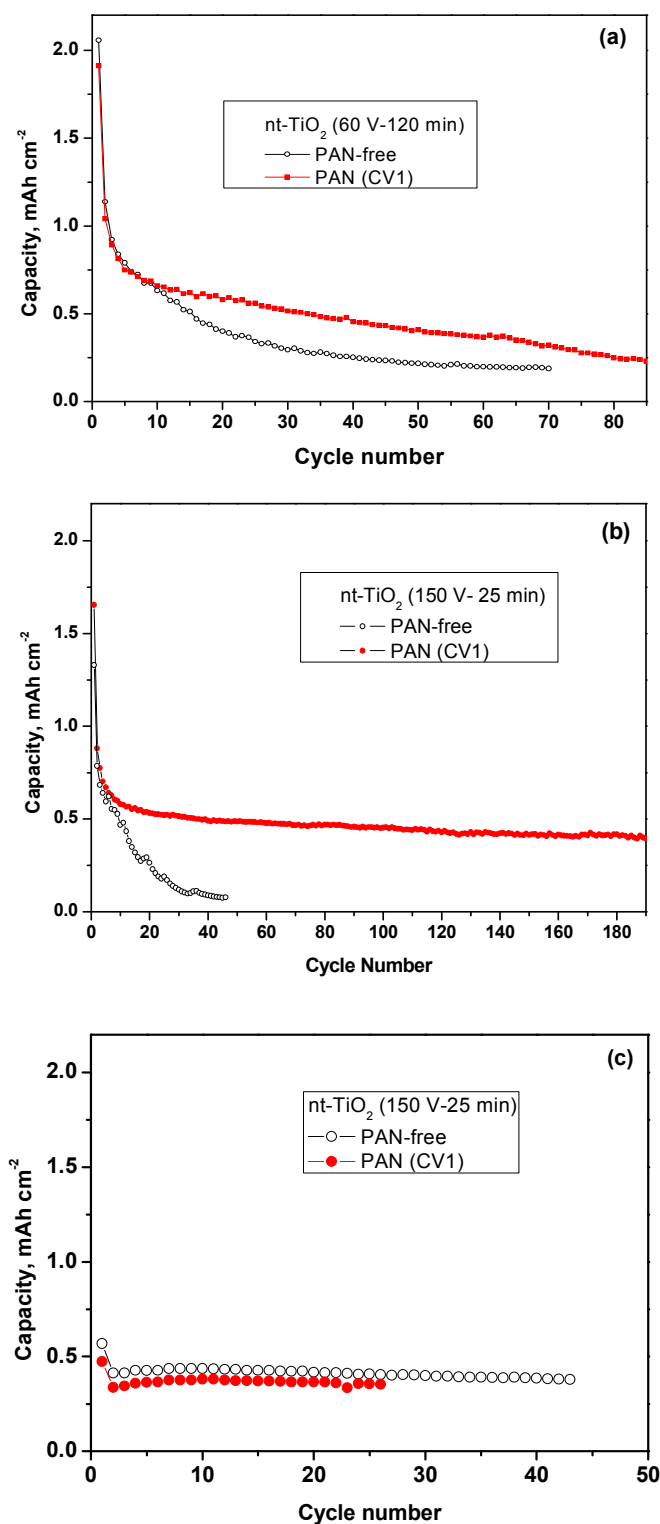
Figure 10. Areal capacity as a function of cycle number for electrode of titanium anodized at 60 V (a) and 150 V (b) before and after electrodeposition of PAN with imposed potential window: 0.0-3.0 V. (c) Titanium anodized at 150 V before and after electrodeposition of PAN, with imposed potential window: 1.0–3.0 V. All experiments were carried out with current density of 100 μAcm^{-2}.

Since the kinetics of the electrochemical processes is important to achieve high-power density batteries and in order to study if the PAN coating affects the rate performance, charge-discharge cycling experiments were carried out at several C rates in the 0.0–3.0 V of potential range (Figure 11).
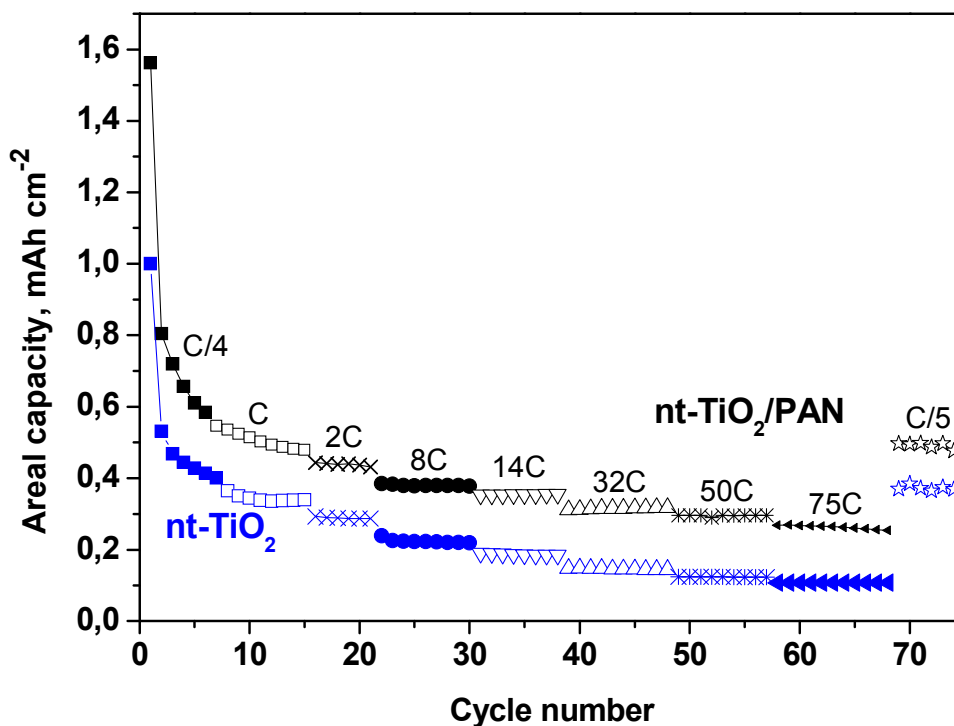
Figure 11. Areal capacity as a function of cycle number for or nt-TiO$_2$ (150 V- 25 min) and nt-TiO$_2$/PAN (150 V- 25 min) at variable current intensity. Potential range: 0.0–3.0 V.

We previously reported that although the thin films of nt-TiO$_2$ exhibit good electrochemical performance even at high rate, the capacity of the longer titania nanotubes are more affected by the increase of the current intensity than the shorter nanotubes, and that at high rates amorphous nt-TiO$_2$ can maintain larger capacities than crystalline anatase nt-TiO$_2$ [4]. In Figure 11 we can see that nt-TiO$_2$/PAN(CV1) exhibits superior capacities than PAN-free nt-TiO$_2$ even at high current densities. This feature would involve that the PAN coating allow an adequate electrode-electrolyte contact, stable SEI, and facile electronic and ionic transport along the nanotubes, while buffering the volume/strain changes. It is worth recalling that a thicker PAN layer (CV10)

261

deteriorates the cycling performance. In addition, the feature that the resulting capacity is significant even at very high rates (0.26 mAh/cm^2 at 75C) is in line with a very important contribution of the surface Li-storage in amorphous nt-TiO$_2$. By comparing

Figures 10b and 11, it can be observed that the sample without PAN initially intercalated more lithium at slow kinetics (Figure 10b, C/5 rate) but soon suffered structural stresses leading to electrical disconnections and loss of capacity. This is probably indicating that the mechanism of the reaction at high currents and low currents differs in the relative contribution of intercalation and surface reactions. The fact that the capacities are good for both samples at high kinetics would agree with the reaction on the surface, not in the bulk. PAN appears to protect more on the effects of intercalation of Li in the bulk than on the surface, maybe due to structural buffering and/or electrical connection preservation.

Finally, the impedance spectra of sample nt-TiO$_2$/PAN (150 V– 25 min) (Figure 12b) differs from that of nt-TiO$_2$ (150 V– 25 min) (Figure 12a).

Two depressed semicircles at high and medium frequencies (surface layer and charge transfer, respectively) and a sloped line at low frequencies (lithium diffusion in the electrode) are observed. The occurrence of two semicircles would be in good agreement with the formation of the SEI film. In this way, a change in slope in the low frequency region is observed after electropolymerization, probably indicating changes in lithium-ion diffusivity, directly connected with PAN diffusivity. On increasing cycle number there is no apparent deterioration of this behavior for nt-TiO$_2$/PAN. From the impedance spectra in the low-frequency region, the diffusion coefficient (D) of lithium in the electrode can be calculated using the procedure described in the literature [27– 29]. Thus, we have obtained that the D values are 9×10^{-12} and 2×10^{-12} cm^{2}s^{-1} for nt-TiO$_2$/PAN and nt-TiO$_2$, respectively. As found in the literature, the D values for amorphous TiO$_2$ nanotubes are higher than those commonly found in crystalline anatase nanotubes [30].
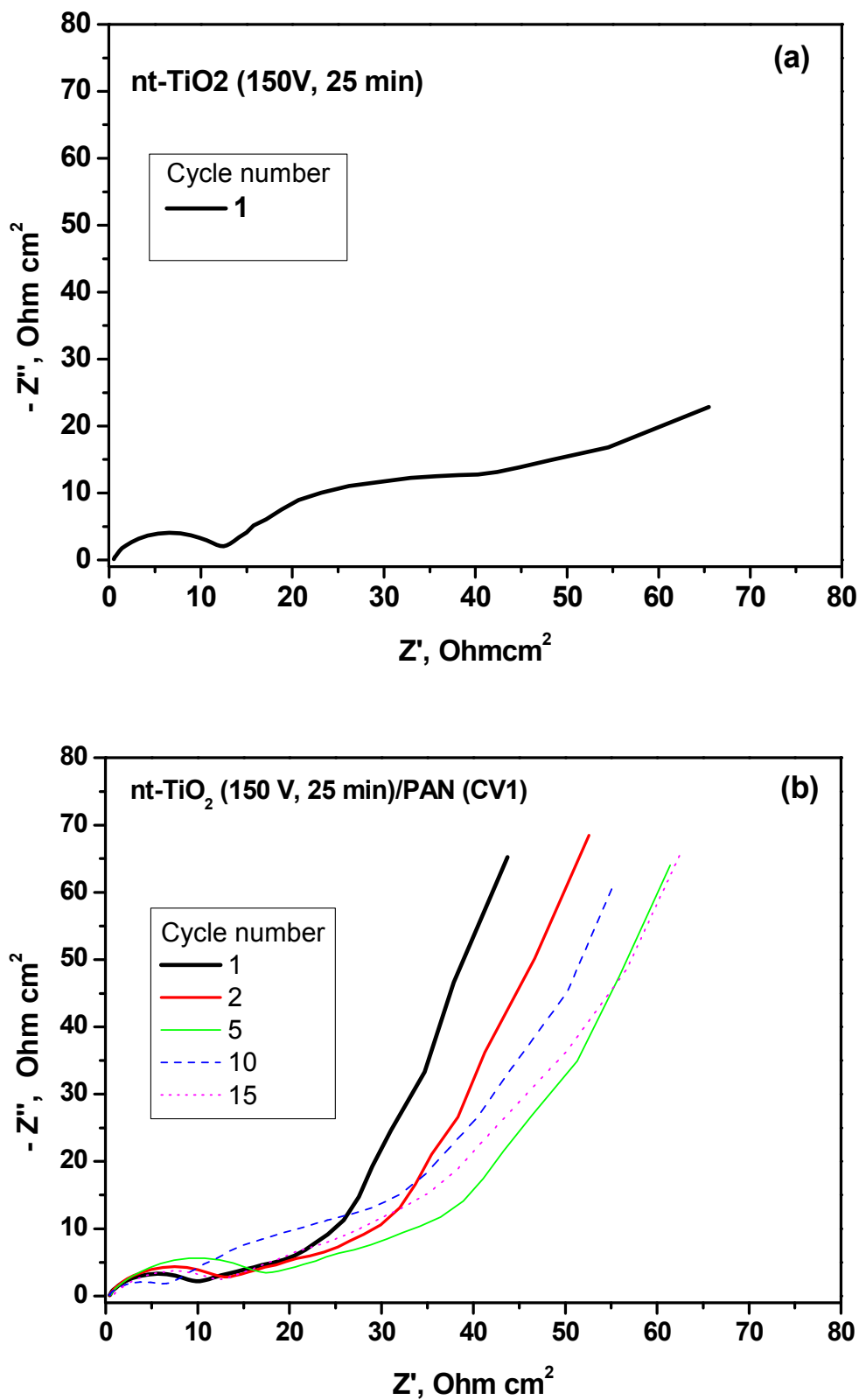
Figure 12. (A) Impedance spectra for nt-TiO$_2$ (150 V- 25 min). (B) Impedance spectra for nt-TiO$_2$/PAN (150 V- 25 min).

In order to further analyze the impedance spectra, the spectra were fit with the following equivalent circuit $[R_e + R_{sl}/Q_{sl} + (R_{ct} + W)/Q_{ct}]$ [12], and the results of the fitting for the resistance values are shown in Figure 13. R represents resistor, Q constant phase element and W Warburg element.
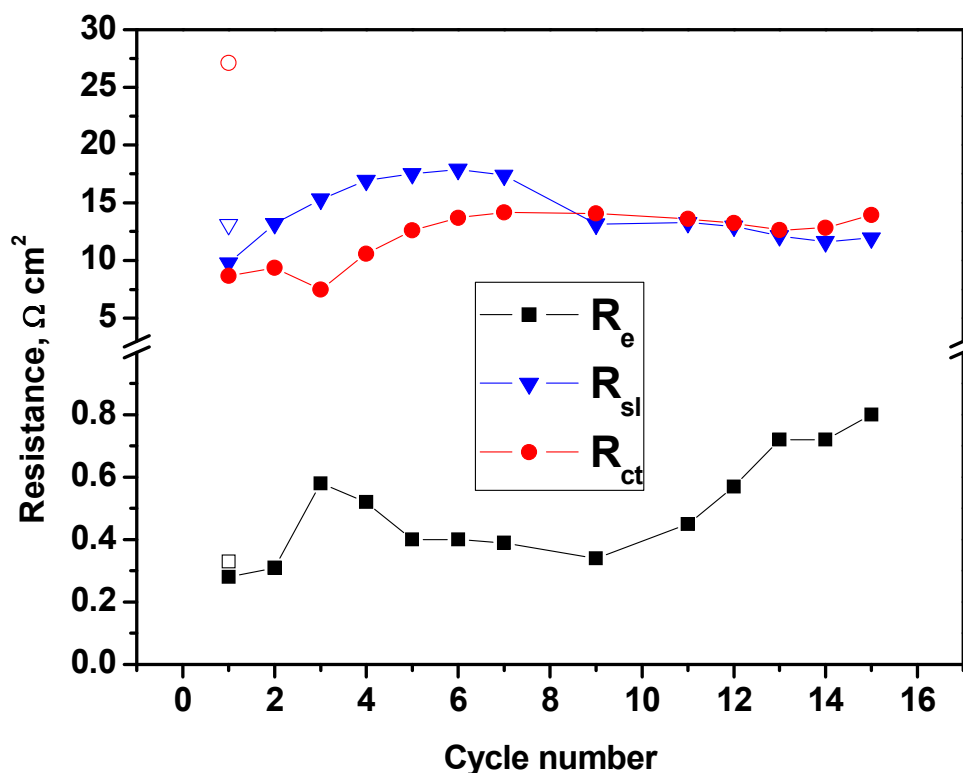
Figure 13. Area-normalized resitance values obtained from the fitting of the EIS results for -TiO$_2$ (150 V-25 min)/PAN (CV1). Re: electrolyte resistance. R$_{sl}$: surface layer resistance. R$_{ct}$: charge transfer resistance. For the sake of comparison, the resistance values for PAN-free nt-TiO$_2$ are shown like open symbols.

For all the electrodes the pure resistance of the electrolyte (R_e) is in the range of 0.3–0.8 Ω cm^2. The difference between the R_e values of nt-TiO$_2$ and nt-TiO$_2$/PAN is within the experimental error. In other words, the PAN film does not increase the resistance of the cell due to the thin film character and good ionic conductivity of the PAN layer. Taking from the literature a value of ionic conductivity of $\sigma = 4.8 \times 10^{-5}$ S cm^{-1} for PAN-Li$^+$ [31], and that a value of $R_e =0.3$ Ω cm^2 is exclusively due to the conductivity of Li$^+$ ion through the PAN layer on nt-TiO$_2$/PAN, the calculated thickness

of the PAN layer is d = 0.14 μm. This value is reasonable, if we take into account that only one voltammetric cycle was used for electrodepositing the PAN film on nt-TiO_2 and that a thickness of d = 0.48 μm was found in our previous studies using five voltammetric cycles in PAN/CoSn alloy [12]. The initial resistances to lithium diffusion through the surface layer (R_{sl}), obtained from the depressed semicircle at high frequencies, are also comparable for nt-TiO_2 and nt-TiO_2/PAN. An additional explanation of the semicircle at high frequencies in self-organized anatase electrodes is that it is controlled by the "surface states" for lithium [32], and consequently it would involve that nt-TiO_2 and nt-TiO_2/PAN have similar capacity to react with lithium at their surfaces as expected. In contrast, the charge transfer resistance (R_{ct}) obtained from the depressed semicircle at intermediate frequencies decreases after forming the PAN film on nt-TiO_2. This last result is consistent with a better cycling performance for nt-TiO_2/PAN when the lower potential limit is 0.0 V. Most probably, PAN-free nt-TiO_2 reacts more extensively with the electrolyte near 0.0 V and changes R_{ct} because of electrical contact loss. The irreversible electrolyte decomposition in the first discharge of nt-TiO_2 has been suggested by other authors even when cycling within the potential window of 3.0–1.0 V [33]. Another explanation may be that the PAN-layer buffers the volume change and strains of nt-Li_xTiO_2 that are expected for extended reaction with lithium (x > 0.5), which is known that can increase the charge transfer resistance [33], and consequently the electrical contact is improved. Similarly, we found that the PAN-layer decreases the R_{ct} values of CoSn alloys, as reported elsewhere [12]. Other authors recently found that the coating of $LiFePO_4$ with conductive polymer polyaniline effectively reduce its charge transfer impedance [34,35]. It is worth to note here that in addition to the lithium ionic conductivity, the very thin films of PAN can be electronic conductors [36], and consequently the polymer may improve the connectivity between the nanotubes and then the surface charge transfer reactions can be enhanced by the PAN coating and the apparent diffusion rate improved.

4.2.4 Conclusions

For amorphous nanotubes of TiO_2, the surface Li-storage seems to play an important role and the interface TiO_2/electrolyte is critical for achieving excellent electrochemical performance and it can be improved by coating the nanotubes. The electrodeposition of polyacrylonitrile on titanium oxide nanotubes of different aspect ratios has been successfully achieved. The lithium-ion conductor polyacrylonitrile film can improve the electrochemical cycling of the titanium oxide nanotubes electrode in a wide potential range and even at very high rates as a result of the change of the electrode/electrolyte interface properties. The thin film character of the PAN coating can provide an effective path for both electronic and ionic transport and the rate capability is not deteriorated. The improvement of the electrochemistry after electrodeposition of polyacrylonitrile is more evident for the lower aspect ratio nanotubes. To prepare well-formed titanium oxide nanotubes of lower aspect ratio we used high anodization voltage and short anodization time which allow achieving high capacity values in the order of 0.25 mAh cm^{-2} μm^{-1}. However at low rates and wide potential range (0.0–3.0 V), capacity retention was only excellent after coating with PAN. These results open exciting ways to improve significantly the performance of self-organized titania nanotubes as advanced electrode for lithium-ion batteries. Other polymers and copolymers with further electrochemical stability and/or activity may be studied.

References

1. L. V. Taveira, J. M. Macak, H. Tsuchiya, L. F. P. Dick, and P. Schmuki, *J. Electrochem. Soc.* **152**, B405 (2005).

2. J. M. Macak, H. Tsuchiya, and P. Schmuki, *Angew. Chem., Int. Ed.*, **44**, 2100 (2005).

3. G. F. Ortiz, I. Hanzu, T. Djenizian, P. Lavela, J. L. Tirado, and P. Knauth, *Chem. Mater.*, **21**, 63 (2009).

4. J. R. González, R. Alcántara, F. Nacimiento, G. F. Ortiz, J. L. Tirado, E. Zhecheva, and R. Stoyanova, *J. Phys. Chem. C*, **116**, 20182 (2012).

5. M. Zukalova,M. Kalbac, L. Kavan, I. Exnar, andM. Gratzel, *Chem. Mater.*, **17**, 1248 (2005).

6. J. Wang, J. Polleux, J. Lim, and B. Dunn, *J. Phys. Chem. C*, **111**, 14925 (2007).

7. W. J. H. Borghols, D. L¨utzenkirchen-Hecht, U. Haake, W. Chan, U. Lafont, E. M. Kelder, E. R. H. van Eck, A. P. M. Kentgens, F. M. Mulder, and M. Wagemaker, *J. Electrochem. Soc.*, **157**, A582 (2010).

8. N. A. Kyeremateng, F. Dumur, P. Knauth, B. Pecquenard, and T. Djenizian, *Electrochem. Commun.*, **13**, 894 (2011).

9. U. G. Nwokeke, F. Nacimiento, R. Alcántara, J. L. Tirado, and F. Nacimiento, *Electrochem. Solid-State Lett.*, **14**, A148 (2011).

10. J. F. M. Oudenhoven, L. Baggetto, and P. H. L. Notten, *Adv. Energy Mater.*, **1**, 10 (2011).

11. G. El-Enany, M. J. Lacey, P. A. Johns, and J. R. Owen, *Electrochem. Commun.*, **11**, 2320 (2009).

12. F. Nacimiento, R. Alc´antara, J. R. Gonz´alez, and J. L. Tirado, *J. Electrochem. Soc.*, **159**, A1028 (2012).

13. F. Nacimiento, R. Alc´antara, U. G. Nwokeke, J. R. Gonz´alez, and J. L. Tirado, *Ultrason. Sonochem.*, **19**, 352 (2012).

14. U. Diebold and T. E. Madey, *Surface Science Spectra*, **4**, 227 (1997).

15. R. H. Bradley, X. Ling, I. Sutherland, and G. Beamson, *Carbon*, **32**, 185 (1994).

16. G. Beamson and D. Briggs, *High Resolution XPS of Organic Polymers*,Wiley (1992).

17. C. Kozlowski and P. M. A. Sherwood, *Carbon*, **25**, 751 (1987).

18. R. Nordberg, H. Brecht, R. G. Aldridge, A. Fahlmann, and J. R. Van Wazer, *Inorg. Chem.*, **9**, 2469 (1959).

19. J. Wang, Y. Zhou, Y. Hu, R. O'Hayre, and Z. Shao, *J. Phys. Chem. C*, **115**, 2529 (2011).

20. L. Glasser and H. D. B. Jenkins, *J. Am. Chem. Soc.*, **122**, 632 (2000).

21. *Handbook of Chemistry and Physics*, p. 5–72 to 5–75. CRC Press, New York, 1993.

22. J. Yan, H. Song, S. Yang, and X. Chen, *Mat. Chem. Phys.*, **118**, 367 (2009).

23. D. Deng, M. G. Kim, J. Y. Lee, and J. Cho, *Energy Environ. Sci.*, **2**, 818 (2009).

24. S. K. Cheah, E. Perre, M. Rooth, M. Fondell, A. Harsta, L. Nyholm, M. Boman, T. Gustafsson, J. Lu, P. Simon, and K. Edstrom, *Nano Lett.*, **9**, 32030 (2009).

25. N. Plylahan, N. A. Kyeremateng, M. Eyraud, F. Dumur, H. Martinez, L. Santinacci, P. Knauth, and T. Djenizian, *Nanoscale Res. Lett.*, **7**, 349 (2012).

26. M. G. Choi, Y. G. Lee, S. W. Song, and K. M. Kim, *J. Power Sources*, **195**, 8289 (2010).

27. G. Q. Liu, L.Wen, G. Y. Liu, Q. Y.Wu, H. Z. Luo, B. Y.Ma, and Y. W. Tian, *J. Alloys Compd.*, **509**, 6427 (2011).

28. P. Krtil and D. Fattakhova, *J. Electrochem. Soc.*, **148**, A1045 (2001).

29. M. D. Levi and D. Aurbach, *Electrochim. Acta*, **45**, 167 (1999).

30. H. T. Fang, M. Liu, D. W. Wang, T. Sun, D. S. Guan, F. Li, J. Zhou, T. K. Sham, and H. M. Cheng. *Nanotech.*, **3**, 225701 (2009).

31. Y. T. Chen, Y. C. Chuang, J. H. Su, H. C.Yu, and Y. W. Chen-Yang, *J. Power Sources*, **196**, 2802 (2011).

32. P. Ktril, D. Fattakhova, L. Kavan, S. Burnside, and M. Gr̈atzel, *Solid State Ionics*, **135**, 101 (2000).

33. Y. K. Zhou, L. Cao, F. B. Zhang, B. L. He, and H. L. Li, *J. Electrochem. Soc.*, **150**, A1246 (2003).

34. W. M. Chen, L. Qie, L. X. Yuan, S. A. Xia, X. L. Hu,W. X. Zhang, and Y. H. Huang, *Electrochim. Acta*, **56**, 2689 (2011).

35. C. Su, G. Lu, L. Xu, and Cheng Zhang, *J. Electrochem. Soc.*, **159**, A305 (2012).

36. C. Reynaud, C. Boiziau, C. Juret, S. Leroy, and J. Perreau, *Synth. Met.*, **11**, 159 (1985).

Capítulo 5.-

Resumen y conclusiones finales

5.1   Resumen

Para la realización de esta Tesis Doctoral han sido sintetizados y caracterizados nuevos materiales híbridos basados en compuestos de estaño o de titanio modificados con carbono o con poliacrilonitrilo para su empleo como electrodo negativo en baterías de ion litio.

Con el objeto de proceder a una exposición ordenada de los resultados obtenidos, este resumen ha sido dividido en tres bloques:

1- *Materiales híbridos de cobalto-estaño y fase carbonosa.*

2- *Materiales híbridos de cobalto-estaño y poliacrilonitrilo.*

3- *Películas finas electrodepositadas.*

1- *Materiales híbridos de cobalto-estaño y fase carbonosa.*

Se han preparado diferentes compuestos de Co-Sn-carbono mediante reducción carbotermal de los óxidos metálicos en presencia de un precursor de carbono. Con este fin, se han empleado diferentes precursores de carbono, desde un gel orgánico resorcinol-formaldehido a diferentes residuos del petróleo proporcionados por Repsol, como son un coque verde de petróleo y un residuo de pirólisis de fuel oil. Los dos últimos ejemplos constituyen subproductos de bajo coste de la industria del petróleo a los que se pretende aportar un valor añadido mediante su aplicación en baterías de ión-litio. Con el objeto de conseguir una mezcla homogénea de los materiales, se han empleado procedimientos tales como la gelificación en reflujo, la molienda mecánica de precursores sólidos y la agitación de precursores fluidos. Para cada uno de estos materiales, se han empleado diferentes proporciones Sn/Co y metal/carbono con el fin de evaluar el papel, tanto de los elementos metálicos como de la fase carbonosa en el comportamiento electroquímico.

Los diagramas de difracción de rayos X de las muestras carbonizadas han presentado un grupo de reflexiones estrechas que fueron atribuidas a la presencia de varias fases metálicas como Sn, $CoSn_2$ y CoSn. También se ha observado, en menor medida para aquellas muestras con gran contenido en cobalto, un conjunto de reflexiones que fueron asignadas a Co_3Sn_2 e incluso a $Co_3SnC_{0.7}$. La evaluación de los

diagramas sugirió una reducción carbotermal eficiente durante la carbonización a 800° C. Las micrografías han mostrado que la presencia de cobalto y fase carbonosa favorece la formación de partículas metálicas nanométricas bien dispersas en la matriz carbonosa. La espectroscopia Mössbauer de ^{119}Sn ha demostrado ser una técnica de interés para desvelar la presencia de fases Co-Sn amorfas y por tanto indetectables mediante difracción de rayos X. Así pues, se correlacionó una alta capacidad electroquímica con la presencia de la fase $CoSn_2$, mientras que fases ricas en cobalto como Co_3Sn_2 y $Co_3SnC_{0.7}$ fueron perjudiciales para obtener un buen rendimiento electroquímico.

Las muestras que emplearon un gel orgánico, preparado por el método del resorcinol-formaldehido, como precursor de la fase de carbono requirieron contenidos bajos de cobalto (Sn/Co = 95:5) para mejorar la capacidad de retención, en comparación con la muestra sin cobalto. Valores de capacidad superiores a 330 mAh g^{-1} se mantuvieron después de 30 ciclos. Una mejora adicional del rendimiento electroquímico se consiguió optimizando la proporción metal:carbono (MO_x:R). Así, la muestra con un moderado contenido en carbono MO_x:R = 1.5 contribuyó positivamente a mejorar la retención de capacidad. Así pues, se registró un alto valor de capacidad reversible de 475 mAh g^{-1} tras el segundo ciclo y superiores a 380 mAh g^{-1} tras 30 ciclos.

Los materiales híbridos preparados por molienda mecánica de los óxidos metálicos con un coque verde de petróleo han permitido constatar la importante influencia de la matriz carbonosa en la retención de la capacidad. Así pues, la evaluación de las estequiometrias $Sn_{27}Co_{14}C_{59}$, $Sn_8Co_4C_{88}$, y $Sn_4Co_2C_{94}$, con similares relaciones Co/Sn pero progresivo aumento de la contribución de la fase de carbono, ha revelado una mejor retención de la capacidad para la muestra con contenidos intermedios de carbono. Asimismo, la alta contribución de la fase $CoSn_2$ en $Sn_7Co_1C_{92}$, tanto en muestras originales como cicladas fue la responsable de un buen rendimiento electroquímico. Se han registrado valores de capacidad de 400 mAh g^{-1} después de 40 ciclos a 35 mA g^{-1}. Estos resultados fueron confirmados por la baja impedancia interna medida en $Sn_7Co_1C_{92}$ después de varias descargas.

La ventaja del empleo de un residuo de la pirolisis del fueloil (FOP) como fase carbonosa se debe al estado fluido que alcanza durante el proceso de copirólisis y reducción carbotermal, lo que asegura la formación de partículas intermetálicas

submicrométricas de Co-Sn homogéneamente embebidas en la matriz de carbono. La constancia de los valores de resistencia interna en los electrodos conteniendo cobalto a lo largo del ciclado de la celda ha permitido justificar la mejor retención de la capacidad. En cambio, el peor comportamiento observado en la muestra FOPSn30Co15 ha sido atribuido a la mayor contribución de la fase rica en cobalto $Co_3SnO_{0.7}$ observada por espectroscopia Mössbauer.

2- *Materiales híbridos de cobalto-estaño y poliacrilonitrilo.*

Una mezcla entre oxalato de cobalto, oxalato de estaño y moléculas de poliacrilonitrilo (PAN) dispersadas ha sido utilizada como un nuevo material activo en electrodos para baterías de ión litio. Las composiciones de las muestras han sido analizadas usando FTIR, microanálisis con detector EDAX y análisis de C-N. El electrodo muestra buena retención de la capacidad en el caso de que el límite de potencial impuesto se encuentre por debajo de 2,0 V. El mecanismo de la reacción entre los oxalatos-PAN y el litio ha sido estudiado mediante el uso de DRX ex-situ y espectroscopia Mössbauer de ^{119}Sn. Los materiales del electrodo se vuelven irreversiblemente amorfos al comienzo de la reacción, cuando el oxalato de estaño es descompuesto y se detecta Sn(IV). A continuación, los iones metálicos son reducidos y se forman aleaciones amorfas de estaño-cobalto. Finalmente, aleaciones de Li-Co-Sn se forman reversiblemente cerca de 0,0 V. Los grupos oxalatos y el PAN forman una matriz electroquímicamente inerte. Debido a la matriz, se evita la agregación de las partículas amorfas en partículas cristalinas durante el ciclado. La extracción de litio en los valores de potencial cerca de 2,0 V produce interacciones estaño-oxígeno y este hecho perturba la matriz y origina una pérdida de capacidad.

Electrodos compuestos de $CoSn_x$-PAN han sido preparados a través de la reducción de iones de estaño y cobalto con $NaBH_4$(aq) en presencia de PAN (previamente disuelto en dimetilformamida). Diferentes cantidades relativas de PAN fueron usadas. El producto resultante consiste en nanopartículas intermetálicas o aleaciones estaño-cobalto rodeadas por una capa basada en PAN. El óxido de estaño ha sido detectado como un componente menor en varias muestras. Después del

calentamiento bajo atmósfera inerte de los materiales híbridos CoSn$_x$-PAN, las moléculas orgánicas previenen el crecimiento de los granos intermetálicos y forman una capa de carbono amorfo. El electrodo que contiene CoSn$_2$ nanométrico y PAN ha presentado un comportamiento electroquímico en celdas de litio muy bueno debido a la estabilidad estructural de la matriz de PAN y al pequeño tamaño de los granos metálicos. Para las muestras donde la fase intermetálica principal es CoSn$_2$ nanocristalino las capacidades reversibles máximas observadas fueron de alrededor de 600 mAh g^{-1} y se lograron excelentes capacidades de retención para electrodos compuestos de PAN-CoSn$_2$. De acuerdo con los resultados de Mössbauer de ^{119}Sn, en el proceso de carga (extracción de litio) puede tener lugar la segregación de aleaciones basadas en estaño en regiones ricas y pobres en cobalto.

Como debido a motivos económicos y ambientales la sustitución de cobalto por hierro puede ser ventajosa, hemos intentado preparar materiales compuestos FeSn$_x$/PAN siguiendo el mismo procedimiento. Sin embargo, al contrario que los compuestos CoSn$_x$/PAN, la reducción de Fe(II) y Sn(II) conduce a Sn cristalino.

El método sonoquímico se usó para preparar materiales de electrodo que contienen nanopartículas intermetálicas (CoSn$_x$) y PAN. La irradiación de ultrasonidos de alta intensidad ha sido aplicada para lograr partículas de pequeño tamaño. Después del calentamiento a 490º C bajo un flujo de Argón, el polímero PAN está parcialmente carbonizado y las nanopartículas metálicas están rodeadas por una matriz carbonosa. La principal fase metálica es CoSn$_2$. El recubrimiento carbonoso y los óxidos de la superficie han sido examinados mediante XPS. El electrodo resultante de fase carbonosa-CoSn$_2$ (CoSn$_2$@C) ha mostrado un comportamiento electroquímico mejorado (alrededor de 450 mAh g^{-1} después de 50 ciclos) en comparación con estudios previos para el CoSn$_2$ cristalino puro. La reacción entre el CoSn$_2$@C y el litio ha sido estudiada mediante el uso de XRD y espectroscopia Mössbauer de ^{119}Sn. La formación de grandes granos de fases cristalinas de Li$_x$Sn después de la primera descarga está descartada. El pequeño tamaño de partículas que se consigue mediante el uso de la ultrasonicación y la matriz carbonosa contribuyen a mantener las interacciones Sn-Co durante el ciclado electroquímico. La agregación de partículas metálicas nanométricas durante el ciclado electroquímico pueden ser suprimidas por la matriz carbonosa (PAN pirolítico).

3- *Películas finas electrodepositadas*.

Películas híbridas orgánicas-inorgánicas han sido preparadas y probadas en celdas de litio. Así, películas de cobalto-estaño y PAN electrodepositadas sobre un sustrato plano de titanio han sido estudiadas como un nuevo electrodo para baterías de ión litio. Para la preparación del electrodo, en primer lugar, cobalto y estaño fueron electrodepositados sobre un sustrato de titanio y el producto principal fue una aleación Co-Sn amorfa en XRD y metaestable. En segundo lugar, el PAN fue depositado sobre el sustrato Co-Sn/Ti a través de la electropolimerización del monómero (acrilonitrilo). La película metálica electrodepositada contenía Sn, aleación amorfa de Co-Sn y fases intermetálicas distribuidas en una película fina y partículas submicrométricas. La presencia de la película de PAN ha sido corroborada mediante el uso de FTIR y SEM equipado con microanálisis. La película de PAN se gelifica en contacto con la disolución electrolítica (1 M $LiPF_6$ en EC:DEC). Las propiedades interfaciales del material electroquímicamente activo basado en estaño son modificadas mediante la electrodeposición del PAN, como ha sido observado mediante el uso de espectroscopia de impedancia electroquímica. Se han logrado capacidades por área del orden de $mAhcm^{-2}$.

Nanotubos amorfos y auto-organizados de TiO_2 (nt-TiO_2) con diferentes relaciones de aspecto fueron preparados por anodización de titanio. La morfología y la relación de aspecto de los nanotubos pueden ser controladas al seleccionar parámetros de la anodización tales como el voltaje impuesto y el tiempo. Ya que la superficie de los nanotubos amorfos de TiO_2 es crítica para lograr altas capacidades, estabilidad en el ciclado y rendimientos a velocidades altas en baterías de litio, y con el fin de mejorar la estabilidad de los electrodos nt-TiO_2, PAN ha sido depositado por electropolimerización. Después de la electropolimerización, los datos de microscopia electrónica, mapas de composición y XPS han confirmado que el PAN electrodepositado cubre por completo la superficie de los extremos abiertos de los nanotubos. El material de electrodo resultante ha sido probado en celdas de litio, mostrando capacidades reversibles por área del orden de 0.5 mAh cm^{-2} y un buen comportamiento en el ciclado dentro de una amplia ventana de potencial (0,0-3,0 V). La mejora electroquímica es más evidente para nt-TiO_2 con baja relación de aspecto, con valores de capacidad normalizados por la longitud del nanotubo de alrededor de 0.25 mAh cm^{-2} μm^{-1} a velocidad lenta. Una capacidad por área de 0.26 mAh cm^{-2} es

suministrada a una velocidad de 75C. La capa de PAN conductora de iones asegura el acceso de los iones litio a los nanotubos, protege la superficie del extremo abierto de reacciones indeseables con el electrolito y proporciona una mejorada estabilidad mecánica al alectrodo y menor resistencia a la transferencia de carga.

5.2   **Summary**

In this doctoral thesis new hybrid materials based on tin or titanium composite modified with carbon or polyacrylonitrile have been synthesized and characterized for using as negative electrode in lithium ion batteries.

In order to clearly describe the results, the report is sectioned in three main chapters:

4- Hybrid materials of cobalt-tin and carbonaceous phase.

5- Hybrid materials of cobalt-tin and polyacrylonitrile.

6- Electrodeposited thin films.

1- Hybrid materials of cobalt-tin and carbonaceous phase.

Various Sn-Co-C composites are prepared by carbothermal reduction of metal oxides in the presence of a carbon precursor. We chose different carbon precursors, including a resorcinol-formaldehyde organic gel and different petroleum residua, as a green coke petroleum and a Fuel Oil Pyrolysis, both provided by Repsol. The latter ones are low cost by-product from the petroleum industry. In order to achieve a homogeneous mixture of these materials, procedures such as gelification under reflux, mechanical milling of solid precursors or stirring of fluid precursors are employed. For each of these materials, different Sn/Co and metal/carbon ratios are proposed in order to evaluate the role of both of the metallic elements and the carbonaceous phase in the electrochemical behaviour.

The X-ray diffraction patterns of the annealed samples show a set of narrow reflections that are ascribed to the presence of various intermetallic phases as Sn, $CoSn_2$ y CoSn. Also, a set of reflections ascribable to Co_3Sn_2 and $Co_3SnC_{0.7}$ are observed to a lesser extent for those samples with high cobalt content. The evaluation of the patterns suggests an efficient carbothermal reduction during the carbonization at 800º C. The electron micrographs show that the presence of cobalt and carbonaceous phase favors the formation of nanosized metal particles highly dispersed in the carbon matrix. ^{119}Sn Mössbauer spectroscopy evidenced to be a useful technique to reveal the presence of Co-Sn amorphous phases and therefore undetectable by X-ray diffraction. Thus, a high

electrochemical capacity was correlated to the presence of $CoSn_2$, whilst rich cobalt phases as $Co_3SnC_{0.7}$ and Co_3Sn_2 are deleterious for a good electrochemical performance.

Samples based on a resorcinol-formaldehyde organic gel precursor, required a low cobalt content (Sn/Co = 95:5) in order to improve the capacity retention, as compared to the cobalt free sample. Capacity values higher than 330 mAh g^{-1} were maintained after 30 cycles. An additional improvement of the electrochemical performance was achieved by optimizing the metal:carbon ratio (MO_x:R). Thus, the sample with a intermediate carbon content MO_x:R = 1.5 positively contributed to improve the capacity retention. A high reversible capacity value 475 mAh g^{-1} was reached after the second cycle and capacity values higher than 380 mAh g^{-1} were maintained after 30 cycles.

The hybrid materials prepared by mechanical milling of the metal oxides with a green petroleum coke revealed the strong influence of the carbon matrix in the capacity retention. Thus, the evaluation of different stoichiometries, as $Sn_{27}Co_{14}C_{59}$, $Sn_8Co_4C_{88}$, and $Sn_4Co_2C_{94}$, with similar Co/Sn ratio but progressive increase of the contribution of carbon phase, showed improved capacity retention for the sample with intermediate carbon content. Also, the high contribution of $CoSn_2$ in both the $Sn_7Co_1C_{92}$ original sample and cycled electrodes is responsible for the good electrochemical performance. Capacity values of 400 mAh g^{-1} at 35 mA g^{-1} were recorded after 40 cycles. These results are supported by the low internal impedance measured in $Sn_7Co_1C_{92}$ electrodes after several discharges.

The advantage of using a pyrolysis fuel oil residue as a carbon precursor resides in the fluidized state reached during the co-pyrolisys stage and carbothermal reduction. It ensures the formation of submicrometric Co-Sn intermetallic particles homogeneously embedded in the carbon matrix. The constancy of the internal resistance values recorded for the electrodes containing cobalt during cell cycling may justify their good capacity retention. However, the low performance observed in the FOPSn30Co15 sample was attributed to the increased contribution of cobalt rich phase $Co_3SnO_{0.7}$ observed by Mössbauer spectroscopy.

278

2- Hybrid materials of cobalt-tin and polyacrylonitrile

A mixture between cobalt oxalate, tin oxalate and dispersed polyacrylonitrile (PAN) molecules has been used as a new electrode active material for lithium ion batteries. The samples compositions were analyzed using FTIR, microanalysis with EDAX detector and C-N analysis. The electrode shows good capacity retention in the case that the imposed potential limit is below 2.0 V. The mechanism of the reaction between oxalates-PAN and lithium was studied by using ex-situ XRD and ^{119}Sn Mössbauer spectroscopy. The electrode materials become irreversibly amorphous at the beginning of the reaction, when tin oxalate is decomposed and Sn(IV) is detected. Then, the metallic ions are reduced and amorphous tin–cobalt alloys are formed. Finally, Li-Co-Sn alloys are reversibly formed near 0.0 V. The oxalate groups and the PAN form an electrochemically inert matrix. Due to the matrix, the aggregation of the amorphous particles into crystalline particles upon cycling is avoided. The extraction of lithium at the potential values near 2.0 V yields to tin–oxygen interactions and this feature disturbs the matrix and yields to capacity fade.

Composite electrodes $CoSn_x$-PAN were prepared throughout the reduction of tin and cobalt ions with $NaBH_4$ (aq.) in the presence of PAN (previously dissolved in dimethylformamide). Different relative amounts of PAN were used. The resulting product consists of tin–cobalt intermetallic nanoparticles or alloys surrounded by a PAN-based shell. Tin oxide was detected like a minor component in several samples. After annealing under inert atmosphere the $CoSn_x$-PAN hybrid materials, the organic molecules prevented the growth of the intermetallic grains and formed an amorphous carbon layer. The electrode containing nanosized $CoSn_2$ and PAN shows an excellent electrochemical behavior in lithium cells due to the structural stability of the PAN matrix and the small size of the metallic grains. For samples where the main intermetallic phase was nanocrystalline $CoSn_2$ the observed maximum reversible capacities are around 600 mAh g^{-1} and excellent capacity retention was achieved for PAN–$CoSn_2$ composite electrodes. According to ^{119}Sn Mössbauer results, in the charge process (lithium extraction) the segregation of tin-based alloys into Co-rich and Co-poor regions can take place.

As due to economic and environmental reasons the substitution of cobalt by iron can be advantageous, we tried to prepare $FeSn_x$/PAN composite materials following the

same procedure. However, in contrast to $CoSn_x$/PAN composites, the reduction of Fe(II) and Sn(II) leads to crystalline Sn.

The sonochemical method was used to prepare electrode materials containing intermetallic nanoparticles ($CoSn_x$) and PAN. The high-intensity ultrasound irradiation is applied to achieve small particle size. After annealing at 490°C under Ar-flow, the polymer PAN is partially carbonized and the metallic nanoparticles are surrounded by a carbonaceous matrix. The main metallic phase is $CoSn_2$. The carbonaceous coating and the surface oxides have been explored by using XPS. The resulting $CoSn_2$-carbonaceous phase electrode ($CoSn_2$@C) shows improved electrochemical behavior (ca. 450 mAh g^{-1} after 50 cycles) in comparison with previous reports on pure crystalline $CoSn_2$. The reaction between $CoSn_2$@C and Li has been studied by using XRD and ^{119}Sn Mössbauer spectroscopy. The formation of large grains of crystalline Li_xSn phases after the first discharge is discarded. The small particle size which is achieved by using ultrasonication and the carbonaceous matrix contribute to maintain the Co–Sn interactions during the electrochemical cycling. The aggregation of the nanosized metallic particles upon electrochemical cycling can be suppressed by the carbonaceous matrix (pyrolytic PAN).

3- *Electrodeposited thin films.*

Organic-inorganic hybrid films have been prepared and tested in lithium cell. Electrodeposited PAN and cobalt-tin films on titanium flat substrate are studied as a new electrode for lithium ion batteries. For the preparation of the electrode, firstly, cobalt and tin are electrodeposited on titanium substrate and an XRD-amorphous and metastable Co-Sn alloy is the main product. Secondly, PAN is deposited on the Co-Sn/Ti substrate through electropolymerization of the monomer (acrylonitrile). The electrodeposited metallic film contains Sn, amorphous Co-Sn alloy and intermetallic phases distributed in a thin film and submicrometric particles. The presence of PAN film was corroborated by using FTIR and SEM equipped with microanalysis. The PAN film in contact with the electrolyte solution (1 M $LiPF_6$ in EC:DEC) is gelled. The interfacial properties of tin-based electrochemically active material are modified via electrodeposition of PAN, as is observed by using electrochemical impedance spectroscopy. Areal capacities in the order of mAh cm^{-2} have been achieved.

Amorphous and self-organized TiO_2 nanotubes (nt-TiO_2) with different aspect ratios were prepared by titanium anodization. The morphology and aspect-ratio of the nanotubes can be controlled by selecting the anodization parameters such as imposed voltage and time. Since the surface of the amorphous TiO_2 nanotubes is critical to achieve high capacity, cycling stability and high rate performance in lithium batteries, in order to improve the stability of nt-TiO_2 electrodes, PAN has been deposited by electropolymerization. After electropolymerization, electron microscopy, composition mapping and XPS data confirmed that electrododeposited PAN covered the complete surface of open ends of the nanotubes. The resulting electrode material was tested in lithium cells, and showed reversible areal capacities in the order of 0.5 mAh cm^{-2} and good cycling behavior and within a wide potential window (0.0–3.0 V). The improvement of the electrochemistry is more evident for the lower aspect ratio nt-TiO_2, with capacity values normalized by the nanotubes length of around 0.25 mAh cm^{-2} µm^{-1} at slow rate. An areal capacity of 0.26 mAh cm^{-2} is delivered at 75C rate. The ion-conducting PAN layer ensures lithium ion access to the nanotubes protects the open end surface from undesirable reactions with the electrolyte and provides enhanced mechanical stability to the electrode and lower charge transfer resistance.

5.3   Conclusiones finales

Las conclusiones generales, obtenidas a la vista de los resultados presentados y discutidos en esta tesis doctoral, son las siguientes.

1. Materiales hibridos de Sn-Co-C se obtuvieron mediante un método de polimerización resorcinol/formaldehído combinado con la reducción carbotermal de los óxidos metálicos durante la carbonización. Los diagramas de difracción de rayos X revelaron la presencia de estaño y de fases cobalto-estaño que aparecen homogéneamente dispersos en la matriz de carbono.

2. La introducción de pequeñas cantidades de cobalto fue suficiente para alcanzar una mayor capacidad en comparación con el coque y las muestras libres de cobalto. La muestra con una relación molar de Sn/Co igual a 85:15 y una proporción mayor de óxido de metal - resorcinol, generó valores de capacidad cerca de 380 mAh g^{-1} después de 30 ciclos.

3. El efecto beneficioso de la presencia del cobalto fue refrendado con las medidas de impedancias. Así pues, los compuestos que contienen cobalto mostraron un menor aumento de la resistencia a la transferencia de carga tras el ciclado que las muestras libres de cobalto. Por lo tanto, la componente cinética parece desempeñar un papel importante en la mejora de la retención de la capacidad observada en estos materiales de Sn-Co-C.

    Las conclusiones 1-3 se desprenden del artículo 2.1

4. Los materiales híbridos de Sn-Co-C preparados por reducción carbotermal de los óxidos metálicos con un coque verde, como fuente de carbono, revelaron tanto por espectroscopia Mössbauer de ^{119}Sn como por difracción de rayos X, el predominio de fases de Sn y CoSn$_2$ para aquellas muestras que contienen una elevada proporción Sn/Co.

5. Se observó una dispersión homogénea de partículas metálicas sub-micrométricas en la matriz de carbono. A diferencia de las muestras con menor contenido en carbono donde aparecen granos metálicos aislados de elevado tamaño.

6. Las muestras con estequiometría $Sn_7Co_1C_{92}$ y $Sn_8Co_4C_{88}$ son capaces de mantener 400 mAh g^{-1} a 35 mA g^{-1} después de 40 ciclos. El buen comportamiento electroquímico de estos materiales híbridos está respaldado por medidas de impedancia y puede relacionarse con la mayor contribución de la fase $CoSn_2$, revelada por espectroscopia Mössbauer de ^{119}Sn.

7. La presencia de $Li_{13}Sn_5$ al final del primer ciclo en electrodos de composición $Sn_7Co_1C_{92}$ puede contribuir a la irreversibilidad de los primeros ciclos. Sin embargo, después de cinco ciclos, la contribución de $CoSn_2$ es significativa mientras que casi desapareció $Li_{13}Sn_5$, lo que explica la mejor retención de la capacidad observada en ciclos posteriores.

Las conclusiones 4-7 se desprenden del artículo 2.2

8. Hemos propuesto un método simple y rentable económicamente para la preparación de materiales híbridos Sn-Co-C. El estado fluido del precursor de carbono, FuelOil de Pirolisis (FOP), durante la reacción de copirólisis garantiza una alta dispersión de las fases intermetálicas en la matriz carbonosa.

9. La pérdida de capacidad observada durante los primeros ciclos se atribuyó a la presencia de una fase rica en cobalto $Co_3SnC_{0.7}$ detectada por difracción de rayos X y espectroscopia Mössbauer de ^{119}Sn. Estos resultados revelaron el efecto perjudicial de fases con un gran contenido de cobalto para el rendimiento electroquímico de estos materiales en celdas de litio.

Las conclusiones 8-9 se desprenden del artículo 2.3.

10. Después de la reacción electroquímica de la mezcla de oxalatos de estaño y de cobalto con litio se forma una aleación amorfa Li_yCoSn_x.

11. La matriz que contiene compuestos inorgánicos (litia y oxisales de litio) y orgánicos (PAN) puede mejorar el ciclado electroquímico impidiendo la cristalización y el aumento del tamaño de partículas.

Las conclusiones 10-11 se desprenden del artículo 3.1

12. El polímero PAN estabiliza la formación de aleaciones amorfas de Co-Sn y con pequeños tamaños de partícula obtenidas mediante la reducción química de Co(II) y Sn(II) con $NaBH_4$. Sin embargo, la reducción de Fe(II) y Sn(II) conduce a la formación de β-Sn cristalino. El material compuesto amorfo $CoSn_x@PAN$ presenta una capacidad gravimétrica en celdas de litio de alrededor de 480 mAh g^{-1}, siendo este valor superior a la capacidad máxima obtenida para el grafito.

13. El tratamiento térmico a temperaturas moderadas de estos materiales híbridos orgánicos-inorgánico lleva a la descomposición parcial del PAN (carbonización) dando lugar a una matriz carbonosa que rodea a las nanopartículas metálicas, y la cual contribuye a la estabilización del electrodo durante el ciclado electroquímico.

14. Electrodos con cantidad relativa de poliacrilonitrilo más baja presentaron capacidades reversibles en los primeros ciclos elevadas (alrededor de 600 mAh g^{-1}). El polímero (PAN) y los óxidos presentes pueden contribuir a la estabilización de las fases intermetálicas.

15. La formación de la capa pasivante (en inglés SEI) y litia (Li_2O) durante la descarga de la celda así como la formación de aleación amorfa Li_ySnCo_x al final de la descarga fueron corroboradas mediante el estudio del mecanismo de reacción usando diversas técnicas. Igualmente, en el proceso de carga se deduce la existencia de interacciones entre átomos de estaño y cobalto con oxígeno ($CoSn_xO_y$).

16. El pequeño tamaño de partículas que se consigue por el uso de la ultrasonicación de alta intensidad (método sonoquímico) y la matriz carbonosa contribuyen a mantener las interacciones entre átomos de estaño y de cobalto durante el ciclado electroquímico, evitando la agregación de las partículas metálicas nanométricas.

Las conclusiones 12-16 se desprenden de los artículos 3.2 – 3.3 – 3.4 – 3.5

17. Las películas finas de Co-Sn electrodepositadas sobre un sustrato de titanio dan lugar a electrodos con grandes capacidades por unidad de área.

18. La deposición de PAN mediante electropolimerización del monómero sobre los electrodos de cobalto-estaño da lugar a electrodos con interfaces más estables.

   Las conclusiones 17-18 se desprenden del artículo 4.1.

19. Una película de PAN conductora de iones litio puede mejorar el ciclado electroquímico de los electrodos formados por nanotubos de óxido de titanio en un amplio rango de potencial e incluso a velocidades altas. Siendo la mejora de la electroquímica más evidente para nanotubos con bajas relaciones de aspecto dando lugar a altos valores de capacidad normalizados por la longitud del nanotubo del orden de 0.25 mAh cm^{-2} μm^{-1}.

20. El carácter de película fina del recubrimiento de PAN sobre los nanotubos de TiO$_2$ proporcionan una ruta eficaz para el transporte tanto iónico como electrónico y la capacidad se ve levemente atenuada con el incremento de la velocidad de carga-descarga.

21. Estos resultados abren caminos interesantes para mejorar significativamente el rendimiento de nanotubos de óxido de titanio auto-organizados como electrodo avanzado para baterías de ión litio.

   Las conclusiones 19-21 se desprenden del artículo 4.2.